Semiconductor Dosimetry of Epithermal Neutron Beams for Boron Neutron Capture Therapy

A thesis submitted in fulfilment of the

requirements for the award of the degree

DOCTOR OF PHILOSOPHY

from

UNIVERSITY OF WOLLONGONG

by

Martin G Carolan, BSc (Hons)

Department of Engineering Physics

2003

TABLE OF CONTENTS

STATEMENT OF ORIGINALITY

I, Martin G Carolan, declare that this thesis, submitted in partial fulfillment of the requirements for the award of Doctor of Philosophy, in the Department of Engineering Physics, University of Wollongong, is wholly my own work unless otherwise referenced or acknowledged. The document has not been submitted for qualifications at any other academic institution.

Martin G Carolan

May 2003

Acknowledgements

I would like to acknowledge my supervisor Dr Jagdish Mathur who has demonstrated extraordinary patience during my completion of this thesis. His guidance and encouragement have been essential to the final completion of this work. It has been a privilege to work under him and to benefit from his many years of experience as a physicist.

I would also like to thank Prof Barry Allen from the Centre For Experimental Radiation Oncology at St George Hospital. He has been an important role model since my first contact with him as an undergraduate. His leadership of the Australian BNCT group is well known and I am fortunate he gave me this opportunity to contribute to that project. Together with Dr Mathur he has guided me through an honours project and this thesis. I am enjoying the satisfaction of my current career in Medical Physics due to the inspiration and opportunities that he has provided.

I am grateful to have been able to collaborate with Professor Anatoly Rosenfeld on much of the material in this thesis as well as other related projects during my candidature. This thesis would not exist without the MOSFET and PIN diode dosimetry concepts he has introduced. I have learnt an enormous amount about semiconductor dosimetry from Professor Rosenfeld's vast experience and expertise in this area. I have enjoyed the example of his dynamism, his encouragement and his friendship.

Many people have helped me along the way, either by teaching, useful advice and discussions or by assisting with operation of equipment. A special recognition is due in this regard to Harry Meriaty, Steve Wallace, Ned Blajevoic, Julia Mallesch, Yohannes Setiawan, Doug Moore, Roger Martin, Baiba Harrington, Greg Storr, Paul Miskelly, Geoff Constantine, Greg Kaplan, Terry Wall, Steve Grow, Howard Linklater, Peter Anthony, and Peter Ihnat.

Special thanks is also due to Dr Ray Moss, Prof Richard Maughan and A/Prof Jeff Corderre and their respective teams for so generously providing assistance and allowing access to their neutron beams.

My colleagues at Wollongong Hospital, Prof Peter Metcalfe, A/Prof Marty Butson and Dr Barry Elison have been generous in their encouragement, assistance and the time they have allowed me to devote to this project.

Thankyou to my parents and brothers and sisters who have supported me during this project. Thanks also to my tolerant and patient wife Fiona and the little family of my own, Felicity, Isabelle and Cormac, that I have acquired since commencing this project.

PUBLICATIONS

1. **M.G. Carolan**, G. Constantine, R. Godfrey, H.A. Meriaty, G. Storr, B.J. Allen, " A Filtered Neutron Beam at HIFAR" in *Advances in Neutron Capture Therapy.* R Barth and A Soloway Eds. Plenum Press New York 1994, pp 72- 76

2. **M.G. Carolan**, A.B. Rosenfeld, S.A. Wallace, H.A. Meriaty, G.J. Storr, V.I. Khivrich, R.L. Moss, B.J. Allen, "Silicon Dosimetric Diode for BNCT Using Accelerator Neutron Sources" in *Proceedings of the First International Workshop on Accelerator Neutron Sources for BNCT,* Jackson Wyoming USA, September 1994, , CONF-940976, pp. 299-309.

3. **M.G. Carolan**, S.A. Wallace, B.J. Allen, A.B. Rosenfeld, J.N. Mathur, H.A. Meriaty, F. Stecher-Rassmussen, R.L. Moss, C.P.J. Raaijmakers, M.W. Konijnenberg, "Validation of Monte Carlo Dose Planning Calculations by Epithermal Beam Dose Distribution Measurements in Phantoms" in *Proceedings of 6th International Symposium on Neutron Capture Therapy,* November 1994, Kobe Japan, Y. Mishima Ed. , Plenum Press New York.

4. J.L. Mallesch, D.E. Moore, **M.G. Carolan**, K. Narayan, B.J. Allen, "Microvasculature casting technique for capillary endothelial damage after boron neutron capture therapy damage", in *Proceeedings of the 6th International Symposium on Neutron Capture Therapy,* November 1994 Kobe Japan, Y. Mishima Ed. Plenum Press NY New York.

5. A.B. Rosenfeld, **M.G. Carolan**, G.I. Kaplan, B.J.Allen, V.I. Khivrich, "MOSFET Dosimeters: The Role of Encapsulation on Dosimetric Characteristics in Mixed Gamma-Neutron and Megavoltage X-ray Fields", in *IEEE Trans. Nuc. Sci.* 1995, *NS42, N6 Dec 1995* pp1870-1877.

6. MJ Butson, AB Rosenfeld, JN Mathur, **MG Carolan**, TPY Wong, PE Metcalfe, "A new radiotherapy surface dose detector: The MOSFET", *Med. Phys. 23(5), May 1996 pp655-658.*

7. Khivrich VI, Varentsov MD, Litovchenko PG, Anokhin AI, Zinets OS, Reinhard MI, Rosenfeld AB, **Carolan M**, Alexiev D, "High purity silicon as a basic

material for manufacturing of radiation detectors and integral neutron radiation dosimeters", *IEEE Trans Nuc Sci 43(6) Dec 1996, pp:2687-2692*.

8. AB Rosenfeld, GI Kaplan, **MG Carolan**, BJ Allen, RL Maughan, M. Yudelev, C. Kota, " A New Approach to Simultaneous Macro and Micro Dosimetry in Neutron Therapy with a MOSFET probe", *Journal of Brachytherapy International, 1997;13:129-136*.

9. AB Rosenfeld, GI Kaplan, **MG Carolan**, BJ Allen, R Maughan, M Yudelev, C Kota "Simultaneous macro and micro dosimetry with MOSFETs ", *IEEE Trans. Nuc. Sci.vol . 43, No. 6, Dec 1996, pp2693-2700*

10. **MG Carolan**, AB Rosenfeld, BJ Allen, "Dosimetry of BNCT Epithermal Neutron Beams Using MOSFET and PIN Diode Neutron Dosimeters" in proceedings of the *6th International Radiopharaceutical Dosimetry Symposium, Gatlinberg* TN May 1996.

11. **MG Carolan**, BJ Allen, AB Rosenfeld, JN Mathur, "Characterisation and use of MOSFET gamma dosimeters and silicon PIN diode neutron dosimeters for epithermal neutron beam mixed field dosimetry" in *Proceedings of the Seventh International Symposium on Neutron Capture Therapy*, Zurich, November 1996.

12. Kaplan GI, Rosenfeld AB, Allen BJ, Booth JT, **Carolan MG**, Holmes-Siedle A. “Improved spatial resolution by MOSFET dosimetry of an x-ray microbeam” *Med Phys. 2000 Jan;27(1) :239-44*.

ABSTRACT

Boron neutron capture therapy (BNCT) is a binary targeted therapy that uses suitably designed pharmaceuticals to deliver ^{10}B to tumor cells. The region is then irradiated with neutrons and neutron capture by the ^{10}B nucleus leads to the emission of an alpha particle and lithium ion. These have very short ranges similar to the dimensions of a biological cell and therefore the technique could have potential for selective killing of tumour cells. In order to achieve adequate neutron fluxes at the site of the tumour epithermal (0.5 eV – 10s of keV) neutron beams are used. A review of the general details of BNCT is presented in this thesis.

This thesis investigates the use of two semiconductor devices for measuring the neutron and gamma dose components involved in epithermal neutron beams used for BNCT.

The silicon lattice in PIN diodes undergoes displacement damage when irradiated with neutrons. This leads to a change in the forward bias voltage of the diode that is proportional to the neutron dose received.

To verify that the energy dependence of this effect follows the published silicon displacement damage KERMA (*Kinetic Energy Released per Mass of Absorber*) data measurements were performed using quasi-monoenergetic neutrons obtained from a Van de Graff accelerator (Ansto) in the energy range from 90 keV – 890 keV. These measurements were in agreement with the published data for silicon displacement damage KERMA. A sensitivity factor for the diodes was also derived from these measurements. The thermal neutron sensitivity of the PIN diodes was then determined using the TC-10 thermal neutron column on the Moata reactor at Ansto. The sensitivity results were in general agreement with the Van de Graff derived

sensitivity factor.

Since the silicon damage KERMA is not the same as the tissue KERMA function PIN diodes are not intrinsically tissue equivalent. A Monte Carlo (MNCP) ideal beam study was undertaken to see if for some limited energy range tissue dose could be parameterised in terms of silicon damage dose and foil activation. This was found to be approximately true for neutron energies from thermal to 100 keV. Coefficients are given that allow tissue dose to be determined on the basis of a single PIN diode and activation foil measurement in spectra where the maximum neutron energy is 100 keV or less.

MOSFETS can be used as gamma radiation dosimeters by measuring the change in threshold voltage (simplistically understood as the potential applied to the gate to initiate current flow from source to drain electrodes) that occurs when they are exposed to radiation. The MOSFETs used in this study were characterised using a Varian 2100C medical linac beam and low energy x-rays from a superficial x-ray unit. The sensitivity of the MOSFETs was measured with different potentials applied to the gate during irradiation. Depth dose profiles in 6 MV x-ray beams were measured and found to be in good agreement with both ionisation chamber measurements and MCNP simulations. This good agreement was also obtained for the buildup region.

Although the silicon oxide layer of the MOSFET is not intrinsically very sensitive to neutron irradiation the presence of encapsulating materials leads to the generation of secondary photons and electrons which lead to shifts in threshold voltage and therefore confound gamma ray measurements in mixed neutron / gamma fields. To determine the energy dependant neutron response function of the MOSFET

a detailed MCNP simulation was used. A lithiated shield was also incorporated into this model. The calculated neutron response functions were used to correct for neutron contributions to MOSFET measurements in mixed fields.

MOSFET thermal neutron responses were measured using a series of measurements with MOSFETS both with and without lithiated covers exposed in the the Moata thermal neutron column at Ansto. The measurements were repeated with various gate potentials. The gamma doses measured were consistent with gamma doses measured using paired ionisation chambers.

The Petten HB11 facility is briefly described as are phantoms and MCNP models fabricated by S Wallace for an associated work. Measurements using PIN diodes and MOSFETs in phantoms exposed in the HB11 beam are described. Foil activation data is compared to MCNP calculations to validate the MCNP models used. This thesis presents a number of results that have been recalculated in more detail and with various parameters changed. In particular the effect of variations in phantom hydration have been incorporated as have response functions for MOSFET detectors and associated shields.

PIN diode measurements in a Perspex cube phantom exposed in the HB11 beam show good agreement with MCNP calculated silicon displacement dose. Similarly good agreement is obtained for a cylindrical phantom filled with tissue equivalent gel when the hydrogen content of the gel in the original model is corrected for dehydration. Measurements in a more complex skull phantom show larger discrepancies between the experimental results and a MCNP simulation especially at depth. The discrepancies range from 25 – 300% in absolute terms but are only 2-3% of the maximum silicon dose.

MOSFET measurements performed in the Perspex cube phantom using lithiated covers show excellent agreement with ionisation chamber measurements (also with lithiated covers). Measurements in a cylinder phantom and head phantom using lithium/perpex covered MOSFETs are compared with Monte Carlo calculations of induced gamma dose. In this case the measured gamma doses at approximately 2 cm depth appear to be too low. Further investigation involving a detailed MCNP simulation including the lithiated MOSFET covers in the model indicated that the covers suppress the thermal neutron flux at the measurement point and therefore the gamma dose is also reduced. Measurements at greater depths show a similar effect but to a lesser extent.

The epithermal neutron beam at the Brookhaven Medical Research Reactor (BMRR) is described is described. PIN diode and MOSFET measurement results in a Perspex cube phantom are also presented. Reasonable agreement between calculated and measured PIN diode results is observed. MOSFET measurements show good agreement with the known percentage depth dose curve for the total gamma dose. However there is a discrepancy in the absolute magnitude of the measured gamma doses. It is proposed that this is also due to thermal neutron flux depression arising from the use of relatively thick lithiated neutron shields around the MOSFETS.

In summary; It is demonstrated that PIN diodes could be useful for verifying treatment planning dose distributions in epithermal neutron beams. This includes the possibility of on line real-time measurements. They could also be used in conjunction with an activation foil to yield tissue equivalent dose measurements where the maximum neutron energy is less than 100 keV. Lithium shielded MOSFET measurements can be reconciled with calculated gamma dose distributions when the

effect of flux depression is taken into account. However the perturbations introduced by the shield mean that the measured dose does not represent the dose at the measurement point in the absence of the shield. In order to use MOSFETs for gamma dosimetry in epithermal neutron beams different encapsulation is required to minimise neutron response and eliminate the need for lithiated covers. It is suggested that MCNP simulations of MOSFETs similar to the models in this thesis would provide an adequate tool for optimising the appropriate encapsulation.

TABLE OF FIGURES

TABLE OF TABLES

CHAPTER 1 INTRODUCTION

This thesis describes the development and application of a number of techniques useful for the dosimetric characterisation of mixed gamma and neutron fields such as are to be found in boron neutron capture therapy (BNCT). Because of the very different biological effects of neutron and gamma (γ) radiation the accurate quantification of each of the radiation components present in a epithermal neutron beam is of paramount importance. This detailed knowledge is required both for the purpose of better understanding radiobiological effects in basic radiobiology studies and also for the purpose of predicting dose distributions within patients being exposed to epithermal neutron beams for therapy (treatment planning and treatment plan verification).

BNCT is a binary therapy for cancer which makes use of a boron (^{10}B) laden drug which accumulates preferentially in the tumour cells that are the object of the treatment. The region of the target tumour cells is then irradiated with neutrons. Neutrons with thermal energies have a relatively high probability of reacting with ^{10}B due to the large capture cross section of the boron. The ^{10}B cross section is up to 3 orders of magnitude greater than the capture cross sections of most nuclides naturally occurring in any significant quantity in the body. The capture of a thermal neutron by ^{10}B leads to a reaction which results in the emission of an alpha particle (α) and a lithium (^{7}Li) ion. These are both high linear energy transfer (LET) particles with short ranges (~10 μm) and therefore highly effective in damaging the DNA of cells. The short range of these particles ensures that tumour cells can be killed very

selectively if the boron is localised in the target cells or on the surface of the cells. This means that the pattern of energy deposition on a microscopic scale is paramount in understanding the biological effects of this mode of cancer therapy.

The neutron beams of choice for BNCT applications have neutron energies in the epithermal range (~1 eV - ~ 30 keV) and are derived from nuclear reactors or accelerator based neutron sources. In both cases these beams are moderated and filtered to tailor the neutron spectrum to that desired, however, some fast neutrons, thermal neutrons and γ radiation are inevitably present in the final beam.

The techniques used for measuring neutron and gamma doses in mixed fields are many and varied. Amongst the most frequently used are ionisation chambers (IC), proton recoil proportional counters, thermoluminescent dosimeters (TLD), activation foils and track etch detectors. Each of these have many advantages and some disadvantages depending on the part of the neutron energy spectrum to be measured, the actual quantity to be measured (e.g. flux or dose), the spatial resolution required or the speed with which results are required. For absolute neutron spectrum determinations resonance activation foils and proton recoil proportional counters can be considered as the gold standards. Resonance activation foils allow accurate absolute flux measurements at neutron energies corresponding to the resonances in the cross sections of the foil being used. The foils commonly used have resonances that span the epithermal part of the spectrum in a discontinuous way. Proton recoil spectroscopy by contrast provides continuous spectral information and has the good energy resolution for the faster end of the neutron spectrum.

For determining doses rather than fluxes paired ionisation chambers offer greater ease of operation, and in principle at least, the possibility of a more or less

direct readout of tissue equivalent (TE) dose. However in practice obtaining true tissue equivalence and correct calibration is a non trivial exercise. TLDs offer high spatial resolution but require significant deconvolution to extract mixed field dose components. Track etch detectors (e.g. CR-39 polycarbonate film) offer very high spatial resolution for the recording of individual high LET particle tracks. They can therefore be used for mapping of thermal neutron flux by using a suitable converter/radiator or for recording fast neutron dose via proton recoil tracks. Track etch detectors are perhaps most useful for microdosimetry studies where they can be used to record individual particle tracks the position of which can then be related back to histological or biological features of interest (e.g. cells, microvasculature or regions in tumours[1]).

In addition to experimental measurement techniques, Monte Carlo radiation transport computer simulations are increasingly used to determine doses in complex geometries in mixed neutron - γ fields. For most materials and neutron energy ranges of interest for BNCT, neutron cross section data and the physics of the Monte Carlo codes are adequate to provide accurate calculations of dose. However these Monte Carlo dose calculations depend for their accuracy on an accurate knowledge of the geometry and isotopic make up of the materials being simulated as well as an accurate knowledge of the initial neutron spectrum as an input to the calculation. Therefore it is essential that the results of Monte Carlo simulations are verified experimentally. Once verified for some standard geometry and material configurations for a given neutron beam facility more weight can be placed on the computed results of simulations for more complex geometries (e.g. patients) which are less amenable to invasive experimental measurements.

The work described in this thesis will focus on dosimetry considerations for BNCT with a particular emphasis on the development and application of some new detectors. These are the MOSFET and PIN diode dosimeters.

Metal Oxide Semiconductor Field Effect Transistors (MOSFETs) change their electrical characteristics in response to gamma radiation, and to a lesser extent and dependant on their encapsulation, in response to neutron irradiation. MOSFETs have very small physical dimensions (several 10's or 100's of μm) giving them good spatial resolution. They can be configured for use in an active mode to provide real time dose data which could be useful for on line monitoring of patient doses. They can also be used in passive mode unconnected to any external circuit as an integrating dosimeter which stores the accumulated dose information for periods of months or years with very little fading.

PIN diodes have previously been applied to fast neutron dosimetry as personnel accident dosimeters and for military applications. Like the MOSFET they have the advantage of small size (junctions with dimensions of a few mm). The mode of operation of PIN diodes relies on the characteristic behavior of charge carriers in intrinsic high resistivity silicon. When silicon is exposed to neutron radiation lattice defects are introduced into the silicon crystal. These act as recombination centres for charge carriers. As the neutron dose and thus the number of recombination centres increases the carrier lifetime decreases due to the larger probability of carriers recombining at lattice defect sites. This is macroscopically observable as an increase in the forward bias voltage of the diode. The change in bias voltage is proportional to the neutron dose being measured.

One advantage of using silicon for fast neutron dosimetry is that the energy

response function of the silicon at neutron energies above 200 keV is approximately proportional to tissue KERMA (kinetic energy released per mass of absorber). That is, the silicon response function in a fast neutron spectrum is tissue equivalent. Unfortunately this is not the case for lower energy neutrons although PIN diodes do respond to all parts of the neutron spectrum of interest for BNCT.

In this thesis the photon and neutron responses of MOSFETs and PIN diodes are characterised. Response as a function of accumulated dose, neutron and photon energy and temperature are all investigated. The photon response of the MOSFET is investigated experimentally using x-ray and gamma photon sources. The neutron response of the MOSFET and the dependence of this response on the encapsulation of the device is investigated both experimentally and with Monte Carlo radiation transport simulations. The response of the PIN diode is measured in a number of different neutron fields derived from reactors and accelerators.

Measurements using PIN diodes and MOSFETs in phantoms exposed in epithermal neutron beams are described. These included measurements in the HB11 BNCT beam at the High Flux Reactor (HFR) in Petten, The Netherlands as well as measurements on the epithermal BNCT beam at the Brookhaven Medical Research Reactor at Brookhaven National Laboratory (BNL), USA.

CHAPTER 2 REVIEW OF BNCT

INTRODUCTION

In this chapter the basic principles of BNCT will be explained, a brief summary will be given of neutron sources for BNCT, dosimetry techniques for determining the physical dose components of importance and radiobiological considerations in determining the effect of this dose. The most commonly used boronated pharmaceuticals and their behaviour will be briefly summarised as well as treatment planning techniques and the characteristics of some tumours proposed for BNCT treatment. Finally a history of clinical trials of BNCT will be summarised.

THE PRINCIPLES OF BNCT

BNCT relies on a thermal neutron induced reaction in the ^{10}B isotope. This reaction has a thermal neutron cross section of 3838 barns as shown in Figure 2-1 and proceeds as follows:

$$^{4}He + {}^{7}Li + 2.79 \text{ MeV } (6.3\%)$$

$$\nearrow$$

$$^{10}B + n_{th} \rightarrow {}^{11}B$$

$$\searrow$$

$$^{4}He + {}^{7}Li^{*} + 2.31 \text{ MeV } (93.7\%)$$

$$\downarrow$$

$$^{7}Li + \gamma + 0.48 \text{ MeV}$$

In the 6.3% probability branch the energy of the α particle is 1.78 MeV and of the ^{7}Li ion, 1.01 MeV. The ranges in water of the α and ^{7}Li particles in this case are 8.9 μm and 4.5 μm. For the 93.7% branch the α particle and ^{7}Li ion energies are 1.47 MeV and 0.84 MeV respectively. The ranges in water in this case are 7.2 μm for the α and 4.1 μm for the ^{7}Li ion. These ranges were determined by Charlton and Allen[2] using the TRIM code of Ziegler[3]. The 0.48 MeV γ emitted in 93.7 % of reactions will have a mean free path of approximately 10 cm in tissue.

When a ^{10}B(n,α)^{7}Li reaction occurs most of the energy will be deposited within approximately 9 μm of the interaction. This is of the same order of magnitude as the diameter of most biological cells. A consequence of this is that if ^{10}B can be delivered to the target cells and localised on or in them and if a sufficient fluence of thermal neutrons can be delivered to the same region preferential cell kill can be achieved with very high spatial resolution. Another consequence of the short range of these high Linear Energy Transfer (LET) particles is that the efficiency of this cell killing is very sensitive to the location of the ^{10}B. The efficiency of cell killing is quite sensitive to the cell geometry and to whether the ^{10}B is external to the surface of the cell, within the cytoplasm or closely associated with the cell nucleus[2,1].

In addition to the desired ^{10}B(n,α)^{7}Li reactions in the tumour some reactions will occur between incident neutrons and ^{10}B which is not located in the tumour but rather in other organs or the blood stream. This gives rise to an undesirable normal tissue dose. This dose in combination with other dose components due to neutron reactions with other elements in the body will determine the normal tissue tolerance dose limits. These other reactions lead to a non selective dose which is not targeted to the tumour cells. The main elemental components of tissue[4] are listed in Table 2-1 along

with their total thermal neutron cross sections.

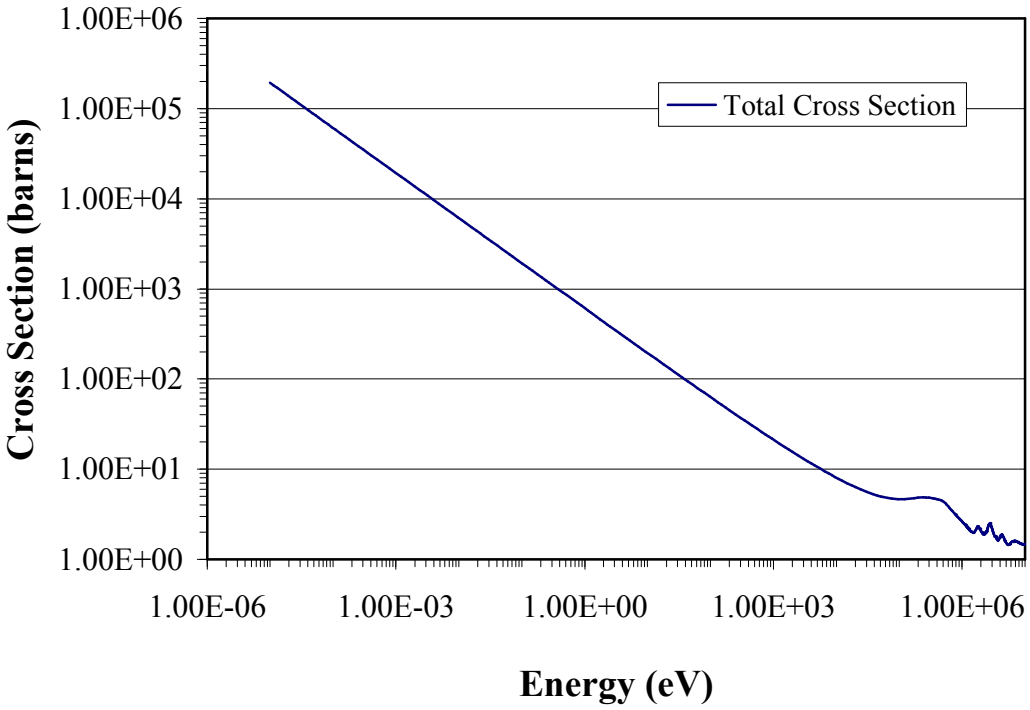

Figure 2-1. Neutron capture cross section for ^{10}B. Note the very large thermal cross section.

Table 2-1. Elemental composition for average soft tissues from ICRU 44 and thermal neutron cross sections[5].

Element	% Mass Composition	Thermal Cross Section (barns)
H	10.5	20.78
C	25.6	4.749
N	2.7	11.67
O	60.2	3.780
Na	0.1	3.496
P	0.2	3.134
S	0.3	1.488
Cl	0.2	45.60
K	0.2	3.926

Cross sections for the main components are plotted in Figure 2-2. From these data it can be seen that the ^{10}B cross section is significantly higher than any of the naturally occurring elements in the body.

The most significant non ^{10}B contributions to normal tissue dose come from:

(1) The $^{14}N(n,p)^{14}C$ reaction. The energy of the proton emitted from this reaction is 0.59 MeV with a range of 10.3 μm in tissue. The recoiling carbon atom has an energy of 0.04 MeV[2].

(2) Gamma rays in the neutron beam and gamma rays generated by capture in the patient or phantom itself. The main reaction in this case is the $^{1}H(n,\gamma)^{2}H$ reaction. The energy of the γ from the $^{1}H(n,\gamma)^{2}H$ reaction is 2.2 MeV. The dose arising from this γ component will be highest in regions of high thermal neutron fluence but diffuse and widely distributed

(3) The $^{1}H(n,n')^{1}H$ proton recoil reaction. The precise contributions will vary depending on the neutron spectrum[6] and the variations in tissue composition from one organ to another. The energy of the knock on protons will be deposited locally.

Because each of these dose components has a different biological effect they all need to be quantified separately and accurately in order to determine the biological effect that a given total physical dose will have. Once each physical dose component is determined the appropriate weighting factor can be applied to determine a dose parameter proportional to the total biological effect (see below).

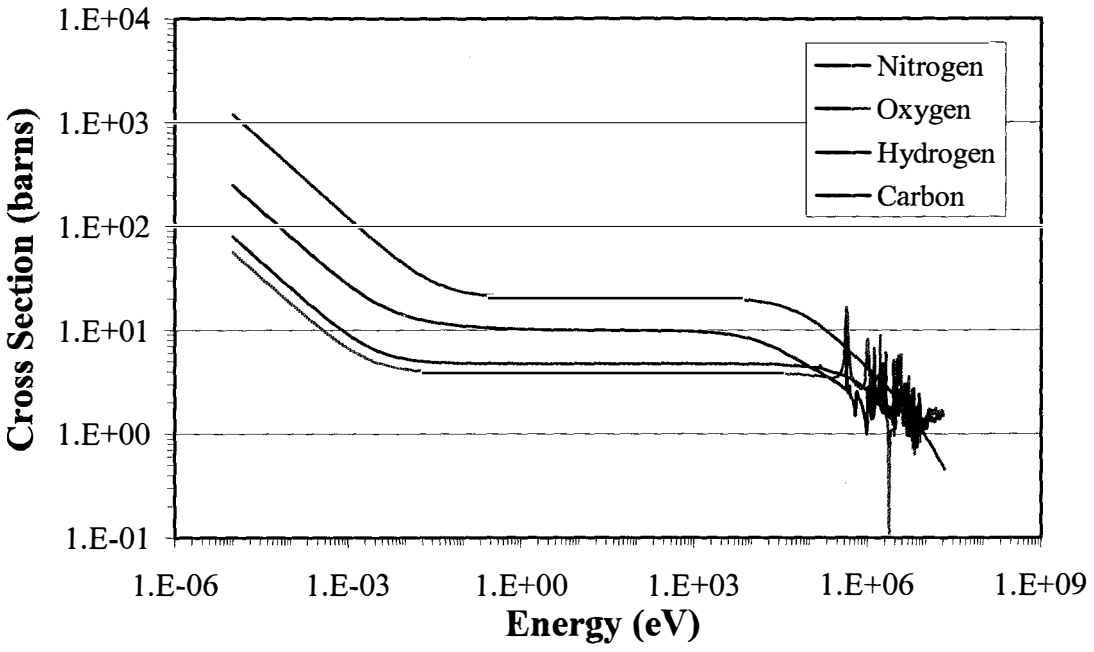

Figure 2-2. Some (total) neutron cross sections for the main elements in the body[5].

NEUTRON SOURCES

NEUTRON BEAM PARAMETERS

Early attempts at BNCT at Brookhaven and latter in Japan made use of thermal neutron beams. Although the ^{10}B cross section is largest at thermal energies inadequate penetration of thermal neutrons confounds the treatment of all but superficial tumours. Thus a therapeutic advantage can only be obtained within a few centimetres of the surface depending on the ^{10}B concentration obtained in the tumour. In a thermal beam the thermal neutron flux falls to approximately half its incident value at a depth of about 2 cm in a tissue equivalent phantom[7].

Therefore to enable the treatment of more deep seated tumours it is necessary to use more energetic and therefore more penetrating neutrons. The use of purely fast neutrons is not ideal either however since although these are more penetrating they will also deliver a non specific high dose due to proton recoil reactions.

The determination of the best neutron energies has been performed using so called "ideal beam" calculations[8,9]. These studies are done using Monte Carlo transport simulations of monoenergetic neutrons in phantoms. The neutron energies, source angular distributions and beam diameters can be varied as can the geometry of the phantom itself.

A number of figures of merit (FOM) parameters are defined to compare different ideal beams[10]. These are the advantage depth (AD), the advantage ratio (AR) and the advantage depth dose rate (ADDR). These are defined for a given beam and phantom configuration and for specified tumour and normal tissue ^{10}B concentrations. The advantage depth is that depth where the total therapeutic dose is equal to the maximum background dose. Since the therapeutic dose will depend upon the tumour ^{10}B concentration the AD will increase as the ratio of tumour to normal tissue ^{10}B concentration increases. The minimum AD is the AD with the ratio of tumour to normal tissue ^{10}B concentrations assumed to be 10. The maximum AD is the AD with this ratio assumed to be infinite, i.e. normal tissue ^{10}B concentration is zero. The maximum AD can be increased by increasing the tumour ^{10}B concentration. The AR is the ratio of the integral of the therapeutic dose to the integral of the background dose over some depth range. The ADDR is the dose rate at the minimum AD.

The ideal beam studies of Yanch and Harling[9,11] studied beam energies

ranging from thermal neutrons through to 800 keV neutrons with emission angles ranging from 0 to 90°. Beam diameters from 6 cm to 33 cm were considered. They assumed a ^{10}B concentration in tumour of 30 μg/g and in normal tissue of 3 μg/g. Results of these calculations showed that for a 6 cm diameter parallel beam neutrons in the energy range from 10 eV - 10 keV have advantage depths greater than or equal to 7 cm. This useable energy range increases as the diameter of the beam increases and for a beam of 14 cm diameter such as may be used in treatments of the brain the useful neutron energy range is from 1 eV to 40 keV. The ADDR has a minimum at an energy of about 2 keV before increasing at higher energies due to fast neutron effects.

Thus from the point of view of treating tumours at depths up to 7 cm, which corresponds with the midline of the brain, neutrons in the energy range from about 1 eV - 40 keV will be adequate although a range from 1eV to 10 keV is more commonly specified as the ideal. This energy range corresponds approximately with the minimum in the neutron tissue KERMA curve shown in Figure 2-3. For neutron beam energies less than the minimum in this curve the $^{14}N(n,p)^{14}C$ contribution increases and will deliver an undesired dose to the surface of the patient since these low energy neutrons do not penetrate far. For neutron energies greater than the minimum in the KERMA curve the $^{1}H(n,n')^{1}H$ proton recoil reaction contribution will increase doses to normal tissue over a depth range that depends on the energy of the primary beam.

The depth of penetration of the beam as well as the induced gamma dose generated in the patient can be further modified by heavy water substitution in the patient (effectively reducing the $^{1}H(n,\gamma)^{2}H$ and the $^{1}H(n,n')^{1}H$ contributions to dose).

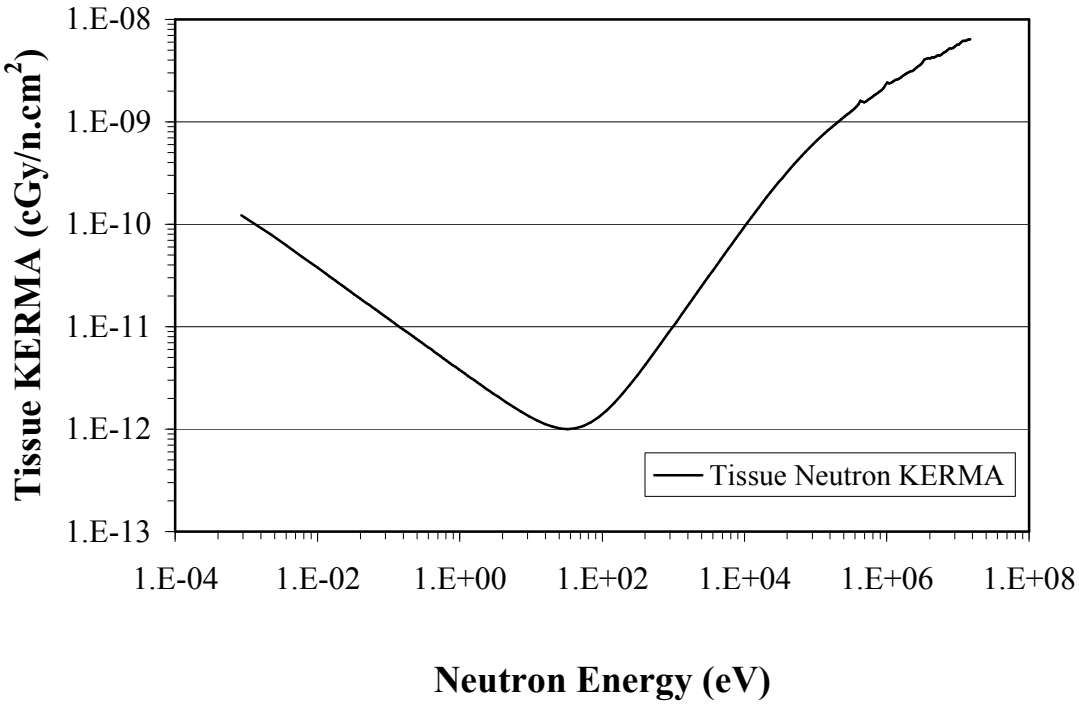

Figure 2-3. Neutron KERMA for tissue as function of neutron energy.

This has been used in clinical applications with thermal BNCT and a simulation study by Wallace et al[12] demonstrated that by replacing 20% of the H_2O in the patient with D_2O a similar advantage can be obtained with epithermal neutron beams. With D_2O substitution it is possible to reduce the induced gamma dose rate by approximately 30% and also to improve the epithermal neutron penetration resulting in a more homogeneous neutron field at depth and therefore improved therapeutic ratios.

The following parameters define the specification of an epithermal neutron beam for BNCT[13].

(1) *Epithermal Beam Intensity* (defined as the flux of neutrons in the beam with energies between 0.5 eV and 10 keV) should ideally be

at least 10^9 neutrons $cm^{-2}.s^{-1}$. Less intense beams than this will require unreasonably long irradiation times (> 1 hour) which presents clinical difficulties in terms of prolonged immobilisation of the patient and may also be sub-optimal in terms of the boron drug biodistribution kinetics.

(2) *Fast neutron flux* component (taken as neutron flux with E >10 keV) should be as low as possible since this will lead to a non targeted normal tissue dose from recoil protons. Reducing the fast neutron component will always be to some extent a compromise with increasing the epithermal flux. The fast neutron component in most operating epithermal beams is typically in the range 2.5 – 13 $\times 10^{-13}$ Gy cm^{-2} per epithermal neutron.

(3) The *gamma ray* component in the beam should be minimised. Some gamma rays are unavoidably generated in the patient ("induced gammas") however the beam gamma KERMA component is typically between 1 – 13 $\times 10^{-13}$ Gy cm^{-2} per epithermal neutron and should be at the lower end of this range.

(4) *Thermal flux* in the incident beam will lead to increased superficial tissue dose and should therefore be minimised. A maximum thermal flux 5% of the epithermal flux has been suggested.

(5) *Neutron current*[a] *to flux ratio* reflects the proportion of forward directed neutrons in the beam. A higher ratio results in minimal

[a] Neutron current is the number of neutrons per second crossing a unit area normal to the direction of neutron flow.

beam divergence and enables better dose delivery at depth. A suggested target for this parameter is 0.7.

(6) *Maximum usable beam diameter* is typically between 12 and 14 cm on exiting beams.

In practice the available neutron source will be the final determinant of the precise range of neutron energies which will be delivered. However preliminary ideal beam calculations determine the preferred neutron energies for the design of neutron sources for BNCT. A combination of moderators, collimators and scattering or attenuation filters is then used to tailor the primary neutron source to the desired spectrum and geometry.

FILTERS AND MODERATORS[13]

To obtain an epithermal neutron beam with the required specifications elaborate arrangements of moderators and filters are required[14]. For reactor designs where the reactor core subtends a large angle at the beam port a moderator based design may be possible (eg Choi et al[15]). In this case the exit port of the beam effectively views a large section of the core and if an optimised moderator can be introduced into the space in between the core and the exit port fast neutrons from the core can be moderated and collimated (by scattering) to exit the beam port with the required energy spectrum. In this design a spectrum shifter is inserted as close as possible to the core and this serves to moderate and scatter fast neutrons towards the beam port. Materials used for moderators[13] include Al, Al_2O_3, AlF_3, D_2O, C and S. The patented metal ceramic composite of Al and AlF_3 called *FLUENTAL* has been used in the construction of the Finnish BNCT facility on the FiR. These are all light

elements and therefore effective moderators. They do not have long lived activation products and are durable in high radiation environments. Combinations of Al_2O_3 and AlF_3 have been used to good effect for this application because the combined cross sections of the O and F eliminate most of the minima in the Al cross section.

For a given reactor power the main beam design parameter determining the number of available neutrons at the treatment port is the core to patient distance. By reducing this distance the beam intensity can be increased. However this is at the cost of also reducing the neutron current to neutron flux ratio. In practice about 1.5 –2.5m is required to accommodate the necessary filters and moderator components. In some cases the intensity of the beam can be improved by the use of a conical collimator that converges to the beam exit port. This collimator can be lined with high atomic weight neutron reflecting materials[13].

The reduction of unwanted thermal neutron and gamma dose components is achieved by use of filters[13]. Both lead and bismuth are effective attenuators of gamma rays but bismuth has a lower cross section for epithermal neutrons and is therefore more often used. Another material sometimes used (eg Petten HFR HB11 beam) for gamma attenuation is liquid argon. Clearly there are extra difficulties arising from incorporating a volume of liquefied gas and the associated cryogenics into a beam line and this material is not used elsewhere for this purpose. To eliminate thermal neutrons from the beam cadmium, boron or lithium could be used. Cadmium has a sharp cutoff at 0.5 eV but generates an energetic gamma ray upon neutron capture. Whereas ^{10}B generates a low energy gamma ray and ^{6}Li generates no gamma ray but both of these isotopes have *1/v* cross sections and therefore will tend to attenuate some of the desirable epithermal neutrons as well as absorbing the thermal

neutrons.

Where only a narrow beam channel between the exit port and the core is available the reactor power generally needs to be higher[16]. In this case the volume of the beam line is occupied with filters the purpose of which is to attenuate the fast neutron component of the beam as well as the thermal flux and gamma dose components. Filter components typically used or proposed for this purpose include Fe, S, Ni, and Ar.

FISSION PLATES

Another method currently being utilised on some reactors to enhance epithermal beam flux involves the use of a fission plate. This technique introduces a plate of fissile material outside the reactor core and close to the exit of the beam port. In this way the thermal neutron flux in the beam originating from the reactor core is used to generate a high flux of fast neutrons closer to the patient. These are then moderated using the types of moderators described above. An example of this arrangement is the fission plate converter designed for the Brookhaven Medical Research Reactor[17]. In this case the core is surrounded by a graphite reflector. Adjacent to this reflector along the axis of the beam is a 19 cm thick Bi gamma attenuator. Eight fission plates are then interposed in the beam. These are contained in a container filled with moderator/coolant (D_2O) to remove the heat generated in the plates. Each plate contains approximately 1 kg of 20% enriched ^{235}U and measures $100 \times 10 \times 0.3$ cm. This is then followed by a 48 cm thick Al filter and a 24 cm thick Al_2O_3 moderator. A thin layer of Cd (0.05cm) is used to remove thermal neutrons from the beam and a further 10 cm of Bi is used to remove gamma rays

generated in the fission plate / filter / moderator assembly. The design study for this arrangement indicated that the epithermal neutron flux could be boosted by a factor of about 6-7 times the available epithermal flux without fission plates. The expected epithermal flux with the fission plates was 1.2×10^{10} n/cm^2.s. The fast neutron dose per epithermal neutron would also reduced by approximately 30% and the current to flux ratio also improved.

ACCELERATOR SOURCES

Currently used neutron sources for BNCT are reactor based. This is principally due to the availability of such sources and the relatively high fluxes they can deliver. For wider use of BNCT clinically the neutron source should ideally be smaller and less expensive than a reactor so that it could be installed in a hospital radiation oncology centre. Accelerator sources promise this possibility if current clinical trials support the clinical efficacy of BNCT.

Sources of neutrons for BNCT which are under development include a number of accelerator based systems. These make use of various accelerator technologies including tandem electrostatic and (radio frequency quadrapole[18]) RFQ proton accelerators[19]. In general the selection of reactions (targets and projectiles) for accelerator based neutron sources depend upon several factors[20]:

1. Physical stability of the target material under the high temperature conditions generated by high incident beam currents,
2. high natural abundance of the target isotope to reduce cost and also reduce unwanted reaction products from sister isotopes in the target,
3. Suitable reaction Q values and preferably low threshold energies for the

projectile beam. For Q>0 the resultant neutrons will have energies in the MeV range. Therefore ideally -3.0MeV < Q < -0.5MeV is desirable to reduce the required accelerator energy.

4. Suitably large cross section to make the neutron yield efficient.

These criteria were applied to a range of reactions including $^{3}H(p,n)$, $^{7}Li(p,n)$, $^{9}Be(p,n)$, $^{11}B(p,n)$, $^{12}C(d,n)$, $^{19}F(p,n)$, $^{45}Sc(p,n)$ and $^{63}Cu(p,n)$ by Dolan et al[20] who concluded that the lithium reaction was the favoured option. A similar analysis was performed by Brugger and Kunze[21] which also considered a wider range of other reactions including $^{51}V(p,n)$ and $^{65}Cu(p,n)$ both of which produce neutrons of suitable energy (E_n<1 keV for E_p at the reaction threshold energy) but have low cross sections.

The most studied reaction for neutron generation is the $^{7}Li(p,n)^{7}Be$ reaction which has a reaction threshold of 1.88 MeV. This means that proton energies need only be about 2.5 MeV[22]. The optimal energy will depend upon the precise design of the moderator and accelerator arrangement but is probably about 2.8MeV[23]. However to obtain adequate fluences of epithermal neutrons from a clinically useful accelerator source based on this reaction proton currents of the order of 10-20 mA would be required. For target currents of this magnitude heat removal from a lithium target is a significant design consideration. The neutrons generated by the $^{7}Li(p,n)^{7}Be$ reaction have an angular and energy distribution determined by the kinetics of the reaction. In order to use the neutrons generated by this reaction a reflector is located around the target and a moderator is placed on the neutron beam axis between the target and the patient[19,22]. An alternative and perhaps more attractive design

philosophy[24, 25] uses a proton energy very close to the reaction threshold (1.93-1.99MeV) to obtain neutrons at energies where only minimal moderation is required. In this case the reduced neutron yield due to the lower reaction cross section just above the threshold is compensated by the smaller thickness (~5 cm) of D_2O moderator used so that a clinically useful beam intensity may be generated with beam currents as low as 5 mA. Such a system has been shown to probably be feasible for intraoperative BNCT[26].

Other reactions that have been considered in more detail for clinical[27, 28] application include the $^{9}Be(p,n)$ reaction with incident proton energies of 4 MeV[29]. A similar quality beam can be obtained using either lithium or beryllium targets. The use of beryllium as the target has some advantages over lithium due to the better mechanical and physical properties of the former. However a higher energy (4 MeV) accelerator is required for the beryllium reaction compared to the energy of approximately 2.5 MeV (or even less) required for a lithium based neutron source. This may make the lithium target system the less expensive option. One innovative suggestion has been to use a target consisting of lithium contained in a beryllium shell to take advantage of the desirable characteristics of both materials[30].

More recently the $^{13}C(d,n)$ reaction has been studied[31,32] with MCNP simulations and experimental measurements in phantoms. A 4mA beam of 1.5 MeV deuterons could deliver typical treatment doses in under one hour assuming ^{10}B tumour concentrations of 40ppm.

All accelerator based neutron sources require some moderator and filter around the target where the neutrons are produced. Depending on the reaction used and the accelerator energy the average energy of the neutrons produced may be

decreased in order to reduce the amount of moderator required and bring the treatment point closer to the target. However, in general, reducing the projectile energy at energies close to the threshold for the reaction will result in diminished yield thereby offsetting the advantage of decreasing the amount of moderator required.

Generally the moderator extends all around the target to both minimise the leakage of fast neutrons and to moderate and reflect as many of these as possible towards the treatment point. These typically consist of combinations of Al_2O_3, BeO and D_2O. Some additional gamma shielding may be required to remove gamma rays resulting from activation of the target. This could also be minimised by regular replacement of the target.

OTHER NEUTRON SOURCES

Other neutron sources that have been proposed for BNCT include isotopic sources of neutrons such as ^{252}Cf. This isotope of californium spontaneously fissions emitting fast neutrons. These could be used either in combination with filters and moderators to produce an epithermal neutron beam[33] or as a brachytherapy source with boron pharmaceuticals used to enhance the dose to the tumour following moderation of the fast neutrons in the surrounding tissue[34].

A Monte Carlo study by Yanch et al[33] demonstrated that with appropriate arrangements of Al filters and D_2O moderator it was possible to obtain an epithermal neutron beam with dosimetry characteristics similar to a reactor based beam except for the beam intensity which was several times lower than obtainable from a reactor even with a large 1.0g ^{252}Cf source. The limited half life (2.645 years) of ^{252}Cf would

also lead to significant expense with the regular replacement of large sources.

Another study by Yanch and Zamenhof[34] used MCNP to calculate the dose distribution around implanted linear wire sources of ^{252}Cf with different concentrations of ^{10}B in surrounding tissues. The calculated dose profiles in the absence of ^{10}B were found to be in good agreement with measured data. The dose close to the source drops sharply as the fast neutrons are thermalised. The dose at a point 1cm from the source is approximately 10% of the dose maximum around the source. The addition of 50ppm of ^{10}B to the medium has a minimal effect within about 1 cm of the source but increases to represent a physical dose enhancement of between 23 –28% at distances between 5 and 10 cm from the source (where neutrons have thermalised). At a distance of 25 cm from the source the enhancement has dropped to approximately 14%. This study concluded that dose enhancements of this magnitude could under the right circumstances lead to significant improvement in tumour control probability.

Another application of BNCT that has been suggested is the boron enhancement of dose in fast neutron therapy (FNT)[35, 36, 37, 38, 39]. However the flux of high energy (10's of MeV) neutrons used for FNT means that the contribution from boron fissions with thermalised neutrons only provides a dose enhancement of up to about 5%. The additional dose contribution however is observed mostly at the higher end of the microdosimetry spectrum. It has been suggested that filtration and moderation of FNT beams would provide greater ^{10}B dose enhancements that may be more significant[40]. Modifications to the target (addition of Be) to enhance the flux of low energy neutrons from an existing FNT facility at University of Washington State have been successfully implemented[41]. In this case the aim was to of increase the ^{10}B

dose enhancement without substantially changing the depth dose profile or spectrum of the original fast neutron beam.

DOSIMETRY TECHNIQUES

As previously noted each dose component of the BNCT epithermal neutron beam will have a different biological effectiveness. Therefore it is important to accurately measure or calculate each component separately.

FOIL ACTIVATION

The thermal neutron flux can be measured reliably using bare and cadmium covered gold foil activation. Once the thermal flux is known a KERMA factor can be applied for each type of tissue involved and the thermal neutron dose can be determined. If necessary the contributions of each individual element can be determined by using the appropriate thermal neutron KERMA factors. Similarly the ^{10}B dose can be determined using the thermal neutron flux and the KERMA if the ^{10}B concentration is known or is assumed.

IONISATION CHAMBERS

The standard method for determining beam gamma dose and epithermal neutron dose is by using the paired ionisation chamber technique[13]. This technique makes use of a graphite walled ionisation chamber filled with CO_2 and a tissue equivalent (TE) ionisation chamber (made of A-150 material) filled with tissue equivalent gas. A magnesium chamber filled with argon is sometimes used instead of the graphite walled chamber. The graphite or magnesium chamber has minimal

neutron response and is used to measure ionisation due to the gamma dose. The TE chamber responds to both gamma radiation and neutrons in the epithermal neutron beam. By subtracting the gamma dose measured using the graphite or Mg chamber from the dose measured by the TE chamber the neutron dose can be determined.

A detailed description of the paired ionisation chamber technique (and other dosimetry techniques) applied to epithermal neutron beams for BNCT applications has been presented by Rogus et al[42] and by Raaijmakers et al[200]. The reader is directed to these excellent descriptions for more detail and only a brief summary of the methods based on these papers will be presented here for completeness.

The ionisation chambers used by Rogus et al and Raaijmakers et al were manufactured by Far West Technologies and Extradin respectively. The diameters of the chambers are approximately 8mm – 10mm. Tissue equivalent gas composed of 64.4% CH_4, 32.4% CO_2 and 3.2% N_2 by partial pressure was used by both groups. Rogus et al maintained the flow rate of the TE and CO_2 at 20 $cm^3.min^{-1}$ and Raaijmakers used a flow rate of 10 $cm^3.min^{-1}$ for the TE gas and the Ar. The flow rate must be kept constant during calibrations and measurements to avoid changes in gas density and the resultant changes in ionisation. A chamber voltage of 250 V was used by both groups. The wall thickness of the ionisation chambers themselves provide enough buildup to establish charged particle equilibrium for all anticipated neutron energies. However extra buildup caps were used to provide charged particle equilibrium for ^{60}Co gamma energies. In air measurements are performed with the buildup caps on but the presence of some higher energy gamma rays in the neutron beam will lead to a small error.

The response of the two ion chambers in a mixed field is given by Rogus et al[42] as (Raaijmakers et al[43, 200] follow a very similar method):

$$Q_{TE} = A_{TE} D_{\gamma} + B_{TE} D_n + f_{\phi} \phi_{2200}$$

$$Q_{CG} = A_{CG} D_{\gamma} + B_{CG} D_n + f_{\phi} \phi_{2200}$$

where Q_{TE} and Q_{CG} are the charges accumulated by the chambers under irradiation, D_{γ} and D_n are the gamma and neutron dose rates and the factors A and B respectively represent the gamma sensitivity and neutron sensitivity of each chamber. The thermal neutron flux is ϕ_{2200} and f_{ϕ} is the thermal neutron sensitivity of each chamber. The gamma sensitivity A for each chamber is determined by exposure calibration in a ^{60}Co gamma field and application of appropriate exposure to dose conversion factor. If this calibration is performed with air in the chambers then a separate factor to correct for air versus CO_2 or TE gas filling needs to be measured. The neutron sensitivity factors, B are based on the neutron to gamma sensitivity ratio B/A, a quantity that can be calculated using the Bragg-Gray theory or found in the literature. For the TE chamber this factor will be dependant on the ratio of the energy needed to produce an ion pair for photons in TE gas and for neutrons in TE gas (W_g/W_n). Therefore it will change as the spectrum being measured changes leading to an uncertainty in the final result. The contribution from thermal flux is subtracted based on activation foil measurements of the thermal (2200 m.s^{-1}) flux and measured values of the thermal neutron response f_{ϕ}. The measured charges in the ion chambers are corrected for temperature, pressure, gas flow rate and reactor power and conditions.

The estimated contributions from each step of the measurement process to the total uncertainty in gamma dose and fast neutron dose are tabulated by Rogus et al[42].

The estimated total uncertainty in epithermal beam measurements of photon dose is ±9% and for fast neutron dose it is ±17%. Similar uncertainty estimates by Raaijmakers et al were ±5% for photon dose and ±13% for fast neutron dose at 1 cm depth in a phantom but this dropped off to ±18% at 2 cm depth.

In addition to these standard methods of measurement for the dose components in epithermal beam BNCT several other dosimetry techniques are used more or less commonly. These include thermoluminescent dosimeters (TLD)[43,44] ferrous sulphate gel dosimetry[45,46], and acrylamide polymer dosimetry gel[47] and semiconductor dosimeters in various forms including the ones described in this thesis. For the initial spectral characterisation of epithermal beams various types of activation foils and foil stacks may be used as well as proton recoil spectrometry.

RADIOBIOLOGY

As previously noted the dose absorbed in tissue containing ^{10}B exposed in an epithermal neutron beam consists of several components: gamma dose, neutron dose (mainly proton recoil), dose from the $^{14}N(n,p)$ reaction and dose from the $^{10}B(n,\alpha)$ reaction including the prompt gamma ray[48]. Each of these dose components will have a different relative biological effectiveness (RBE) principally due to the different linear energy transfer (LET) of these dose components[49]. In the case of the proton recoil dose the RBE may change as the average energy of the neutrons changes with depth in the tissue[50]. The proportions of each of these dose components will also change with location in the irradiated tissue, i.e. the epithermal flux decreases with depth and the thermal flux while also diminishing constitutes a larger proportion of

the total neutron flux at greater depths. It has been shown by Woollard et al[51] that it is reasonable to use the same RBE for the proton recoil and $^{14}C(n,p)$ components of the dose throughout the treatment volume for typical epithermal neutron beam spectra.

The RBE of a particular radiation is traditionally defined as the ratio of the dose of that radiation to the dose of X-rays (usually 250kVp) that is required to produce some defined biological effect[52]. The value of the RBE will depend on the endpoint chosen, the dose rate and fractionation, the oxygenation of the tissue, the kind of tissue or cells being tested and potentially many other factors. The determination of an appropriate RBE for each of the dose components in BNCT and then its application to a particular physical dose is not a straight forward exercise.

In general and certainly in the clinical situation it is only possible to calculate the reaction rate for the $^{10}B(n,\alpha)$ reaction for some average concentration of ^{10}B in a particular volume. For most biological systems and for most ^{10}B pharmaceuticals the ^{10}B distribution will be highly inhomogeneous. Combined with the short range of the resulting α particles this makes it impossible to calculate a meaningful RBE based on the actual dose distribution (which is highly inhomogeneous on a microscopic scale). Therefore to account for the effect of the microscopic distribution of the ^{10}B and its effect on the 'RBE' for the $^{10}B(n,\alpha)$ reaction in a particular system a compound factor (CF) or compound biological effectiveness factor (CBE) is introduced. This factor accounts for the different biological effects that may be observed for the same average boron concentration but with different microscopic distributions (i.e. predominantly in the cytoplasm, the nucleus or the cell wall, etc) depending on the boronated drug being used. These compound factors are generally determined by in-

vivo or in-vitro measurements of dose effects with and without the ^{10}B pharmaceuticals present.

Compound factors could also be considered as effectively consisting of several other more basic factors[53] that describe the geometry of cells and the ^{10}B distribution within them. These factors take into account the relative contributions to the dose received by the cell nuclei depending on the boron concentration, the microdistribution of ^{10}B in the cells (relative intracellular efficiency), the contribution from ^{10}B in contiguous cells (contiguous cell correction) and fractionation effects. Some of these factors can be derived based on measured microscopic distributions of ^{10}B in particular tissues in conjunction with microdosimetric (often Monte Carlo) calculations of energy deposition in simulated typical cellular geometries.

The methods used for determining RBE and CBE factors are well described by Coderre and Morris in a review paper[54] and the literature referenced therein. The reader is directed to this literature for an extensive review of the topic but a brief summary will be presented here.

The principle high LET dose components arising from the incident neutron beam itself are recoil protons and the 590 keV protons arising from the $^{14}N(n,p)^{14}C$ reaction. The RBE of these protons can be determined by observing the total physical dose (proton dose, D_{proton} and gamma ray dose, D_{γ}) required to achieve a specified biological endpoint in the neutron beam. A similar measurement is performed to determine the x-ray dose ($D_{x\text{-}ray}$) required to reach the same endpoint (*effect*). That is (after Coderre[54]):

$$D_{proton}(effect) * RBE_{proton} + D_{\gamma} = D_{x-ray}(effect)$$

The gamma ray dose component is assumed to have an RBE of 1 and therefore the gamma dose is subtracted from the x-ray dose required to reach the same endpoint. The RBE of the proton dose is simply the ratio of the remaining x-ray dose to the proton dose:

$$RBE_{proton} = \frac{D_{x-ray}(effect) - D_{\gamma}}{D_{proton}(effect)}$$

The proton RBE will be determined in part by the neutron spectrum which dictates the recoil proton spectrum. It ranges from approximately 1 for keV range neutrons up to 6.2 for 350 keV neutrons[6]. For clinically relevant biological endpoints and typical epithermal beam spectra it is probably approximately[54] 3.

Once the RBE of the proton dose has been determined then another measurement can be conducted where ^{10}B is introduced into the biological system. Again the cells are irradiated in the neutron beam to reach some predefined endpoint. A similar exposure using only x-rays is used to reach the same endpoint. Again adapting the exposition of Coderre:

$$D_{x-ray}(effect) = D_{\gamma} + D_{proton} * RBE_{proton} + D_{boron} * CBE$$

Where D_{boron} is the $^{10}B(n,\alpha)^{7}Li$ contribution to the total dose required to achieve the same endpoint (*effect*). The CBE for the boron dose contribution is then:

$$CBE = \frac{D_{x-ray}(effect) - D_{\gamma} - D_{proton} * RBE_{proton}}{D_{boron}}$$

This methodology applied to in-vivo irradiation of 9L gliosarcoma cells and in-vitro survival assay measurements results in CBE factors[54] in the range of 3.4 to 2.8 for the most commonly used boron drugs, BPA and BSH as well as for boric acid relative to 250 kVp x-rays at cell survival levels between 0.1% – 10%. It should be

noted that the actual boron dose D_{boron} and therefore the CBE factor will be sensitive to the assumed (or measured) boron concentration in the cells. A check of consistency of the RBE and CBE factors can be obtained by generating cell survival curves using both x-ray irradiations and neutron irradiations with ^{10}B present. If all assumptions and CBE and RBE factors are correct the two cell survival curves should lie exactly on top of each other when the neutron survival curve is plotted as a function of photon equivalent dose (ie physical dose modified by RBE and CBE factors)[54].

Based on BNCT treatments of melanoma in six humans at the Musashi Institute of Technology reactor and the Kyoto University reactor the *overall* biological effectiveness factor for $^{14}N(n,p)$ and $^{10}B(n,\alpha)$ reactions with BPA is estimated to be approximately 2.3-2.5 where the endpoint is moist desquamation of the skin[54,55].

Radiation damage to the CNS occurs via more than one pathway and is a result of vascular damage, demyelination and probably several other factors[56,57]. Determination of BNCT effects on the central nervous system is complex. Depending on the boron compound used tumour control effects as well normal tissue complications are probably mediated by more than one effect. Damage to the micro-vasculature in the CNS leads to normal tissue damage[58] and this effect is probably also responsible for some of the tumour control effects observed.

For a compound like BSH that does not actively cross the blood brain barrier (BBB) except where the BBB is compromised (eg fenestrated capillaries in tumours[59,60]) the concentration of boron within the capillaries and the $^{10}B(n,\alpha)$ reactions occurring in the lumen leads to a geometric sparing of the vascular

endothelial cells. This occurs since the dimensions of the capillary lumens[61] are of a similar magnitude to the range of the reaction products while the endothelial cell walls are very thin and therefore do not absorb much dose. In contrast to this BPA is transported across the BBB and therefore the concentration of ^{10}B in the brain surrounding a capillary is likely to be similar to the concentration in the blood. In this case the endothelial cell walls are more likely to receive a higher dose from the surrounding ^{10}B. This results in a higher CBE for BPA in the CNS. For an endpoint of myeloparesis irradiating rat spinal cord with a single fraction of thermal neutrons[62] the CBE for BPA was found to be approximately 1.3. The CBE for the same effect using BSH[63] was 0.53 with various concentrations of BSH resulting in total physical absorbed doses ranging from approximately 21 – 32 Gy. The difference between the CBE for the two compounds reflects the different distribution of boron between the vasculature and the normal brain surrounding it for these two compounds.

The corresponding CBE factors for tumors using BPA or BSH have been estimated[54] to be approximately 3.8 and 1.2 respectively in a 9L gliosarcoma rat model. These were both based on in-vivo irradiation with in-vitro survival assay. Using overall animal survival data would be a preferable method for determining CBEs where tumor control is the required endpoint. However normal tissue toxicity resulting from large single x-ray fractions prevents this CBE measurement being made. The validity of assaying tumor cell survival to determine tumour control CBE has been questioned on the basis that it may in fact be damage to the vasculature rather than direct clonogenic cell kill which determines tumour control[54].

It has been suggested that theoretically there may be some advantages to fractionation of BNCT treatments. In general the benefits of fractionation that exist

for low LET radiation are smaller or not significant for higher LET radiations[64]. Since BNCT involves both high and low LET components it may be expected that the low LET component of the radiation dose would result in some repairable sub-lethal damage and that fractionation of the dose may allow normal tissue toxicities to be reduced. However no significant effect has been observed in this regard, possibly due to the interaction of high and low LET components resulting in low LET damage being "fixed" by the presence of high LET damage inhibiting repair[54]. Reduction of normal tissue complication probability is not therefore considered an adequate rationale for fractionation in itself.

For tumor cell populations the fractionation benefits of cell cycle redistribution and reoxygenation are not expected to be significant for high LET radiation and have not been observed with BNCT in animal models (mainly 9L gliosarcomas in rats). However an oxygen enhancement effect has been observed for fast neutrons[65]. However these animal models may not be truly representative of real glioblastoma multiformae tumors which may have a significant sub-population of cells in a quiescent phase as opposed to the models where most of the cells were actively proliferating[54]. It has been proposed that a fractionated BNCT treatment could allow the boron delivery agent to perfuse tumour cells not previously accessible for the initial fraction of BNCT. This limited access could arise due to the adverse osmotic and pressure gradients, convoluted tumor vasculature and other factors that conspire to confound the delivery of any therapeutic agent to solid tumors[66]. Some reasons that fractionation (of the boron dose and radiation) may actually lead to worse results include the possibility that biodistributions of subsequent administrations of boronated compounds may be less specific. A high

normal tissue concentration may result from previously damaged vasculature[67] and normal tissue reactions to the previous fractions. On these grounds Corderre concludes that clinical trials of fractionated BNCT are worthy of investigation[54]. In a gliosarcoma model using BPA no loss of therapeutic efficacy was observed for two fractions separated by up to 5 days, however a break of up to 9 days was required to improve normal tissue tolerance (oral mucosa in this case)[68].

It has been proposed that there may be a synergistic effect (supra-additivity[63]) between high and low LET radiations delivered either sequentially or concurrently. If this is the case it may be necessary to consider this supra-additivity[63] in any radiobiological model used for BNCT. Zaider and Rossi[69] proposed a model (based on the theory of dual radiation action[70]) that showed synergistic effects from sequential high and low LET radiations resulting from interactions between sublesions produced by the two types of radiation. This was later extended for application to simultaneous irradiations and compared well with experimental neutron and gamma cell survival data by Suzuki[71]. Earlier data from McNally et al[72] and others demonstrated similar interactions between high and low LET irradiations. Zaider and Wuu subsequently extended the model further to include the effects of variable radiosensitivity of cells due to oxygenation and cell cycle stage[73].

The effects of these synergistic interactions may be expected to be observed as the ratio of high to low LET dose changes with different concentrations of ^{10}B in tissue and different ratios of gamma to neutron doses at different depths in the tissue being irradiated. This would lead to different values of CBE for experiments performed with different concentrations of ^{10}B. It could also cause CBE to vary with position in clinical BNCT. Hitherto no such variation in CBEs with different ^{10}B

doses has been observed[63]. Any synergistic effects between the high and low LET components have so far remained obscured by other variability in the available data from cell and animal models and clinical trials.

BORON DRUGS

The first trials of BNCT in the 1950s used borax ($Na_2B_4O_7.10H_2O$) or sodium petaborate ($Na_2B_{10}O_{16}.10H_2O$). These were not taken up selectively by tumours and therefore the tumours only had a concentration marginally exceeding that in normal tissue for a very short period. Later p-carboxybenzeneboronic acid and sodium decahydrodecaborate were developed and tested. these showed favourable tumour to brain boron ratios of between 5:1 and 8:1 for periods of hours[112]. However histology results showed significant damage to vascular endothelial cells due to high blood boron concentrations. Subsequently new boron compounds were developed which showed improved tumour to blood boron ratios. Sodium Borocaptate referred to as BSH ($Na_2B_{12}H_{11}SH$) was the first of these and was used in the thermal BNCT trials in Japan. BSH has been shown to accumulate in the nuclei of glioma cells[74]. BSH has shown clinically useful uptake levels in human gliomas and minimal normal brain tissue uptake[75].

Another boron drug used for BNCT is p-boronophenylalanine (BPA). The rationale for this is that BPA is an analogue of the amino acid phenylalanine and may be actively taken up by tumour cells due to their increased metabolic rate. In the case of melanoma cells phenylalanine is known to be a precursor of melanin and therefore BPA uptake is enhanced in these cells[76]. Tumour to blood boron ratios of 4.4±3.2 for metastatic melanoma patients have been observed with a maximum ratio of 10. In

high grade gliomas ratios of 2.2±1.2 have been observed[76]. Significant clinical experience has now been gained with BPA (and in particular the BPA.fructose complex used to improve solubility for administration of BPA). Effective biodistribution kinetics models for BPA based on human data have been published[77,78] and show good agreement with experimental observations.

An essential difference in the behaviour of BSH and BPA is that the accumulation of BSH in tumours relies on the diffusion of BSH out of the vasculature in regions where the vasculature is leaky or damaged (eg tumors) whereas BPA is transported across the endothelial cell wall but is selectively accumulated in tumor cells due to their higher proliferative activity. This may mean that BSH is less cell cycle dependant that BPA[79] for some tumors and has lead to the suggestion that combinations of BPA and BSH could be advantageous[80]. This difference has important implications for the radiobiological effects of these boron carriers as noted in the Radiobiology section above.

Other boron compounds investigated[81] include boronated nucleic acid precursors which could be incorporated into the DNA of proliferating cells. Such compounds are attractive because of microdosimetric considerations. A much greater amount of energy can be deposited in the nucleus of a cell if the $^{10}B(n,\alpha)^{7}Li$ reaction occurs there rather than in the cytoplasm or on the external surface of the cell wall. Boronated monoclonal antibodies[82,83], liposomes, combinations of liposomes and antibodies[84] and low density lipoproteins (LDL) have also been investigated.

It may be possible to increase the boron load in tumor cells by administering agents designed to increase the permeability of the blood brain barrier such as Cereport and mannitol[85]. One test of this technique using a nude rat melanoma model

showed a significant improvement in mean survival time and the number of long term survivals when Cereport or mannitol were administered to the animals with BPA prior to neutron irradiation[86]. Minimal difference in normal tissue damage was observed compared to animals treated without mannitol disruption of the blood brain barrier during irradiation[87].

TREATMENT PLANNING

Treatment planning for BNCT involves many variables, elaborate data collection, setup and computation. Therefore only a brief and necessarily superficial overview can be given here. It is necessary to know both the physical dose distribution from the beam component of the epithermal neutron beam and also the boron distribution in normal tissue and tumour. It may be possible to perform some uptake measurements of the boron agent and use these in conjunction with compartment models of the known biodistribution and kinetics for the boron pharmaceutical[77,78]. An attractive way of achieving this is to use positron emitting analogs of the boron therapy agents. This technique can now be used for treatments with BPA[88]. The geometry of the patient anatomy and tumour is determined using CT and MRI as it is for conventional radiotherapy treatment planning.

The treatment planning system used for BNCT trials at BNL was developed specifically for BNCT[89] treatment planning at INEEL. It consists of several modules to allow the import of CT or MRI images, outlining of structures and a Monte Carlo based transport code module. The geometry for the Monte Carlo model is constructed using a B-spline reconstruction from outlined regions on the diagnostic scans. The

output of the calculated dose distributions including CBE modified physical doses can be displayed as isodose contours on the CT or MR images. Dose volume histograms can also be generated.

Treatment planning for patients at the MIT epithermal beam is performed using the MacNCTPLAN package[90]. A PC version is now available. This package combines the proven radiation transport accuracy and power of the MCNP[182] code from Los Alamos with the user friendly graphical interface and image processing capabilities of the public domain NIH Image code. This planning system accepts CT and MRI images. The CT images are used for tissue composition definition while the MRI with and without contrast is used for target delineation.

In NCTPLAN the image data is converted into a voxel model consisting of 11,025 cells each of $1cm^{-3}$ in a parallelepiped box of dimensions $21\times21\times25$ cm[91]. Each $1cm^{-3}$ cell has a composition based on the average composition of the tissue types in the CT pixels that contribute to its volume. The segmentation of the images into different tissue types is accomplished semi-automatically with manual identification of Houndsfield ranges that correspond to particular tissues (using a frequency histogram). Once the dose in each voxel is calculated a $1mm^{-3}$ voxel grid is generated by interpolation and subsequently smoothed using a Fourier transform and ramp filter. Isodose contours are then generated from this array.

An advantage of the MacNCTPLAN system is that as well as calculating the dose distribution within the specific patient the dose distribution within a standard head phantom is also calculated. By making absolute dose measurements at a reference point in the phantom the actual calculated treatment plan dose distribution can be scaled to ensure that the absolute dose is correct. That is the relative dose

distribution in the patient is generated by Monte Carlo (MCNP) and this is then scaled based on phantom measurements to ensure that the absolute dose levels are accurate. During treatment, real-time monitoring of blood boron concentration using prompt gamma detection is performed and in conjunction with readouts from calibrated beam monitors[92] the real equivalent dose is calculated.

A direct comparison[93] has been made by the Petten group between MacNCTPLAN and the code now designated as SERA[94] by INEEL/Montana State University. This found that the accuracy of the MacNCTPLAN was influenced by the approximations involved in the voxel model used. The Finnish BNCT group has developed a new deterministic transport code called Multitrans SP3[95] which has been benchmarked against Monte Carlo calculations and experimental data. Multitrans SP3 shows reasonably good agreement with measurements for neutrons but some discrepancies still exist for gamma doses. It has the advantage of being approximately an order of magnitude faster than the Monte Carlo based techniques. Another deterministic method proposed for BNCT treatment planning is removal diffusion theory[96] which has demonstrated good agreement with MCNP results for test geometries.

TARGET CANCERS

BNCT has been proposed as a treatment modality for a number of different cancers. These include principally gliomas of the brain[97,98,99,100] and cerebral melanoma[101,102]. However in-vitro experiments, investigations of animal models and dosimetry studies for various other neoplasms have included undifferentiated thyroid cancer[103], mammary carcinoma[104], liver tumours[194,105] and pancreatic cancer[106].

GLIOMA

Gliomas constitute approximately 46% of all primary intracranial tumours. Of these 47% are glioblastoma multiforme (GBM) and 36% are other malignant astrocytomas[107]. The prognosis for patients with tumours in either category is poor. The median survivals are only about 8.6 months and 36 months respectively[108] Conventionally these tumours are treated with surgical debulking, chemotherapy and/or external beam radiotherapy.

MELANOMA

The incidence of melanoma[107] in the US in 1996 was approximately 17 cases per 100 000 per year for men and 11.4 cases per 100 000 per year for women. The mortality rates for men and women were 2.3 and 3.2 per 100 000 per year respectively. The higher mortality in men being due to the fact that a larger proportion of melanomas in men occur on the trunk, whereas in women a larger proportion occur on the extremities and therefore the prognosis is better[107]. The incidence of melanoma is increasing fairly rapidly. There was a 140% increase in incidence between 1973 and 1996. However over the same period the mortality rate increased by only 44% among males and 15 % for women. Melanoma is a relatively aggressive tumor and is also relatively radioresistant.

HISTORY OF CLINICAL TRIALS

Boron Neutron Capture Therapy (BNCT) was first proposed by Gordon

Lochler[109] at the Franklin Institute in Swarthmore PA in 1936 shortly after the discovery of the neutron by Chadwick in 1932. It was not until 1951 however that the first clinical trials were begun by William Sweet of the Massachusetts General Hospital[110,109] and others at the Brookhaven Graphite Research Reactor[111]. The ^{10}B compounds used were borax and sodium pentaborate given intravenously. These early attempts were directed at treatment of glioblastoma multiforme and were unsuccessful in terms of controlling this disease. No prolongation of survival time was demonstrated[112]. This was mainly due to inadequate uptake of ^{10}B in the tumour cells and poor penetration of the thermal neutrons being used. These trials were discontinued.

Another series of clinical trials commenced in Japan in 1968. These were lead by Hatanaka[113], who had participated in the initial Brookhaven trials, and were performed on patients having a range of different types of tumours including low to high grade glioblastomas. The ^{10}B drug used was borocaptate (BSH) and a reactor thermal neutron beam was used. Most of these treatments were performed after surgical debulking of the tumour and were intraoperative irradiations. This was required to maximise the neutron fluence at the tumour site due to the poor penetration of thermal neutrons. Some success was claimed for these trials[113] (over 100 patients were treated over the following 20 years). However due to patient selection and lack of control data the outcomes are not considered to conclusively support the efficacy of the treatment[112].

Hatanaka's results have rekindled interest in BNCT and a number of clinical trials using epithermal neutron beams and new boron compounds were commenced at the Brookhaven National Laboratory, the Massachusetts Institute of Technology

and at the European Community Reactor in Petten[114,115], the Netherlands. These commenced with phase I trials to show no detrimental effect and progressed to phase II dose escalation trials. Phase III trials will test efficacy of the treatment. The BNL program was subsequently terminated when the BNL reactor was closed. Other clinical trials are underway or planned in Finland, Czechoslovakia[116] and Japan.

Two trials are currently open at the Beth Israel Deaconess Hospital utilising the MIT epithermal neutron beam. These include a phase II trial for cutaneous melanoma using BPA which is aimed at evaluating tumour response rates, acute and delayed normal tissue skin reactions as well as BPA biodistribution. The other trial is a phase I/II trial of BNCT treatment for cerebral melanoma and glioblastoma multiforme. The aims of this trial are to determine normal brain tolerance doses and the maximum treatment dose that can be given as well as to assess tumour response to BNCT[117].

Some early clinical trial results are available in the journal literature. For the group of 10 glioblastoma patients treated at BNL in 1994/95 using BPA the minimum dose in the tumor ranged from 20 to 32.4 Gy-Eq[118]. The dose to the scalp was from 10–16 Gy-Eq resulting in alopecia in all patients. No treatment related CNS morbidity was observed. Median time to local progression was 6 months post BNCT with a trend to delayed progression with higher tumour doses. Overall 54 patients were treated between 1994 and 1999 at BNL[119]. Patients received 250, 290 or 330mg/kg of BPA as part of the dose escalation. Between 1 and 3 treatment fields were used for total treatment times of 38 –120 minutes. The reference dose levels (dose to 1 cm^{-3} of normal brain at peak thermal flux) were set at either 10.5 , 12.6 or 15 Gy-Eq. Some oedema post treatment was observed and subsequently all patients

were premedicated with steroids and antiseizure agents. No improvement in tumor control was observed with increasing doses when time to progession is used as the endpoint. All recurrences were observed in the region of preoperative oedema and therefore the target volume was expanded to include this volume. At an average brain dose of 6 Gy-Eq no significant CNS toxicity was observed on autopsy.

The Petten trial involves the delivery of four fractions over four consecutive days and uses BSH as the boron agent to treat glioblastoma and gliosarcoma patients. The EORTC BNCT protocol is a post-surgical protocol and of the patients so far reported on in the literature[120] approximately half had complete tumor resection and the other half of the patients had subtotal resection prior to BNCT. The initial group of ten patients received a dose of 8.6Gy-equivalent to the point of maximum thermal flux. Five of these patients received bilateral irradiation and the other half unilateral irradiation of the head. The BSH infusion was tailored to establish an average of 30ppm blood concentration of ^{10}B during the four fractions. Some patients experienced reactions and haematological toxicities which were attributed to BSH and required GSF rescue. However acute radiation related toxicities were milder than observed in patients treated with conventional radiotherapy for the same type of tumors. Late toxicities associated with the BNCT were difficult to distinguish from symptoms of disease progression and post operative sequelae. Overall survival times and early and late toxicities were similar to those that would be expected for conventional radiotherapy.

A novel on-line gamma ray telescope technique for assaying the boron concentration spatial distribution has been applied to some of these patients[121] during treatment.

CHAPTER 3 EPITHERMAL NEUTRON BEAM DOSIMETRY USING PIN DIODES

PIN DIODES

In order to understand the application of PIN diodes to neutron dosimetry in BNCT neutron beams it is first necessary to present a brief summary of the normal behaviour of PIN diodes in the absence of radiation effects. Then a brief summary of radiation interactions with silicon will be presented. From this basis an explanation of the operation of PIN diodes as dosimeters will be given.

A silicon PIN diode consists of a section of intrinsic silicon sandwiched between an n-type section on one side and a p-type section on the other (Figure 3-1). Metallic contacts are attached to both the p and the n type sections. It is assumed that the electron concentration in the n region is the same as the hole concentration in the p region and that carrier mobilities are equal ($\mu_p = \mu_n$) and the diffusion constants are equal ($D_p = D_n$) in each of the regions. There are approximately equivalent concentrations of holes and electrons in the intrinsic region. The p and n type regions are assumed to be very thin in comparison to the intrinsic region so that the electron concentration in the p region and the hole concentration in the n region varies linearly with distance.

The total voltage drop across the diode is the sum of the voltage drop across the two junctions and the voltage drop across the intrinsic "base" section of the diode. Swartz and Thurston[126] have shown that for low current densities in the diode the carrier density depends linearly on the current density in the base. Therefore the conductivity increases proportionally to the current and the voltage across the base is

independent of the current in the base. The voltage across the base depends upon the ratio of the base width to the diffusion length (*W/L*). The total junction voltage under these conditions is proportional to the natural logarithm of the current density. That is, the familiar junction diode equation where current is proportional to *exp(eV/2kT)*. Where *e* is electronic charge, *V* is voltage across junction, *k* is Boltzmans constant and *T* is the temperature.

As the current density in the intrinsic base section of the diode increases[126] the current becomes more dependant on the square of the number of injected carriers. Under these circumstances the voltage across the base of the diode is proportional to the square root of the current density and also depends upon the base width to diffusion length ratio (W/L). For these higher currents the total junction voltage is proportional to the natural log of the current density (current proportional to *exp(eV/kT)*) and to the carrier lifetime, τ.

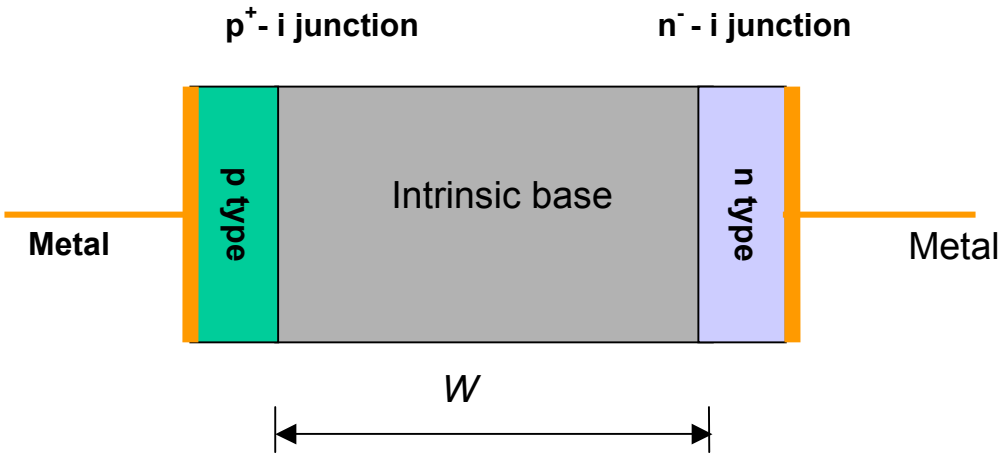

Figure 3-1. Schematic representation of p-i-n diode .

INTERACTION OF NEUTRONS WITH SILICON

Gamma rays impinging on silicon produce primarily ionisation. Neutrons, due to their neutral charge and mass, can collide with silicon atoms and dislodge them from their place in the crystal lattice. This creates a vacancy in the lattice at the point where the atom was dislodged from and the dislodged atom is located in an interstitial site. Thus a lattice defect is created. For energetic neutrons enough energy may be imparted to the atom to enable it to dislodge further atoms. Some of these defects will be stable at room temperatures and will therefore remain present in the lattice structure and are referred to as *displacement damage*[a]. The increased number of mobile vacancies in the semiconductor, prior to formation of stable defects, transiently act as trapping centres for minority carriers. In the operation of PIN diodes as neutron dosimeters we are primarily concerned with the neutron induced formation of defects that are stable at room temperatures.

The amount of energy required to dislodge a silicon atom from its lattice site is 25 eV[122]. An estimate of the number of dislodged atoms is given by Messenger and Ash[122] as follows. The cross section of silicon for 1 MeV neutrons is approximately 5 barns (Figure 3-2). The atomic density of silicon is 5×10^{22} cm^{-3}. This gives a mean free path for 1 MeV neutrons in silicon of λ=4 cm. If each primary displaced atom dislodges a cascade of another 500 atoms then silicon exposed to a 1 MeV neutron fluence of 10^{13} cm^{-2} would result in a fraction of displaced atoms of approximately 2.5×10^{-8} cm^{-3}, or about 1 atom in every 40×10^{6}. For lower neutron energies the

[a] The kinetic energy released per mass absorber through interactions which lead to displacement damage is known as *displacement damage KERMA* or simply *damage KERMA*.

number of atoms in the cascade would be less and as the silicon cross section also decreases for lower energies the number of dislodged atoms and defects formed would be an even smaller fraction per incident fluence.

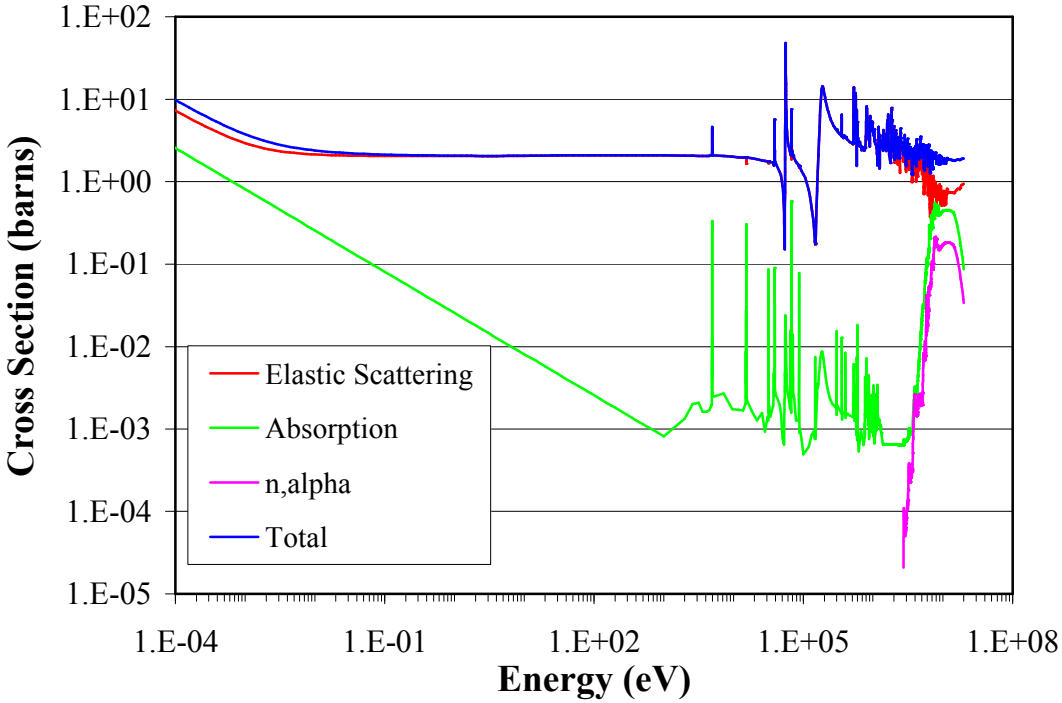

Figure 3-2. Silicon cross sections

For silicon exposed in fast neutron beams there are a number of possible reactions which can occur. These include the $^{28}Si(n,\alpha)^{25}Mg$ and the $^{28}Si(n,p)^{28}Al$ reactions. Since the threshold energies for these reactions are of the order of several MeV such effects will not be so significant for epithermal neutron beams used in BNCT.

If only the total silicon KERMA (i.e. both ionising and non ionising energy loss) is taken into account in calculations of the effect of BNCT beams on PIN diodes then calculations of the dose to silicon will overestimate the amount of damage expected in the diodes. The total silicon KERMA is the sum of the silicon damage

KERMA and the silicon ionisation KERMA. Only the damage KERMA leads to effects on the PIN diodes which are observable after the neutron exposure as an increase in the forward bias voltage of the PIN diode. The partition between damage and ionisation KERMA will vary with different neutron energies due to the silicon scattering cross sections and the number of silicon atoms which can be displaced in knock on collisions induced by a primary of a given energy.

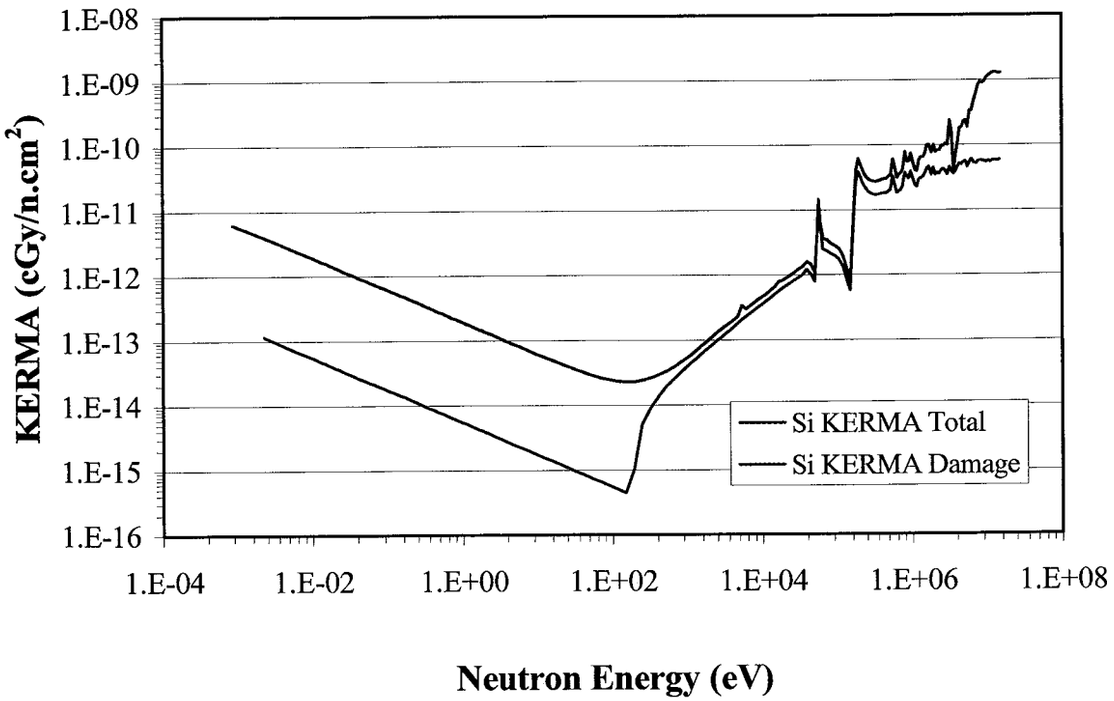

Figure 3-3. Silicon displacement KERMA and total KERMA as a function of neutron energy[125].

The determination of the neutron damage KERMA for silicon (and other materials use in microelectronic manufacturing) has been the subject of intense investigation for several decades[123, 124]. These efforts have mainly been aimed at characterising the behaviour of silicon based microelectronic circuits for avionics, space and military applications where they may be exposed to radiation fields.

Arising from this research are accepted theoretically calculated values of silicon displacement KERMA which have been published as standard data sets for reference[125]. These values have been experimentally validated and found to have uncertainties of less than 10%. The total and displacement damage KERMAs for silicon are shown in Figure 3-3.

NEUTRON INDUCED CHANGES IN PIN DIODE I-V CHARACTERISTIC CURVES

Each dislodged silicon atom which becomes a stable defect in the silicon lattice will act as a recombination site and therefore have the effect of reducing the minority carrier recombination time and conductivity of the silicon. The resulting minority carrier lifetime, τ is given by:

$$\frac{1}{\tau} = \frac{1}{\tau_i} + K\Phi \qquad 3\text{-}1$$

where τ_i is the initial minority carrier recombination time, Φ is the neutron fluence and K is a constant known as the damage constant. K will be a function of neutron energy and of the initial resistivity of the silicon.

The relationship between the current - voltage characteristic of a PIN diode and the neutron fluence it is exposed to was determined by Swartz and Thurston[126]. They showed that under conditions of low injection (small currents) and where the width of the base was small compared to the diffusion length of the charge carriers (small W/L ratios) the overall neutron sensitivity is negative because the junction

voltage decreases with decreasing carrier lifetime and this effect predominates. For low currents but larger *W/L* ratios the voltage sensitivity is positive as a function of neutron exposure due to the base voltage increasing as the carrier lifetime and diffusion length decrease. Under these low current conditions for a given fixed ratio of *W/L* the voltage sensitivity is proportional to $K\tau$ and to KW^2.

For larger injected currents of carriers the voltage drop across the junctions is independent of carrier lifetime. Therefore the change in voltage across the diode as a whole is dominated by the change in voltage across the base section of the diode and the sensitivity is positive for all values of *W/L*. For a fixed *W/L* the sensitivity of the voltage across the diode to neutron fluence is proportional to $K\tau^{3/2}$ and to KW^3.

From these results it can be seen that the approximate sensitivity of PIN diode dosimeters is determined at manufacture and can be increased by making diodes with wider intrinsic silicon base sections. The PIN dosimeter sensitivity could also be increased by using high resistivity silicon with a large initial carrier lifetimes, τ.

The theoretical predictions of Swartz and Thurston were later summarised and experimentally verified by Van Antwerp and Youngblood[127] who present the voltage across the base as:

$$V_b = \frac{2kT}{e}\sinh\left(\frac{W}{2L}\right)\tan^{-1}\left[\sinh\left(\frac{W}{2L}\right)\right] \qquad 3\text{-}2$$

Where *W* is the width of the base region of the diode, *e* is the electron charge, *T* is the temperature and *k* is Boltzmans constant. *L* is the diffusion length which is related to τ the carrier lifetime after neutron irradiation by:

$$L = \sqrt{D\tau} \qquad 3\text{-}3$$

Where D is the diffusion constant (i.e.: $kT\mu/e$, where μ is the carrier mobility).

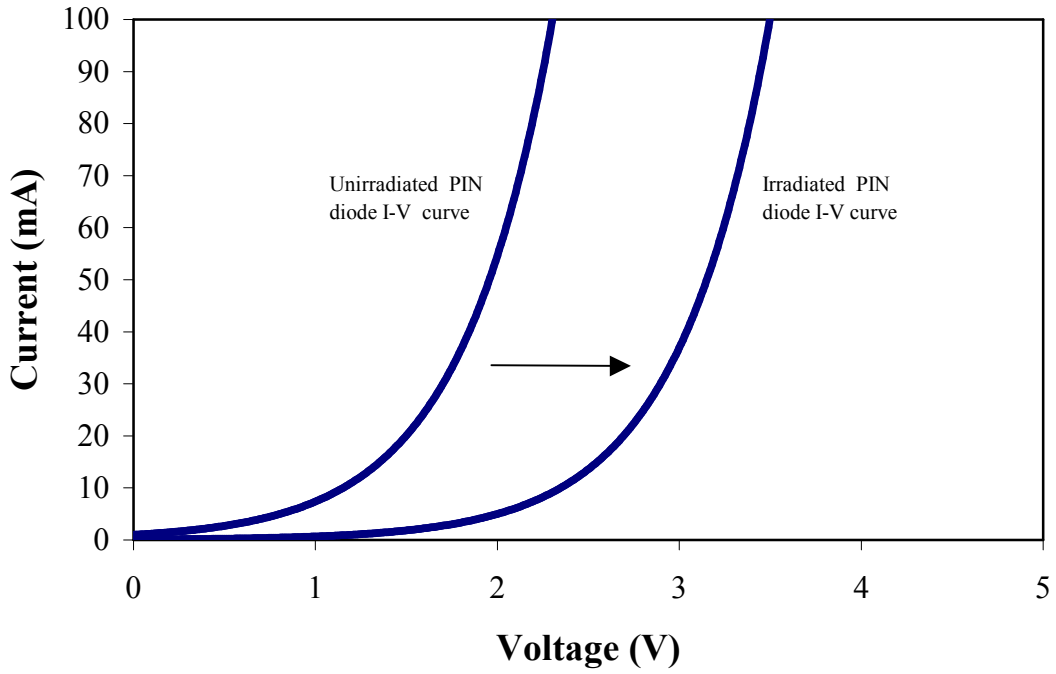

Figure 3-4. PIN diode I-V characteristic curves. The curve on the left represents a PIN diode that has not been exposed to a neutron dose. The carrier lifetime is unmodified. The curve on the right represents a diode that has been irradiated with neutrons with the consequent decrease in carrier lifetime in the base section of the diode and resulting increase in the overall voltage drop across the diode.

PIN READOUT TECHNIQUE

In order to determine the damage imparted to the PIN diodes by neutrons the macroscopic parameter usually measured is the forward bias voltage for a fixed small current. In principle it is possible to directly measure the change in carrier lifetimes by observing the voltage decay across the diode following the disconnection of a forward bias voltage to the diode. This voltage decay represents the recombination of carriers close to the junctions and the slope of the curve allows the carrier lifetime to

be calculated[126]. For more sensitive diodes with a larger *W/L* ratio (i.e. wider base region) this technique is not very accurate. Therefore usually the forward bias voltage is measured.

A number of authors have described PIN diode dosimetry readout systems[128,129].

Awschalam et al[128] describe a reader based on a constant current generator, sample and hold circuit and a analog to digital converter with display. The constant current source was set to 25 mA. The voltage across the diode was measured using a single 10 mS duration pulse of 25 mA during which the forward bias voltage was captured with the sample and hold circuit. A stability of ±1mV was obtained with this reader over the course of several days.

Nagarkar et al[129] describe investigating a reader which used a series of three to five 10 mS duration pulses of 25 mA each. However they found that this method caused heating of the diode with the consequent annealing of the radiation induced defects. They therefore developed a reader that employed a single 1 mS duration 10 mA pulse.

Other authors[127, 130] conducting experiments more aimed at characterising silicon damage cross sections in earlier publications employed constant current (non pulsed) readout circuits with currents of up to 100 mA and as low as 1 mA.

For the PIN diodes used in this work the change in this forward bias voltage is of the order of 200 mV/cGy of silicon displacement damage dose. For most epithermal neutron spectra used in BNCT this corresponds to approximately 1-2 mV/cGy of tissue dose. Therefore to measure neutron doses in the range that is useful for BNCT beam dosimetry changes in the forward bias voltage of a less than 1 mV

should be accurately measurable.

Readouts of the forward bias voltage change accurate to within 1 mV can be easily achieved using a constant current source based on a commercial operational amplifier and a JFET. In practice the readout circuit makes use of a pulsed current source to avoid ohmic heating of the PIN diode. The effect of constant current heating the junction would be to heat the diode and anneal some of the neutron induced defects in the diode.

By using a current source of approximately 1 mA pulsed at a frequency of about 100 Hz and with a pulse period of 1 mS and a peak detector circuit it is possible to readout the diodes with a duty cycle of 0.1. This minimises heating of the diode and annealing of the defects.

That such a biasing scheme leads to minimal heating can be shown by assuming that the voltage drop across the base of the diode is of the order of 1 volt. If the power dissipated in the base of the diode is estimated as approximately VI where V is the voltage drop across the base section and I is the current then the average power dissipated would be of the order of 1mA x 1volt x 0.1 = 0.1 mW. Assuming a heat capacity of 0.7 $J.g^{-1}.K^{-1}$ for silicon and a mass of approximately 2.33 mg ($1mm^3$) of silicon in the diode the temperature rise would be < 0.1°C per second. Therefore the temperature in the PIN diode would be unlikely to rise by more than a few °C during the course of several seconds while it was connected to the pulsed current source for readout. This is important for two reasons; firstly any annealing is avoided and secondly changes in the forward bias voltage of the diode due to thermal effects on silicon conductivity are avoided.

A block diagram of the readout system used to measure the forward voltage

change of the PIN diodes used in this work is shown in Figure 3-5.

The full circuit[131] (including a MOSFET reader incorporated into the same circuit) is shown in Figure 3-6. This circuit was tested on resistors and showed a readout accuracy of ± 4mV over the course of several weeks. A standard resistor was periodically tested to maintain constancy and check calibration. Since most readouts prior to and following irradiation of the PIN diodes were performed in the same session over the course of a few hours the accuracy of the readout circuit was certainly better than ± 1mV and probably better than ±0.5 mV for measurements performed during one experimental session on single day. The precision of the readout was ± 0.1mV.

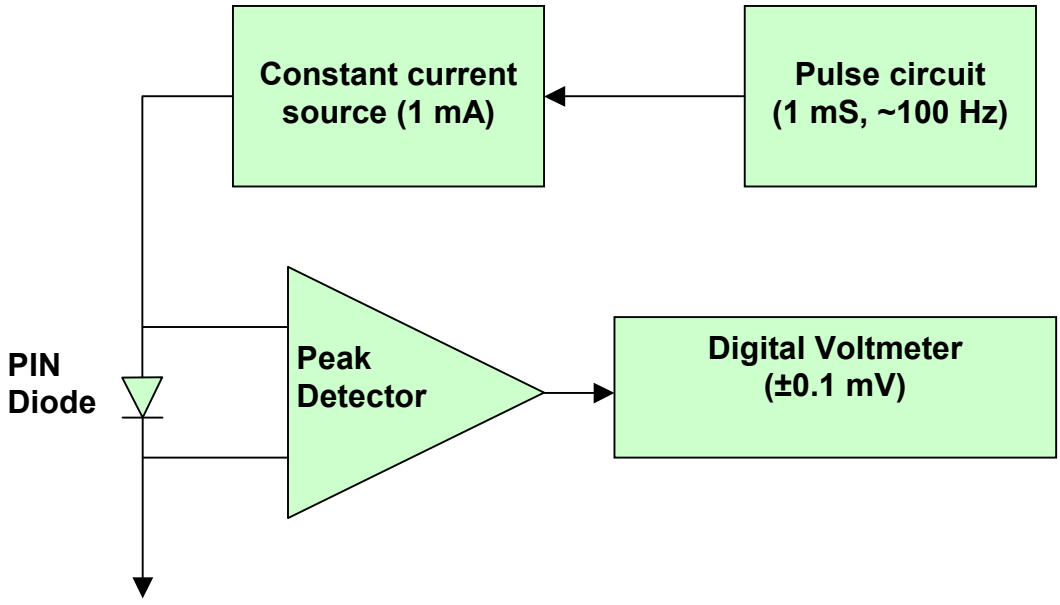

Figure 3-5. Block diagram of PIN diode readout circuit.

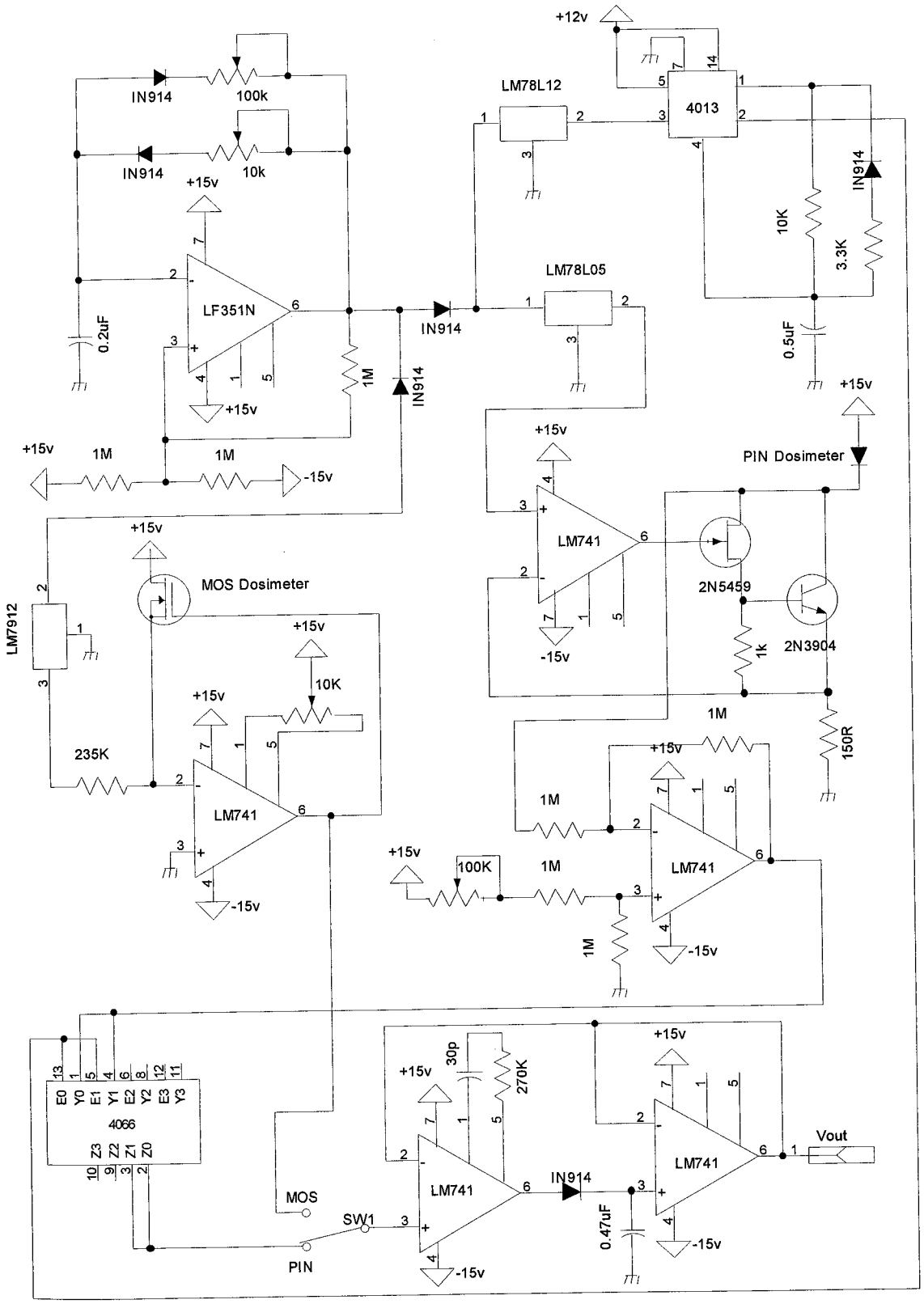

Figure 3-6. Schematic of circuit used to readout the PIN diodes. Design concept Centre for Medical Radiation Physics, University of Wollongong[131].

PIN DIODE SPECIFICATIONS

The PIN diodes were obtained from the Institute of Nuclear Research (INR) Ukraine. They were manufactured with an intrinsic silicon base with a resistivity[132] of approximately 50Ω.cm. The width of the base was approximately 1mm. A PIN diode of the type used in shown in Figure 3-7.

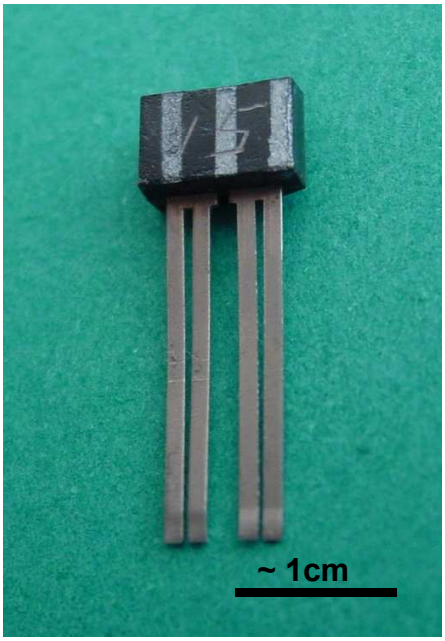

Figure 3-7. Silicon PIN diode supplied by INR Ukraine as used for measurements in this thesis.

I-V CHARACTERISTIC

The I-V characteristic curve for a typical unirradiated diode is shown in Figure 3-8. This was measured directly under constant current conditions rather than with a pulsed current source as is used for readout during dosimetry measurements.

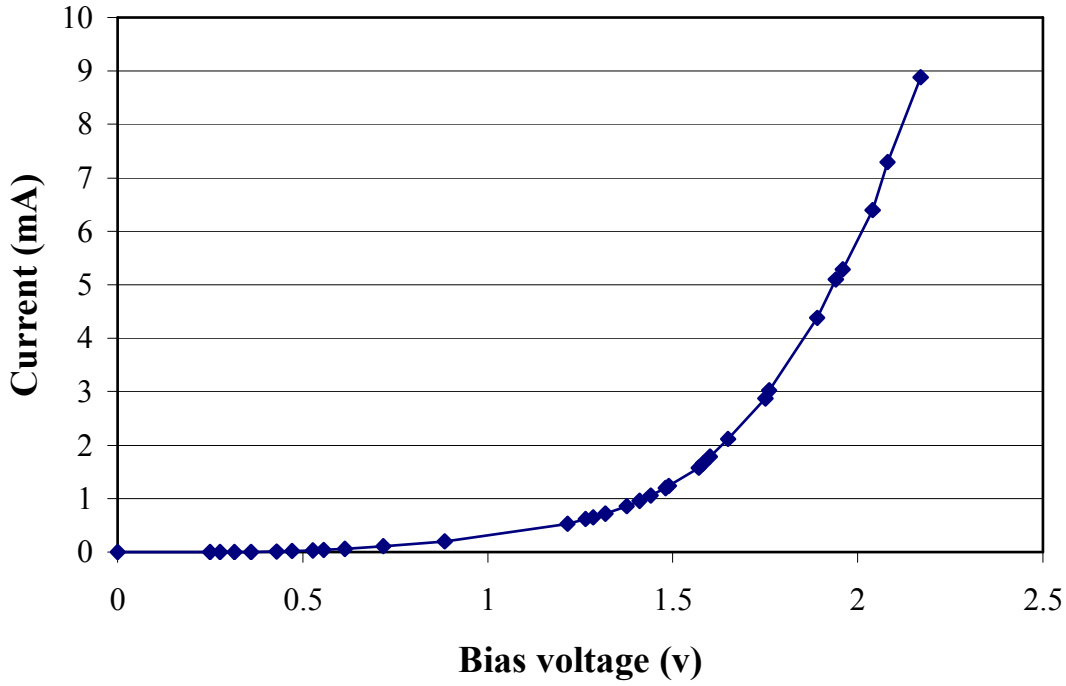

Figure 3-8. Measured forward bias characteristic I-V curve for an unirradiated PIN diode. (Diode #18 from the batch used for all PIN diode measurements described in this thesis.)

TEMPERATURE COEFFICIENT

The PIN diode temperature coefficient was measured as -1.3 mV.°C^{-1}. As expected the relationship between the forward bias voltage of the diode at a constant current of 1mA was linear with temperature changes over the range from approximately 10 - 60 °C. This covers the anticipated operating range of the PIN diodes. The measurement of this temperature coefficient is described in Chapter 11 of this thesis describing the PIN diode measurements on the Petten HFR HB11 beam.

SILICON PIN RESPONSE VERSUS TISSUE EQUIVALENT DOSE.

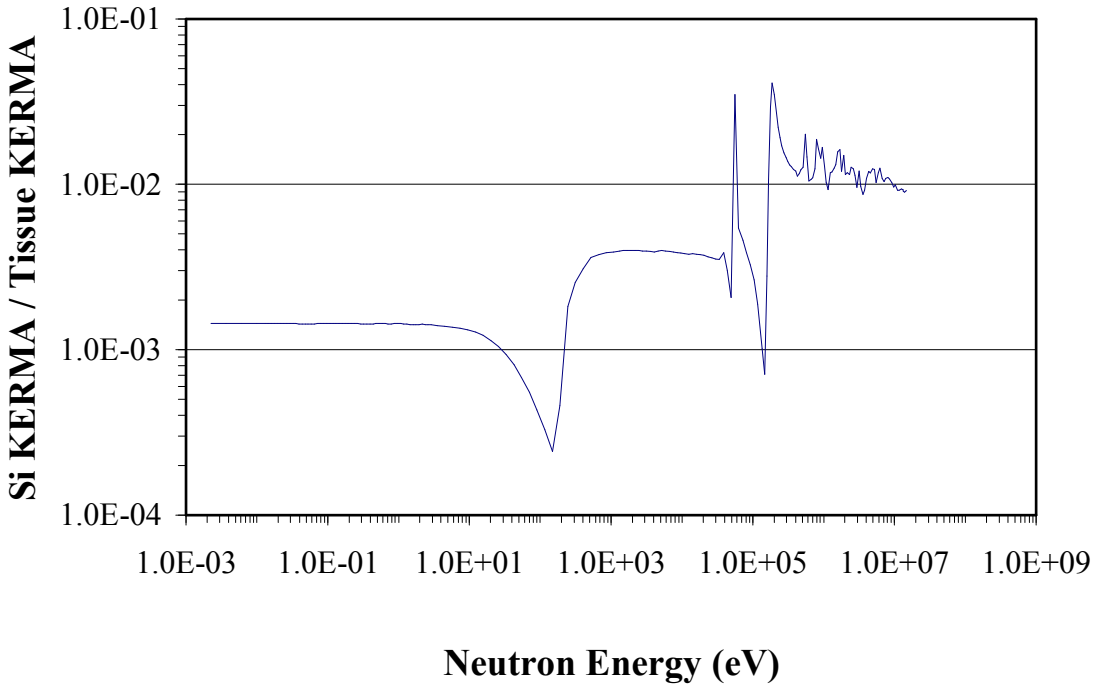

Figure 3-9. The Ratio of silicon displacement KERMA[125] to tissue KERMA[4].

As will be investigated in later chapters the response of the PIN diode forward bias characteristic as a function of neutron energy is proportional to the silicon displacement damage KERMA. Over limited energy ranges this is in constant proportion with tissue KERMA. However the response of a PIN diode to neutron radiation will not be directly proportional to tissue neutron dose for a general neutron spectrum. The ratio of silicon displacement KERMA to tissue KERMA as a function of neutron energy is shown in Figure 3-9. It can be seen that the PIN diode is relatively more sensitive to fast neutrons.

There are two situations where it may be possible to use a PIN diode to measure tissue neutron dose. The first of these is where all of the neutrons present fall into a narrow energy range (eg thermal to several eV) and the silicon to tissue

KERMA ratio is constant over this range. The second possible situation is where the total tissue dose is so dominated by the fast neutron contribution that the thermal neutron contribution is negligible and therefore the under estimate of thermal neutron dose provided by the PIN diode does not introduce a significant error into the total neutron dose measurement. This condition may exist for example in close proximity to californium brachytherapy sources.

However since the PIN diode clearly responds to a wide range of neutron energies it can be used in combination with activation foil measurements to provide estimates of tissue dose over a wider range of energies (approximately thermal to 100 keV). The development of a technique for parameterising tissue dose in terms of PIN diode and foil activation measurements is described in more detail in Chapter 6.

The PIN diode response to a wide range of neutron energies can also be used as a check on Monte Carlo treatment plans and other dose calculations. In this case both the tissue dose and silicon displacement dose are calculated using the Monte Carlo (or other) technique. The accuracy of the tissue dose calculation is then indirectly verified by ensuring that the measured silicon dose matches the calculated silicon dose. If good agreement is obtained between the silicon dose measurement and calculation then confidence is established that the calculated tissue dose is also accurate. This is based on the response of the silicon to a wide range of neutron energies. This is a characteristic not shared by most activation foil measurements where the observed activation is heavily weighted towards activation from thermal and one or two resonance energies.

The small size and ease of readout of PIN diodes make them useful for routine in-vivo measurements of this nature compared to ionisation chambers. They

can also be used in an on-line mode to yield real-time dose measurements for dose mapping in water phantoms or verification of calculated patient dose distributions during treatment.

Some measurements aimed at matching measured and calculated silicon diode responses in phantoms in epithermal beams are described in Chapter 11 and Chapter 13 of this thesis.

ION CHAMBERS

The ionisation chamber measurements performed or referred to as part of this thesis (Chapter 11 and Chapter 12) were made using the techniques and equipment described by Raaijmakers [43,200] and will not be repeated here. They are briefly described in Chapter 2 under the heading of Dosimetry Techniques.

ACTIVATION FOILS

A number of activation foils were used for determining neutron fluences at points throughout phantoms for the studies described in this thesis. Resonance foil activation is one of the best established methods for determining neutron fluxes. It enables very accurate measurements of the neutron flux at the energy of the neutron capture resonance in the foil. However the data obtained from resonance foil activation is point wise flux data for the resonance energies only. Although KERMA per neutron factors can be used to convert these fluences into doses the true dose from a spectrum of neutrons cannot be determined on the basis of foil activation data alone without making some assumptions about the shape of the neutron spectrum at

energies between those where resonances exist.

Unfortunately, although several suitable activation materials exist which have resonances in the range from 1 eV up to tens or hundreds of eV, in commonly used foils there are only sparsely spaced resonances at energies in the keV range which is of importance for any epithermal BNCT beam (Table 3-1.)

Table 3-1. Resonance energies and resonance integrals for some activation foils used for neutron flux measurements.

Foil element	Resonance energy (eV)	Resonance integral (barns)
Au	4.906	1558
Mn	337	14
Cu	580	5.6
In	1.457	3243
Co	132	77

Thus the role of foil activation is primarily to serve as a validation of Monte Carlo transport calculations and for baseline measurements of beam characteristics. Foil activation data because of its absolute nature lends itself to normalisation of Monte Carlo flux data and validation of Monte Carlo transport calculations. Due to the collisional slowing down process of neutrons in a scattering and absorbing medium such as a patient or tissue equivalent phantom measurements made in the 1 eV - 1 keV range will reflect contributions from incident higher energy neutrons as well. Therefore although the multi keV neutron spectral component is not being measured directly using activation foils, in most cases an inaccuracy in the calculation of that component will be reflected in a corresponding inaccuracy in the

number of down scattered neutrons. This may be evident in activation foils. Therefore as a first step in measuring neutron flux distributions activation foils are most useful. They are irreplaceable in the design and development phase of characterising neutron beams. They also allow for very accurate determination of thermal flux and therefore thermal neutron tissue dose from the $^{14}N(n.p)^{14}C$ reaction and the ^{10}B reaction rate and therefore the ^{10}B dose. Ultimately however for routine patient dosimetry a real time readout of dose rather than just fluence would be useful.

In using activation foils a number of factors must be taken into consideration. For most resonance activation foils it is necessary to take into account the self shielding effect of the resonance. Because of the large resonance absorption peak in the neutron capture cross section at the resonance energy the population of neutrons at that energy at a small depth inside the foil will be depressed. Therefore if the fluence calculation derived from the activation of the foil is based on all of the atoms in the foil without some allowance for self shielding then the resulting fluence will be too low. Self shielding increases with foil thickness. Therefore the foil thickness must be known quite accurately and the appropriate self shielding factors applied.

In addition to self shielding effects the thermal neutron activation effects must be accounted for. To determine the neutron fluence at the resonance energy at a particular point the thermal and the resonance activation components must be determined. Usually two foils are used (the cadmium difference method). One is used bare and the other is enclosed in a Cd cover. The effect of the Cd cover is to shield the activation foil from thermal neutrons. The cadmium cut off is at approximately 0.5 eV. Therefore the activation on the Cd shielded foil will be due to neutrons captured by the resonance only. The bare foil will be activated by both thermal

neutrons and the resonance energy neutrons. The Cd cover must be thick enough to attenuate all of the thermal neutrons which in practice is easily achieved by using a thickness of about 1 mm.

The resulting data must be corrected for decay between the time of the exposure and the time of counting. Using the known resonance integral and the thermal capture cross section the fluence to which the foil was exposed can then be calculated.

CHAPTER 4 PHOTON DOSIMETRY USING MOSFET DOSIMETERS

MOSFET OPERATION

MOSFETs are metal oxide semiconductor field effect transistors. A schematic diagram of a MOSFET is shown in

Figure 4-1. In ordinary operation a small voltage applied to the gate electrode is used to modulate or switch the current flow between the source and drain electrodes. The MOSFETS used in this work were developed by INR Ukraine. They were made on a p-type silicon substrate with a resistivity of approximately 10 ohm.cm. The gate electrode is insulated from the substrate by means of a silicon oxide insulating layer which has a thickness of approximately 1μm.

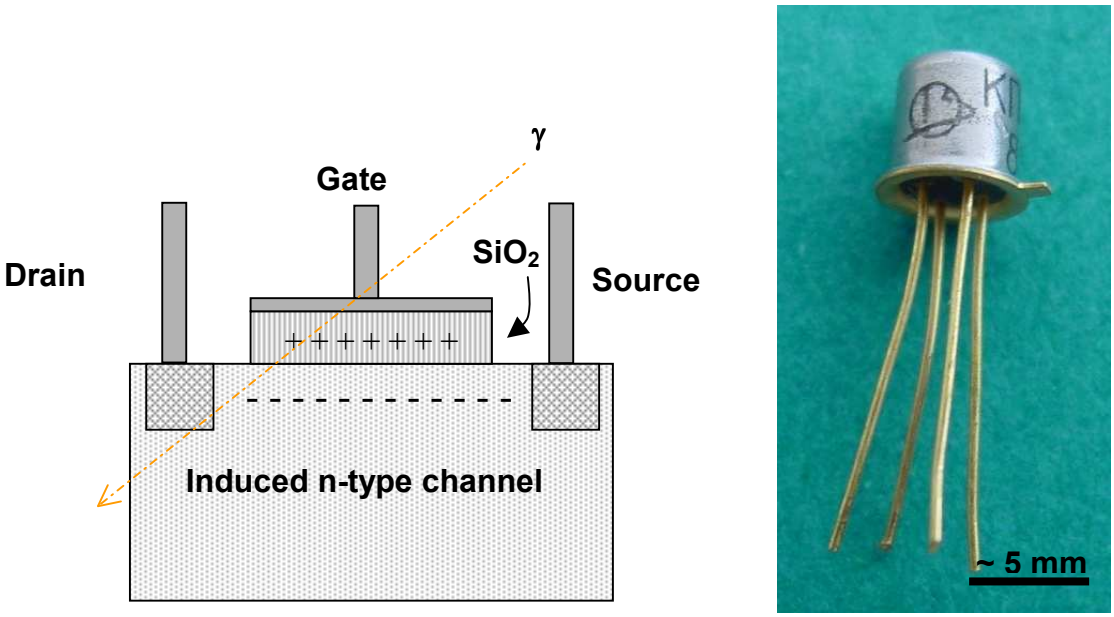

Figure 4-1. Conceptual schematic outline of MOSFET shown with dosimetry MOSFET developed by INR Ukraine.

This is in contrast to commercial MOSFETs where the oxide layer is usually less than one tenth of this thickness. The gate electrode is formed from a thin (approximately 1μm) layer of Al deposited on top of the oxide layer. A schematic representation of the electrode arrangement is shown in Figure 4-2.

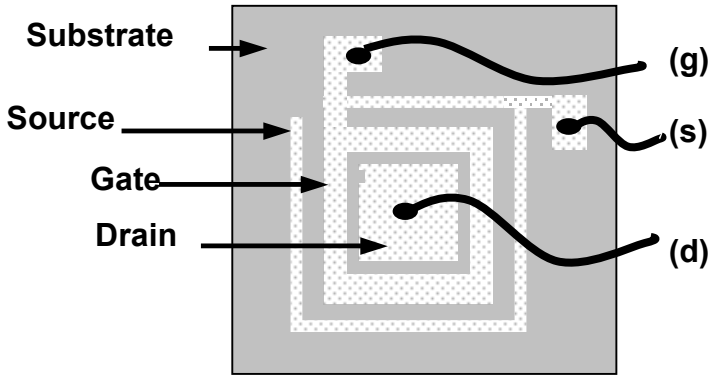

Figure 4-2. Schematic of typical electrode configuration for a dosimetry MOSFET as used in this work.

In normal operation if there is no potential connected to the gate electrode the current between the source and drain electrodes will be zero because of the pn junctions at both. As a positive potential is applied to the gate electrode the holes in the p type substrate will be repelled from the region under the gate. This forms an n-type channel between the source and drain regions which allows a current to flow. The gate voltage at which this channel is established and current begins to flow (the "strong inversion" condition) is called the threshold voltage[133], V_T, and is given by[138]:

$$V_T = \phi_{MS} + \phi_B - \frac{Q_{ox} Q_B}{C_{ox} C_{ox}} \qquad 4\text{-}1$$

where ϕ_{MS} is potential difference due to the work functions of the gate metal and the silicon substrate, ϕ_B is total potential difference due to band bending, Q_{ox} is charge in the oxide due to processing, C_{ox} is the oxide capacitance and Q_B is the charge in the depletion region. As the gate voltage is increased the source drain current increases. This is shown in schematically in Figure 4-3. The source drain current can be modeled as being proportional to the square of the voltage on the gate.

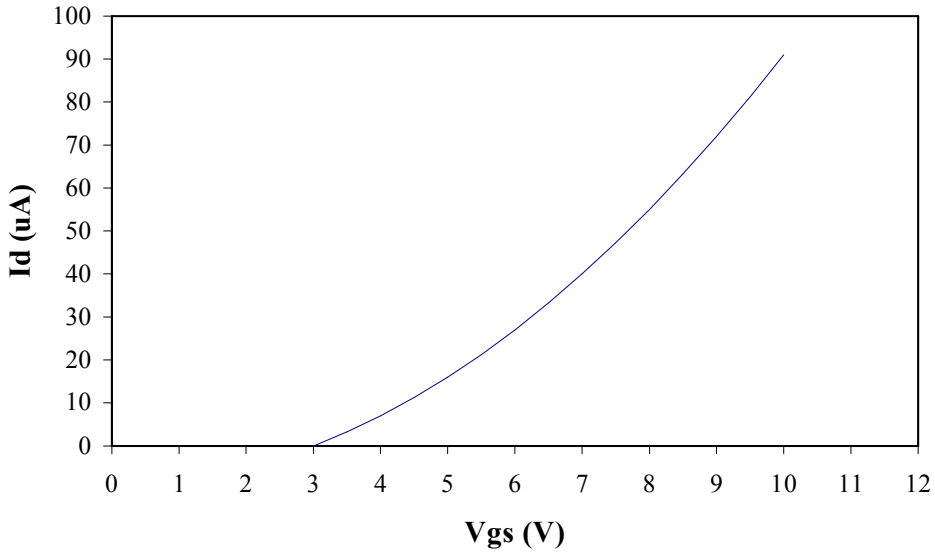

Figure 4-3. MOSFET characteristic curve for an n-channel MOSFET operating in enhancement mode.

When it is necessary to routinely measure the threshold voltage of a MOSFET the potential at which strong inversion occurs as defined in terms of the work function of the MOSFET materials is not the ideal parameter to measure in practice. Instead of this some small I_d is defined as representing the practical threshold condition. This current may typically be of the order of several μA or 10's of μA. So what is actually measured and referred to as "threshold voltage" is actually a potential

applied to the gate that represents the voltage at which a specified level of current flows rather than the true "threshold" voltage at which the MOSFET characteristic curve intercepts the voltage axis on the I_d vs V_g graph (see Figure 4-3). The actual level of current that is chosen to represent the threshold condition for the purposes of measurements is discussed below.

MOSFET THERMOSTABLE POINT.

The slope of the MOSFET characteristic curve is a function of temperature. The temperature dependence of the surface inversion potential causes the threshold voltage (the real theoretical threshold voltage as defined in equation 4-1) to change with temperature. This change has a small negative coefficient typically leading to changes in the threshold voltage in the order of 2-3 mV per °C. This effect dominates the temperature dependence of the characteristic curve at very low drain currents (a few μA). However at higher drain currents the temperature dependence of mobility, μ(T), of carriers within the induced channel will have the main impact on the changes in drain current as a function of temperature. The behavior of μ as a function of temperature is given by:

$$\mu(T) = \mu(T_0) \cdot \left[\frac{T}{T_0} \right]^{-1.5} \qquad 4\text{-}2$$

Therefore the temperature behavior of the transconductance parameter is also proportional to this change in mobility with temperature, ie.

$$\beta(T) = \beta(T_0) \cdot \left[\frac{T}{T_0} \right]^{-1.5} \qquad 4\text{-}3$$

The combination of the small negative temperature coefficient for V_T and the temperature dependence of the transconductance at higher levels of I_d leads to a family of I_d vs V_g characteristic curves having different slopes but intersecting at a common point. This has been called the "thermostable point"[134, 135].

For the purpose of performing routine measurements of the nominal threshold voltage of a MOSFET some small predefined level of I_d is chosen. In order to minimise the temperature dependence of the threshold voltage measurements the value of I_d chosen should be the drain current that corresponds to the thermostable point of the MOSFET. Under these measurement conditions, when no other changes have affected the MOSFET (radiation etc), the measured values of the nominal threshold voltage at the thermostable point should change very little.

For the MOSFETs used in the work described in this thesis the thermostable point was expected to be at approximately 42μA. This was based on information provided by measurements undertaken by G Kaplan[136]. For all the measurements reported in this thesis the nominal threshold voltage represents the MOSFET gate voltage required to establish I_d=42μA. Therefore for brevity and readability any reference in this thesis to threshold voltage measurements refers to Vg(I_d=42μA) except where stated otherwise.

When the MOSFET is employed as a dosimeter the characteristic curve is shifted due to radiation effects as described below. Under these circumstances the drain current at which the thermostable point occurs will also change. Therefore temperature effects can minimised but not eliminated completely by measuring the

MOSFET gate potential at a drain current corresponding to the thermostable point. Variability from one MOSFET to another even within the same batch leads to different thermostable points in each device[134].

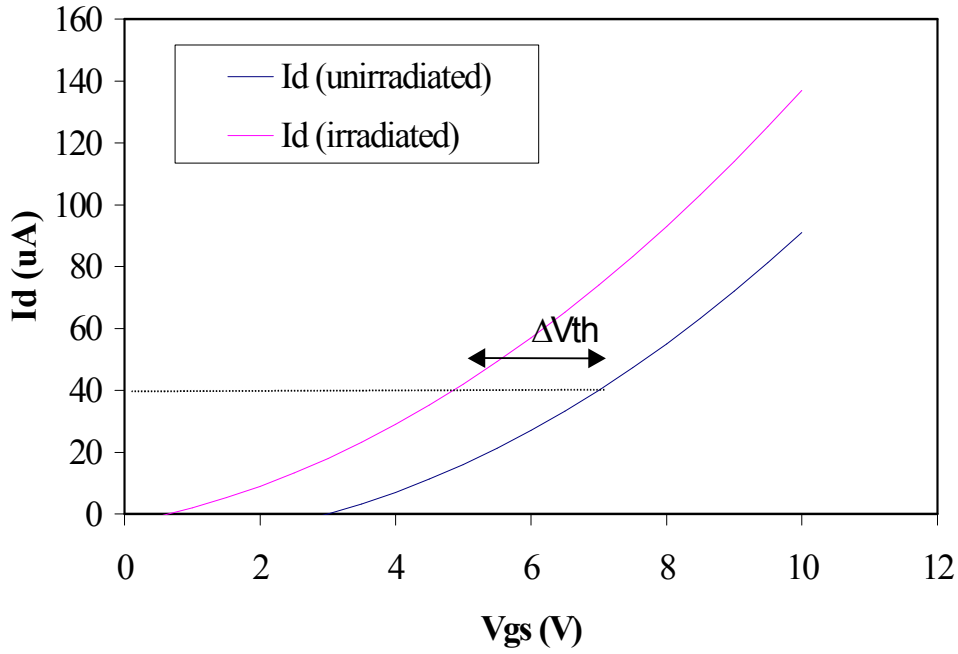

Figure 4-4. Radiation effect on I_d vs V_g characteristic of MOSFET.

EFFECT OF RADIATION ON MOSFET

Under exposure to ionising radiation electron hole pairs are produced in the SiO_2 layer as the Si=O bonds are broken. Some of these electron hole pairs recombine immediately but others become trapped. Holes may be trapped throughout the oxide or at the insulator - channel interface. These trapped positive charges throughout the oxide layer have a similar effect to the application of a positive gate bias. They repel holes from the substrate region underneath the oxide layer thus

setting up an n-type channel between the source and drain regions. This has the effect of moving the I_d versus V_g characteristic curve to the left (Figure 4-4). In effect to maintain the same I_d the voltage applied to the gate of the MOSFET must become more negative to compensate for the presence of radiation induced positive charges in the oxide layer.

In general commercial MOSFETs are made with the oxide layer as thin as possible to minimise their radiation sensitivity. In the case of the MOSFETs which were used for our study the oxide layer is 1 μm in order to increase their sensitivity. The thicker oxide layer impacts on the radiation sensitivity in two ways[137]. The thicker the gate oxide layer the greater the potential which must be applied to the gate to establish an electric field great enough to compensate for the holes distributed in the oxide. The larger the volume of oxide the more electron hole pairs are generated.

The bias applied to the gate will also influence the sensitivity of the MOSFET to radiation. If a positive bias is applied to the gate during irradiation a greater proportion of the holes with some mobility will migrate to regions closer to the SiO_2 / Si interface. The effect of this is that a larger change in the threshold voltage is required to offset it. A second effect of having a bias applied whilst the device is being irradiated is that it decreases the recombination of the electron hole pairs immediately after their formation. This leave more holes free to be trapped and thereby increases the radiation sensitivity.

Other factors which influence the sensitivity of the MOSFET to radiation include the method used to grow the oxide layer on the substrate and any impurities in the oxide layer. This effects the sensitivity via hole and electron transport mechanisms in the oxide and the number of traps available to immobilise the

electrons. The temperature of the device will also influence how may of the electrons and holes are trapped and where they are trapped thereby affecting the threshold voltage change.

A simple model of the threshold voltage change in irradiated MOSFETs was developed by Freeman and Holmes-Seidle[137]. The trapped holes with area charge density Q_{ox} were considered to be located as a sheet of charge at a distance x_1 from the oxide / silicon interface and a distance x_2 from the oxide gate interface. The thickness of the oxide layer was $d_{ox} = x_1 + x_2$. The presence of Q_{ox} in the oxide induces negative image charges in the silicon, Q_s, and in the metal of the gate electrode, Q_m. The magnitude of the charge in the silicon is given by:

$$Q_s = \frac{x_2}{d_{ox}} Q_{ox} \qquad 4\text{-}4.$$

To compensate for this charge in the semiconductor the potential applied to the gate electrode must be reduced by an amount:

$$\Delta V_T = -\frac{Q_{ox} x_2}{\varepsilon_{ox} \varepsilon_o} = -\frac{q N_{ox} x_2}{\varepsilon_{ox} \varepsilon_o} \qquad 4\text{-}5$$

Where ΔV_T is the MOSFET threshold voltage shift, ε_{ox} is the oxide dielectric constant, ε_o is the permittivity of free space, q is the electronic charge and N_{ox} is the number of trapped holes per unit area.

It is further assumed that N_{ox} depends upon the number of holes produced by ionising radiation, g, and the fraction of these, f(E), which escape recombination and are available for transport within the oxide layer. This fraction is a function of the applied electric field, E, in the oxide layer. The number of holes generated, g, can be estimated based on the average energy required to create an electron hole pair in SiO_2 (approx. 18 eV) and the density of the oxide (approx. 2.27 $g.cm^{-3}$). The fraction of

holes that are created and available for transport and that are captured in the trapping zone of the oxide is designated as *A*. For a positively biased gate this gives:

$$N_{ox} = gx_2.f(E).A\ cm^{-2}cGy^{-1} \qquad 4\text{-}6$$

By combining equation 4-5 and 4-6 it can be seen that the threshold voltage shift is (at least initially) a linear function of dose to the oxide layer.

$$\Delta V_T = \left[-\frac{qg}{\varepsilon_{ox}\varepsilon_o} x_2^2.f(E).A \right] D \qquad 4\text{-}7$$

In the case where $x_2 = d_{ox}$, ie all of the trapping assumed to occur right on the oxide silicon interface, then the change in threshold voltage per unit dose is proportional to d_{ox}^2. This is the result given by McGarrity[138].

As the amount of dose absorbed by the MOSFET increases the initial linear relation between dose and ΔV_T eventually saturates[137]. This occurs as traps fill up and therefore the fraction being trapped, *A,* decreases. The electric field also decreases leading to a lower fractional yield f(E).

The amount of change in ΔV_T per unit dose as the MOSFET is exposed to successive radiation doses depends on the potential applied to the gate during the irradiation. This change in sensitivity was measured for the Ukrainian MOSFETs used in this thesis under conditions where no bias was applied to the gate during irradiation. The results of these measurements are described in later chapters. Where necessary a correction for this saturation effect is applied to MOSFET measurements described in this thesis. The change of sensitivity with accumulated dose for the MOSFETs irradiated with a bias applied has also been characterised[136].

It has been estimated that when an electron hole pair is created in the oxide layer the high mobility electrons typically migrate out of the oxide layer within about

2 picoseconds[139, 140]. The holes have lower mobilities and under a positive gate bias migrate towards the oxide - silicon interface where some are trapped. As previously noted the fraction of holes that are available for transport in the oxide layer, sometimes called the fractional yield, f(E), is a function of the electric field in the oxide layer. It is also a function of the pattern of energy deposition along the incident radiation track and the dose rate. Brown and Dozier[141] have modeled the patterns of energy deposition in SiO_2 resulting from different incident energy photons (Co-60 and Cu x-rays). The initial energies of electrons resulting from these incident photons have different track structures. The volumes within which electron - hole pairs would be created for each of these track structures were determined and recombination proportional to the square of the hole density was assumed. A characteristic time during which recombination could occur before the electron - hole pairs were swept apart was defined as a function of the applied electric field in the oxide. The results of this model have achieved a satisfactory match to experimental data[142].

Different fractional yields have been observed experimentally for combinations of various types of radiation and oxide fields. For example[138] at an oxide field of 1 $MV.cm^{-1}$ the fractional yield is 0.85 for 12 MeV electrons[143], 0.7 for Co-60 gamma rays[144] and approximately 0.5 for 5 keV electrons[145].

MECHANISM OF FADING[146]

The time behaviour of the threshold voltage shift is a function of the various trapping mechanisms at work. These include, the speed at which holes are trapped which is almost instantaneous, the slow recombination of holes with electrons at the SiO_2 / Si interface which causes a slight drift in the threshold voltage back to a more

positive value. The possibilities for holes trapped near the oxide - silicon interface are summarised by Fleetwood et al[139]. The first possibility is that the hole is bound in a trap. In the absence of a trap the hole may arrive at the interface and recombine with an electron from the silicon. Alternatively the hole may be trapped at the interface but compensated by a shallow trapped electron. This can in some circumstances be explained as a tunneling effect. The final alternative is that it may not be possible for an electron to transfer from the silicon across to the hole in the oxide layer. However a lattice relaxation associated with the hole transport may take place which allows a defect or impurity atom to form a trap that can capture an electron from the silicon. The charge from this electron becomes deeply trapped and forms a stable dipole with the adjacent trapped hole.

By measuring the thermally stimulated currents from MOS junctions following irradiation it is possible to elucidate the depth of the trapped electrons and holes. As the temperature of the MOS is slowly increased the current arising from electrons and holes escaping from their traps is observed.

Depending on the method of MOSFET manufacture migration of positive ions within the silicon oxide layer can also play some part in the slow drift of the measured threshold voltage following MOSFET irradiation.

Over time the holes trapped in the oxide will anneal out (this can be accelerated by heating the MOSFET - which suggests the possibility of reuse of MOSFETs for dosimetry purposes however this is not explored in this thesis). At room temperatures this process takes place on a timescale of months to years for the MOSFETs that we used. Therefore for measurement techniques that measure the V_{th} just before irradiation and again shortly afterwards (minutes to hours) the effect of

fading is considered to be negligible. Any small initial fading (ie shift in V_{th} back to a more positive value) can be allowed for by always measuring at the same temperature and at a similar delay post irradiation.

EFFECT OF DOSE ENHANCEMENT[a]

As noted above the fractional yield of trapped holes can vary with the energy and type of radiation the MOSFET junction is exposed to. Another effect that impacts upon the sensitivity of MOSFETs and in general may be considered energy dependant is the so called "dose enhancement" effect. The dose enhancement effect occurs at all photon energies but becomes most significant for incident energies below about 100 keV. Dose enhancement is of major interest when considering the appropriate encapsulation and fabrication materials for manufacture of integrated circuits to ensure that they have minimal radiation sensitivity.

Dose enhancement in MOSFETs (and other semiconductor devices) arises at interfaces between materials of different Z. For example between a gold contact bonded to the silicon chip. It can also occur as a result of high Z materials present in the device encapsulation as is the case for the MOSFETs in this study. Incident photons interact[147] in the high Z material overlying or surrounding the sensitive part of the device (SiO_2 for the MOSFETs). From these interactions scattered electrons are produced. These electrons in turn scatter further electrons which deposit their

[a] The term “dose enhancement” to describe detector over-response is unfortunate in the context of BNCT dosimetry where it could be mistaken to imply increased tissue dose. It is used here in the sense of its accepted meaning in semiconductor device radiation effects literature.

energy in the surrounding material. At depths in the silicon or SiO_2 that are greater than the range of the secondary electrons from the high Z material dose equilibrium exists. However at shallower depths there is electronic disequilibrium and the dose is higher than the equilibrium dose in the silicon or SiO_2. The effect is greatest for higher Z materials overlying the silicon or SiO_2 because of the higher photon interaction cross sections of these elements. The effect is also most pronounced at lower energies where the photoelectric effect predominates. At higher energies most interactions are Compton scatters for which the cross section is not very dependant on the Z of the absorbing material. However even where Compton scatters predominate some dose enhancement may be seen due to stopping power differences for the scattered electrons in the two adjoining materials.

For a gold - silicon interface a maximum enhancement factor of approximately 30 has been estimated for 100 keV x-rays and a maximum enhancement of about 2 for ^{60}Co gamma rays[147]. The same authors provide tabulations based on calculation and experiment for estimating the dose enhancement factors for various combinations of chip electrodes and chip encapsulations. For a kovar package with an aluminium electrode covering SiO_2 they estimate an enhancement factor of 1.4 for ^{60}Co gamma rays and a factor of 6.3 - 6.7 for a 15 keV blackbody x-ray spectrum. This combination of packaging and aluminium electrode corresponds in general to the structure of the MOSFETs that were used in this thesis. However calculated enhancement factors such as these (especially the low energy x-ray estimate) should be treated as estimates only since more recent experiments and simulations by Fleetwood et al[148] have demonstrated inconsistencies between simulated and measured enhancement factors. This is attributed by Fleetwood et al to

shortcomings in the TIGER simulation code used for many of the dose enhancement factor calculations. In particular this may be due to the know inaccuracies of the TIGER code treatment of low energy electron scattering in low Z materials at the time those calculations were performed. The failure of the simulations to track electrons with energies < 1keV was also pointed out by Fleetwood to be a potential source of inaccuracy since these low energy electrons have been shown to be important in the pattern of dose deposition and the response of MOSFETs[149]. Hamm[149] used the OREC code to simulate transport of electrons and calculate dose and hole distributions in silicon and silicon oxide layered structures. Analog electron transport was used down to an energy 20 eV below which a condensed history model was implemented. These simulations demonstrated that transport of electrons with energies below 9 eV made a significant impact on the spatial distribution of dose and hole formation in sub μm SiO_2 layers. Therefore transport of electrons down to very low energies is probably necessary for accurate calculation of dose enhancement factors.

When using any MOSFET as a dosimeter the possible implications of dose enhancement need to be considered particularly where measurements are being made in low energy x-ray environments. Failure to take dose enhancement effects into account could lead to overestimates of measured dose at low energies. The conversion from absorbed dose in silicon to absorbed dose in tissue also needs to be taken into account. For this reason the approximate dose response as a function of energy for the MOSFETs used in this thesis was experimentally measured and is described in later chapters. However for application to measuring gamma dose rates in epithermal neutron beams the contribution of very low energy x-rays is not

expected to be great enough to warrant any special treatment of the raw measured data to correct for dose enhancement effects. If the MOSFET is calibrated in terms of threshold voltage change per unit of tissue dose in a high energy gamma field and measurements are performed in a high energy gamma field then a single gamma calibration factor should be adequate.

It should be noted however that measurements performed in the presence of neutrons will lead to some effective "dose enhancement" or over response due to neutron interactions in the MOSFET packaging. The application of neutron shielding and calculation of the energy response function for these neutron contributions is discussed in Chapter 5.

READOUT CIRCUIT FOR DETERMINING MOSFET THRESHOLD VOLTAGE, V_T

As previously noted, for routine measurements of V_T a drain current was chosen to match the expected thermostable current. A constant current source was used to apply the appropriate gate voltage to achieve this drain current. The voltage applied to the gate could then be determined. The basic measurement configuration is shown in Figure 4-5.

Because of the virtual ground conditions at the summing point on the inverting input of the operational amplifier the current determined by V_1/R sets the magnitude of the current through the MOSFET by negative feedback. The MOSFET gate potential is controlled via the amplifier output to maintain a current equal to V_1/R (typically a few tens of μA). In practice V_1 is provided by a regulated reference

source (eg an LM7912 regulator or similar). The reference voltage may also be pulsed to minimise noise in the measured output voltage from the operational amplifier. For pulsed readout a sample and hold circuit or a peak detector is used to store the magnitude of the output voltage from the operational amplifier which is then read on a standard laboratory digital voltmeter.

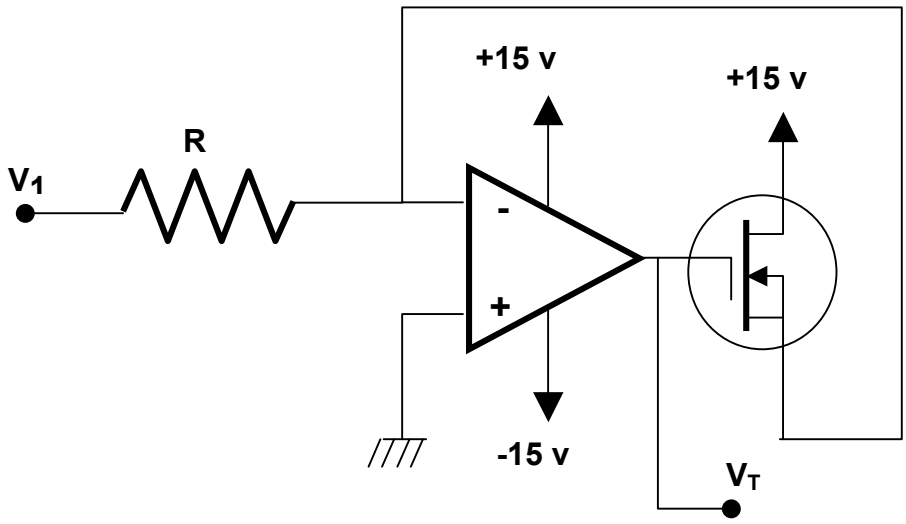

Figure 4-5 MOSFET readout circuit. In practice V_1 is usually pulsed and V_T is sampled using a peak detector or sample and hold circuit connected to a digital voltmeter.

ACCOUNTING FOR THERMAL EFFECTS DURING EXPERIMENTS

As discussed above, the characteristic curve of a MOSFET undergoes small changes with temperature. Despite attempting to measure the threshold voltage at a drain current as close to the expected thermostable point as possible it was observed that the measured threshold voltage increased as the ambient temperature is increased. The temperature dependence of the MOSFETs used was measured over the range of temperatures which were expected to occur in our experiments and in

normal operation. This measurement was achieved simply by immersing the MOSFET protected by a waterproof sleeve in a heated water bath. As the bath cooled the temperature was measured with a mercury thermometer and this was noted along with the threshold voltage. The results of these measurements are given in a later experimental chapter. The variation of V_T over the expected range of temperatures shows an approximately linear relationship and is thus easy to correct for in dosimetry measurements if the temperature is known. The shift in V_T per °C was assumed to be constant over the range of measurement conditions occurring in our experiments (ie despite radiation induced shifts in the Id vs Vg characteristic curve).

An alternative technique that has been used for correction of temperature effects[150] involves the use of two MOSFETs on the same substrate that have different gate biases applied during the irradiation. The sensitivity of the threshold voltage to temperature effects is assumed to be the same but due to the different gate biases applied during irradiation (and therefore different radiation sensitivities) the change in V_T for each MOSFET is different. The difference in the threshold voltage changes between the two MOSFETs will be proportional to the radiation dose received and any shift in V_T due to temperature changes will cause the V_T on both MOSFETs to be shifted by the same amount. Therefore temperature independence is obtained.

AUTOMATIC CORRECTION FOR THERMAL EFFECTS

Because the source and drain connections on the MOSFETs are actually p-n junctions it is possible to utilise this structure to determine the temperature of the MOSFET. This can be achieved by measuring the forward bias voltage drop across these p-n junctions. The change in bias voltage with temperature for a given current

should obey the familiar diode equation:

$$I = I_0\left[e^{\frac{eV}{kT}} - 1\right] \qquad 4\text{-}8$$

where V is the applied bias, I_0 is the saturation current, k is Boltmann's constant, e is the electronic charge and T is temperature.

The bias voltage for a nominated current across the source-substrate junction can be measured at a known temperature or at several temperatures. Then for each readout of the MOSFET threshold voltage the temperature is calculated from the source - substrate bias voltage. The temperature calculated from the bias voltage of the source substrate junction can then be used to read a lookup table to determine the appropriate temperature correction to the measured threshold voltage. In this way any temperature variations in the dosimeter response can be internally corrected for. This technique was not implemented for the measurements performed in this thesis[151].

MOSFETS AND NEUTRONS

As described above MOSFETs are sensitive to x-ray and gamma radiation and this sensitivity is well characterised and has been extensively studied. The response of MOSFETs to neutrons is much lower and is not so extensively described in the literature, particularly with respect to any neutron induced threshold voltage changes.

Typical (non dosimeter) MOSFETs are immune to 1 MeV equivalent neutron fluences[152] of up to 10^{14} n.cm^{-2}. Thick oxide (dosimetry) MOSFETs have been reported[153] to have sensitivities of up to 0.025 mV.cGy^{-1} (tissue dose) for 3 MeV

neutrons and 12 volt bias on a 0.2μm gate oxide. Displacement damage in MOSFETs due to neutrons is generally of minor consequence due to the low resistivity silicon used for MOSFET fabrication. Possible neutron effects on the oxide layer are limited to single event upsets (SEU) in memory chips and single event induced burnout (SEB) or gate rupture in power MOSFETs[154]. Neither of these effects are relevant when considering the threshold voltage change in small signal dosimetry MOSFETs.

In the literature most discussion of electronic device neutron sensitivity (MOSFETS, PIN diodes and other devices) is focused around the effects of fast neutrons. This is because most of the literature is concerned with neutron radiation effects from either cosmic origins, high energy accelerators or nuclear weapons. It is true that these high energy neutrons have minimal effect on MOSFETs. However when large fluxes of lower energy neutrons are considered (eg epithermal neutron beams for BNCT) sufficient neutron interactions occur in the MOSFET to have a significant effect on the threshold voltage. Despite the limited intrinsic sensitivity of MOSFETs to neutrons the impact of neutrons interacting with the MOSFET packaging needs to be considered[155]. The measurement of, and attempts to correct for this MOSFET sensitivity to neutrons is discussed in later chapters. Ultimately the optimum design for MOSFETs intended for use in neutron fields should have very minimal packaging composed of low cross section materials. Certainly the traditional kovar encapsulation is (as will be demonstrated in later chapters) sub-optimal for measurements in epithermal neutron beams.

CLINICAL APPLICATIONS OF MOSFET DOSIMETRY.

The use of MOSFETs for dosimetry in medical or pre-clinical situations[156], [157] has recently begun to attract more interest and applications to diagnostic radiology[158, 159, 160, 161, 162, 163, 164], external beam radiotherapy[165, 166, 167, 168, 169, 170], including IMRT[171] and microbeam treatments[172 ,173], as well as therapeutic nuclear medicine[174, 175, 176] have been reported.

One of the principle attractions of MOSFETs for dosimetry is their small size and the potential for online readout[175, 157, 134]. This makes them suited for some measurements that have previously been performed using TLDs or film.

Dong et al[158, 159] have applied MOSFET dosimeters to the measurement of skin surface entrance doses in mammography and observed good linearity over the dose ranges typically used. Good energy linearity (~3%) was also reported however this was over the very limited range of tube potentials from 25 - 30 kV. For a more general application at a wider range of diagnostic x-ray energies[163] the effects of dose enhancement need to be considered and the encapsulation materials carefully selected. This applies to both surface dose measurements but also to measurements at multiple points within phantoms such as were performed by Hintenlang et al[160] and Sessions et al[161]. Both of these studies used MOSFETs in phantoms to measure diagnostic radiography doses in pediatric phantoms. In this case spectral changes in the incident beam may lead to significant variations in MOSFET response at different depths in the beam. This may in part account for the larger discrepancies observed between MCNP calculated doses and MOSFET measurements that were observed by Sessions et al for points in the phantom that lay outside the field.

The changes in energy response (at diagnostic x-ray energies) of commercial MOSFET dosimeters were investigated by Edwards et al[177] using a quasi-monoenergetic x-ray source (Pantak H320). They investigated the response of Thompson and Neilson MOSFETs over an energy range from 12-208 keV. The maximum relative sensitivity was found to occur at an energy of 33 keV. The response at this energy relative to the response to 6MV x-rays was approximately 4.2-4.4. A similar result was obtained by Kron et al[178] using different MOSFETs exposed in a sychrotron beam. This enabled the MOSFET energy response to be determined using truly monoenergetic x-rays ranging in energy from 10 - 99.6 keV. In this study an over-response of approximately 7 times was observed for the MOSFETs.

The design of some commercial MOSFET dosimetry systems that incorporate the MOSFET on a small circuit board covered with a bubble of polymer material has also been shown to lead to significant angular dependence of the devices. This is to be expected in air and also at diagnostic x-ray energies but has also been reported for in phantom measurements[162].

The low doses in diagnostic radiology limit the accuracy of MOSFET measurements for typical radiographic exposures since even commercial dosimetry MOSFETs sold as "high sensitivity" have sensitivities of approximately 3mV.mGy^{-1}. This leads to a 25% uncertainty (95% CI) for a single measurement of a 1.5 mGy surface dose[163]. One approach to overcoming this limited sensitivity is to stack several MOSFETs in a series in order to increase the total measured threshold voltage change[179]. A sensitivity of approximately 5 mV.cGy^{-1} was achieved for a stack of 3 MOSFETs irradiated with no bias. This is slightly greater than three times

the sensitivity of a single equivalent MOSFET. Accurate compensation for thermal effects is required for this arrangement[180].

In radiotherapy the MOSFET is being used for high spatial resolution measurements in sharp dose gradients such as x-ray beam penumbra[166] where reproducible spatial resolutions of the order of 0.1 mm have been observed. Doses in the buildup region of megavoltage x-ray beams have also been measured using MOSFETs. These surface dose measurements[168, 165] gave results within ±2% of doses measured using an Attix chamber and within ±3% of doses measured using TLD extrapolation techniques.

The intrinsic high spatial resolution of the MOSFET can be further improved and exploited by using it in the edge on configuration (as proposed by A Rosenfeld[181]). This allows it to be applied to characterisation of x-ray microbeams. Instead of having the radiation incident on the top surface of the junction (ie normal to the plane of the gate electrode) the MOSFET is turned on its side so that the 1μm edge of the SiO_2 is presented to the incident beam[173]. Using this method Kaplan and Carolan et al[173] achieved a spatial resolution of approximately 1 μm in measurements of the profile of a 200μm wide collimated x-ray microbeam. The same technique was first used by Rosenfeld et al[181] to measure syncrotron microbeams at the KEK Photon Factory in Japan and the Syncrotron National Light Source at BNL, USA. A spatial resolution equivalent to the thickness of the gate oxide was again demonstrated.

Automated multiple MOSFET readout systems have facilitated the use of MOSFETs for IMRT treatment plan verification. Chuang et al [171] have used a phantom with multiple MOSFET access holes for comparison of measured dose with dose calculated on a IMRT treatment planning system (Corvus) and found the

measurements to agree with calculations to within 5%. This compares to 3% differences between ionisation chamber measurements and calculated doses.

In the field of radioimmunotherapy MOSFETs have been applied to internal dose measurement. The determination of internal doses in radioimmunotherpay requires knowledge of the internal dose rate in organs over time. With gamma emitters this can be achieved using gamma camera images at different time points subsequent to radionuclide administration. However when selecting radionuclides for therapy applications gamma emitters are usually avoided in favour of pure beta emitters to allow more specific dose delivery. MOSFETs fitted into catheters[175] have been inserted into mice receiving antibodies labeled with Y-90. This allowed real time monitoring of the dose rate in the tumour volume over a period of 23 hours post injection. Measurements with this system have been calibrated in standard volumes and validated against EGS4 calculations[176].

CHAPTER 5 MONTE CARLO CHARACTERISATION OF MOSFET NEUTRON RESPONSE

MOSFET NEUTRON RESPONSE CHARACTERISATION.

As will be demonstrated by experimental results in later chapters MOSFET dosimeters respond to neutron irradiation as well as photon irradiation. In order to characterise the energy dependence of this response accurately a large number of measurements would need to be performed using a range of monoenergetic or at least well defined neutron sources of different energies. Unfortunately the availability of neutron sources covering the energy range of interest (thermal to a few MeV) makes a purely experimental determination of the MOSFET neutron response impractical. However the interaction cross sections of the individual materials used in MOSFET construction are well known. The MOSFET neutron response (in terms of threshold voltage change per unit neutron flux at a particular energy) will be a complex function of these cross sections. It will result from both direct neutron interactions in the silicon oxide layer of the MOSFET as well as interactions of a spectrum of secondary particles in the silicon oxide layer. These secondary particles arise from interactions of neutrons within the packaging of the device and are expected to be the main contributors to the MOSFET neutron reponse.

To use MOSFETs in mixed neutron gamma fields it is necessary to determine the neutron response so that it can be taken into account when gamma dose measurements are performed. For this purpose the neutron energy response of the MOSFET and its package was calculated using MCNP4a[182] Monte Carlo radiation

transport code. Clearly it is not possible to directly determine the threshold voltage response of the MOSFET to neutrons using MCNP4a. The approach taken was to model the detail of the MOSFET geometry and thereby simulate the neutron induced production of secondary particles in the silicon and the MOSFET package. A region of interest corresponding to the approximate location of the silicon dioxide layer of the MOSFET was used to tally fluxes of neutrons, photons and electrons.

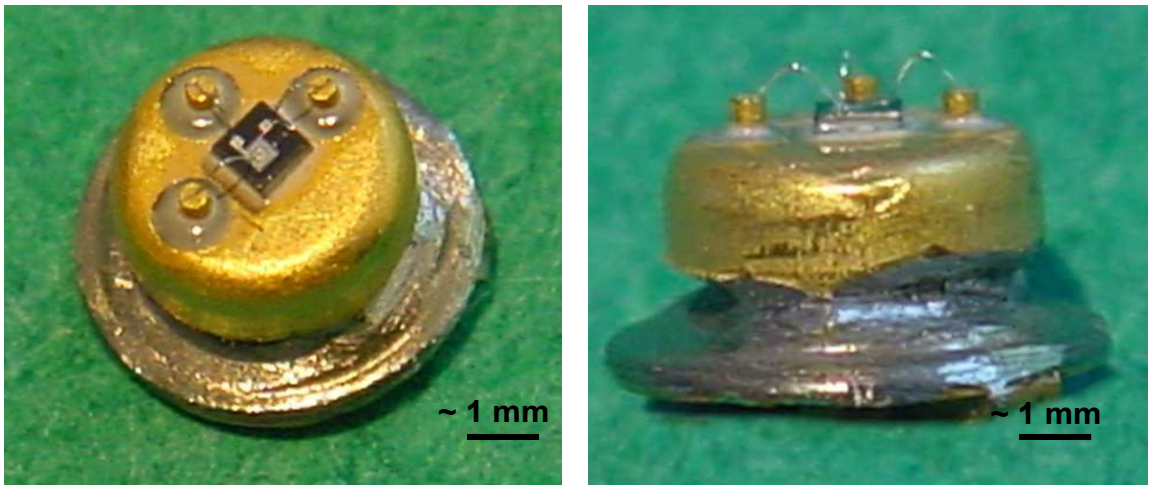

Figure 5-1. Photograph of the MOSFET with the lid removed showing internal structure to be modeled using MCNP.

MCNP MODEL OF MOSFET

The geometry of the MOSFET and its package was determined by removing the encapsulation and measuring its dimensions with a micrometer. (MOSFET with lid removed shown in Figure 5-1.) A diagram of the geometry based on these measurements that was assumed in the model is shown in Figure 5-2. The simulation of the MOSFET was also repeated with the inclusion of the LiF epoxy shield as was used in the measurements. The lithiated shield is shown in Figure 5-3 and the model geometry in Figure 5-4.

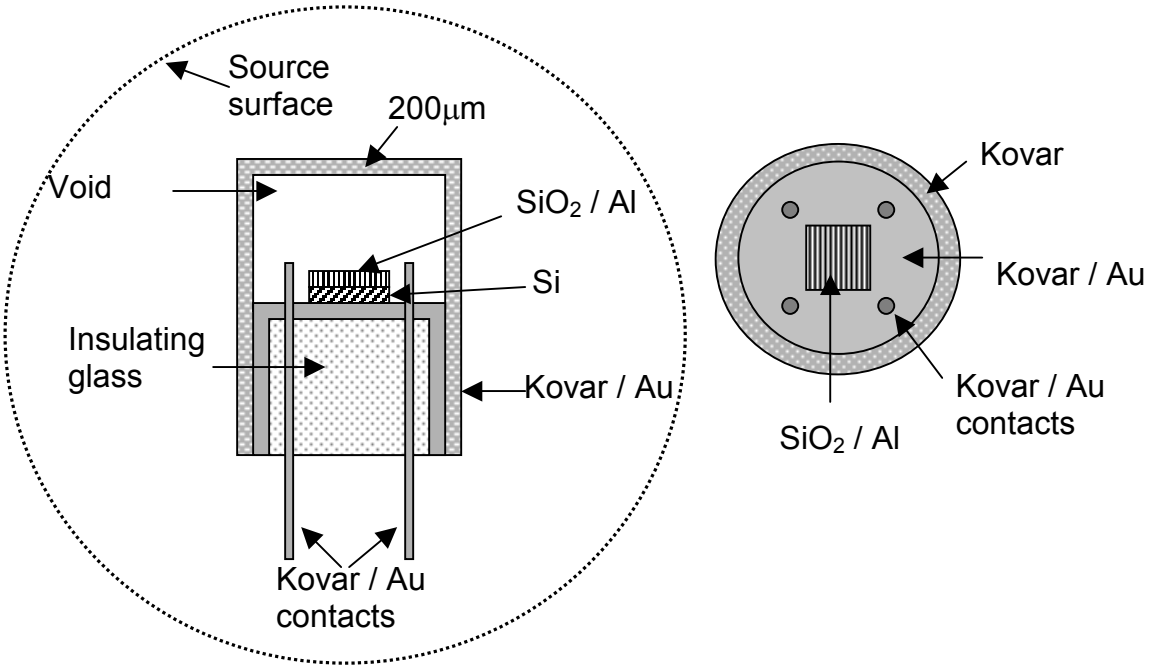

Figure 5-2. The geometry of the MOSFET assumed in the MCNP4a model used to determine the neutron response of the MOSFET. Not to scale.

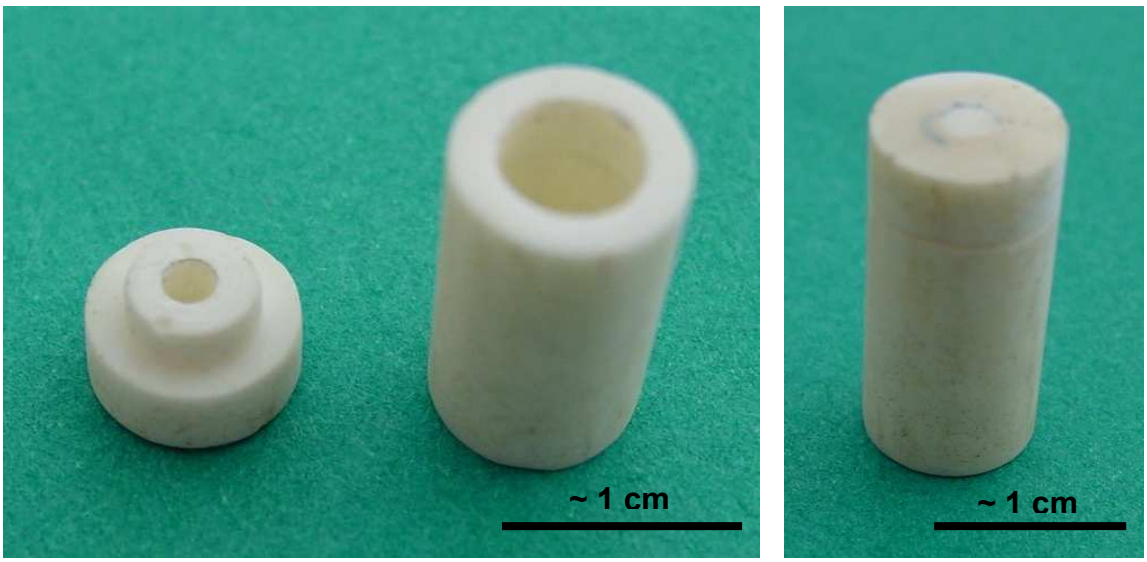

Figure 5-3. Lithium Fluoride / epoxy shield used to reduce neutron contribution to MOSFET measurements of gamma dose.

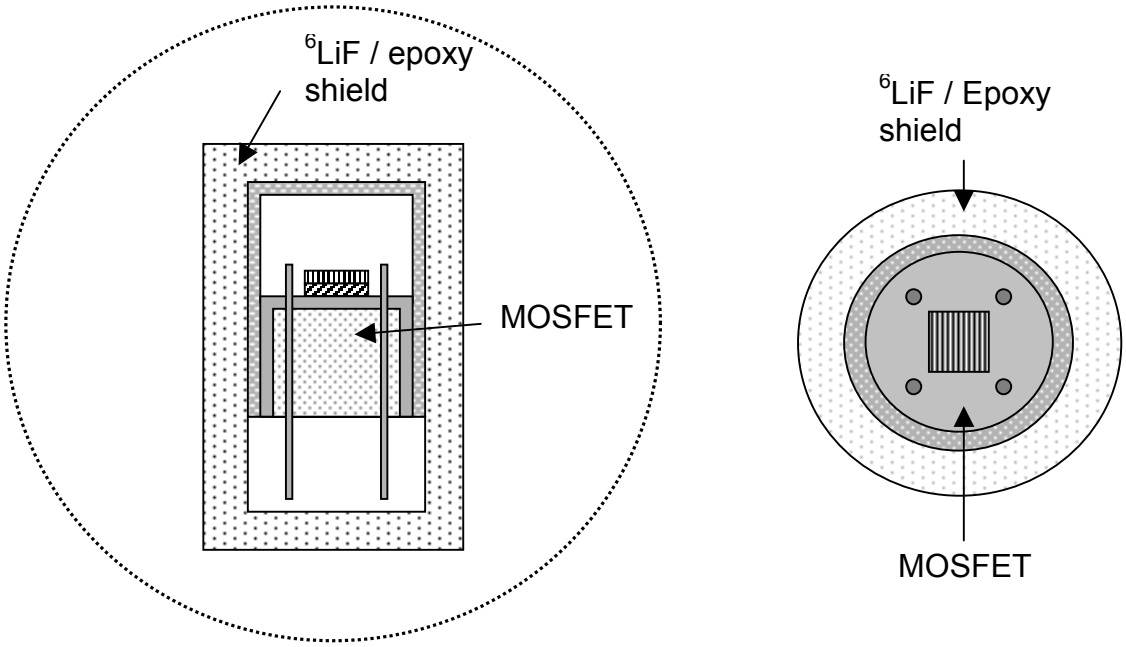

Figure 5-4. The geometry of the MOSFET including the LiF epoxy encapsulation.

The MOSFET structural geometries shown were entered into an MCNP input file. The only significant departure from equivalence with the real geometry was in the definition of the SiO2 volume. In the actual MOSFET this is about 1μm thick and several 10s of μm in length and width. To increase the efficiency of the calculation the SiO_2 layer in the MCNP input was defined to be volume 150μm thick and 2 mm on edge. This increases the probability of secondary particles generated in the MOSFET encapsulation contributing to the tallies. This volume is much larger than the actual oxide layer however it is still small compared to the dimensions of the MOSFET package. Therefore the efficiency of the calculation can be improved with this larger tally volume without a large effect on the accuracy of the calculation. As discussed below the quantities that were tallied were based on fluxes through the tally volume rather than explicit energy depositions in the tally volume (using the MCNP *f8 tally for example).

A spherical shell neutron source centered around the MOSFET was defined. Such a source allows the simulation of the MOSFET in an isotropic neutron field. The neutron response function derived using such a source definition will be the average response considering neutrons from all angles. As a first approximation of the MOSFET response when it is embedded in a phantom this was considered a reasonable assumption.

SOURCE DEFINITION

There are a number of ways of approaching the design of the simulation. Rather than doing a series of simulations using a different monoenergetic sources of neutrons for each one it was decided to break the spectrum up into a number of energy ranges or groups. It would be possible to determine a MOSFET neutron response function with very fine energy resolution using a series of monoenergetic sources. However this would introduce the risk of using a source energy that either coincided with or missed altogether a fine structure in the cross section of one of the MOSFET materials. Therefore with insufficient monoenergetic energy points in the response function it would be possible to significantly under or over estimate the energy response for one part of the spectrum. The alternative to this is to break the spectral range of interest into a series of uniformly sampled discrete groups. By doing this the entire neutron spectrum (within the range of interest) is sampled. The use of energy groups of finite width has the effect of smoothing the calculated response function. However all of the spectrum does contribute to the final result. On the assumption that the spectra to be measured were reasonably slowly changing functions of energy seventeen energy bins spanning the energy range from 10^{-3} eV to

1 MeV were used. The energy bins used are shown in Table 5-1.

Since the a priori knowledge of the expected neutron energy response function was not great a number of separate MCNP runs were performed. A separate run was used for each source energy group. This allowed the easy redefinition of the energy bins if necessary without having to re run the simulation for all energies. Using separate runs for each energy bin also allowed more histories to be selectively run for particular parts of the neutron spectrum if this was found necessary in order to improve the variance of the results due to lower neutron responses at those energies.

Table 5-1. Energy groups used for determination of MOSFET neutron energy response function.

Energy Group	Lower Bound (MeV)	Upper Bound (MeV)
1	0.001e-6	0.01e-6
2	0.01e-6	0.05e-6
3	0.05e-6	0.1e-6
4	0.1e-6	0.5e-6
5	0.5e-6	1e-6
6	1e-6	5e-6
7	5e-6	10e-6
8	10e-6	50e-6
9	50e-6	100e-6
10	100e-6	500e-6
11	500e-6	0.001
12	0.001	0.005
13	0.005	0.01
14	0.01	0.05
15	0.05	0.1
16	0.1	0.5
17	0.5	1.0

MATERIAL DEFINITIONS

A number of simulations were run, each one incorporating more detail of the materials the MOSFETs are made of. The packaging of the MOSFETs is made of an alloy known as kovar. This is made of iron, cobalt and nickel in the proportions of 0.54, 0.17 and 0.29 by weight with a density of 8.401 $g.cm^{-3}$. The kovar base inside the cap and the leads were coated in gold. This was incorporated into the model by assuming that the kovar in the base and the leads contained 3.28% gold by weight. This gold was assumed to be homogeneously distributed throughout the kovar rather than plated on the inner surface. The cap itself was not gold plated and therefore was assumed to be only kovar. The space inside the kovar base was filled with glass. The precise makeup of this is unknown so it was assumed to have the following constituents[182]; boron, aluminium, sodium, oxygen, silicon in the proportions of 0.037, 0.01, 0.041, 0.535, 0.377 by weight with a density of 2.23 $g.cm^{-3}$.

Because MOSFET measurements (detailed in later chapters) were conducted with ^{6}LiF epoxy shields most of the simulations performed included these shields. Two different sets of lithiated (^{6}Li enriched) epoxy shields were simulated and used in measurements. Measurements performed at the Petten HFR epithermal neutron beam used shields with a wall thickness of 0.24 cm and an end cap thickness of 0.34 cm. For the purposes of these simulations the constituency of the lithiated shielding material was assumed to be 44.6% PMMA and 55.4% ^{6}LiF by weight. The density was measured as 1.69 $g.cm^{-3}$. For the measurements performed on the BMRR epithermal beam at BNL thicker shields were used. The wall thickness was 0.568 cm and the end caps were 0.8 cm thick on top and 0.6cm thick on the base. The material was defined as 43% PMMA and 57% ^{6}LiF by weight with a density of 1.69 $g.cm^{-3}$.

The MCNP input files for these simulations are given in Appendix A.

TALLIES

The objective of the simulation is to calculate the threshold voltage response of the MOSFET to irradiation with neutrons of different energies. The threshold voltage change depends on the amount of ionisation in the silicon oxide layer and the number of electrons and holes that remain trapped in this insulating layer after the irradiation.

A tally of the neutron flux through the silicon oxide layer is not adequate for this purpose because:

1. The neutron flux in the silicon oxide volume does not take into account the interaction probability of the neutrons with the silicon oxide.
2. The neutron flux in the silicon oxide layer does take into account the attenuation of neutrons in the surrounding package materials but does not take into account doses to the silicon oxide due to secondary particles generated by neutron interactions in the surrounding package.

Therefore neutron flux in the silicon oxide layer of the MOSFET is not an adequate proxy for determining the number of electrons and holes immobilised in the silicon oxide layer.

The average neutron dose in the silicon oxide layer as calculated by MCNP would be a better quantity to calculate but is not adequate either because:

1. Although the (energy dependent) probability of interaction in the silicon oxide layer is taken into account much of the kinetic energy

released in these interactions is carried away by secondary particles and therefore escapes the silicon oxide volume (which is of the order of 1μm thick).

2. Although the neutron attenuation in surrounding materials is taken into account the energy deposited in the silicon oxide layer by the secondary particles from these interactions is not included in the tally.

The photon flux in the silicon oxide volume is not adequate for determining the MOSFET response because:

1. The probability of interaction with the silicon oxide is not taken into account.

The photon flux multiplied by a photon heating factor is not an ideal proxy for the number of electrons and holes generated and immobilised in the silicon oxide layer but could be used. In this case:

1. The neutron attenuation in the surrounding package is implicitly taken into account.
2. The probability of the photon interaction in the silicon oxide layer is taken into account.
3. Some of the interactions of the photons in the silicon oxide layer will result in secondary electrons that may in fact escape the oxide layer so that not all of the energy released in the interaction is deposited in the oxide layer cell of the model. However the use of the photon heating tally multiplier in MCNP implicitly assumes that all of the energy released in the interaction would be deposited in the cell where the interaction takes place. Therefore the dose deposited by photons in the

(very thin) oxide layer may be over estimated by use of this technique. If on average the proportion of the released energy lost from the oxide cell is similar over the whole range of source neutron energies for this set of simulations then the neutron response should be approximately correct. This would be true if the photon energy spectrum in the oxide layer is similar for all energies of the source neutrons.

4. Since a photon heating tally counts only photon flux and multiplies this by an energy dependent heating factor for the cell in question no contributions from non photon secondary particles from surrounding cells will be included. Electrons generated as a result of neutron or neutron induced photon interactions in surrounding material will not be taken into account if they enter the oxide layer volume.

Taking the photon flux in the cell and multiplying it by a photon kerma factor for the material involved using an FM card in MCNP is essentially the same as using the heating multiplier as discussed above.

The actual number of electrons traversing the oxide layer can be calculated using an electron flux tally in MCNP. This technique:

1. Implicitly takes into account neutron (and secondary photon) attenuation in surrounding materials,
2. Includes the electrons arising from neutron induced photon interactions in both the oxide layer and the materials surrounding the oxide layer.
3. Does not take into account the interaction probability of the electrons in the oxide layer.

Of all the methods of estimating the neutron induced electron and hole population in the oxide layer the electron flux may be the best. A short coming of this method is that many more source neutron histories need to be run in order to achieve reasonable statistical certainty. Using a track length estimate of photon flux (or this flux multiplied by a dose factor) is able to reduce the variance of the resultant tally more quickly because all of the photons passing through the volume of interest can contribute to the tally even if they do not actually under go any interaction in the oxide layer cell.

In principle an improvement on simply counting the electron flux in the silicon oxide cell would be to tally the amount of dose deposited by the electrons in the volume of interest. This can be achieved using a *f8 tally in MCNP. However the size of the cell defining the silicon oxide layer involved is such that this is calculationally very inefficient since the path lengths in the oxide layer are very short. The actual silicon oxide layer is of the order of 1μm thick and the region under the gate electrode is about 50μm wide.

The problem was run in neutron, photon and electron mode in order to track all of the particles generated by the incident source neutrons. The following tallies were generated during each simulation run; photon flux, photon heating, photon flux * silicon gamma kerma, electron flux and average neutron dose.

RESULTS

The tallies as a function of the source neutron energy groups are shown in the following figures for a MOSFET contained in a ^{6}LiF-epoxy shield. Note that with the

exception of the tally of SiO_2 neutron KERMA in the oxide layer all the other response curves have approximately the same form.

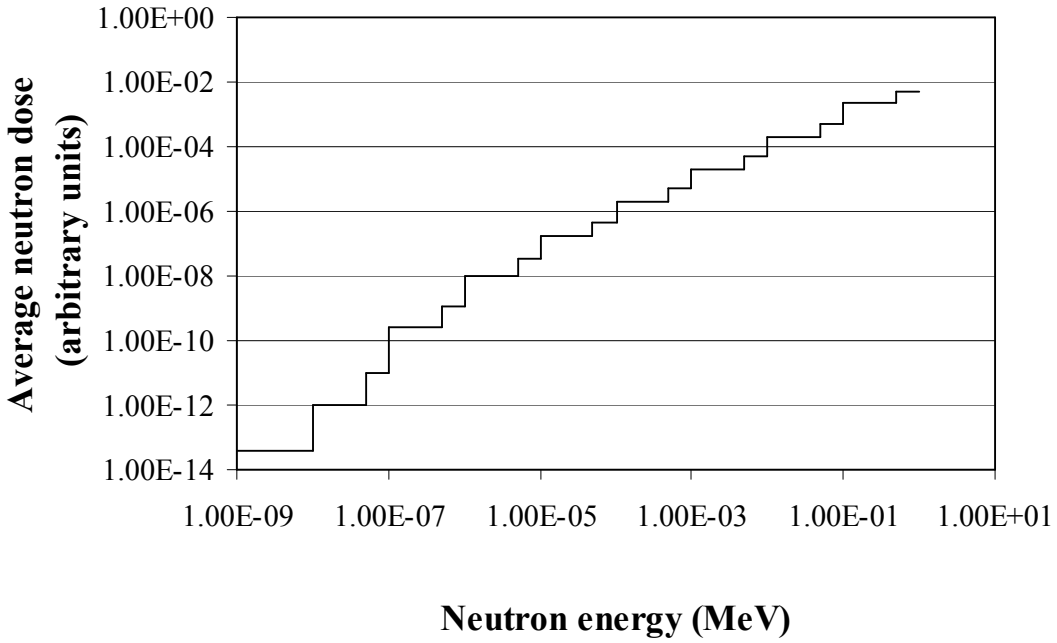

Figure 5-5. MCNP calculated MOSFET average neutron response. Neutron flux times SiO_2 neutron kerma.

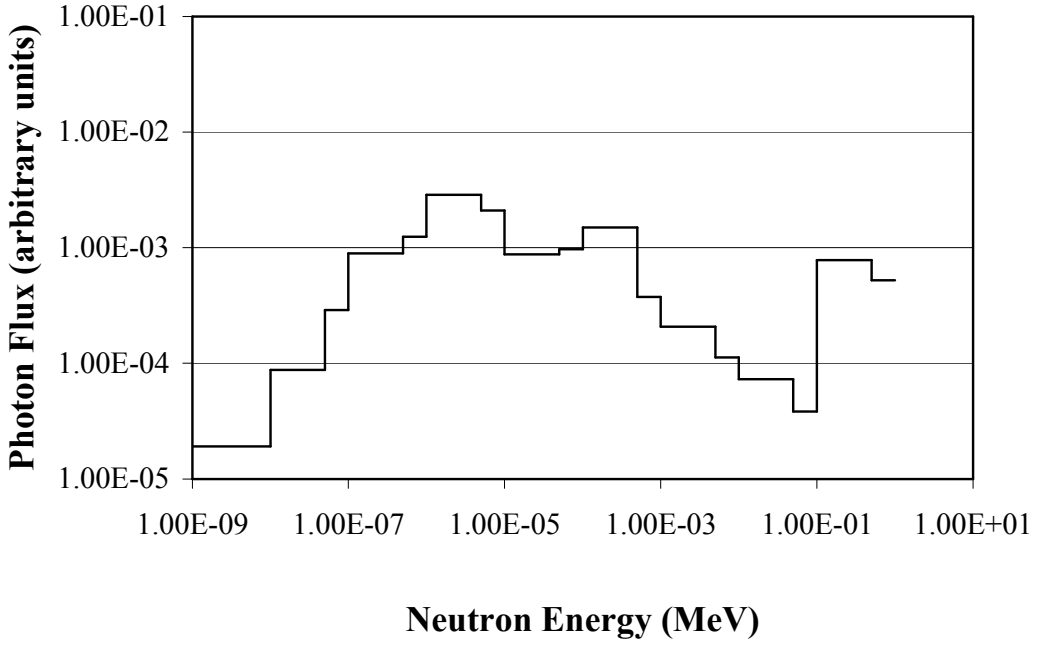

Figure 5-6. MCNP calculated photon flux in the silicon oxide layer as a function of the incident neutron energy.

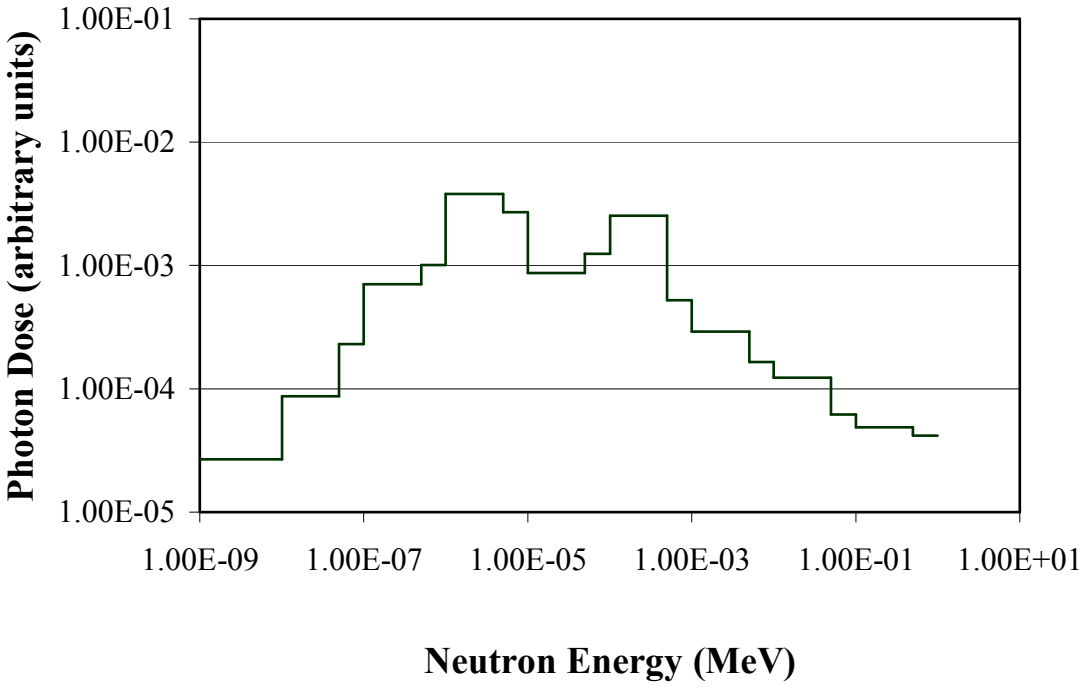

Figure 5-7. MCNP calculated photon heating in silicon oxide layer. (-6 tally multiplier).

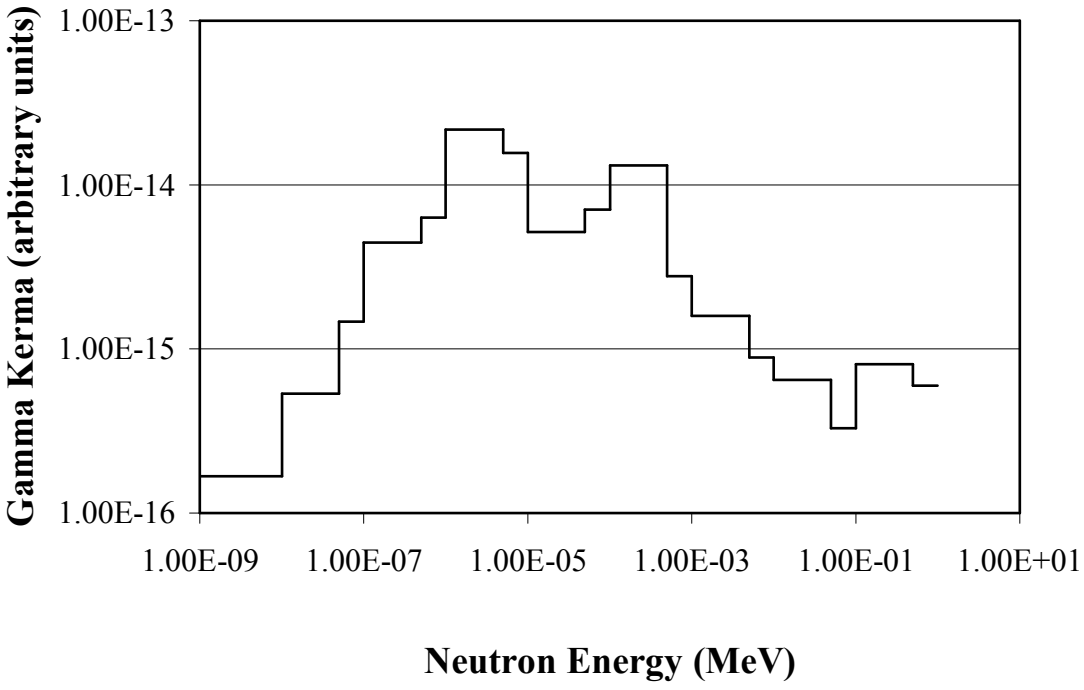

Figure 5-8. MCNP MOSFET neutron response for MOSFET in thick LiF shield (as used in BMRR measurements). Gamma flux multiplied by the SiO_2 photon kerma.

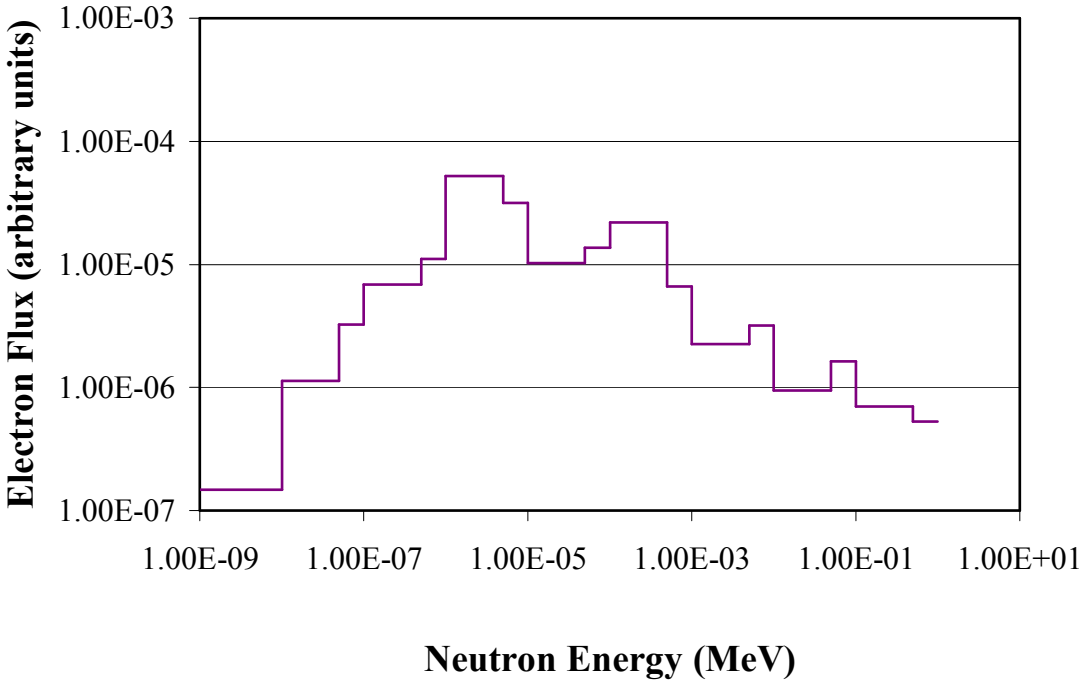

Figure 5-9. MOSFET neutron response. Electron flux in SiO_2 layer. Note that the statistical uncertainties for some of this data are in the range of 10 – 100%.

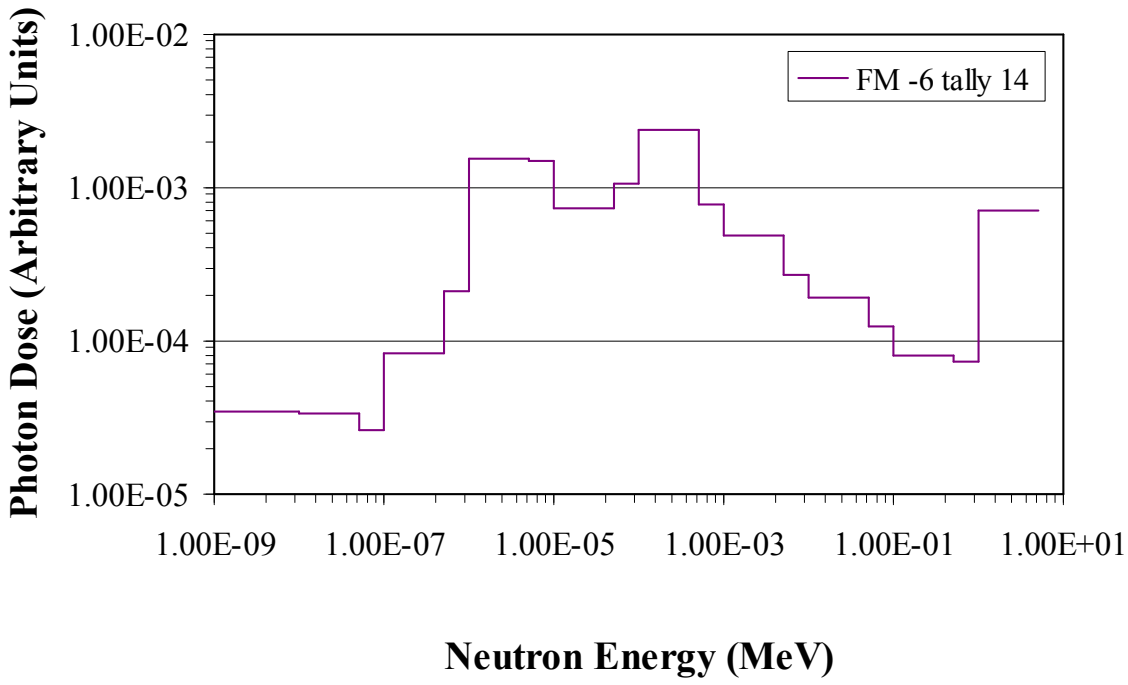

Figure 5-10. MCNP calculated photon heating in silicon oxide layer for MOSFET with thick LiF shield

For the sake of comparison the response function of a MOSFET encapsulated in the thicker lithiated shielding (as used for the BNL experiments) is shown in Figure 5-10.

Comparing Figure 5-7 and Figure 5-10 shows that the thicker shielding does reduce the neutron response by a small amount. As expected this is especially so for thermal neutrons. Unfortunately further increasing the size of the shielding eliminates any size advantage the MOSFET has. Increasing the amount of lithiated shielding also contributes to a possible reduction in neutron flux not only within the shield but also in the surrounding medium. This suppression of neutron flux may in turn reduce the level of induced gamma dose at the measurement point.

A preferable option is therefore to make use of MOSFETs without encapsulation such as kovar and to eliminate other materials such as gold from the packaging as far as possible. Once the amount of encapsulation around the MOSFET junction is sufficient to absorb recoil protons and other ions generated by neutron reactions in the surrounding phantom the neutron sensitivity should be as low as possible. If the encapsulation material is of minimum size, is low Z and does not contain hydrogen then the MOSFET junction should be approximately in equilibrium with the photon and electron flux in the surrounding tissue materials. This should enable measurements of gamma dose with minimal neutron contribution. A MOSFET design with the junction in a graphite encapsulation of suitable thickness to block most neutron generated secondary charged particles originating outside the device would be a good configuration to evaluate. All kovar and gold should be eliminated except for the essential electrical contacts and even these should be made from an alternative material if possible. Unfortunately implementation of such a

design was beyond the scope of this thesis.

NORMALISATION OF THE CALCULATED NEUTRON RESPONSE FUNCTIONS

In order to use these response functions to correct actual MOSFET measurements in neutron beams they have to be normalised or calibrated in terms of the MOSFET threshold voltage change per unit neutron response. The overall scheme used to normalise the calculated MOSFET neutron responses is shown in Figure 5-11.

For the Petten HFR measurements the response curves shown above were used as tally multipliers in a subsequent MCNP simulation of an experiment where the MOSFETs were irradiated using the HB11 epithermal neutron beam in Petten (described in Chapter 12). The HB11 neutron spectrum was assumed to be known and the gamma dose component of the beam was also assumed to be known.

From this (neutron only) simulation the integral MOSFET neutron response in terms of the above response functions was determined. The threshold voltage changes from the real experiment were then used with this data to find the MOSFET neutron response in terms of mV of threshold voltage shift per unit of the response functions above. The units of these response functions were in terms of fluxes per source particle as per the usual MCNP conventions.

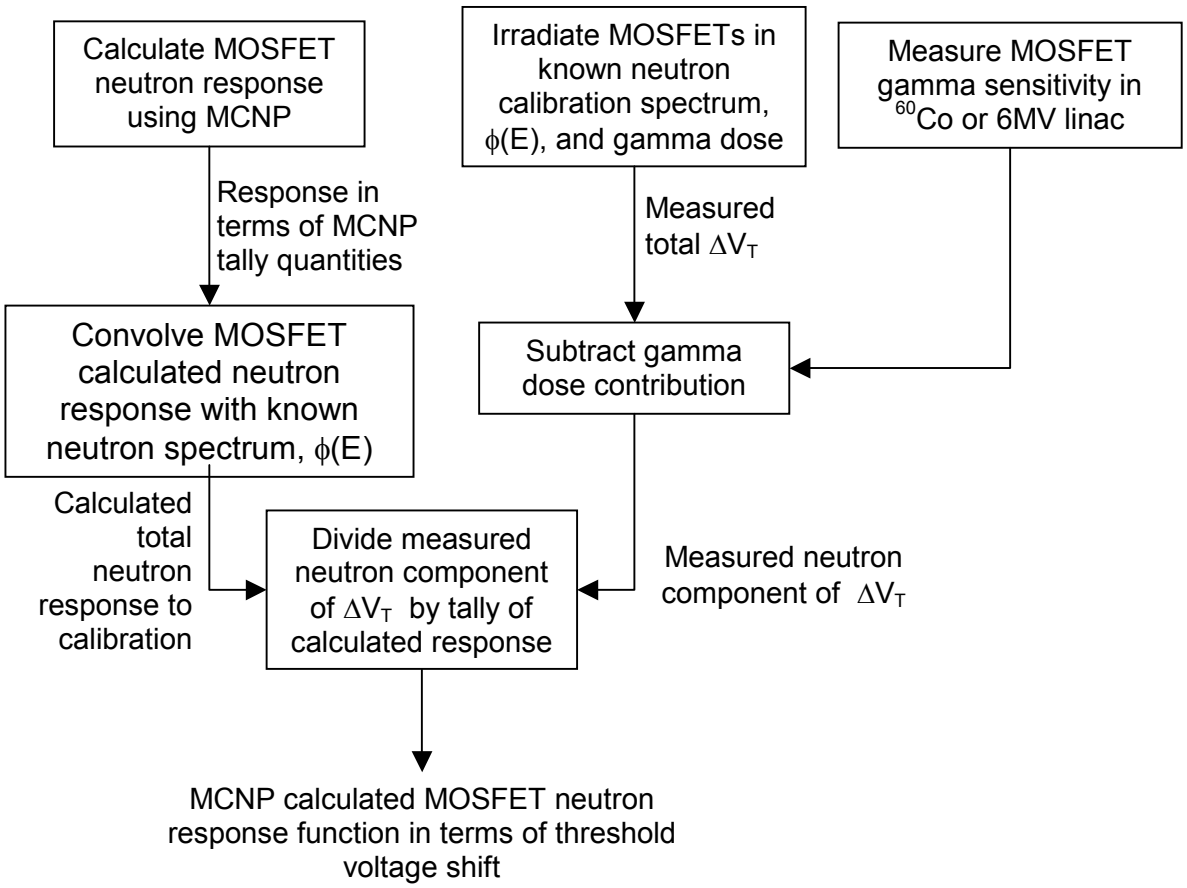

Figure 5-11. Overview of technique used to normalise the MOSFET neutron response functions determined using MCNP.

An alternative method used the observed threshold voltage change of MOSFETs irradiated in the MOATA TC-10 thermal column at Ansto. In this case it was assumed that thermal neutron fluence in the TC-10 facility was known on the basis of gold foil activation measurements and also that the gamma dose rate was known on the basis of previous ionisation chamber measurements at the TC-10 facility. Under these circumstances a direct determination of the MOSFET thermal neutron sensitivity was possible (in terms of mV of threshold voltage change per $n.cm^{-2}$). This factor can then be used to calibrate the thermal part of the response functions shown above and the rest of the curve is then normalised to this.

NORMALISATION OF MOSFET NEUTRON RESPONSE USING HB11 AT PETTEN AND BMRR AT BNL.

A MCNP model of the HB11 beam was used to convolve the HB11 neutron spectra at the measurement point (20 cm from the face of the beam port) with the MOSFET neutron response functions derived from the detailed MCNP model of the MOSFET described above. The details of the HB11 beam model were the same as those used for all of the MCNP simulations of that facility in this work and are described in more detail in the chapter on the measurements at the Petten reactor. The model of the beam geometry included collimators and treatment room but did not include the model of the reactor core. At the point where the MOSFETs were exposed a thin tally volume (0.25 cm) was used to determine the neutron flux with a f4 type tally. Three such tallies were generated. One was multiplied by the MOSFET energy dependent response function based on the photon kerma in the silicon oxide layer of the MOSFET (i.e. the one shown in Figure 5-8). The second was multiplied by the response function represented by the photon heating tally in the silicon oxide layer of the MOSFET (Figure 5-7). The third tally was multiplied by the energy dependent electron flux in the MOSFET oxide layer (Figure 5-9).

This results in three numbers, each one representing the neutron response for a MOSFET exposed at the measurement point in the HB11 beam as determined using each of the three different curves for MOSFET neutron responses. Note that the units of the calculated response functions are in terms of either MeV per source neutron (for the KERMA and heating tally) or electron flux per cm^2 per source neutron for the electron flux representation of the response function. When these response

functions are then used as histogram tally multiplying factors in the HB11 beam model the final quantities will be per source neutron in the HB11 beam model. Using the measured threshold voltage changes in the HB11 beam a normalisation factor can be determined which converts the response functions (or MCNP tallies multiplied by the response functions) to units of threshold voltage change per source neutron (as per Figure 5-11).

The determination of the response function and normalisation was performed in a similar manner for the MOSFET detectors in the thicker shielding which were used for the measurements at BMRR. Again the spectrum of the bare beam at BMRR was assumed to be known and was used as the calibration spectrum for determining the normalisation factors for the response functions.

USE OF CALCULATED RESPONSE FUNCTIONS TO CORRECT MOSFET MEASUREMENTS IN MIXED GAMMA NEUTRON FIELDS.

Once the MOSFET response functions have been generated and normalised in some known neutron spectrum they can be used to correct MOSFET measurements of gamma dose where there is a significant neutron contribution. Firstly a measurement using the MOSFET is made. The threshold voltage change is recorded. The neutron spectrum at the measurement point also needs to be known. This spectrum is multiplied by the MOSFET neutron response function and the previously determined normalisation factor is applied to yield the neutron component of the threshold voltage change. This neutron component is subtracted from the total measured threshold voltage change. The remaining component of the threshold

voltage change is attributed to gamma dose. The known gamma sensitivity factor is then applied to determine the measured gamma dose.

This technique was used to apply the neutron response functions calculated in this chapter to correct gamma dose measurements performed in phantoms in the Petten HB11 and BMRR epithermal neutron beams. The results of these measurements are detailed in later chapters.

CHAPTER 6 MONTE CARLO IDEAL BEAM STUDY OF PIN DIODES FOR EPITHERMAL NEUTRON DOSIMETRY

INTRODUCTION: USING PIN DIODES AND FOIL ACTIVATION TO MEASURE TISSUE NEUTRON DOSE

In this section an attempt is made to demonstrate that it is possible to experimentally measure the tissue dose at a point in a phantom or patient by means of silicon PIN diode and activation foil measurements.

Both of these measurement techniques are relatively easily applied and due to the small size of the detectors involved lend themselves to high resolution spatial measurements. They are also insensitive to the photon component of the mixed field. These qualities of such a technique are advantages not necessarily shared by paired ionisation chamber techniques.

AIM

The hypothesis is that it should be possible to parameterise the neutron contribution to tissue dose at a point in the mixed epithermal neutron and photon field in terms of silicon displacement damage KERMA and one or more foil activation terms (for some predefined range of neutron energies). That is:

*Tissue Dose = A * (Si Damage KERMA) + B * (Foil Activation)*

Where A and B are coefficients to be determined. The silicon damage KERMA can be measured using silicon PIN diodes. Likewise foil activation can be measured directly in the normal way.

ASSUMPTIONS

For the proposed technique to be generally applicable, it is not adequate to demonstrate simply that the tissue dose can be expressed as a function of silicon dose and foil activation at some point in a particular epithermal neutron spectrum. Such a demonstration would be subject to unknown inaccuracies for any different epithermal spectrum or at any points other than those where the relationship was demonstrated. To be generally applicable the relationship between neutron tissue dose, silicon displacement damage and foil activation must be shown to hold and for all anticipated neutron spectra. Even then some assumptions need to be made regarding what constitutes "all anticipated neutron spectra".

It was assumed that the spectra to which this technique is to be applied are epithermal neutron spectra designed for BNCT use. It was further assumed that if a series of (simulated) monoenergetic neutron beams ranging in energy from 0.25 eV up to 1 MeV were applied to a brain tissue equivalent phantom and the spectra at points along the beam axis of this phantom were considered then this should constitute the basis set of all anticipated spectra. In practice even the small component of neutrons with energies greater than 1 MeV in some epithermal beams may invalidate this assumption at shallow depths in phantoms. Although all real BNCT treatment beams will not be ideal monoenergetic beams clearly a linear combination of ideal beams can be used to construct the desired spectrum of any

actual beam. Likewise the moderated spectrum of an actual epithermal neutron beam at some point in a phantom will be a linear combination of the moderated spectra of the individual ideal beams that combine to make the actual spectrum of the incident epithermal beam. That is if an incident monoenergetic neutron beam, $\phi_{inc}(E_1)$, with energy E_1, impinges on a phantom then at some point *x* in that phantom the resultant spectrum is $\phi_{E1}(E,x)$. A more general incident spectrum can be represented as a linear combination of monoenergetic beams, i.e.:

$$Incident\ Spectrum = \sum_{0}^{n} a_n \phi_{inc}(E_n) \qquad 6\text{-}1$$

The resulting spectrum at some point *x* in the phantom is then:

$$Moderated\ Spectrum(x) = \sum_{0}^{n} a_n \phi_{En}(E,x) \qquad 6\text{-}2$$

As an initial approximation it was assumed that the variations in density and materials encountered within the body would not cause the neutron spectra in that region to depart so radically from the spectra found in the phantom as to invalidate the relationships between tissue dose, silicon dose and foil activation derived on the basis of the spectra in the homogeneous tissue phantom. It is noted however that of course the variations in materials and densities encountered in the body will lead to very different KERMA's and doses as the tissue elemental constituency changes. In order to determine the doses appropriate to the different tissue types it would be necessary to derive a separate relationship between the dose for each tissue type and the measured parameters, i.e. silicon dose and foil activation.

(A simulation with an incident neutron energy of 10 MeV was also run.

Although neutrons of this energy constitute a small fluence component of most proposed epithermal BNCT neutron beam sources they can make a significant contribution to the PIN diode response.)

METHOD

A series of Monte Carlo (MCNP4a) simulations were performed. The input file for the MCNP model is included in Appendix C. The problem geometry was a cylindrical phantom of ICRU 92 brain equivalent material at room temperature with density 1.04 $g.cm^{-3}$. The phantom was 16.0 cm in diameter and 23.0 cm long. A parallel neutron beam of 10.0 cm diameter was normally incident on one end of the cylinder.

The resultant moderated neutron spectrum and some tallies modified by KERMA factors and foil activation cross sections were tallied in coaxial cylindrical volumes of diameter 0.5 cm along the axis of the phantom. The first tally cell on the front face of the cylinder was 0.25 cm thick. The next 30 tally cells were each 0.5 cm thick. This resulted in a neutron spectra being tallied in 31 volumes along the axis of the cylinder from the front face upon which the neutron beam was incident to a depth of 15.25 cm. The size of the tally cells (0.5 cm) was chosen to approximate the order of magnitude of the dimensions of the PIN diodes and activation foils. This minimises the effect of averaging the resultant neutron spectra over a volume that is larger than the measurement devices to be used. Since the spectra are expected to be quite well moderated and far from monoenergetic at most points in the phantom the effect of averaging the neutron spectra over volumes slightly larger than the detectors in question is probably not great in terms of deriving the required relationships

between the measured quantities and tissue dose. However it was considered best to avoid this potential source of error.

In addition to the neutron spectra the following quantities were tallied in each cell; silicon damage KERMA, brain tissue equivalent KERMA, gold foil activation, copper foil activation and manganese foil activation. Each of the foil activations was broken up into sub and super cadmium cutoff energy bins. The silicon damage KERMA and the tissue KERMA was also broken up into several energy bins to allow retrospective analysis of the contributions of each part of the spectrum if necessary.

A series of simulations was performed with monoenergetic neutron beams ranging from 0.25 eV to 10 MeV. The energies used were; 0.25 eV, 1 eV, 10 eV, 100 eV, 500 eV, 700 eV, 1 keV, 2 keV, 5 keV, 10 keV, 20 keV, 30 keV, 50 keV, 100 keV, 1 MeV and 10 MeV. Each simulation was run for 100 minutes on a 366 MHz Pentium II PC. The number of histories run during this time varied depending on the source energy.

The tallies of KERMAs and foil activations for each of the cells along the axis of the phantom were extracted to a Microsoft Excel spreadsheet. These quantities were then plotted as a function of depth in the phantom for each incident energy. The raw MCNP output quantities were in terms of $cGy.cm^2$ per source neutron for the KERMAs and activation reactions per source neutron for the foil activation results. This resulted in the tissue and silicon KERMA values in each tally being numerically many orders of magnitude smaller than the activation quantities due to the units used for each. To overcome this for the purpose curve fitting and regression analysis the silicon KERMA was scaled by a factor of 10^{16} and the tissue

KERMA was scaled by a factor of 10^{13}.

These MCNP tally quantities were not converted to experimental observable quantities (i.e. PIN diode bias voltage change and saturation activities) at this stage.

A least squares regression analysis was used to fit the tissue dose at each point in the phantom as a function of the silicon damage KERMA, and the foil activation (Microsoft Excel Regression Analysis Tool). This could be achieved with minimal residuals for the depth dose curves associated with individual ideal beams. However to be generally applicable it is necessary to achieve a good fit for all of the ideal beam depth dose curves at once. This ensures that the coefficients derived in this process will be as accurate as possible for the whole range of neutron energies encountered in an epithermal neutron beam.

Various forms of relationships between the tissue dose and the silicon dose and the foil activations were tested. Initially a simple linear combination of all terms was tested. This included silicon damage KERMA, sub-cadmium cutoff and total activations for gold, manganese and copper foils. One by one the least significant terms were omitted from the regression analysis in order to get the simplest expression possible. The fitted curves derived using this process were assessed on the basis of the residuals and by visually checking to see at what energies and at what depths deviations from the calculated tissue dose occurred. Where agreement could not be achieved over all energies the effect of removing the higher energy ideal beam data was investigated. However this is not considered a good solution overall since it will result in inaccurate results if high energy neutrons are present in the spectrum being measured. This is particularly so due to the higher response of silicon at higher neutron energies.

Once a set of coefficients was derived a MCNP simulation was performed using a realistic epithermal neutron beam spectrum incident on the same phantom. The silicon dose and foil activations in each tally cell in the phantom were calculated. This data in conjunction with the previously determined coefficients was used to calculate the expected tissue dose at each point along the phantom axis. These predicted values were then compared with the direct MCNP calculated values of the tissue dose at the same points. The correct factors for conversion from MCNP tally quantities to experimentally observable quantities were then determined to allow application to experimental data.

RESULTS

From the curves shown in Figure 6-1 to Figure 6-15 it can be seen that the tissue and silicon damage KERMA curves are well behaved as expected, so are the foil activation curves. The fluctuations in some of the activation curves are due to statistical error in some tallies at some energies. The problem is then one of choosing the best combination of parameters that will describe the tissue depth dose curves over as wide a range of incident neutron energies as possible. The process used was guided by a number of objectives. To minimise the number of experimental pieces of data required, e.g. use total foil activation if possible to avoid the need for cadmium covered foil measurements and to use as few different types of foils possible. To obtain an expression using the smallest number of parameters derived from the experimentally observable quantities adequate to describe the tissue dose for the neutron energy range of interest.

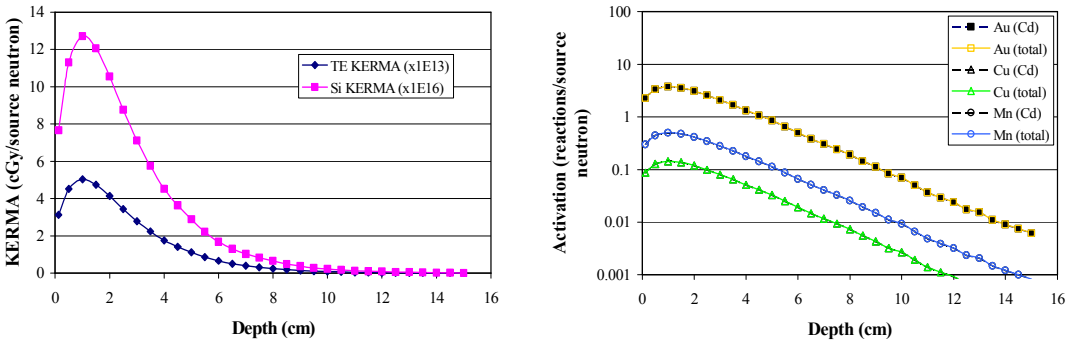

Figure 6-1. Tissue, Silicon KERMA and foil activation for a 0.25 eV ideal beam.

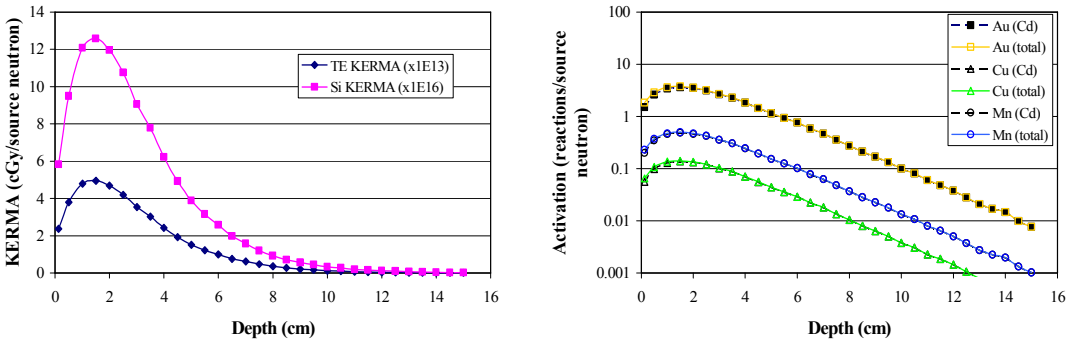

Figure 6-2. Tissue, Silicon KERMA and foil activation for a 1 eV ideal beam.

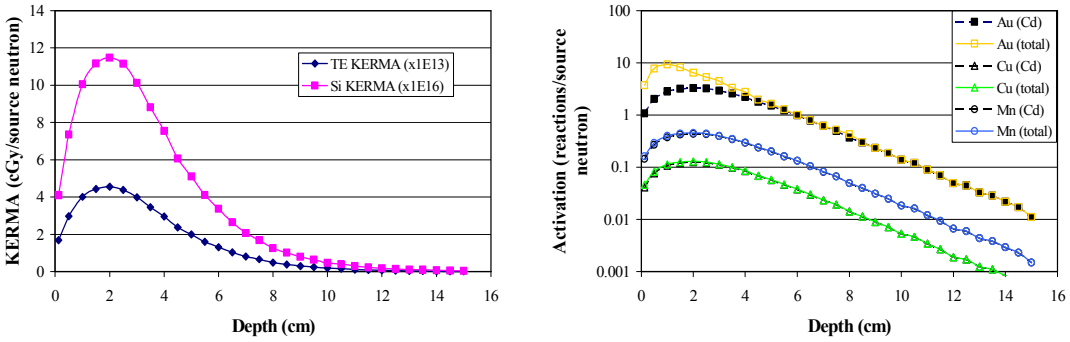

Figure 6-3. Tissue, Silicon KERMA and foil activation for a 10 eV ideal beam.

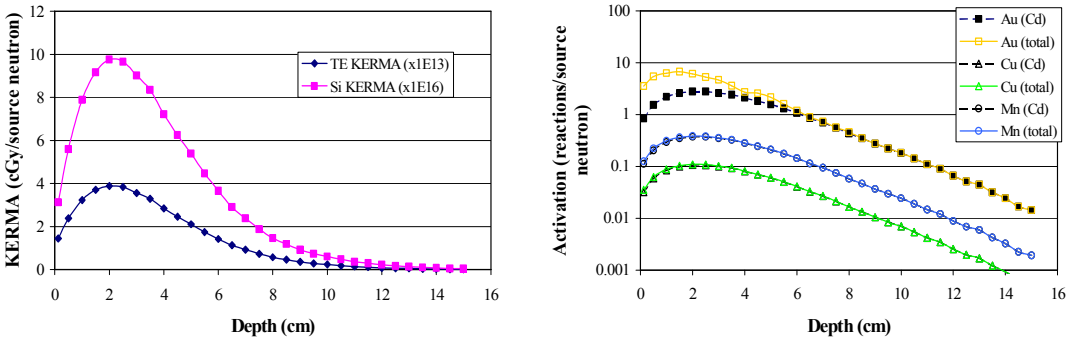

Figure 6-4. Tissue, Silicon KERMA and foil activation for a 100 eV ideal beam.

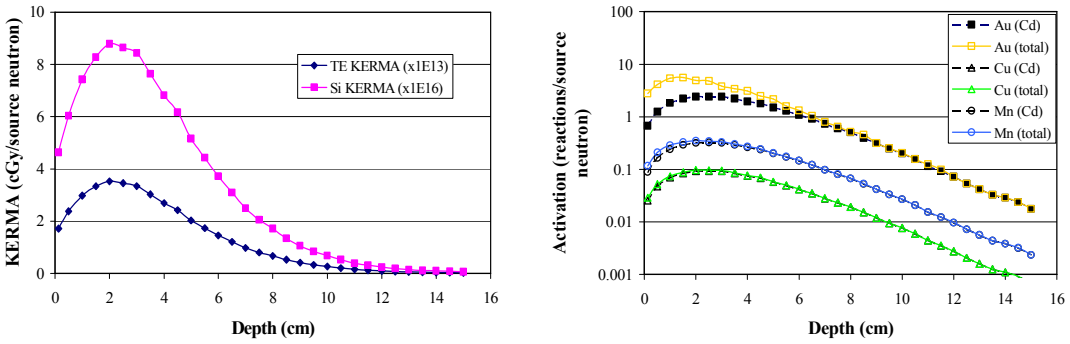

Figure 6-5. Tissue, Silicon KERMA and foil activation for a 500 eV ideal beam.

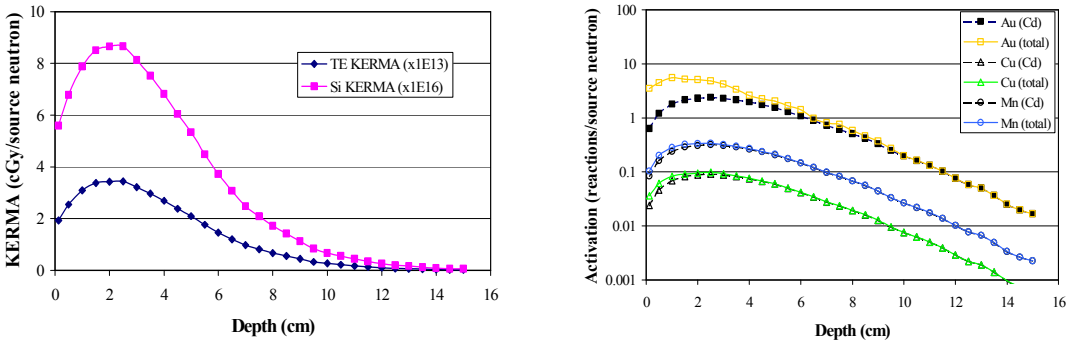

Figure 6-6. Tissue, Silicon KERMA and foil activation for a 700 eV ideal beam.

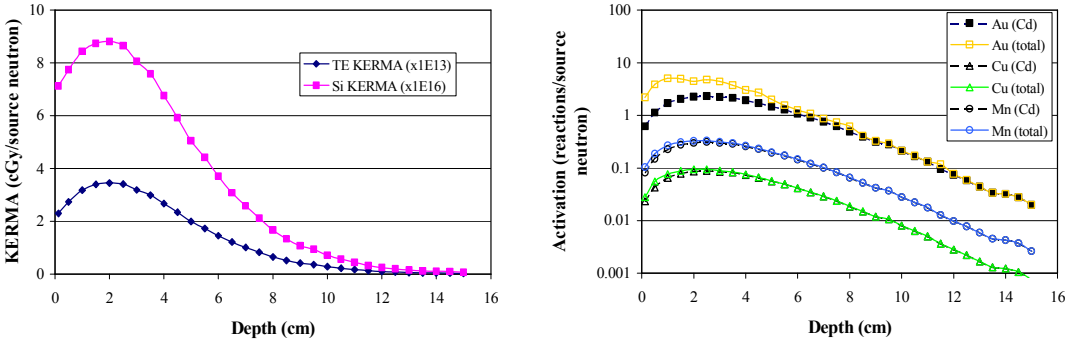

Figure 6-7. Tissue, Silicon KERMA and foil activation for a 1 keV ideal beam.

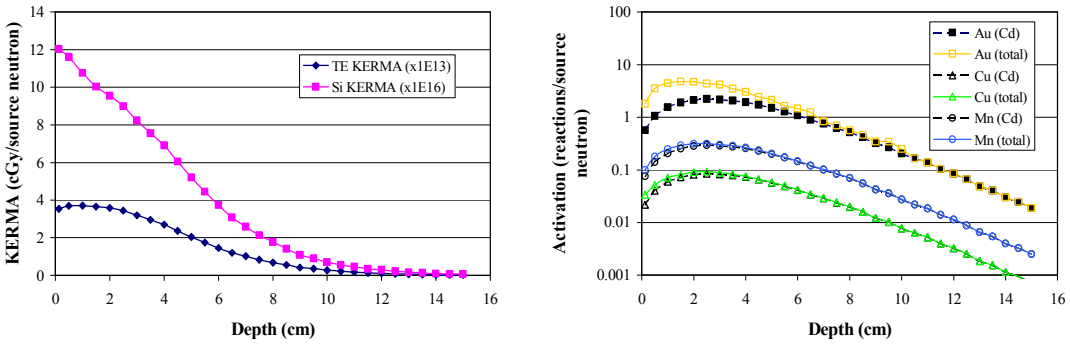

Figure 6-8. Tissue, Silicon KERMA and foil activation for a 2 keV ideal beam.

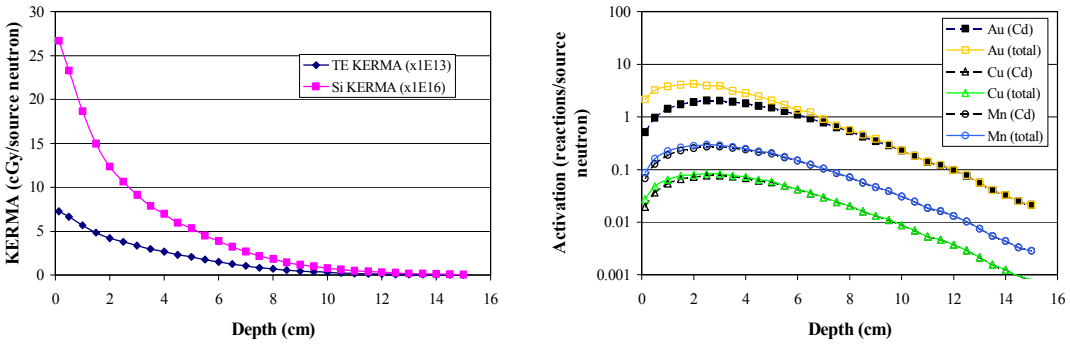

Figure 6-9. Tissue, Silicon KERMA and foil activation for a 5 keV ideal beam.

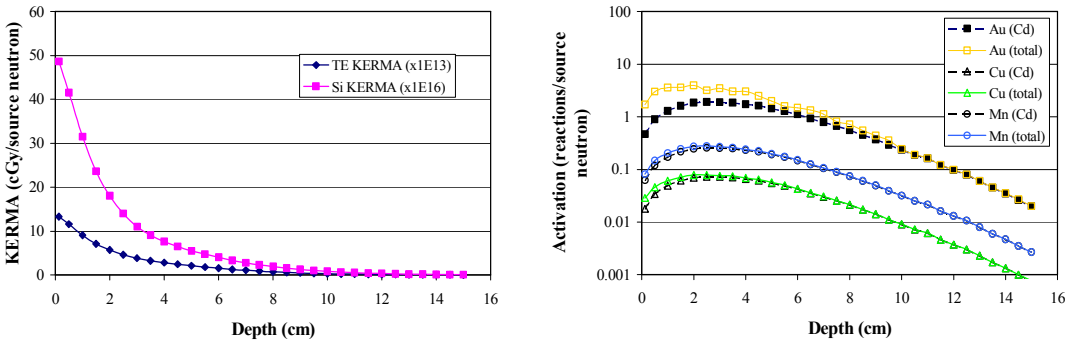

Figure 6-10. Tissue, Silicon KERMA and foil activation for a 10 keV ideal beam.

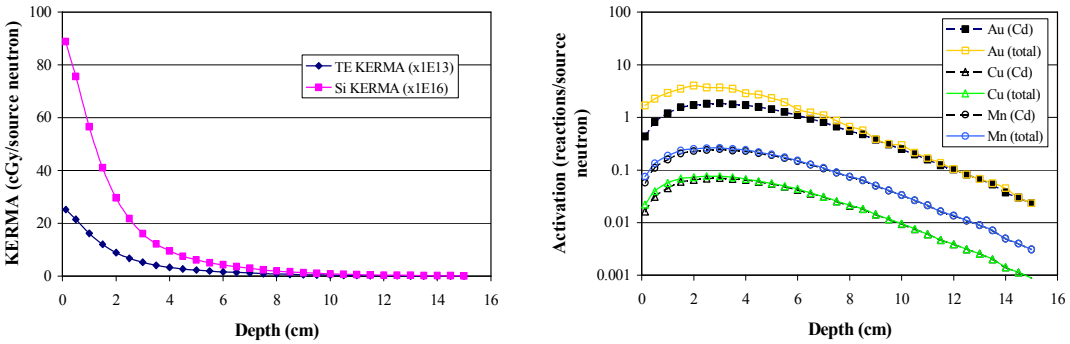

Figure 6-11. Tissue, Silicon KERMA and foil activation for a 20 keV ideal beam.

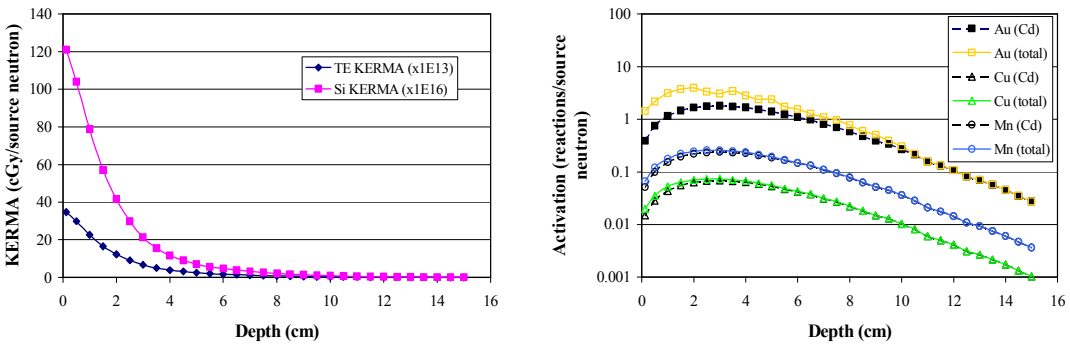

Figure 6-12. Tissue, Silicon KERMA and foil activation for a 30 keV ideal beam.

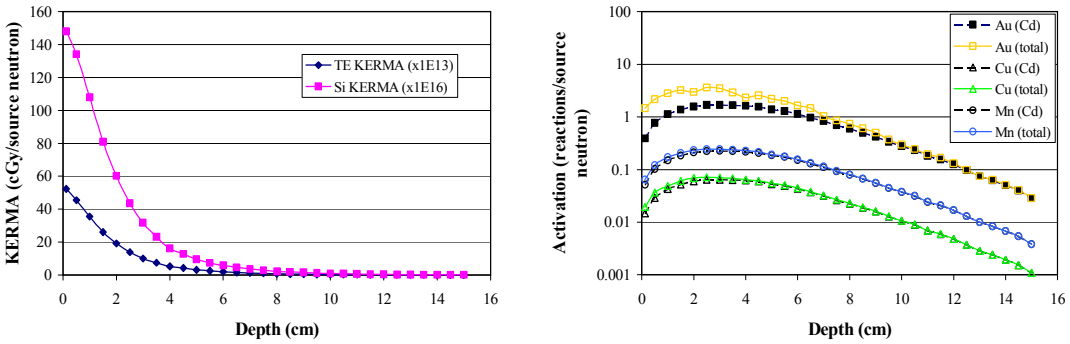

Figure 6-13. Tissue, Silicon KERMA and foil activation for a 50 keV ideal beam.

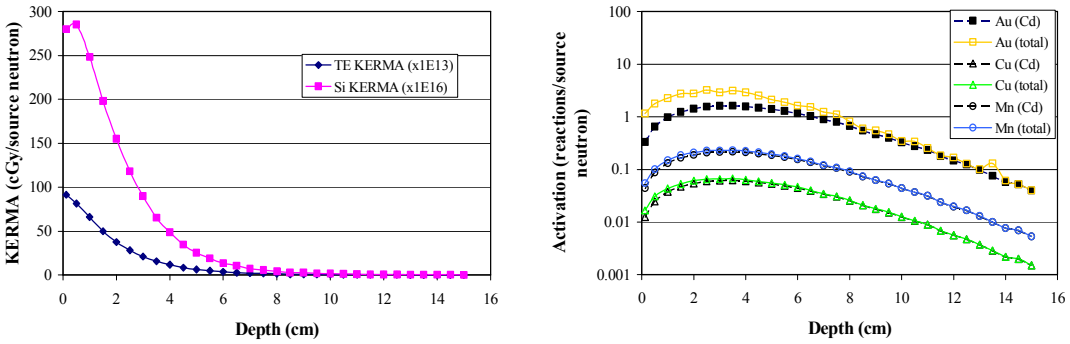

Figure 6-14. Tissue, Silicon KERMA and foil activation for a 100 keV ideal beam.

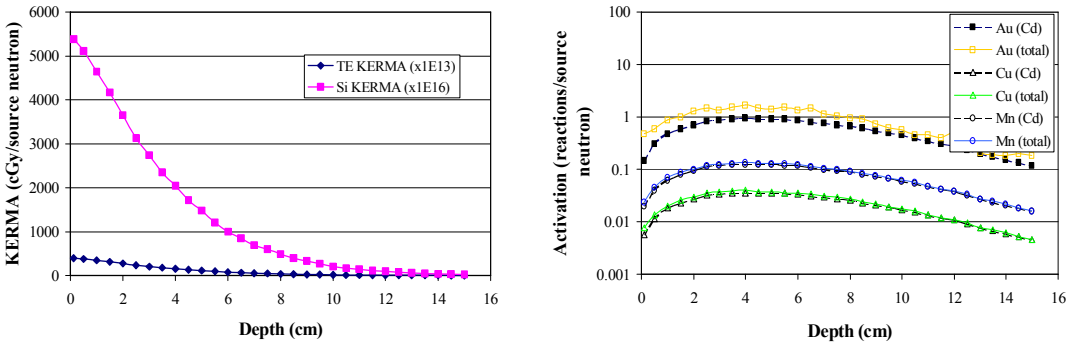

Figure 6-15. Tissue, Silicon KERMA and foil activation for a 1 MeV ideal beam.

The initial strategy was to use regression analysis to fit the data starting at the lowest energies first. This is because for any initial neutron beam energy it must be assumed that all lower energies are present due to neutrons slowing down in the moderating media of tissue. As a satisfactory fit was obtained higher incident neutron energies were included.

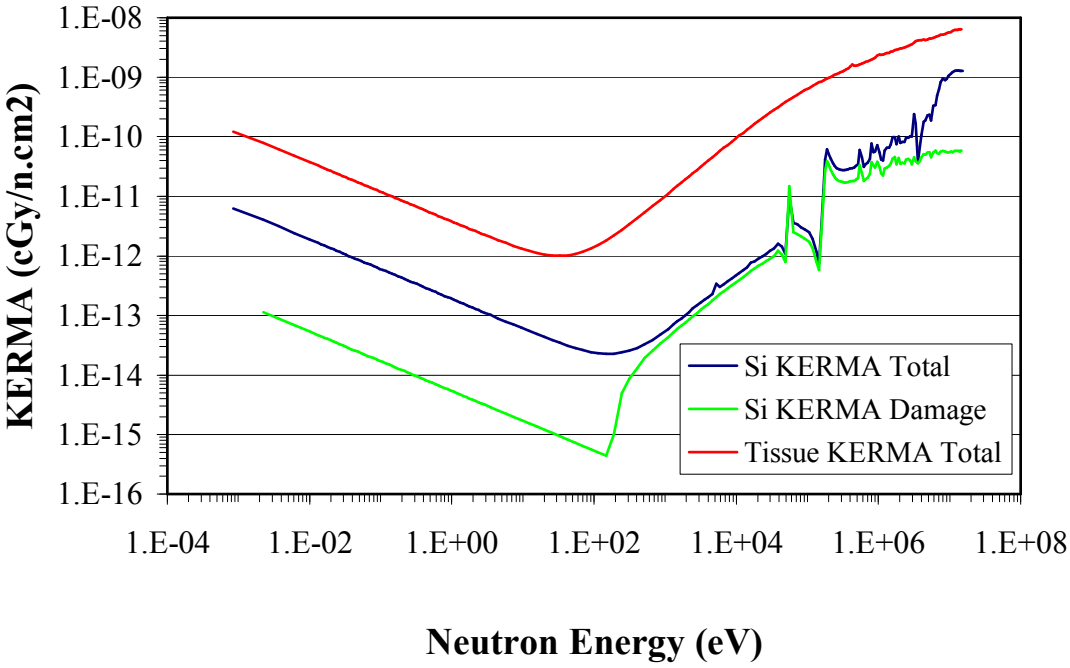

Figure 6-16. Silicon[125] and tissue[4] KERMAs.

An inspection of the tissue and silicon damage KERMA's as a function of energy as shown in Figure 6-16 suggests that there are several discrete neutron energy ranges where there is a simple ratio between the silicon and the tissue doses. However these ratio's vary from one section of the curves to another and dramatically so once energies approaching 100 keV are reached. At this point fine structure in the silicon KERMA curve will prohibit using any simple energy index parameter to "scale" the silicon dose as measured by a PIN diode to a tissue equivalent dose.

SPECIAL CASE: E_N < 10 EV

For an environment with only sub 10 eV neutrons present the relationship is trivial. This can be seen from Figure 6-16. A linear regression with only one parameter (Silicon damage KERMA) is adequate. When the regression analysis is

done for the 0.25, 1 and 10 eV depth dose curves the following result is obtained.

$$D_{TE} = a_1 D_{SI} \qquad 6\text{-}3$$

Where D_{TE} is the MCNP tissue dose tally in cGy, D_{SI} is the MCNP silicon damage KERMA tally in cGy and $a_1 = 0.3950(\pm 0.0009) \times 10^3$. (Confidence interval at 95% level.) The r^2 was 0.999. The resulting depth dose curves for the ideal beams are shown in Figure 6-17. When the same value of a_1 is used for depth dose curves with incident neutron energies of up to 500 eV a satisfactory fit is observed. As the incident neutron energy increases the scaled silicon KERMA tends to over estimate the tissue dose at shallow depths. At 500 eV the over estimate is approximately 7% for depths less than 0.5 cm. This can be also be seen in Figure 6-17.

However with an incident neutron energy of 700 eV (not shown in figure) this over estimate has reached 14.5% for depths of less than 0.5 cm. The deviations from tissue equivalence at depths greater than 1.0 cm are still less than 1%.

TWO PARAMETER FIT

If two parameters are used it is possible to extend the energy range over which a satisfactory fit is achieved. Using a linear combination of the silicon damage KERMA and sub-cadmium cutoff contribution to the gold foil activation for energies between 0.25 eV and 30 keV achieved an acceptable fit with r^2=0.9996.

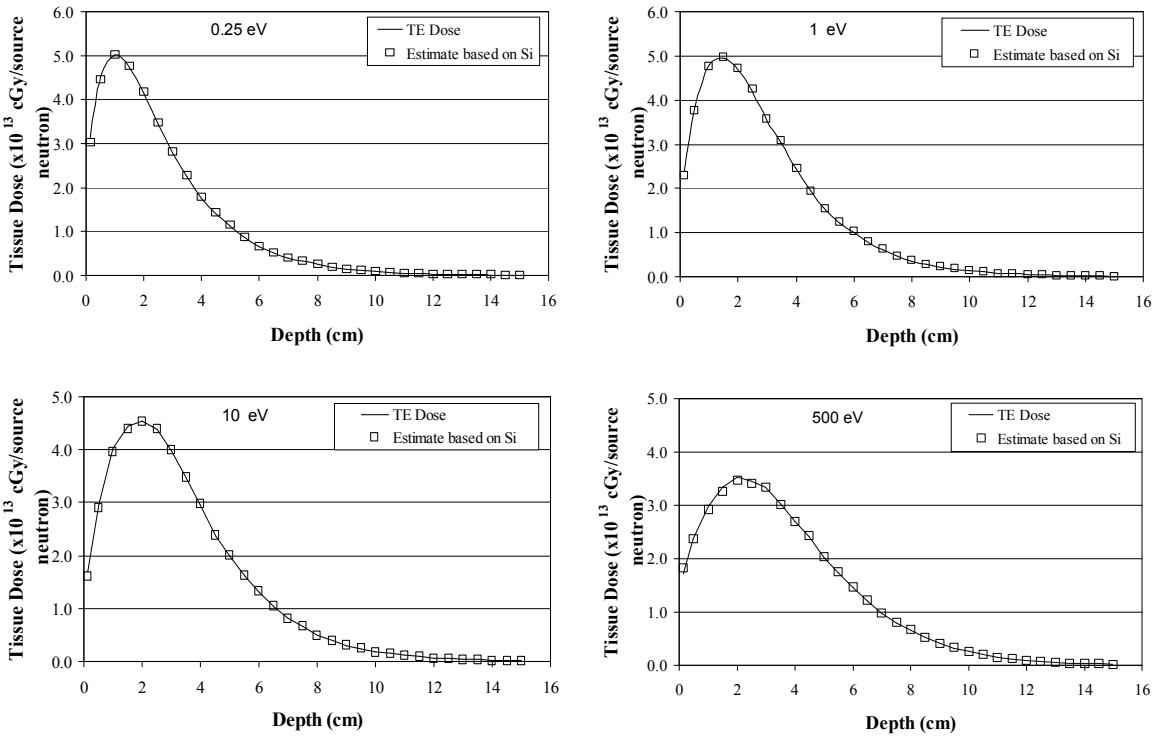

Figure 6-17. Silicon KERMA based estimate of tissue dose for 0.25, 1, 10 eV and 500 eV ideal beams using single factor to scale silicon damage KERMA to tissue dose. Coefficient based on depth dose curves for ideal beam with energies 0.25 eV - 10 eV.

The tissue dose D_{TE} (cGy) was fitted with silicon damage D_{SI} (cGy) and foil activation *Act* (Bq/atom):

$$D_{TE} = a_1 D_{SI} + b_1 Act \qquad 6\text{-}4$$

The coefficients were $a_1=0.2817(\pm 0.0006)\times 10^3$ and $b_1= 0.394(\pm 0.007)\times 10^{-13}$, where a_1 is the coefficient for the silicon KERMA tally and b_1 is the coefficient for the sub cadmium cutoff activation tally (dimensions: cGy.atoms/Bq). These curves are shown in Figure 6-18 and Figure 6-19. Deviations of the estimate from the calculated tissue equivalent depth dose profiles occurred predominantly within the first 1 cm of the depth dose profile. All deviations were less than 3% except for the first 1.5 cm at some ideal beam energies. All deviations greater than 3% were less than 10% except for a 14% underestimate at 0.125 cm depth in the 100eV beam.

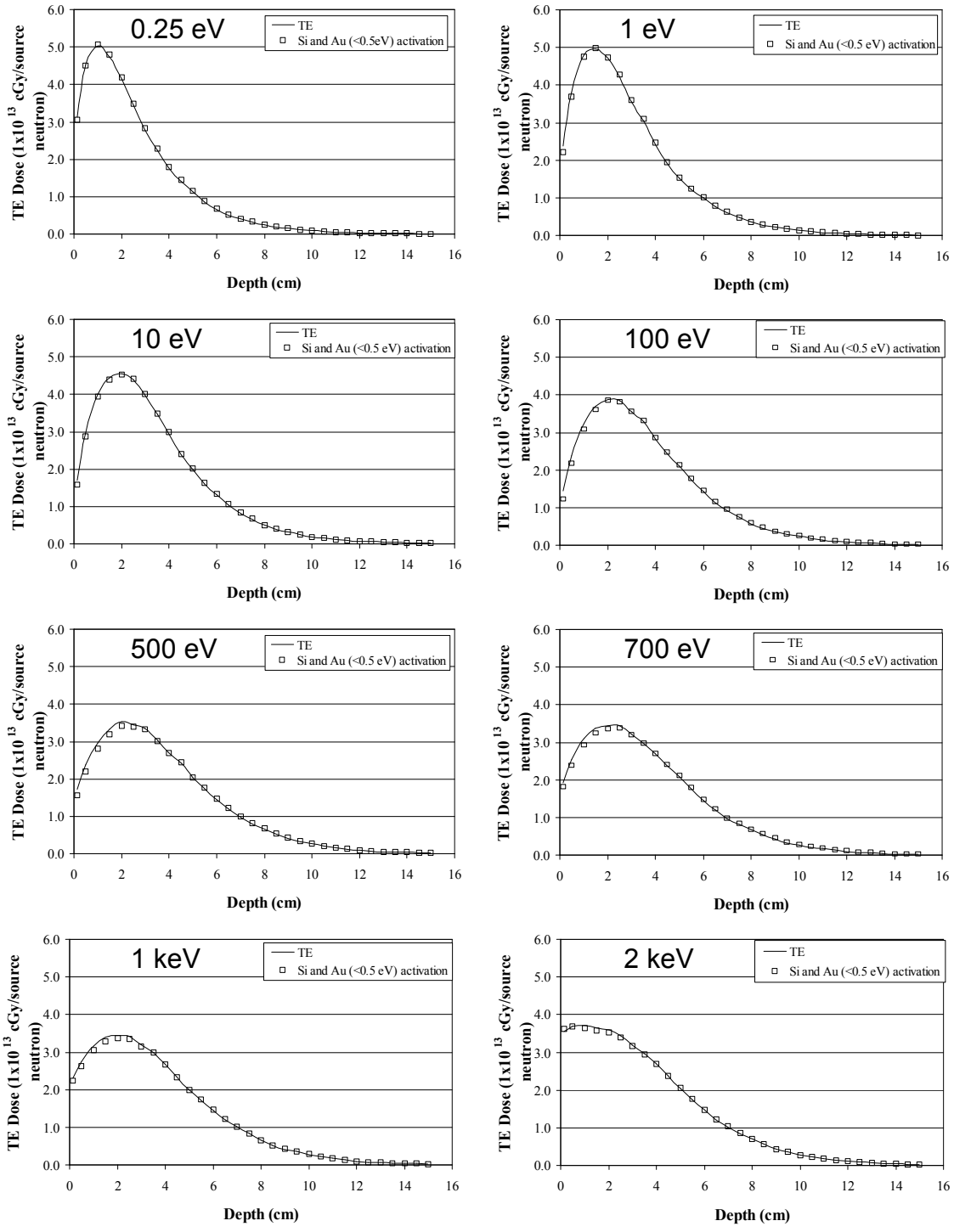

Figure 6-18. Tissue equivalent dose and fitted curve based on silicon KERMA and sub cadmium cutoff gold foil activation (0.25,1, 10, 100, 500, 700, 1000, 2000 eV ideal neutron beams). Coefficients based on ideal beams from 0.25 eV - 30 keV.

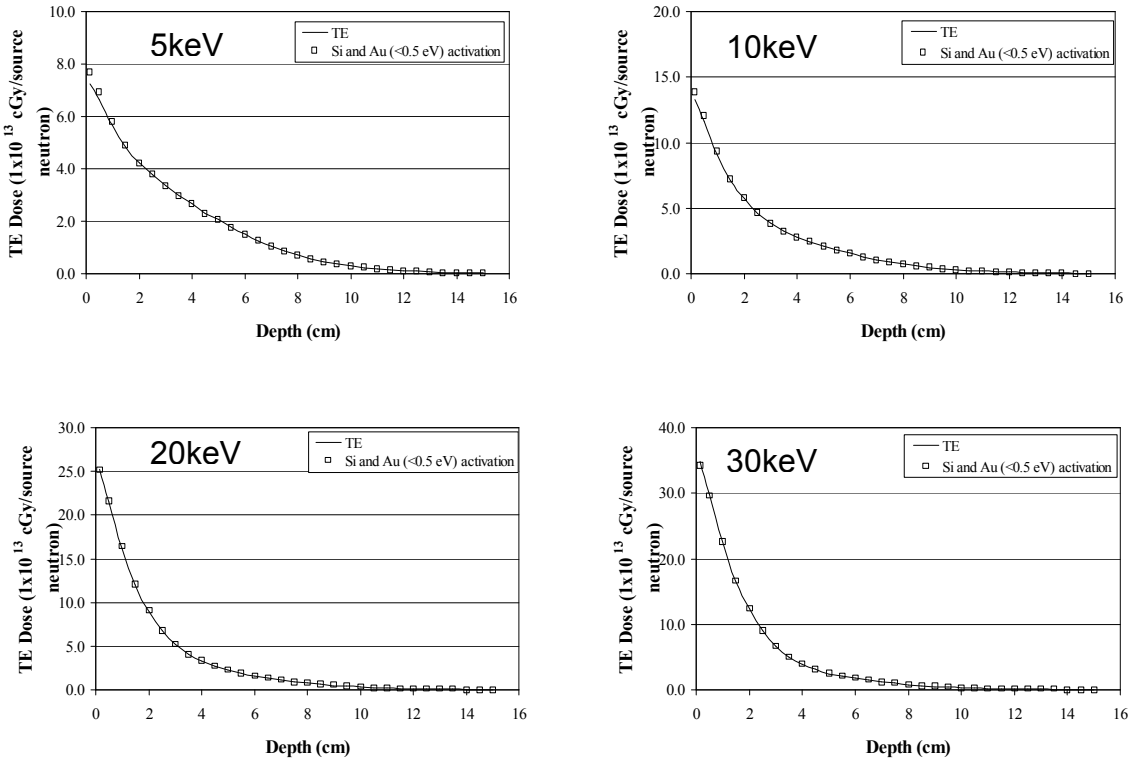

Figure 6-19. Tissue equivalent dose and fitted curve based on silicon KERMA and sub cadmium cutoff gold foil activation (5, 10, 20, 30 keV ideal neutron beams). Coefficients based on fitting ideal beam depth dose curves from 0.25 eV - 30 keV.

Similar results were observed over the 0.25 - 30keV energy range using the silicon KERMA and the total copper foil activation (Figure 6-20 and Figure 6-21). In this case the coefficients were $a_1=0.2806(\pm0.0007)\times10^3$ and $b_1=9.98(\pm0.19)\times10^{-13}$ for the silicon KERMA and the copper activation tallies respectively.

A similar or marginally superior fit was achieved with the silicon KERMA and the total manganese activation ($r^2=0.99$) for the same neutron energy range. The coefficients were $a_1=0.2808(\pm0.0006)\times10^3$ and $b_1=2.846(\pm0.051)\times10^{-13}$ respectively. The calculated tissue dose and estimates based on calculated silicon damage and manganese activation are shown in Figure 6-22 and Figure 6-23.

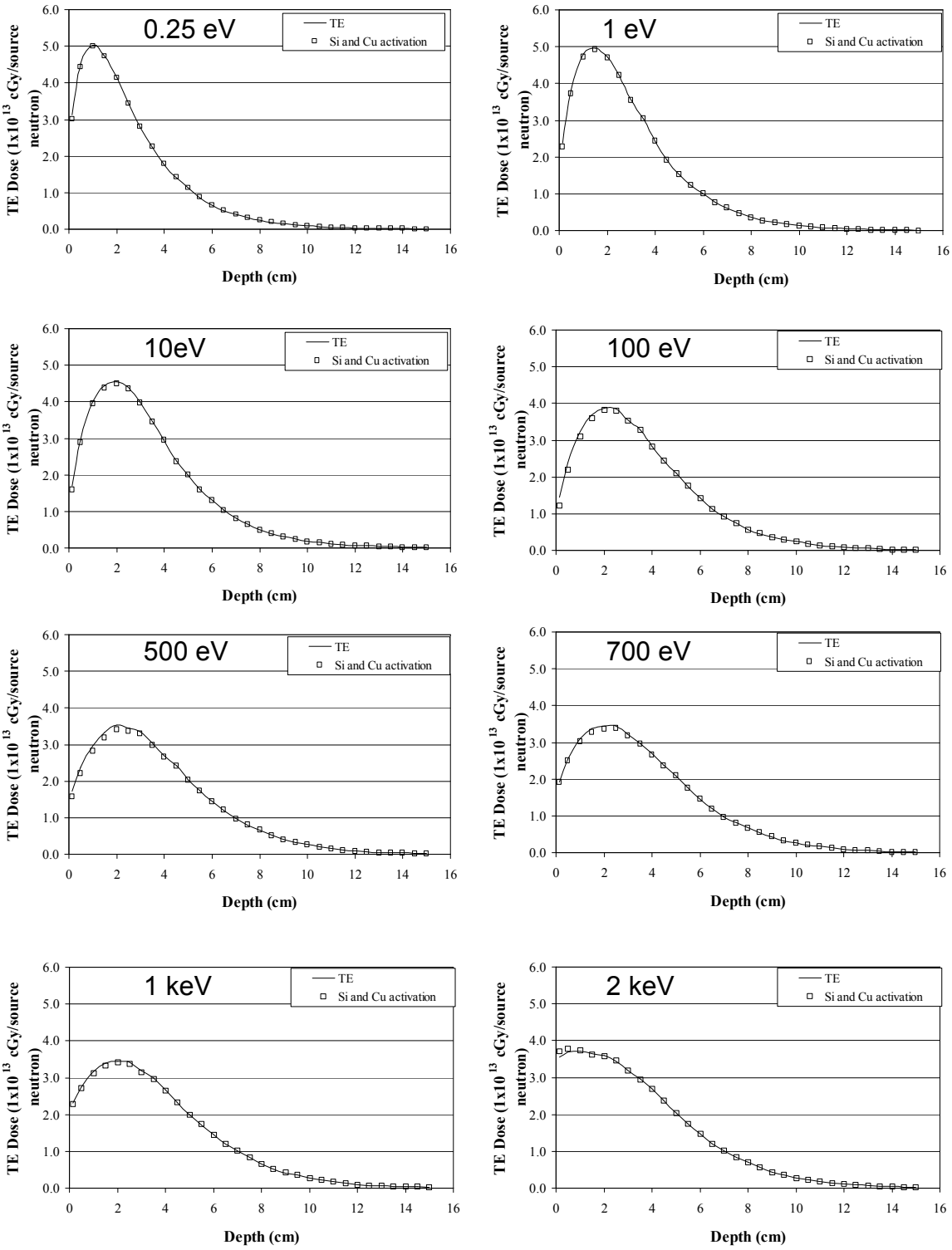

Figure 6-20. Tissue equivalent dose and fitted curve based on silicon KERMA and copper foil activation (0.25,1, 10, 100, 500, 700, 1000, 2000 eV ideal neutron beams). Coefficients based on fitting ideal beam depth dose curves from 0.25 eV - 30 keV.

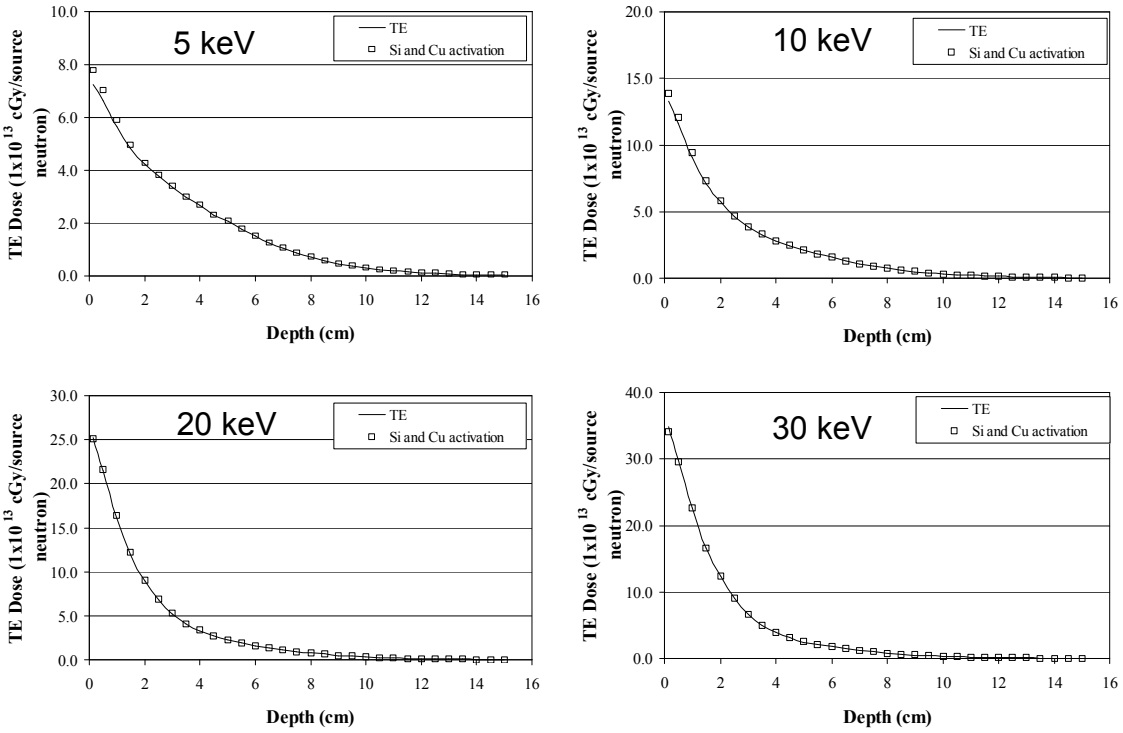

Figure 6-21. Tissue equivalent dose and fitted curve based on silicon KERMA and copper foil activation (5, 10, 20, 30 keV ideal neutron beams.

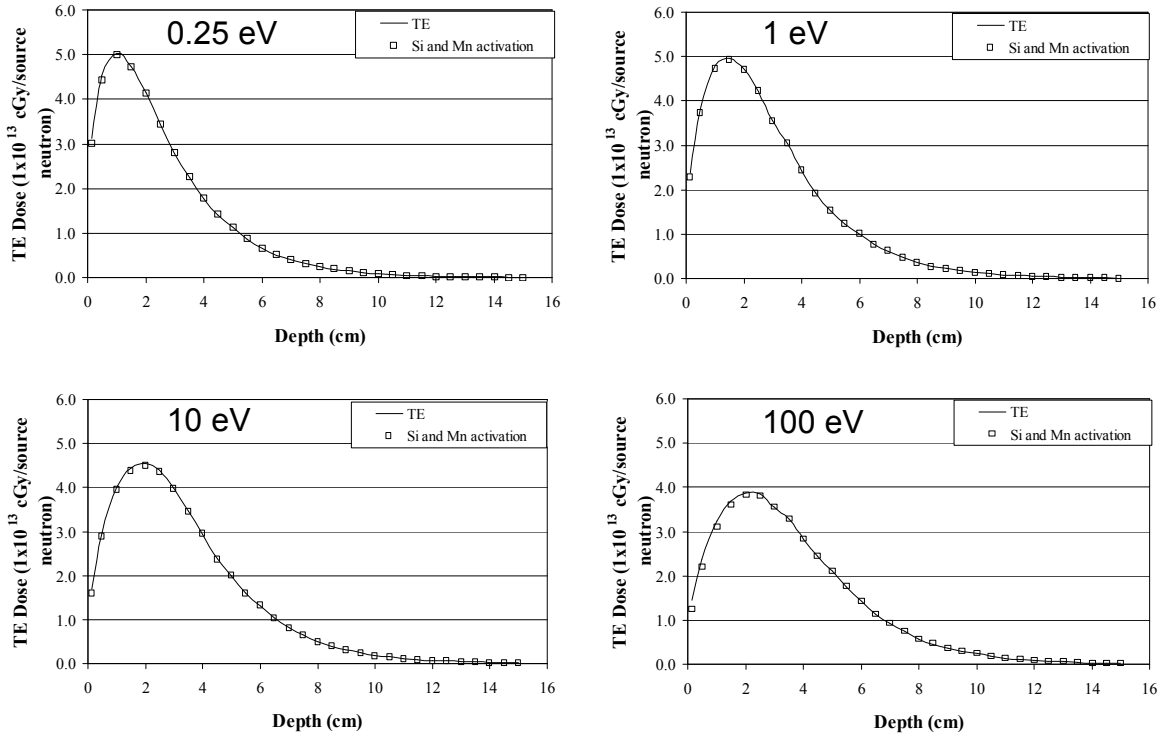

Figure 6-22. Tissue equivalent dose and fitted curve based on silicon KERMA and manganese foil activation (0.25,1, 10, 100, eV ideal neutron beams).

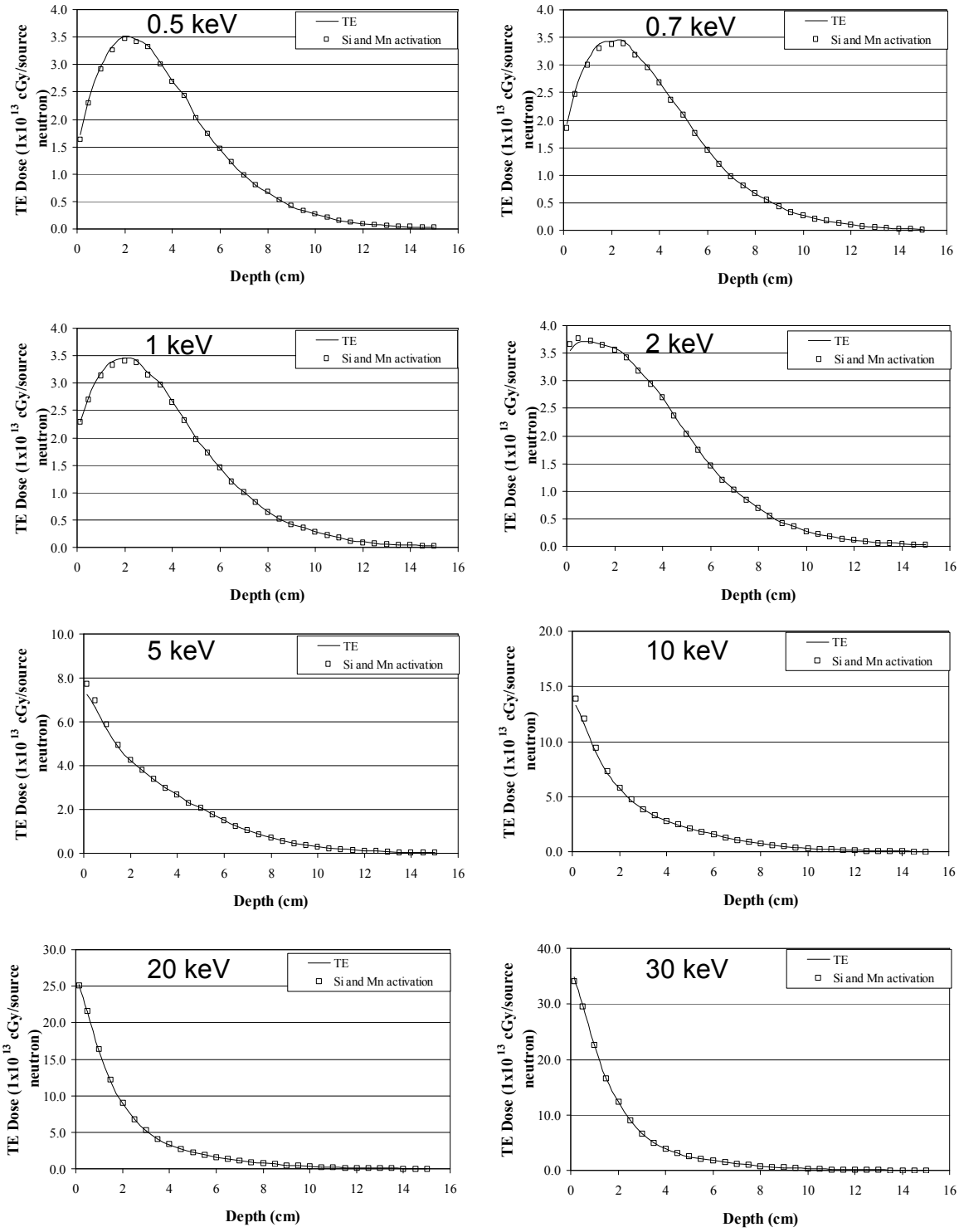

Figure 6-23. Tissue equivalent dose and fitted curve based on silicon KERMA and manganese foil activation (0.5, 0.7, 1, 2, 5, 10, 20, and 30 keV ideal neutron beams). Coefficients based on fitting ideal beam depth dose curves from 0.25 eV - 30 keV.

EXTENSION TO NEUTRON ENERGIES > 30 KEV

Attempting to fit a linear combination of foil activations and silicon dose to sets of ideal beam depth dose (TE) profiles that included neutron energies greater than 30 keV significantly increased the errors in the estimate of the tissue dose.

Regression fits of tissue dose to linear combinations of silicon damage kerma and total manganese and total copper activation were obtained for ideal beam energies up to and including 100 keV. The fitted tissue dose curves for ideal beams based on a linear combination of silicon damage and copper activation are shown in Figure 6-24 and Figure 6-25. In this case the coefficients are $a_1 = 0.287(\pm 0.0035)\times 10^3$, $b_1 = 7.55(\pm 2.3)\times 10^{-13}$.

For incident ideal beam energies less than 5 keV these coefficients lead to an under estimate of the tissue dose which is most pronounced between depths of 1 - 3.5cm in the phantom. Over this depth range the average magnitude of the underestimate of the tissue dose based on silicon damage and copper activation is approximately 5 - 6 % when the incident energy is less than 5 keV. For energies from 5 keV to 30 keV the magnitude of the underestimate at these depths is approximately 1%. At 50 keV the under estimate is about 7% and at 100 keV the silicon and copper activation based value overestimates the actual tissue dose by an average of 19% over depths from 1 to 3.5 cm.

At depths from 4 cm to 15cm in the phantom the average discrepancy between the estimate based on the silicon damage / copper activation and the tissue dose is 4 - 5% underestimate. This is true of all the beam energies except for the 100 keV beam where the silicon / copper data exceeds the tissue dose by 5% on average.

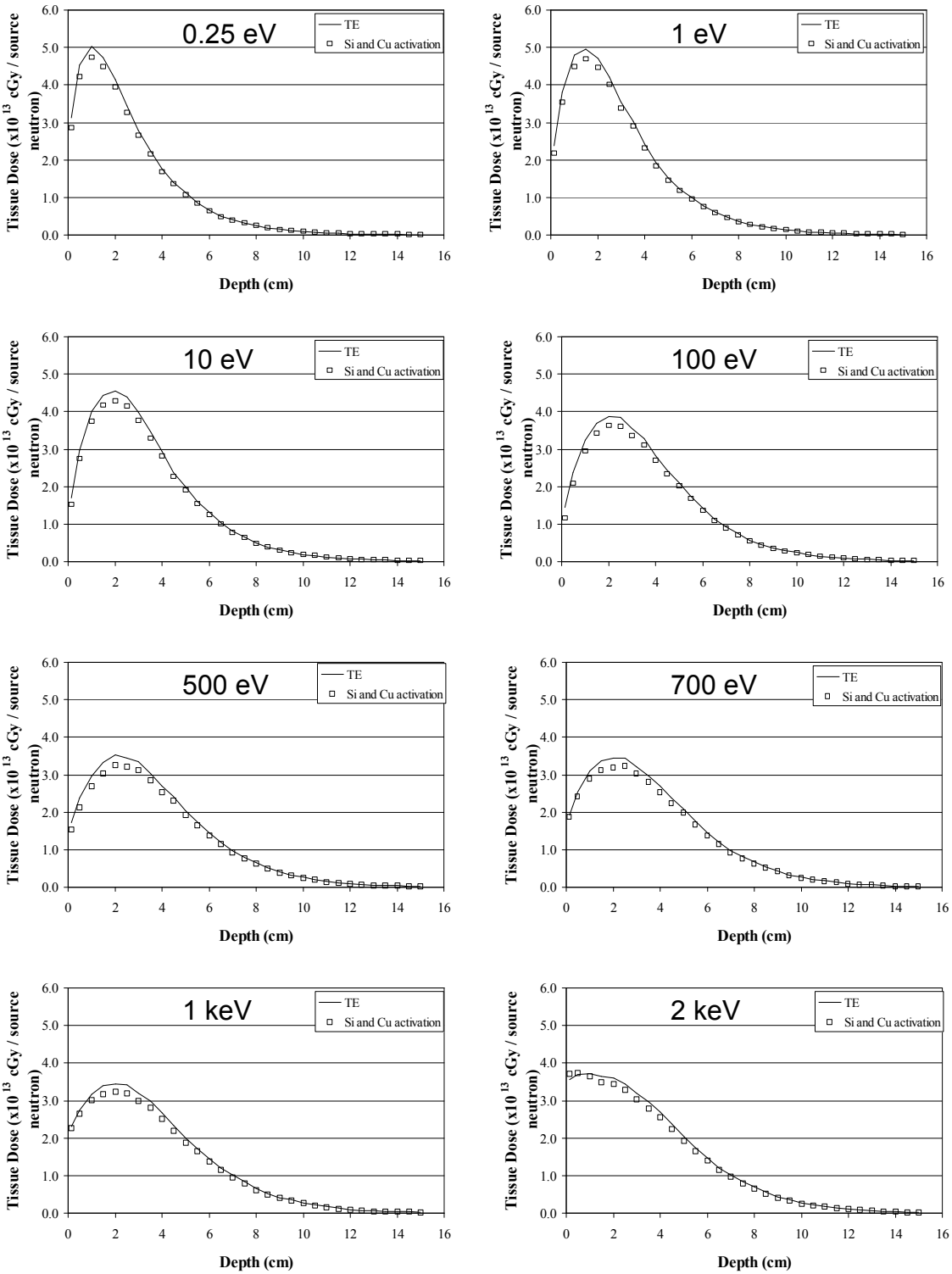

Figure 6-24. MCNP calculated TE dose (solid curves) in a cylinder phantom exposed to ideal beams of 0.25, 1, 10, 100, 500, 700, 1000 and 2000 eV neutron beams. The data points show an estimate of tissue dose based on MCNP simulated silicon kerma and copper foil activation. Coefficients based on ideal beam energies from 0.25 eV -100 keV.

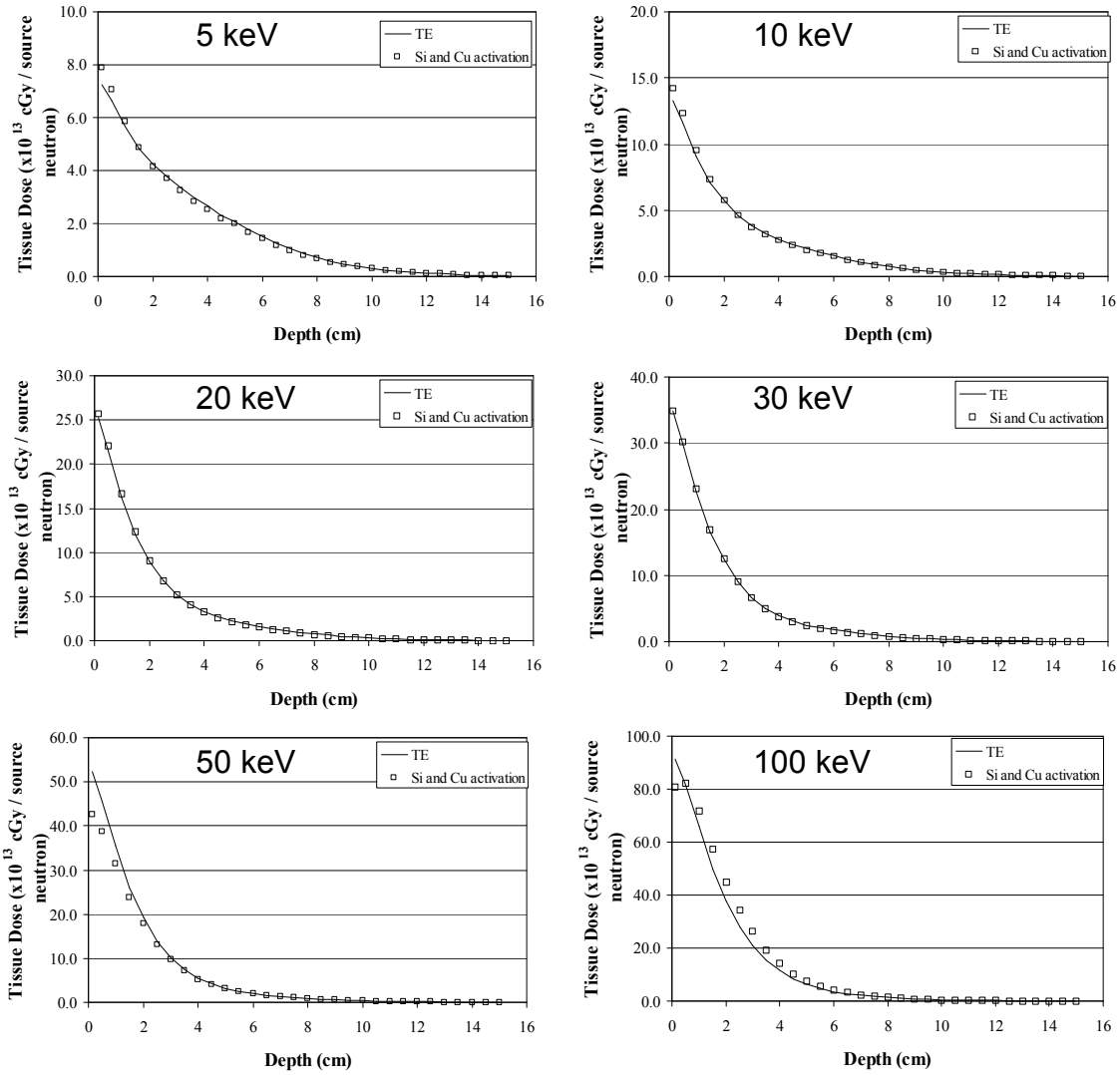

Figure 6-25. MCNP calculated TE dose (solid curves) in a cylinder phantom exposed to ideal neutron beams of 5, 10, 20, 30, 50 and 100 keV. The data points show an estimate of tissue dose based on MCNP simulated silicon kerma and copper foil activation. Coefficients based on ideal beam energies from 0.25 eV -100 keV.

The same procedure was followed for the silicon damage and manganese activation data. The results for these are shown in Figure 6-26 and Figure 6-27.

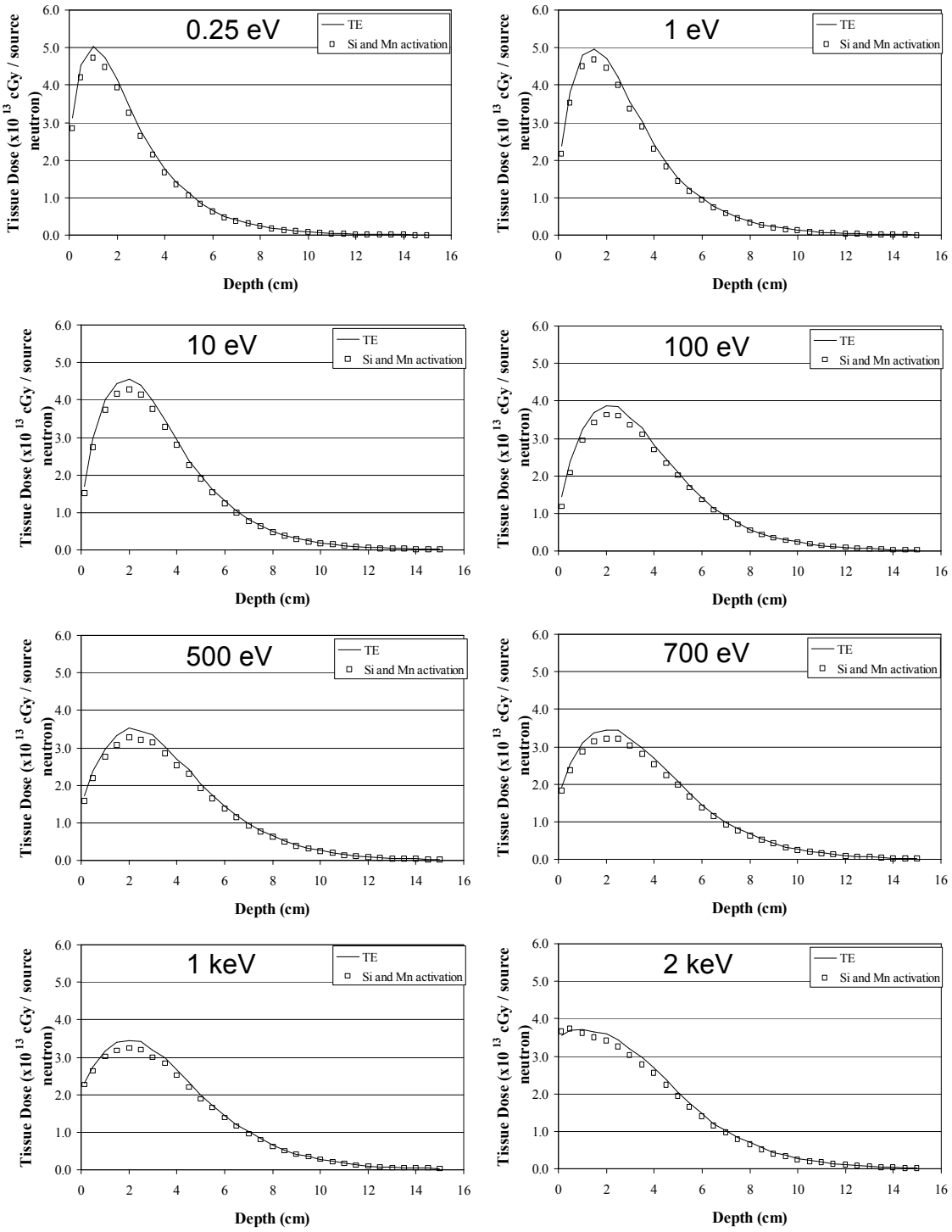

Figure 6-26. Ideal beam study. Silicon damage KERMA and Mn activation estimate of tissue dose, 0.25, 1, 10, 100, 500, 700, 1000 and 2000 eV neutron beams. Coefficients based on ideal beam energies from 0.25 eV -100 keV.

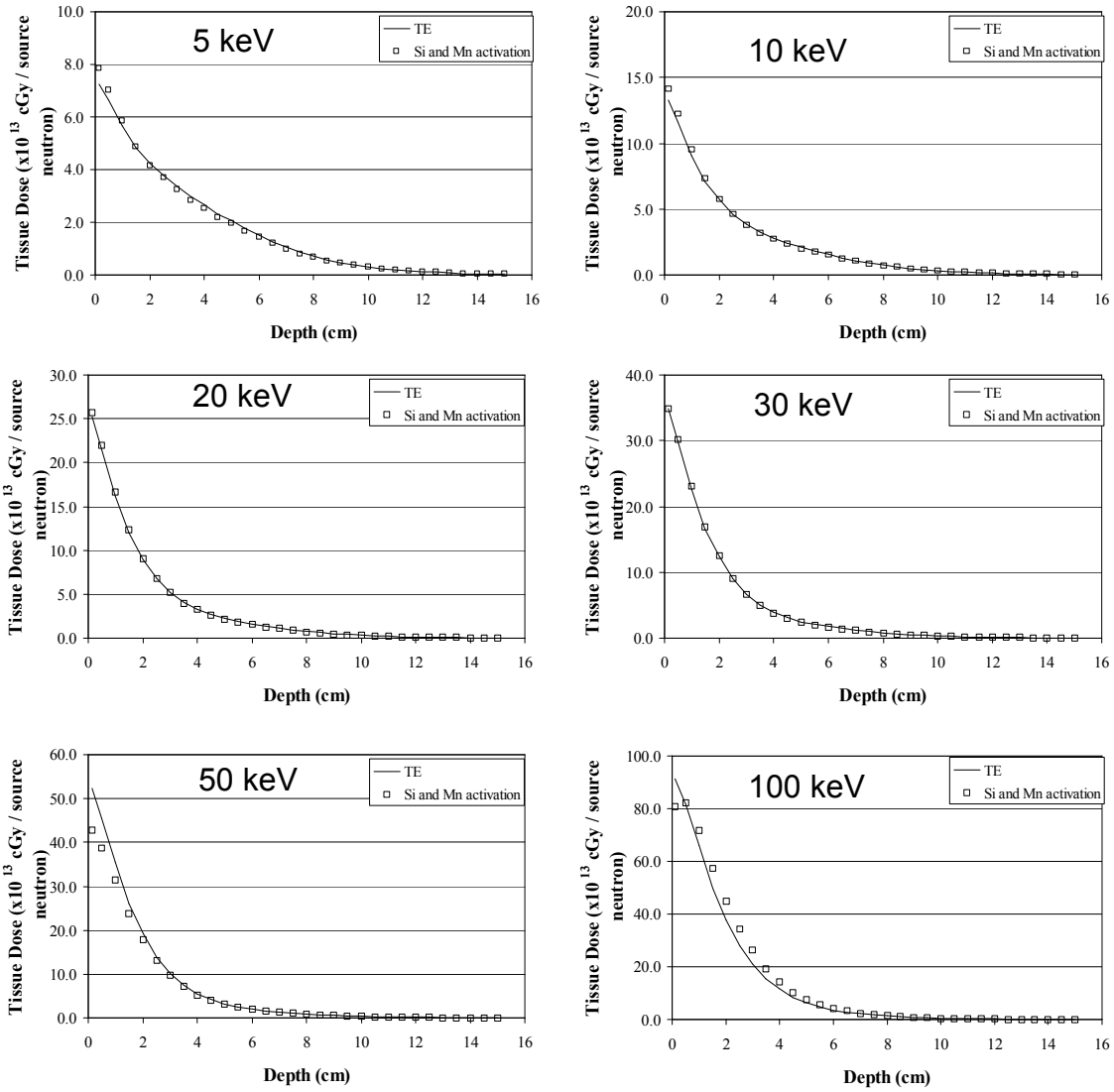

Figure 6-27. Ideal beam study. Silicon damage dose and manganese activation estimate of tissue dose. Incident neutron beam energies of 5, 10, 20, 30, 50 and 100 keV. Coefficients based on ideal beam energies from 0.25 eV -100 keV.

When the MCNP calculated tissue dose is fitted to a linear combination of the silicon damage dose and the manganese activation the coefficients are found to be; $a_1 = 0.2874(\pm 0.0035)\text{x}10^{3}$ and $b_1 = 2.157(\pm 0.66)\text{x}10^{-13}$.

The accuracy of this fit was similar to the results using silicon damage and copper activation detailed above. At 2 keV and below the fitted data tended to underestimate the tissue equivalent dose at depths between 1 and 3.5 cm. The

average magnitude of this underestimate was 5 -7 % for ideal neutron beam energies of 2 keV and below. For energies between 5 keV and 30 keV the average difference for depths from 1 cm to 3.5 cm was between -1% and +1%. At 50 keV the silicon and manganese data underestimated the tissue dose by an average of 7% over the same range of depths. For the same depths the estimate of tissue dose in the 100 keV beam was approximately 20% in excess of the MCNP calculated tissue dose. At depths of 4 cm or greater the silicon and manganese based estimate of tissue dose was on average between 4 and 5% below the calculated tissue dose for all ideal beam energies tested except 100 KeV. In the 100 keV beam the average silicon and manganese based estimate was 5% above the tissue dose at depths greater than 4 cm.

Unfortunately if the coefficients (a_1 and b_1) derived on the basis of ideal beams having energies between 0.25 eV and 100 keV are applied to ideal beams with neutron energies of 1 MeV or 10 MeV a large over estimate of the real tissue dose occurs. If the coefficients based on silicon damage dose and copper activation are used this results in the tissue dose at all depths being overestimated by a factor of between 3.4 and 3.9 for a 1 MeV ideal neutron beam and between 2.75 and 2.87 for a 10 MeV beam. In the case of the silicon damage dose and the manganese activation the magnitude of the resulting overestimate of the tissue dose is the same as for the silicon and copper activation with neutron energies of 1 MeV and 10 MeV. This can be seen in Figure 6-28 for the case of the silicon and manganese based estimate of tissue dose in 1 and 10 MeV beams.

Therefore in any practical application to neutron beams where neutrons with energies greater than 100 keV contribute a significant proportion of the total dose this measurement technique is not accurate. This is seen in Figure 6-29 for the case of a

cylinder phantom irradiated in the HB11 beam of the HFR at Petten.

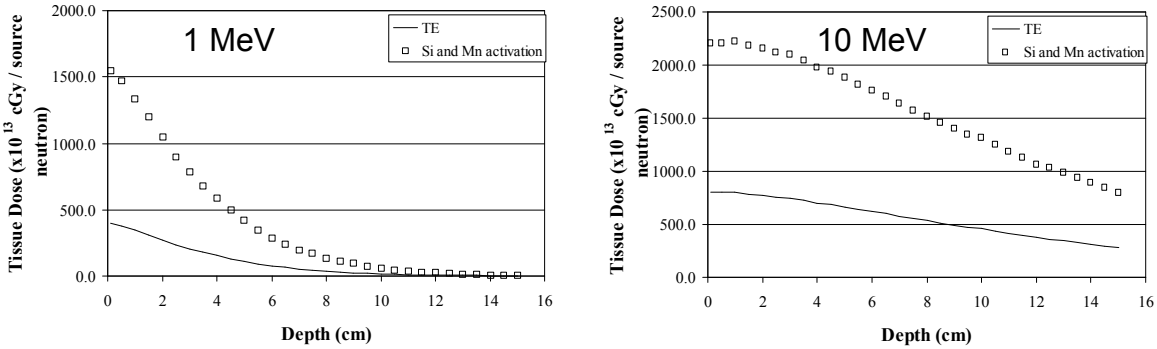

Figure 6-28. MCNP calculated tissue equivalent dose in a phantom compared with an estimate of tissue dose based on the silicon damage dose and manganese foil activation. The ideal beam neutron energies were 1 MeV and 10 MeV but the coefficients used derived from ideal beam with energies between 0.25 eV and 100 keV.

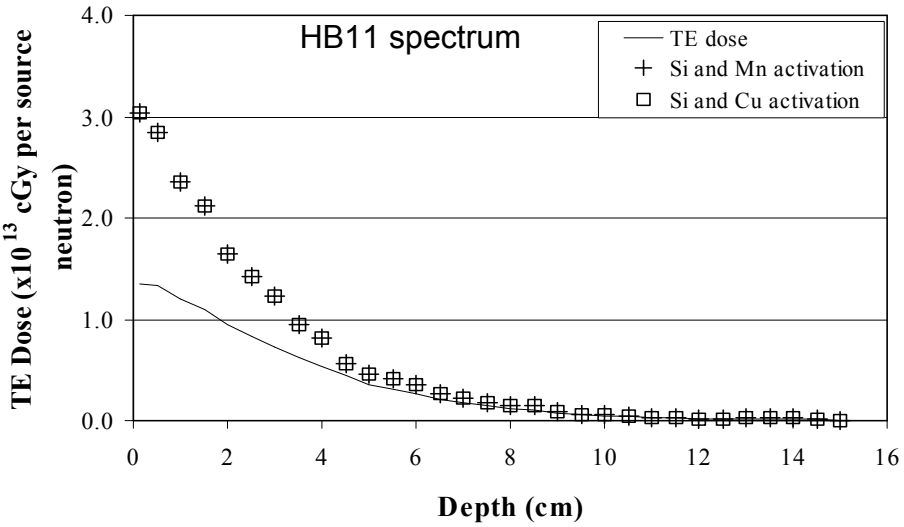

Figure 6-29. MCNP calculated tissue dose in a cylinder exposed in Petten HB11 epithermal neutron beam. Also shown are the estimates of tissue dose based on silicon damage dose in combination with copper or manganese activation.

CONVERSION OF UNITS

The results of the ideal beam simulation studies that are presented above and that were used to determine regression coefficients are in terms of the raw MCNP tally quantities. In order to use the regression fits derived above with measured experimental data the units of the regression coefficients need to be converted to more directly applicable ones. This change reflects the difference between the units of the MCNP tallies and the units commonly used for experimental measurements.

For the silicon damage kerma in the simulations the tally multiplier dimensions and units are silicon damage dose per unit neutron flux, $cGy.cm^2$. When multiplied by the track length estimate of neutron flux (tally type 4 with units of flux per source neutron) this gives a tally quantity of silicon damage kerma in cGy per source neutron.

For experimental measurements the directly observed quantity for the PIN diodes will be the change in the forward bias voltage observed during the irradiation time. The units will be mV per unit time. Dividing the observed diode forward bias change by the diode calibration factor ($mV.cGy^{-1}$) yields a measured value for silicon damage dose in cGy per unit time.

The tissue kerma factors used in the simulations were in terms of dose per unit neutron flux ($cGy.cm^2$). When multiplied by the neutron flux in the tally cell per source neutron this gives the tissue kerma in cGy per source neutron. The units of tissue dose (rate) that we require in an expression for practical use are cGy per unit time.

For the foil activation data the tallied quantity is given by:

$$Act = \int_0^{E\max} \phi(E) R_n dE \qquad 6\text{-}5$$

where ϕ(E) is the neutron flux in the tally cell (cm^{-2} per source neutron) and R_n(E) is the cross section for the (n,γ) activation reaction (in barns per atom) for the activation foil being used. Therefore the units of the quantity above are barns.cm^{-2} per atom per source neutron. This quantity was left unscaled during the regression curve fitting.

A quantity more directly related to experimental measurements can be obtained by multiplying this tally by a factor of 10^{-24} cm^2.$barn^{-1}$ and the number of source neutrons per second. This converts the tally to a saturation activity with dimensions of reactions per atom per second.

The experimentally measured foil activation per atom at a time *t* after an irradiation of duration t_e is given by:

$$R(t, t_e) = \frac{A_{meas}(Bq) AW(g/mol)}{fM(g) N_A(atoms/mol)} \qquad 6\text{-}6$$

Where N_A is Avagadro's number, A_{meas} is measured activity of the foil, *M* is the mass of the foil in grams, *AW* is the atomic weight of the foil material, and the abundance of the isotope in foil that undergoes activation is *f*. From this the saturation activity can be found using:

$$R_0 = \frac{R(t, t_e)}{(1 - e^{-t_e/\tau}) e^{-t/\tau}} \qquad 6\text{-}7$$

Where R_0 is the saturation activity in Bq per atom, τ is the half-life of the activated isotope in the foil divided by *ln(2)*.

The tissue dose in cGy can therefore be represented as

$D_{TE} = A\, D_{SImeas} + B\, R_o$

Where D_{SImeas} is silicon damage dose measured with a PIN diode, R_o is saturation activity derived from measured foil activities and the coefficients are related to the previously derived a_1 and b_1 by $A = a_1$ and $B = 10^{24}\, b_1$.

CONCLUSIONS

Due to the nature of the silicon displacement damage KERMA cross section PIN diodes respond to a wide range of neutron energies. While over some limited energy ranges there is a direct proportional relationship between silicon damage KERMA and tissue KERMA this is not generally true. Therefore silicon PIN diode responses cannot be assumed to be tissue equivalent in typical epithermal neutron beam spectra. However due to some similarities in the KERMA energy response curves for tissue and silicon it is possible to make a linear combination of silicon damage KERMA and gold, copper or manganese foil activations that approximates tissue equivalence over a limited range of neutron energies.

MCNP simulations were used to determine tissue dose, silicon displacement damage and gold, copper and manganese foil activations in a tissue equivalent phantom exposed to ideal beams ranging in energy from 0.25 eV up to 10 MeV. Using linear regression of the depth dose curves for each of these quantities it was possible determine a coefficient that can be used to scale silicon damage dose to give

tissue equivalent dose for incident neutron energies less than 10 eV. This factor was found to be 0.395 x 10^3. This factor was found to be able to scale silicon depth dose distributions to tissue depth dose distributions for incident monoenergetic neutron beams up to 500 eV. Discrepancies were less than 7% for a 500 eV incident beam.

For higher energies it was necessary to add a foil activation term. Using the activation of gold below the cadmium cutoff in combination with silicon achieved a reasonably good prediction of tissue dose for incident beam energies up to 30 keV. For all depths greater than 1.5 cm the maximum deviation between the calculated tissue dose and the silicon/gold foil estimate was approximately 3%. In some energy ranges deviations of about 10% were observed in the first 1.5 cm of the phantom.

Similarly accurate predictions of tissue dose for this energy range were achieved using silicon and copper foil total activation or manganese foil total activation. From a practical point of view estimates based on total foil activation are preferable to ones based on sub cadmium cutoff activation because no cadmium covered measurements would need to be made in this case. No advantage was obtained by using more than one type of foil or by including separate terms for activation above and below the cadmium cutoff.

When ideal beam energies up to 100 keV are included in the determination of the silicon and activation coefficients the estimated values of tissue dose become less accurate. For silicon and copper or silicon and manganese at depths in the phantom greater than 4 cm the predicted tissue dose is 4-5% less than the MNCP calculated tissue dose. The largest discrepancies tend to be at shallow depth (<3.5 cm) and for the high (100 keV) and low (<5 keV) energy extremes. However the discrepancy is still only about 5-6% for energies <5 keV at depths less than 3.5 cm. Errors of up to

20 % are evident for the 100 keV beam for these superficial depths.

Application of coefficients derived using ideal beam energies up to 100 keV to beams with higher energy neutrons present does not yield good results. This is to be expected due to the structure of the silicon damage kerma curve for these higher energies. The sharp increase in the silicon damage KERMA for energies greater than 100 keV means that any spectral component >100 keV leads to a significant over estimate of the tissue dose as was observed for the case of the HB11 spectrum. The discrepancy decreases with depth in the phantom as the incident beam becomes more moderated.

For similar reasons using coefficients derived from ideal beams with E > 100 keV leads to very poor fits for lower energies.

Therefore the technique is probably only relevant to neutron sources where the maximum energy present is ≤ 100 keV. This may be the case for some accelerator based neutron sources or for quasi-thermal neutron sources. One possible solution to these energy limitations may be to find some experimentally observable parameter in terms if silicon damage and foil activations that indicates when higher energy spectral components are present so that different coefficients can be applied to determine tissue dose. Preliminary investigations show that simple ratios of silicon damage and foil activations are probably not adequate for this.

Further refinements could involve the calculation of coefficients to convert from silicon damage and foil activation to doses for the various ICRU tissue compositions.

PIN diodes have been used for several decades as dosimeters to estimate approximate tissue dose in high energy (>1 MeV) neutron environments. The

simulations and analysis presented here demonstrate that in combination with a single activation foil they could also be applied to measurement of tissue dose in neutron beams with energies less than 100 keV.

CHAPTER 7 CHARACTERISATION OF PIN DIODES USING THE ANSTO VAN DE GRAFF ACCELERATOR

AIM

The PIN diode is assumed to respond to neutron irradiation damage with an energy dependence that matches the published silicon damage KERMA[125] curve shown in Chapter 3. In order to verify that the PIN diodes being used follow this energy response some experiments were conducted with approximately monoenergetic neutrons obtained from the Ansto Van de Graff accelerator[183].

METHOD

The L2 facility on the 3 MeV single ended Van De Graff accelerator was used. This beam is usually used to produce beams of a few 100keV using protons accelerated onto a lithium target. For the current work approximately monoenergetic neutrons from the Li(p,n)Be reaction at seven energies in the range from 90 keV to 900 keV were used. This covers a range of neutron energies of prime interest for PIN diode applications in BNCT. A PIN diode was irradiated at a point 5 cm from the lithium target on the beam axis (i.e. at 0°). Estimates of the neutron flux were derived from two methods; long counter measurements and yield calculations based on a known approximate lithium target thickness of 50 keV.

The experimental set up was as shown in Figure 7-1.

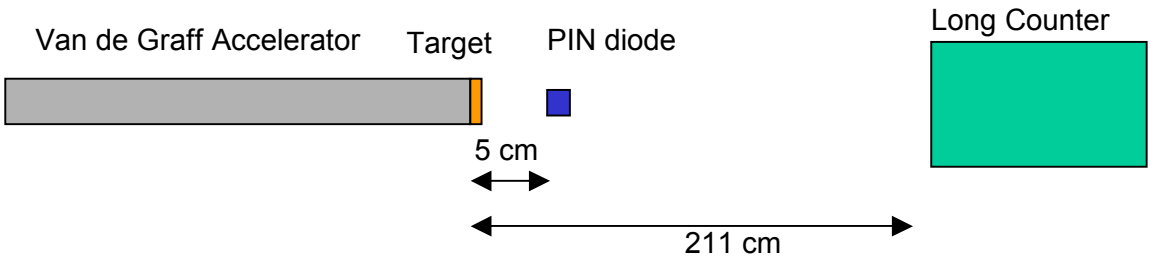

Figure 7-1. Van de Graff PIN diode irradiation experimental set up.

LONG COUNTER CALIBRATION

The long counter was calibrated using an Am Be source of known activity. The dependence of source detector distance was determined using this source. Small corrections were made to take into account the change in effective centre of the long counter with variations in neutron energy. A correction was also applied to account for the difference in efficiency of the long counter at Am Be neutron energies (4.2-4.5 MeV) compared to the energies used to irradiate the PIN diode (90 - 990 keV). A separate energy dependant efficiency factor was determined for each irradiation energy used in the PIN diode experiment. The details of the long counter calibration can be found in Appendix D.

PIN DIODE IRRADIATIONS

The following data was recorded for a series of PIN diode irradiations using the setup described above. Table 7-1 shows the flux at the irradiation point for the PIN irradiations.

Table 7-1. Neutron fluxes at measurement point for PIN diode irradiations using Ansto Van De Graff Accelerator.

Nominal En (keV)	Long Counter Efficiency	Raw counts	Corrected counts	Flux at 5 cm ($n.cm^{-2}$)
90	7.16×10^{-3}	2.065×10^{7}	2.88×10^{9}	7.00×10^{9}
140	7.23×10^{-3}	2.426×10^{7}	3.36×10^{9}	8.14×10^{9}
165	7.26×10^{-3}	2.935×10^{7}	4.04×10^{9}	9.80×10^{9}
196	7.30×10^{-3}	1.983×10^{7}	2.72×10^{9}	6.59×10^{9}
230	7.35×10^{-3}	1.154×10^{7}	1.57×10^{9}	3.81×10^{9}
350	7.50×10^{-3}	2.267×10^{7}	3.02×10^{9}	7.33×10^{9}
891	8.20×10^{-3}	1.483×10^{7}	1.81×10^{9}	4.39×10^{9}

The corrected long counter counts is the total number of neutrons emitted from the target that are subtended by the front surface of the long counter. The flux at 5cm is simply the number of neutrons passing through a $1cm^2$ area orthogonal to the axis of the beam, at a point 5 cm from the target. This flux was calculated assuming that the distribution of neutron flux across the surface of the long counter was uniform. This condition would be approximately true for the isotropic AmBe source used for calibration of the long counter. In the case of the accelerator produced neutrons however the flux density would be higher close to the central axis and this effect would increase with the energy of the proton beam. Therefore the fluxes quoted may slightly under estimate the actual flux at the point where the PIN diode was irradiated. However this effect would be small compared to the other uncertainties in this experiment.

The change in forward bias voltage per unit flux is given in Table 7-2 and shown in Figure 7-2. This information is adequate to give a picture of the energy dependence of the PIN diode over the range of energies used.

Table 7-2. PIN ΔV_f per target source neutron as function of energy.

Nominal E_n (keV)	Flux (n.cm^{-2})	V/(n.cm^{-2})
90	7.00×10^{9}	4.86×10^{-13}
140	8.14×10^{9}	2.46×10^{-13}
165	9.80×10^{9}	1.02×10^{-13}
196	6.59×10^{9}	1.82×10^{-12}
230	3.81×10^{9}	4.73×10^{-12}
350	7.33×10^{9}	2.59×10^{-12}
891	4.39×10^{9}	4.79×10^{-12}

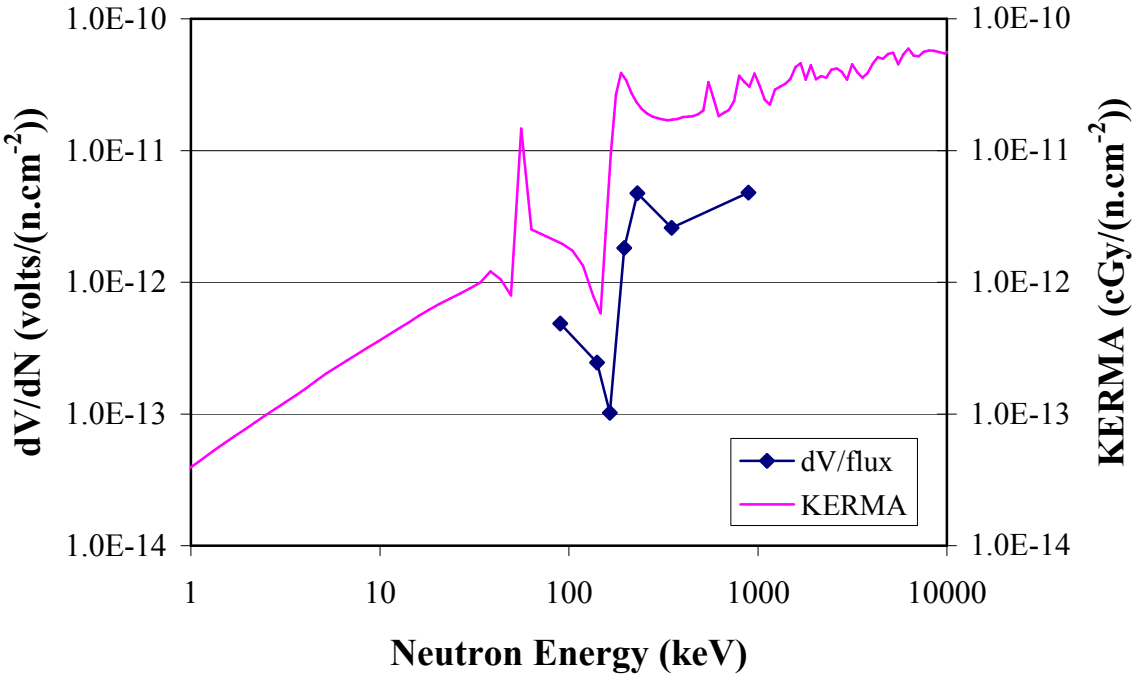

Figure 7-2. Change in forward voltage per source neutron (left axis) compared with silicon damage KERMA (right axis).

It can be seen that the PIN diode experimental data has a similar form to the known silicon damage kerma. It can also be seen that the minimum in the PIN diode response does not quite match up with the minimum in the KERMA data. This is because no account has been taken of the Li target thickness. The nominal neutron energies are simply the proton energy minus the reaction threshold energy. The Li target is known to be approximately 50 keV thick. Therefore we can expect that on average protons will loose approximately 25 keV before interacting to yield a neutron. Thus the mean neutron energies should be approximately 25 keV less than the nominal maximum neutron energies given above. In this case the PIN data in Figure 7-2 more closely resembles the KERMA curve. This is shown in Figure 7-3.

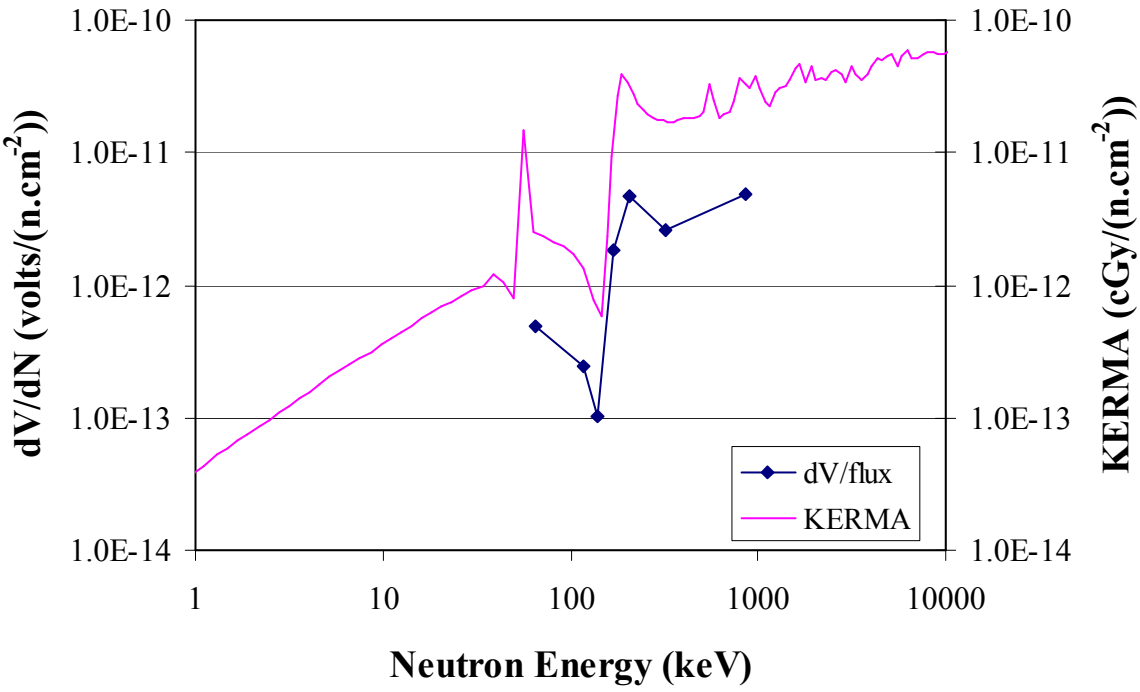

Figure 7-3. PIN response and KERMA with the pin response adjusted to take account of target thickness.

From these two pieces of data an approximate calibration factor (V/cGy) for the PIN diode can be derived. If the target thickness is assumed to be 50 keV and the

average proton energy lose in the target before generating a neutron is assumed to be 25 keV then the approximate PIN calibration factors are given in column 4 of Table 7-3. These calibration factors assume a single energy KERMA factor based on a monoenergetic neutron beam of the energy shown in the table (i.e. 25 keV less than the incident proton energy).

The actual neutron spectrum will be spread over at least 50 keV due to the target thickness. Therefore it is probably more correct to estimate the calibration factors based on the average of the damage KERMA function over a 50 keV energy range centered on a neutron energy 25 keV less than the incident proton energy. The calibration factors assuming KERMA averaged over ±25 keV are shown in column 5 of Table 7-3.

Table 7-3. PIN diode approximate calibration factors

Neutron energy (keV)	**PIN diode response V/(n.cm^{-2})**	**Si Damage KERMA cGy/(n.cm^{-2})**	**PIN calibration factor (mono) (V/cGy)**	**PIN calibration factor (average) (V/cGy)**
65	4.86×10^{-13}	2.52×10^{-12}	1.93×10^{-1}	1.44×10^{-1}
116	2.46×10^{-13}	1.40×10^{-12}	1.75×10^{-1}	1.80×10^{-1}
140	1.02×10^{-13}	6.83×10^{-13}	1.49×10^{-1}	4.78×10^{-1}
171	1.82×10^{-12}	1.57×10^{-11}	1.16×10^{-1}	1.02×10^{-1}
205	4.73×10^{-12}	3.20×10^{-11}	1.48×10^{-1}	1.56×10^{-1}
325	2.59×10^{-12}	1.71×10^{-11}	1.51×10^{-1}	1.51×10^{-1}
866	4.79×10^{-12}	3.24×10^{-11}	1.48×10^{-1}	1.48×10^{-1}

The average calibration factor is 133 mV.cGy^{-1} with a standard deviation of 44mV.cGy^{-1}. This is lower than other estimates based on irradiations in filtered

neutron beams in Petten (Chapter 11). The spread in these values is at least in part attributable to the large uncertainty in some of the measured forward bias voltage changes. A plot of the calibration factors showing estimated uncertainties is given in Figure 7-4.

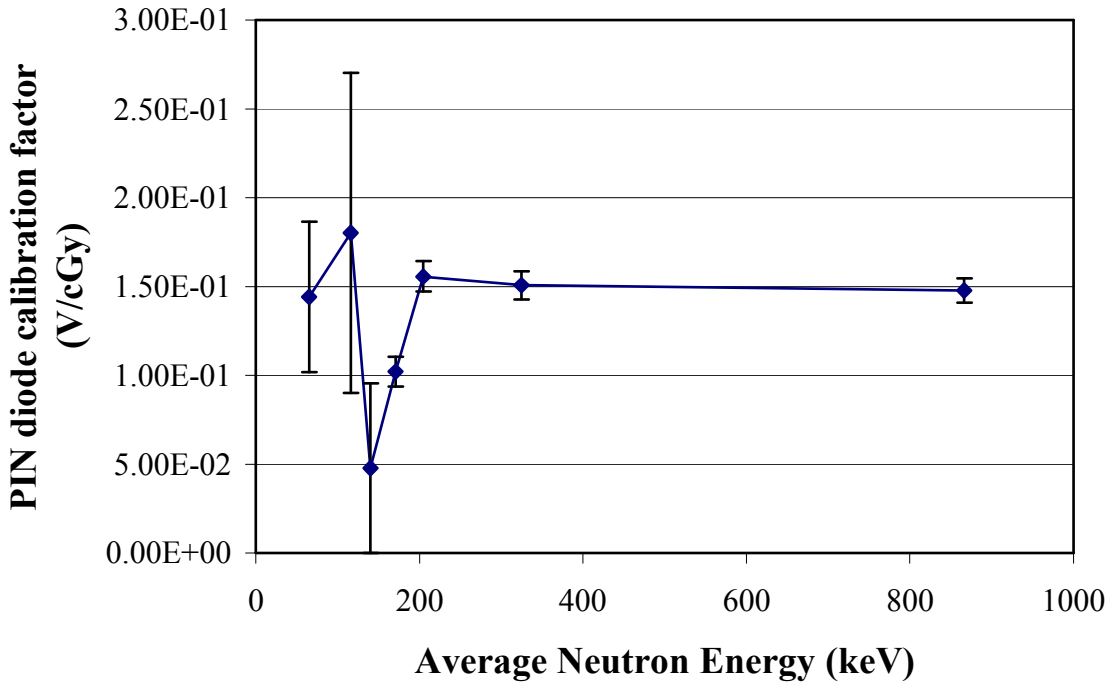

Figure 7-4. Uncertainties in PIN diode calibration factor. The error bars show the propagated uncertainty due to the readout uncertainty of the change in forward bias voltage only. The uncertainty in the absolute calibration due to the efficiency of the long counter is not included in these error bars.

CONCLUSIONS

Over the neutron energy range studied in this set of experiments (60 – 900 keV) the PIN diode response follows the silicon damage KERMA. This is clear qualitatively from Figure 7-3. The ratio of the threshold voltage change per unit flux to the KERMA (cGy per unit flux) has a standard deviation of 44 mV/cGy. Part of

this can probably be accounted for by the large uncertainties in some of the forward voltage measurements. The data points with large uncertainties are also associated with regions of the KERMA function where the KERMA is rapidly changing with respect to neutron energy. This makes the calibration factor very sensitive to the mean energy and the spread of energies present in the neutron beam used for the measurements. Unfortunately the precise thickness of the target was not able to be determined and hence nor can the exact spectrum of neutron energies be known. The target was nominally 50 keV thick with a probable uncertainty of at least ±10 keV. If the measurements with the greatest uncertainty due to these reasons are excluded the standard deviation in the calibration factors is approximately 5 mV/cGy. This is certainly adequate to show that the pin diode follows the silicon damage KERMA in its response to neutron irradiation. While this was expected it was still necessary to validate the behavior of the PIN diodes prior to using the published silicon damage KERMA function as the assumed PIN response in Monte Carlo calculations and other measurements. In order to obtain more precise values for the PIN diode neutron dose calibration factors a more accurately known and characterised neutron source is required. Apart from the ill defined neutron spectrum used here the absolute calibration of the long counter is inadequate to base the PIN diode calibrations on. The long counter calibration was based on an AmBe source of well known activity. However the assumptions implicit in extrapolating the efficiency of the long counter from an isotropic (or nearly isotropic) AmBe source to a significantly lower energy spectrum of non isotropic neutrons can not be quantified accurately enough to give a confident absolute calibration for the PIN diode. Not with standing this the relative calibration factors derived here are adequate to show that the PIN diode responds in a

similar way to silicon neutron damage KERMA.

CHAPTER 8 MOSFET MEASUREMENTS IN A 6MV MEDICAL LINAC BEAM

To characterise the MOSFET dosimeter response in a purely photon field experiments were conducted using the MOSFET dosimeters in a megavoltage x-ray beam. These measurements involved measuring the dose at various depths in tissue equivalent material exposed to x-ray beams from a Clinac 2100C medical linear accelerator. Depth dose curves were measured with the MOSFETs and compared with MCNP calculations and also depth dose curves measured with ionisation chambers. The measurement of doses in the steep dose gradients of the buildup regions was investigated. The angular dependence of the surface dose in a 6 MV beam was also measured with the MOSFET.

These investigations were subsequently extended by Butson, Carolan and Kron et al[165, 166, 184].

Measurements were also performed using the linear accelerator to determine the change in MOSFET sensitivity as a function of the bias applied to the gate electrode of the MOSFET.

A Pantak therapax superficial/orthovoltage therapy unit was used to determine the variation in MOSFET response as a function of photon energy.

MATERIALS AND METHODS

LINAC

The x-ray source used was a Varian Clinac 2100C linear accelerator located at the Illawarra Cancer Care Centre in Wollongong. The linac was operated at 6MV in the normal service mode at a dose rate of 200 monitor units per minute. The linac dose per monitor unit had previously been calibrated using a thimble ionisation chamber with a calibration factor traceable to the national standard. With this calibration the dose rate per monitor unit at a depth of 1.5 cm in the phantom when the surface of the phantom is located at a distance of 100 cm from the source (SSD=100 cm) is 1 cGy per monitor unit for a 10 cm × 10 cm square field.

For each irradiation of the MOSFETs at a different depth the Linac was set to deliver 10 monitor units. This corresponds to a dose of 10 cGy at a depth of 1.5 cm for a 10 cm × 10 cm square field.

MOSFETS

The MOSFETS used were the same devices used throughout this thesis (produced by INR, Ukraine).

Three sets of data were recorded. One with a MOSFET in its normal TO-18 packaging, one with the top lid of the kovar TO-18 package cut off and another with the kovar cap completely removed to leave the MOSFET device exposed (i.e. no encapsulation). This configuration allowed measurements in the buildup region of the

depth dose curve without interference from the MOSFET encapsulating material.

Measurements were performed with both MOSFETs simultaneously. A bias of 10 v was applied to the gate electrode of the MOSFET during the irradiations. The MOSFET threshold voltage was measured before and after each irradiation using the pulsed constant current source previously described. The threshold voltage was measured approximately 1–2 minutes following the completion of each irradiation.

PHANTOM

The measurements were conducted in a slab phantom consisting of multiple layers of RMI[185] Solid Water. The dimensions of the phantom were 30 cm × 30 cm square and 30 cm thick (along the beam axis). A 1 cm thick disc of solid water (approx 2.5 cm in diameter) was machined to allow two MOSFETS to be recessed into it. Two holes within 1 cm of the centre of this disc of solid water allowed the MOSFETS to fit into the solid water with minimal air spaces surrounding them. The MOSFETs were positioned with the device gate electrodes parallel to the surface of the phantom. The encapsulated MOSFET was located so that the top surface of the package was level with the surface of the solid water. The MOSFET with the encapsulation removed was located so that the MOSFET junction itself was within less than 0.5mm of the top surface of the solid water. The small circular Solid water plug assembly containing the two MOSFETS was then inserted into a 30 cm square slab of Solid Water. This slab with a small central circular recess was originally designed and used for holding an Attix ionisation chamber. A narrow channel (approx. 2 mm × 2mm) from the centre to the edge of the Solid Water slab allowed

fine cables to be connected for applying bias and reading out the MOSFETs. After the cables were soldered to the MOSFETS the whole assembly was put together and molten wax was used to fill any small remaining cavities surrounding the insert with the MOSFETS. When filling the air gaps with wax care was taken to leave the top surface of the unencapsulated and open topped MOSFETs exposed. A schematic view of the phantom assembly is shown in Figure 8-1.

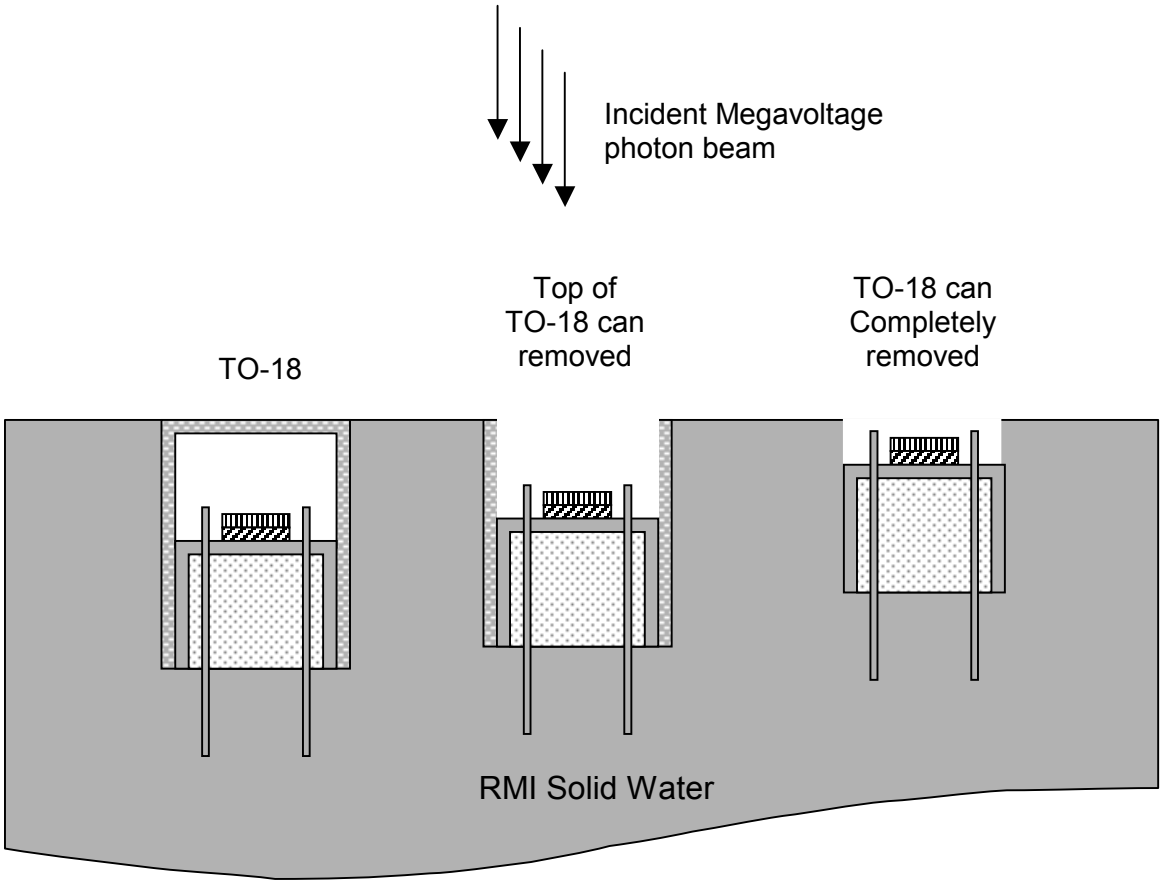

Figure 8-1. Configuration of MOSFET dosimeters with and without encapsulation removed from measurement of photon dose in 6MV linac beam. Not to scale.

In order to record the dose at various depths slabs of solid water were removed from the base of the phantom and added to the top of the phantom. This

maintained the SSD at 100 cm and gave dose measurements at points throughout the phantom.

In the superficial regions the depth of the MOSFETs was incremented by 1 mm steps. After a depth of 1.5 cm (approximately D_{max}) was reached measurements were made at depth increments of 20 mm.

MCNP MODEL OF THE PHANTOM.

The experimental arrangement was modeled using MCNP4A. The phantom was modeled as a 30 × 30 × 30 cm cube of ICRU 92 brain equivalent material. Impinging upon the top surface of this phantom was a 6 MV photon beam. Tallies of energy deposition along the central axis (which was also the central axis of the photon beam) of this phantom were made for comparison with the MOSFET and ionisation chamber measurements.

The model was relatively simplistic since it was not the intention to develop a detailed model of a Clinac 2100C photon beam. The aim was simply to establish that reasonable agreement could be obtained between the model, MOSFET and ionisation chamber dose measurements. The phantom model was a 30 cm cube of ICRU 92 brain equivalent material. The top layer was divided into 1 mm layers for the first 1 cm. From a depth of 1 cm to 2 cm the phantom was divided into 2 mm thick layers and beyond 2 cm into 1 cm thick layers. The tallies were calculated at depths defined by these layers and by other surfaces that defined a volume with a square cross section of 0.5 × 0.5 cm along the central axis. In a 10 × 10 cm field a tally volume of this size in the middle of the field should represent the dose recorded by dosimeters

smaller than this dimension along this axis.

The x-ray source was modeled as an isotropic point source. The energy distribution used was based on that given by Mohan [186] for a 6MV Clinac 2100C photon beam. The point source was located at a distance of 100 cm from the phantom surface. The 10 cm square field incident on the phantom surface was defined by "virtual" collimators set at a distance of 50 cm from the phantom surface. These collimators were simple void regions with photon and electron importances set to zero. In this way any particles entering the collimator cells were killed and did not contribute any further to the calculation. Clearly in this approximation no collimator or other "head" scatter is taken into account. No flattening filters were included in the model nor was any angular dependence of the energy spectrum. The empty space between the photon source and the phantom surface was left as a void, i.e. no air was included. These approximations may effect the calculated surface doses due to omission of air scatter and scattered x-rays generated in the head. However we do not expect these effects to contribute significantly to our measurements. The role of air scatter and surface dose was further investigated by this author with simulations and measurements in separate work that is described by Butson et al[187].

In order to accurately determine the energy deposited in the buildup region using 1 mm thick tally volumes along the beam central axis it was necessary to set the ESTEP parameter to 40 to ensure adequate electron transport sub-steps in each 1 mm thick tally volume[188]. In each tally volume a *f8 tally was used to calculate the total energy deposited by the electrons.

RESULTS

The known depth dose profile for a 10 cm square 6 MV beam incident on water as measured using diodes in a Scanditronix RSA water tank is shown in Figure 8-2. This curve constitutes the standard depth dose curve against which other measurements and calculations will be compared. It has been verified to coincide well with the depth dose curve as measured using a Farmer ionisation chamber for depths greater than D_{max}.

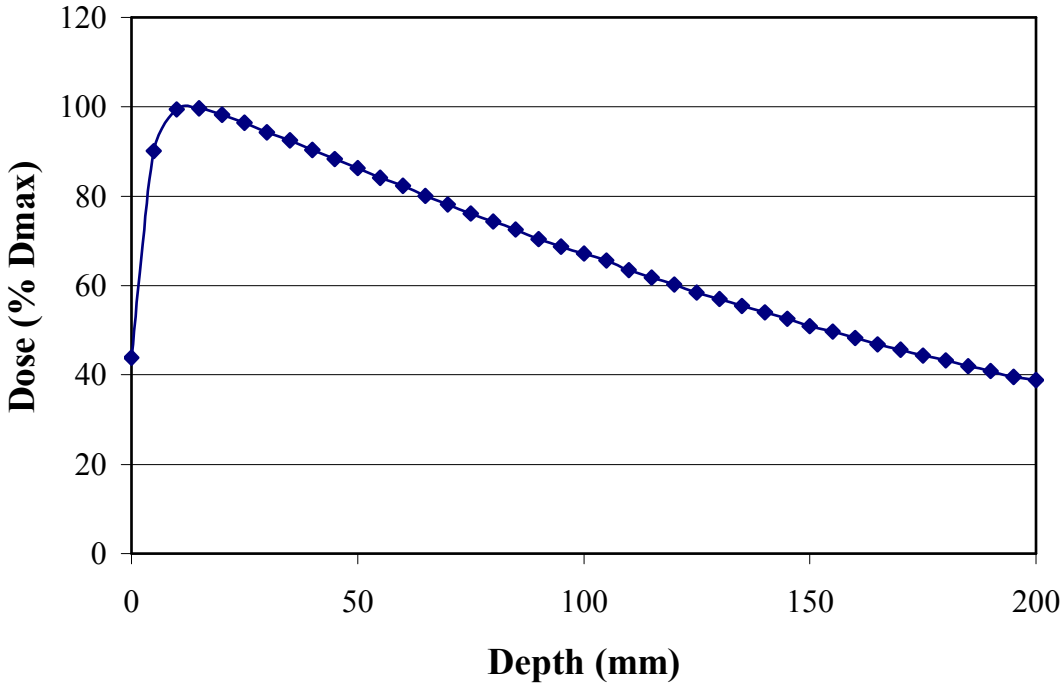

Figure 8-2 Depth dose curve measured in a 10 x 10 cm square field at an SSD of 100 cm for a 6MV photon beam from the Illawarra Cancer Care Centre Varian Clinac 2100C linear accelerator. Note the limited accuracy at depths <1.5 cm as described in the text below.

In order to compare and verify the MCNP model of the photon beam Figure 8-3 shows the same data (solid line) with the calculated MCNP data superimposed.

Except for the statistical errors in the tallies there are no large deviations from the curve measured with the diode for depths beyond D_{max} at approximately 1.5 cm depth. In the buildup region there is a discrepancy. The MCNP calculations predict a lower surface dose than is observed with the diode measurements. This is expected since the most superficial tally from the MCNP model is the average dose within the first 1 mm of the buildup curve. The dimensions and encapsulation of the Scanditronix diode are of the order of several millimetres. Therefore we cannot expect to measure the doses in this superficial region accurately with the diode. The MCNP model does not account for scattered radiation from the accelerator head. If this was included in the model slightly higher surface doses may be observed in the results of the simulation. Despite this we can expect that the MCNP model may give a more accurate estimate of the dose at the surface of the phantom.

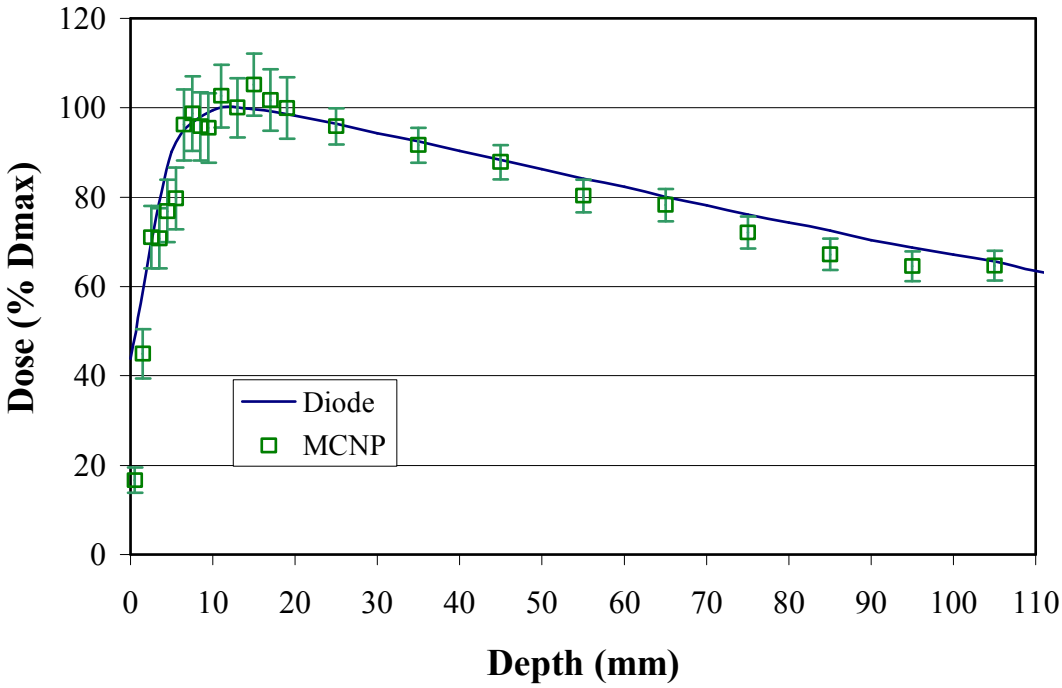

Figure 8-3. Buildup and depth dose curve as calculated using MCNP compared to the depth dose curve measured using a Scanditronix diode in a water tank.

When a fully encapsulated MOSFET is used to measure the depth dose curve in solid water a similar effect is seen in the buildup region. The effective Z and electron density of the kovar cap is significantly higher than the Z and electron density of tissue or water. Therefore a depth dose curve measured with the fully encapsulated (TO-18 packaged) MOSFET appears to move the buildup part of the curve towards the surface when compared with the MCNP calculated depth dose curve or even the diode depth dose curve. This is shown in Figure 8-4. The "surface dose" measured by the diode was 43.9 % of the maximum dose. The most superficial dose measured by the fully encapsulated MOSFET was 64.8% of D_{max}. These compare to a surface dose integrated over the first millimetre of the phantom predicted by MCNP to be 16.7% of D_{max}. However at depths beyond D_{max} where electron equilibrium exists there is reasonably good agreement between the diode and the encapsulated MOSFET. It should also be remembered that for this encapsulated MOSFET the silicon oxide layer was approx 2 - 3 mm below the surface level of the surrounding phantom.

The experimental error in the determination of the MOSFET threshold voltage was estimated to be approximately ± 2mV at the time of measurement. This was based on the fluctuations observed in the digital voltmeter readout used for the measurements and was thought to arise from the noisy electrical environment around the linac where the measurements were performed. More adequate shielding of cables on subsequent measurements enabled this variation to be reduced. A 2 mV uncertainty in measurements of threshold voltage propagates to give an overall uncertainty of approximately ± 4% of D_{max}. (The measured change in threshold voltage for this series of measurements was approximately 90 mV at D_{max}.) For

clarity these error bars are not shown in Figure 8-4 however they encompass the expected depth dose curve beyond D_{max} as measured by the diode.

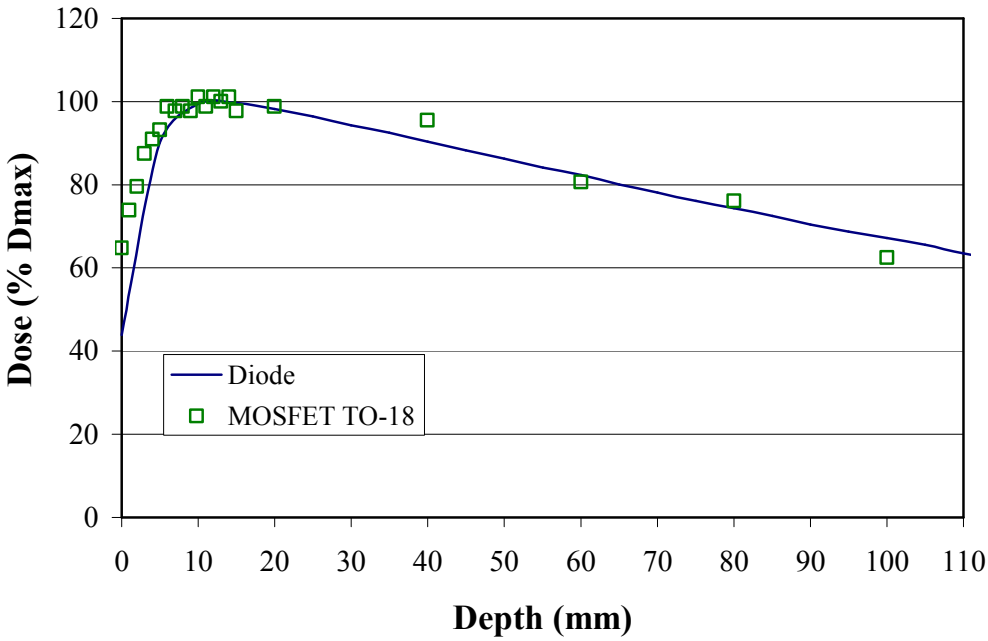

Figure 8-4. Depth dose curve in a 10 x 10 cm square 6 MV photon beam as measured using a MOSFET in TO-18 encapsulation and a Scaditronix diode.

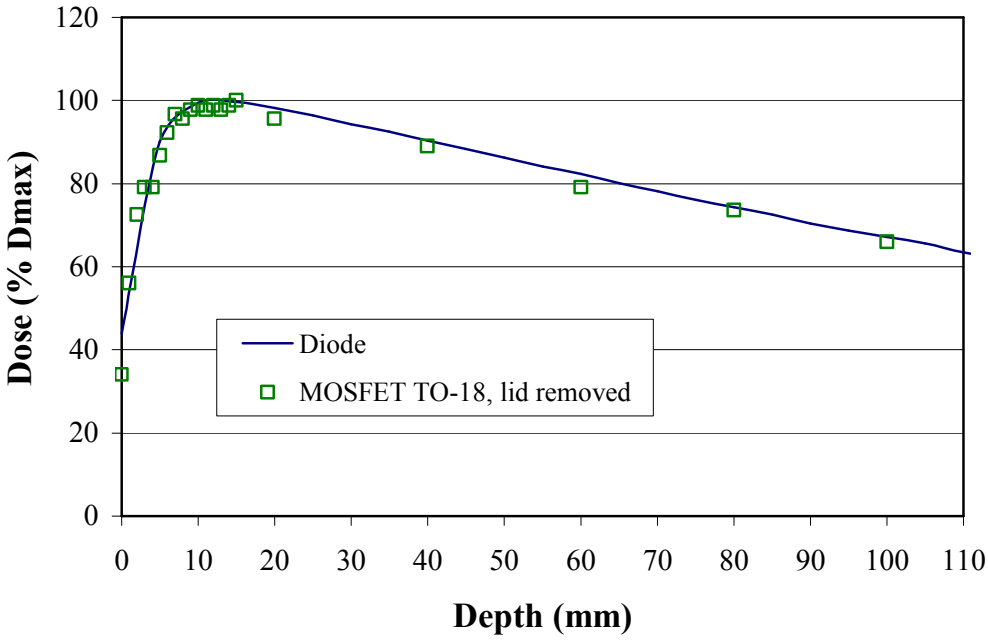

Figure 8-5. Comparison of 6MV, 10 x10 cm field depth dose curve measured using a MOSFET with the top surface of its lid removed and measured with diode.

When the lid of the MOSFET was removed in an attempt to eliminate the source of the extra buildup and therefore give a more faithful measurement of the tissue doses in the buildup region of the phantom a significant change was observed in the MOSFET measurement of surface dose. This yielded a surface dose of 34 % of D_{max} as opposed to 64.8 % for the intact MOSFET package. This is lower than the most superficial dose as measured by the diode but still in excess of the MCNP predicted dose for the 1 mm at the surface. It can be seen that much better agreement is also obtained between the depth dose curve for the MOSFET and the diode at depths beyond D_{max}. This is not due to the removal of the MOSFET lid but rather to improved accuracy of the threshold voltage readout achieved with shorter and better shielded cables.

Even with the lid removed, due to the remaining part of the MOSFET encapsulation it was not possible to position this MOSFET so that the junction was within less than 1 mm of the phantom surface level. That is the MOSFET was recessed into the solid water in such a way that the remaining portion of the packaging was flush with the phantom surface. This locates the actual junction approximately 3 mm below the surface of the phantom (although open from the front). In this arrangement photons can be scattered from the surrounding phantom and kovar onto the junction resulting in the effective depth of the junction being greater than what would be expected just from the air layer in front of it.

For another series of measurements with the MOSFET encapsulation fully removed it was possible to measure even lower surface doses as a proportion of D_{max}. In this case the MOSFET junction was located within less than a millimetre of the surface. The resulting depth dose curve can be seen in Figure 8-6. The measured

surface dose using the MOSFET in this arrangement was 16.1 % of the D_{max} which is approximately the same as the dose predicted by MCNP for the first 1mm of tissue (16.7%).

One method often used for determining superficial doses in megavoltage photon beams is to use thin entrance window ionisation chambers such as the Attix chamber. Superficial doses were measured in the solid water phantom with the same x-ray beam and field size using an Attix chamber.

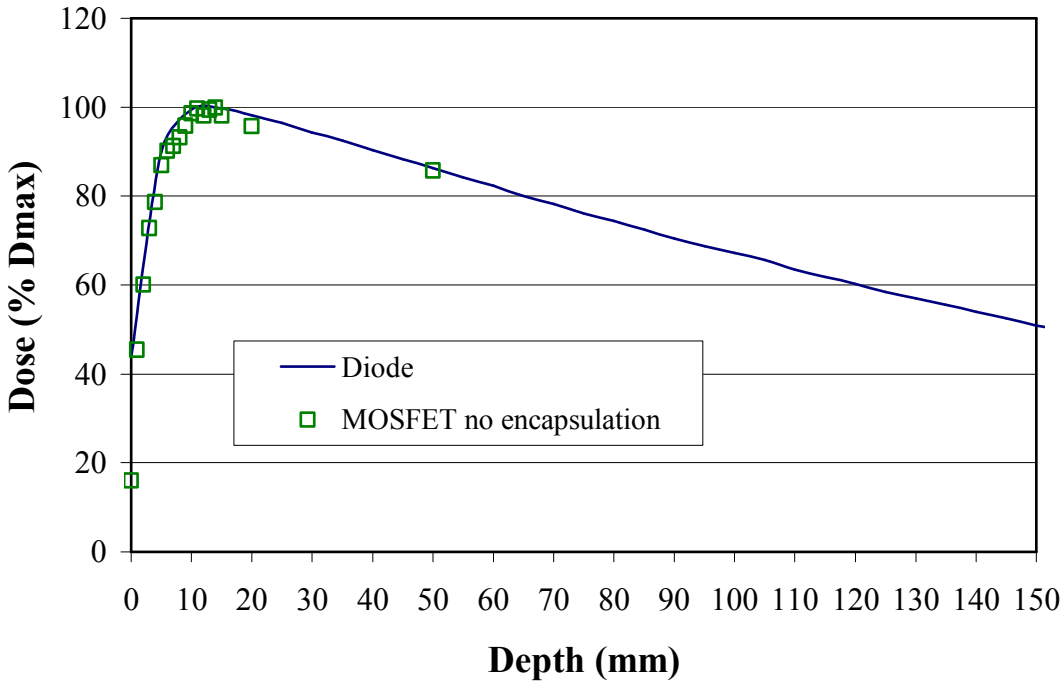

Figure 8-6. MOSFET measurements of dose in first 5 cm of solid water phantom exposed to 10 x 10 cm field from a 6 MV photon beam.

These Attix chamber measurements are compared to two sets of unencapsulated MOSFET depth dose data in the surface / buildup region which is shown in Figure 8-7. Clearly very good agreement is obtained for these two methods.

To directly compare the MOSFET dose measurements in the buildup region and the MCNP calculations for the same depth both of these sets of results are

plotted along with the Attix chamber measurements in Figure 8-8. It should be noted that for each 1 mm thick MCNP tally cell in the first 1 cm of the phantom the corresponding data point is plotted at the average depth of the volume. (E.g.. The data point for the tally volume extending from 0mm to 1mm deep is plotted at 0.5 mm in Figure 8-8.)

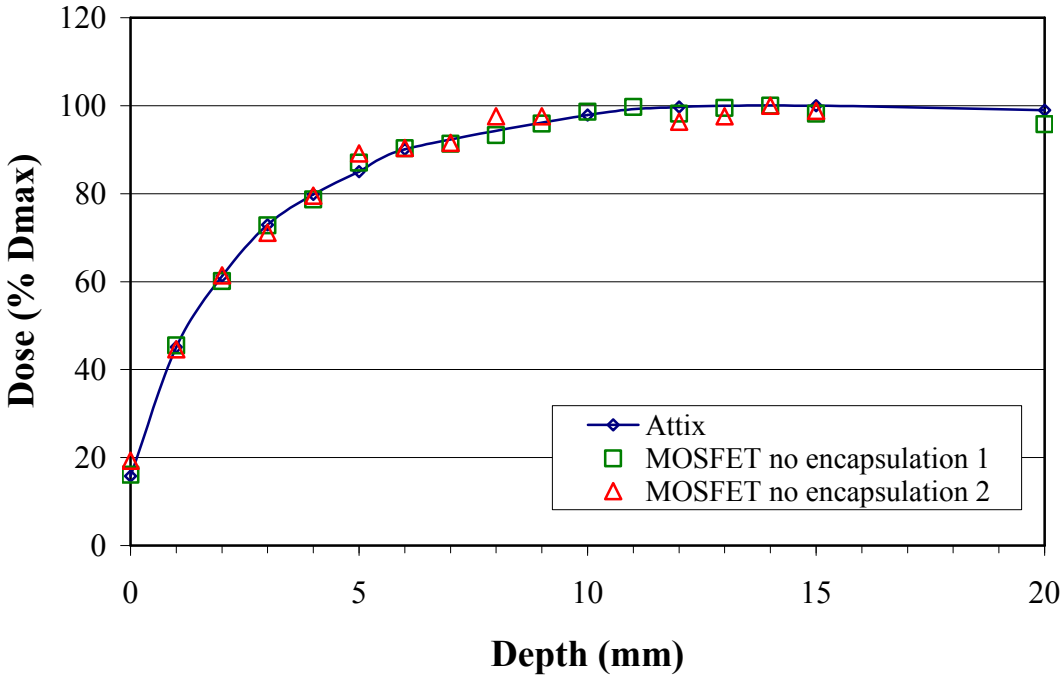

Figure 8-7. Dose in buildup region of 6 MV photon beam as measured by Attix ionisation chamber and a two MOSFETs with encapsulation removed.

The data points for the Attix chamber and the MOSFET are plotted at depths corresponding approximately to the front surface of the detector. This may account for the slight discrepancy between the MCNP results and the measured data. However allowing for the statistical uncertainty in the MCNP results reasonably good agreement is seen even in this region of steep dose gradient.

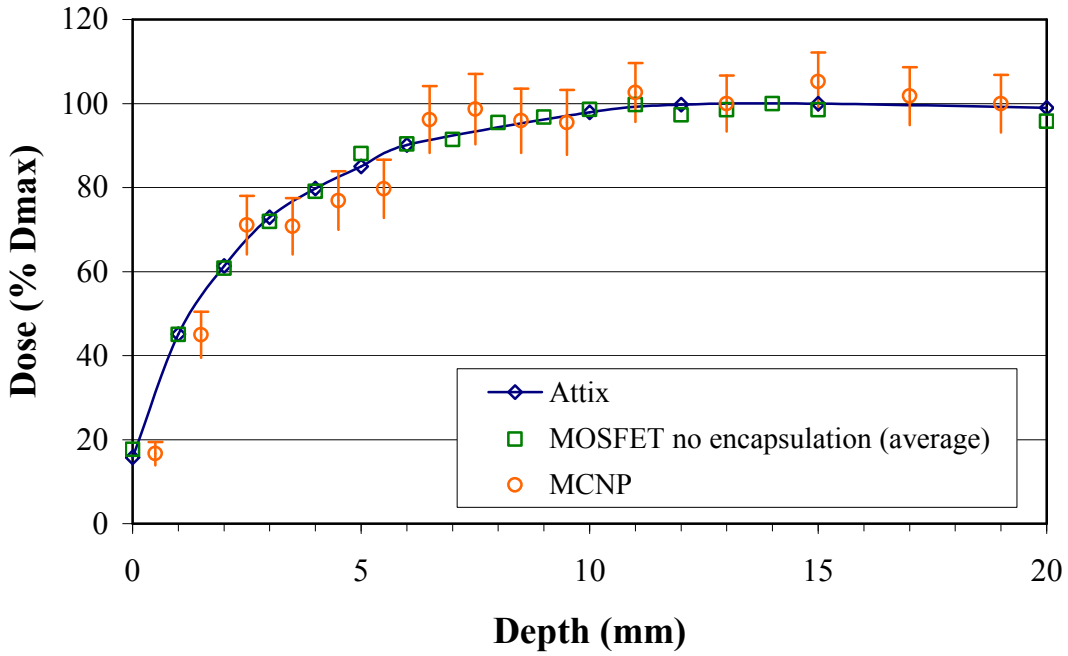

Figure 8-8. A comparison on Attix chamber, MOSFET and MCNP Monte Carlo calculated doses in the buildup region of a 10 x 10 cm square 6 MV photon beam incident on a solid water phantom.

ANGULAR RESPONSE OF MOSFET MEASURED SURFACE DOSE

Whilst characterising the MOSFET in the 6 MV x-ray beam some additional data was collected with the MOSFET on the surface of the solid water phantom but with different incident beam angles, Figure 8-9. All other parameters were the same as for the measurements above. Measurements of the surface dose[a] as a function of incident beam angle using an Attix chamber with the same phantom and linear accelerator are also shown for comparison. The Attix chamber measurements significantly exceed the MOSFET measurements for incident beam angles greater

[a] Attix chamber measurements made by M Butson and M Perez, Illawarra Cancer Care Centre, Oct 1994.

than about 40°. Due to its design this is unlikely to be due to scattering contributions from the wall of the Attix chamber. The much smaller thickness of the MOSFET junction and essential lack of a "wall" in its unencapsulated form lead to less contribution from scatter originating at the sides of the MOSFET.

It should be noted that the angular dependence of the dose measurements shown in Figure 8-9 represent the dependence of dose at the surface of a phantom exposed to a megavoltage x-ray beam. The angular dependence shown does not represent the intrinsic angular response of the MOSFET itself.

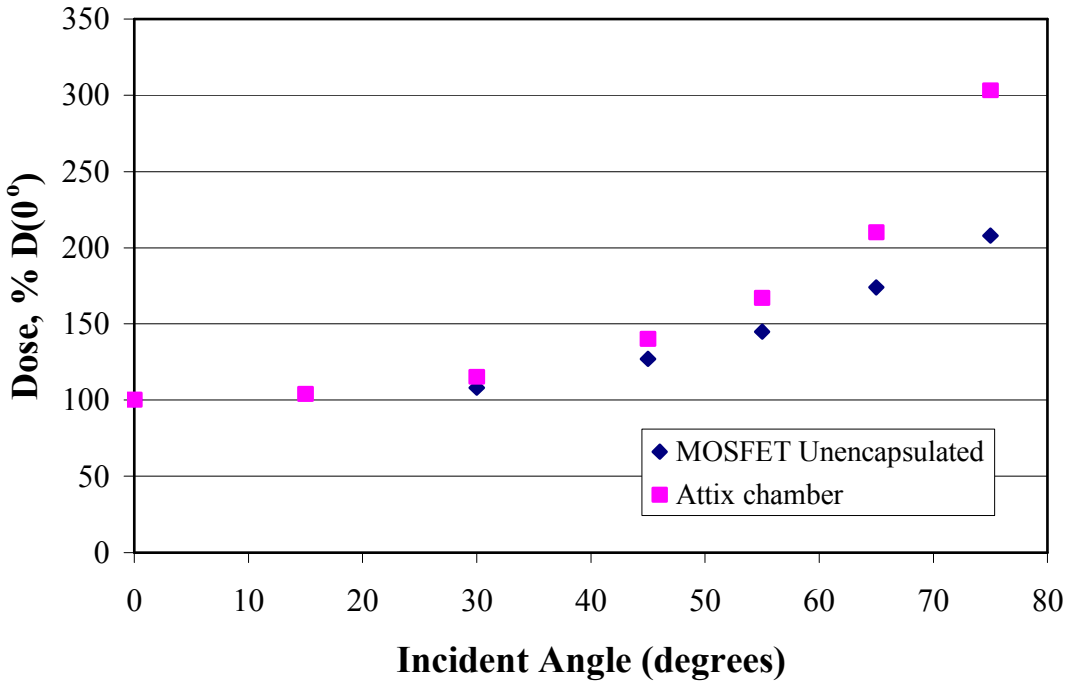

Figure 8-9. Surface dose measured in a 6 MV beam, field size 10 x 10 cm, using an unencapsulated MOSFET and an Attix ionisation chamber.

MOSFET SENSITIVITY AS A FUNCTION OF GATE BIAS

The sensitivity of the TO-18 packaged and the unencapsulated MOSFETs

was measured with different gate bias voltages applied during the irradiations. Using the same phantom and 10 x 10 cm square 6 MV x-ray beam the MOSFET dosimeter was located at a depth of 1.5 cm from the surface of the phantom on the central axis of the normally incident photon beam. During the irradiations biases of 0, 5, 10 and 15 volts (± 0.05 V) from a stabilised DC power supply were applied to the gate electrode of the MOSFETs. Ten monitor units of 6MV beam were delivered to the MOSFETs at each applied bias with the threshold voltage of the MOSFETs being readout between each irradiation.

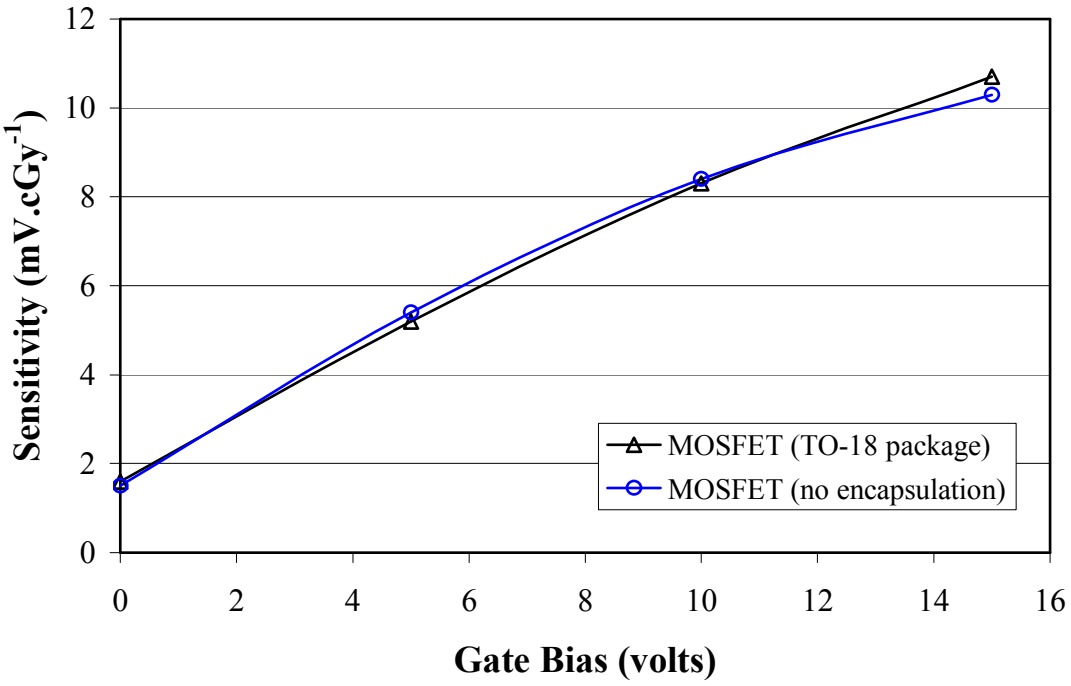

Figure 8-10. Sensitivity of two MOSFETs as a function of applied gate bias during irradiation. Measurements made at 1.5 cm depth in solid water phantom. Therefore sensitivity is not package dependant.

At a depth of 1.5 cm and an SSD of 100 cm for a field size of 10 x 10 cm ten monitor units corresponds to a 10 cGy dose to the MOSFETs for each measurement.

The sensitivities of these MOSFETs as a function of gate bias can be seen in

Figure 8-10. A second order polynomial curve was found to fit this data very well (r^2=0.999). The fitted sensitivity curve was:

$$\text{Sensitivity (mV/cGy)} = -0.012\ V_g^2 + 0.788\ V_g + 1.59$$

Where V_g is the bias applied to the gate during irradiations and the sensitivity is the change in threshold voltage observed per cGy.

PHOTON ENERGY RESPONSE.

In addition to the measurement of the depth dose curve measurements performed using MOSFETs on the 6 MV linear accelerator x-ray beam some further measurements were performed aimed at further characterising the MOSFET response to photons of different energies. Although the main gamma dose contribution anticipated in BNCT applications will arise from photons with MeV energies it is possible that lower energy photons from neutron activation of detector or phantom materials may also contribute. Therefore any variation in response for lower energy photons should be characterised (e.g. dose enhancement).

METHODS

These measurements were performed using a Pantak Therapax 300 Superficial /Orthovoltage treatment unit. The accelerating potential of the Pantak can be varied from 50 kVp up to 300 kVp. The MOSFETS were irradiated with x-rays of

50kV, 75kV, 100kV, 125kV, 150kV, 200kV and 250kV which are the standard potentials used for treatment on the Pantak at the Illawarra Cancer Care Centre. The 5 cm diameter applicator with a FSD of 30 cm was used for the irradiations. To determine the x-ray dose in the middle of the field for each potential a field factor and monitor unit calibration factor is applied. Between 10 and 15 monitor units were applied to the MOSFETs at each potential and the appropriate factors for each different x-ray energy were then applied. The monitor unit calibration factor varies with beam potential. The MOSFETs were irradiated mounted on a thin perspex rod to minimise any backscatter contributions. They were located at an FSD of 30 cm in the middle of the field (beam axis).

The measurements were repeated for both a TO-18 packaged MOSFET and also for a MOSFET with the encapsulation removed. During irradiation the MOSFETs had a bias of 5.422 volts applied to the gate electrode. According to the relationship given in the previous section this would correspond to a sensitivity of 5.5 mV/cGy in a 6MV photon beam.

RESULTS

The results of these measurements are shown in Figure 8-11. Measurements in air such as these show a difference in response between the TO-18 packaged MOSFET and the unencapsulated MOSFET because the extra thickness of kovar around the TO-18 MOSFET generates extra scattered electrons which interact with the MOSFET junction. This is not the case for the unencapsulated MOSFET. However the unencapsulated MOSFET does show some increased response at low photon energies. The TO-18 MOSFET response drops off for incident beam energies below ~125 kVp. This is due to filtering through the kovar encapsulation.

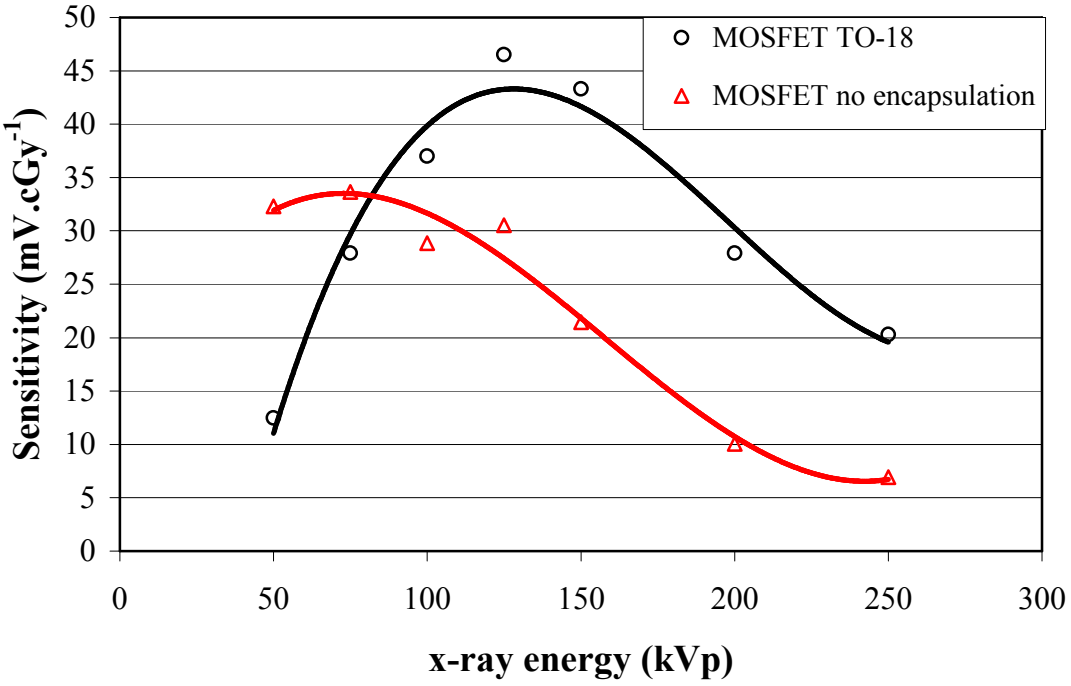

Figure 8-11. Measured energy response of MOSFETs to low energy x-rays.

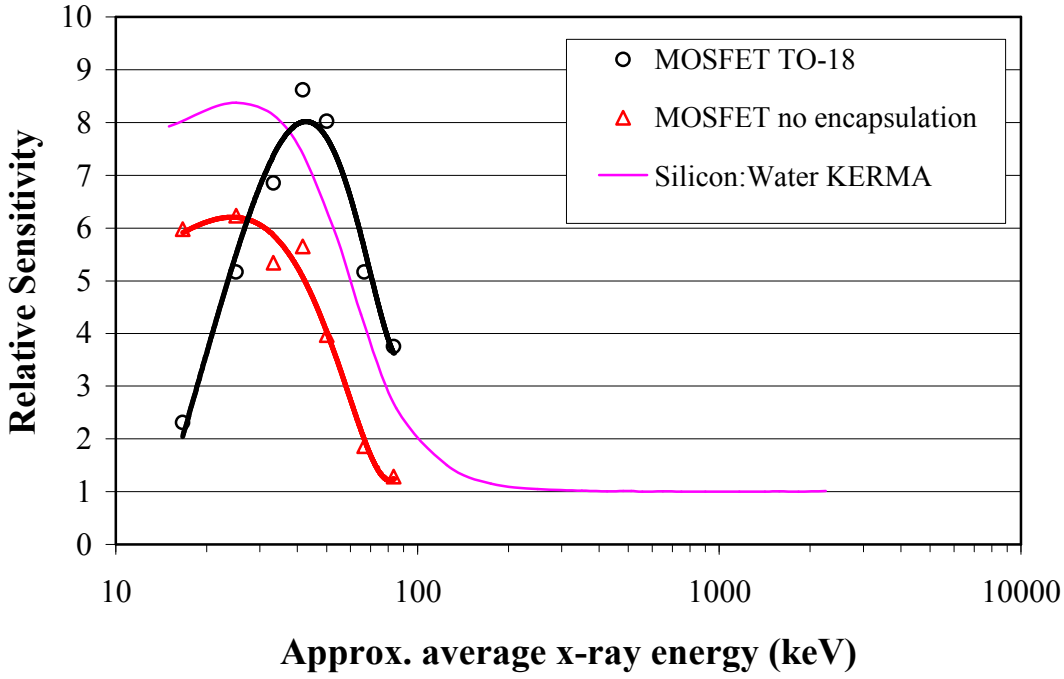

Figure 8-12. MOSFET sensitivity at low energies relative to 6MV response. Also shown is the ratio of silicon photon KERMA to water photon KERMA (from endfb-v data).

The enhancement of response for both of these MOSFETs at low energy is due to the difference in silicon or silicon oxide photon KERMA and tissue KERMA. Note that the units of sensitivity in Figure 8-11 are mV/cGy of tissue dose since the calibration factors for exposures with the Pantak unit are always in terms of tissue dose.

If the same sensitivity data is normalised to unity for the 6 MV response per cGy we have a normalised plot of the dose enhancement as a function of energy. This is shown in Figure 8-12.

The energy of the response data in Figure 8-12 is expressed as the average effective photon energy of the beams from the Pantak Therapax 300. The effective energy is approximately 1/3 of the peak accelerating potential (kVp)[a]. Also shown for comparison is a plot of the ratio of silicon photon KERMA to water photon kerma over the same energy range and normalised to unity at 2 MeV. This curve has the same form as the response of the unencapsulated MOSFET and does not drop off at very low energies like the encapsulated MOSFET response curve. A full Monte Carlo model of the MOSFET and its encapsulation in photon fields of different energies may be expected to demonstrate this fall off at very low energies and to fit the experimental data better.

CONCLUSIONS

The accurately calibrated and well measured depth dose profiles of a medical linear accelerator provide an excellent opportunity for characterising the response of

[a] Copper half value layers (HVL) for the Pantak beams used were: 50kV:0.055mm, 75kV:0.09mm, 100kV:0.15mm, 125kV:0.35mm, 150kV:0.7mm, 200kV:1.5mm, 250kV:2.3mm, 300kV:3.9mm.

the MOSFETs in pure photon fields without interference from any neutron effects.

Using a Varian linear accelerator it was possible to demonstrate a good agreement between MOSFET measurements of the depth dose profile in a solid water phantom. Variations from the known dose as measured using commercial dosimetry diode detectors and ionisation chambers were less than 4% at depths greater than D_{max}. For measuring doses in buildup regions the MOSFET encapsulation was found to cause an over response in the first several mm of a 6 MV beam. By removing the kovar cap and using the MOSFET with the junction exposed a excellent agreement was found with other techniques for the dose in the buildup region.

These measurement also served as a simple test of the MCNP modelling of photon doses in phantoms. A simple MCNP simulation of the 6MV photon beam incident on the phantom showed good agreement with doses measured using the MOSFET at depth in the phantom and with slightly worse agreement in superficial layers of the phantom. The discrepancies at superficial depths result primarily from simple nature of the geometry modeled (i.e. the lack of a detailed model of the accelerator head). However concordance achieved between the MCNP model and the MOSFET measurements in the pure photon field give confidence that similar agreement should be possible for the photon component of a BNCT beam.

A simple empirical relationship between the gate bias voltage and the dose response of the MOSFETs used was determined in the 6 MV linac beam. The measured sensitivity of the Ukrainian MOSFETs used ranged from approximately 1.6 $mV.cGy^{-1}$ to 10.5 $mV.cGy^{-1}$ for gate bias voltages between 0 volts and 15 volts respectively. The sensitivity as a function of gate bias could be fitted well with a simple second order polynomial.

An orthovoltage radiotherapy beam was used to measure the low energy response of the MOSFET. An over response of approximately 8 times relative to the 6 MV beam response was observed for x-ray beams with average energies of approximately 40 - 50 keV. However the filter effect of the kovar lid then sharply reduces this over response to a factor of 2 for energies of approximately 20 keV. The overall shape of the low energy response curve matches fairly well the ratio of silicon photon KERMA to water photon KERMA. It was possible to reduce the over response by removing the MOSFET encapsulation. In this case an over response of approximately 6 times (relative to 6 MV) was observed at average photon energies around 20 - 30 keV. To further reduce the over response at low energies a completely different type of encapsulation (low Z) would be required. Beyond that over response due to the silicon itself and to the dose enhancement effects of electrode materials on the actual MOSFET chip may still arise. For pure photon fields further minimisation of this over response may be achievable using filters optimised using Monte Carlo simulations. However for BNCT applications this would probably be at the expense of increased the neutron response and so was not pursued as part of this thesis. As previously noted the average energy of photons encountered in BNCT related measurements is expected to be more comparable to those in 6 MV beams. However the low energy responses measured in this chapter would allow corrections to be made for sub 100 - 200 keV photons if necessary.

CHAPTER 9 MOSFET AND PIN DIODE MEASUREMENTS IN THE MOATA REACTOR THERMAL NEUTRON FACILITY

The MOATA reactor was a 100kW water moderated and cooled reactor with a graphite reflector. The fuel elements were 80% enriched ^{235}U. MOATA was primarily used for neutron radiography and biological experiments. The neutron irradiation facility used in all of the work described here was a horizontal thermal column designated TC-10 which has previously been described by Allen et al[189]. The beam is heavily moderated and filtered to provide a thermal neutron field with only a small amount of epithermal neutron contamination and a low gamma dose rate. The gamma shielding is in the form of bismuth and lead. The moderator and coolant is light water with a graphite reflector surrounding the core. The thermal flux in the TC-10 irradiation column is approximately 10^{10} $n.cm^{-2}.s^{-1}$ as measured by gold foil activation. The gold activation foil cadmium ratio is 38. The higher energy component of the neutron field is therefore not great but is not well characterised. It is assumed to have the form of a slowing down spectrum. The gamma dose rate as measured by a combination of TLDs and ionisation chambers is approximately 4.8 $Gy.hr^{-1}$.

The biological irradiations performed in the thermal neutron beam include in vitro and in vivo experiments which have been described previously [190], [191].

In the work described in this chapter both PIN diodes and MOSFET

dosimeters were irradiated in the MOATA thermal neutron beam in order to determine their thermal neutron response. MOSFETs and PIN diodes were irradiated with and without thermal neutron shields to separate any thermal neutron response from epithermal neutron or gamma responses. The response of the PIN diode to thermal neutrons and also to the epithermal part of the spectrum in TC-10 is compared. The MOSFET thermal neutron response is determined. The gamma dose rate in TC-10 was measured using the MOSFET detectors with three different gate potentials applied (i.e. at three different sensitivities). The thermal neutron sensitivity is also determined at three different gate potentials.

PIN

The PIN diode response has been measured in epithermal neutron fields using accelerator produced neutrons (Chapter 7). In these measurements the PIN response was found to have an energy dependence corresponding to published silicon damage KERMA data in the literature to within experimental uncertainty. The series of experiments described here aim to approximately determine the thermal neutron response of the PIN diode. This will verify that the PIN forward bias voltage responds in an energy dependent way which matches the known silicon damage KERMA for thermal neutrons.

The TC-10 neutron field is highly moderated and has a gold activation foil cadmium ratio of 38. The MOATA TC-10 beam is known to have a small (~0.8%) epithermal neutron flux component. Any measurements aimed at determining the PIN diode response to thermal neutrons must therefore correct for contributions from non thermal neutrons. Due to the shape of the silicon response function even a

relatively low fluence of non thermal neutrons could obscure the forward bias voltage shift due to thermal neutrons alone.

To allow the effect of non thermal neutron response during the irrradiations using the TC-10 facility to be detected and compensated for the PIN diode was irradiated in both the "bare" beam and also encapsulated in several different thermal neutron attenuating shields. These shields included 1 mm cadmium, epoxy/LiF pots and polymethylmethacrylate vials full of ^{6}LiF powder with the PIN diode embedded in the centre. During the irradiations gold activation foils were used to monitor the flux both inside the shield adjacent to the PIN diode and also in the free beam away from the Cd and Li attenuators.

METHOD

A diagram of the TC10 thermal facility is shown in Figure 9-1. During irradiations the PIN diodes were located on a PMMA rack that was inserted into the channel by means of a pair of long handled tongs. The PMMA rack was positioned reproducibly by pushing it to the far end of the channel. There was no freedom of movement in the lateral or vertical planes when the PMMA rack was inserted into the thermal column channel. The steel and lead plug which seals and shields the TC10 thermal column during reactor operation was manually rolled into position after the PIN diodes (or other samples) had been inserted and before the reactor power was raised. For safety reasons this plug was part of an opto-electronic scram trigger circuit to prevent the thermal column being opened while the reactor was at any power above 20 watts.

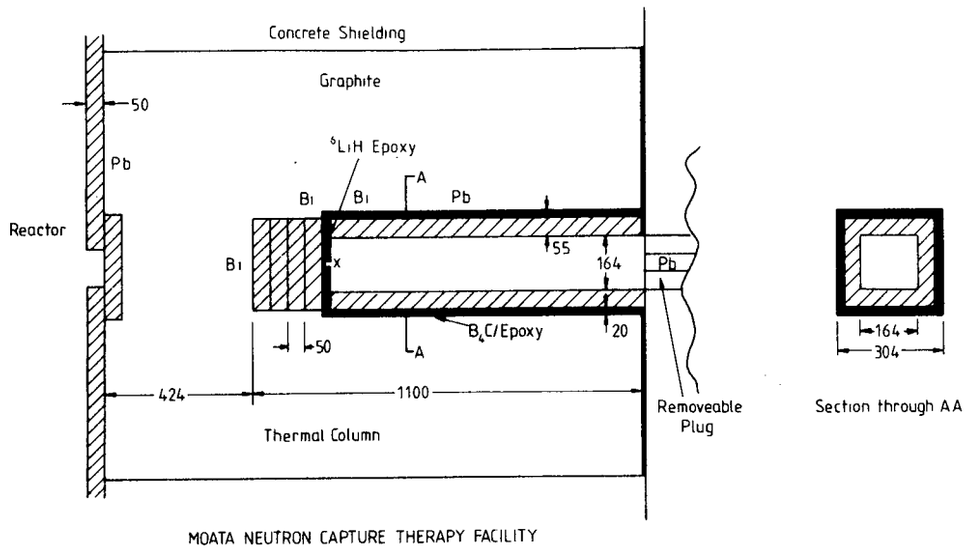

Figure 9-1. Diagram of the TC 10 thermal beam on MAOTA. (Diagram from Allen et al[189]).

Once the PIN diodes were inserted and the shielding plug was in place the MOATA reactor could be raised to full power (100 kW) in approximately 4 – 5 minutes following normal operating procedures. The standard procedure specifies a power increase of 1.7 decades per minute. After the desired amount of time at full power operation a shim rod scram was executed to reduce the power to less than 20 watts allowing the samples to be accessed. The reduction to 20 watts and removal of the irradiated samples usually takes approximately 5-10 minutes following standard operating procedures. The fluxes in the TC10 thermal column during the periods of increasing and decreasing power were assumed to be equivalent to 1 minute at full power based on the power versus time curves for the reactor.

The PIN diode irradiations were performed in a number of separate reactor runs. The same procedure was followed in each case. The PIN diode forward bias voltage and the temperature were measured and recorded. Gold foils of known weight and thickness were then attached to the PIN diodes using adhesive tape. The

PIN diodes were then placed on the PMMA rack. The PIN diodes to be irradiated bare were attached to the rack with adhesive tape. The cadmium covered PIN diode was wrapped in a single layer of 1mm Cd sheet. The edges of this cadmium envelope were overlapped to prevent thermal neutron leakage. The cadmium wrapped PIN diode was attached to the rack with adhesive tape and irradiated separately from all other samples to ensure that the cadmium did not introduce any thermal flux depression which could interfere with other measurements. In the case of the PIN diodes encapsulated in lithium fluoride powder small polycarbonate sample vials (3.5cm diameter, 8cm length) were half filled with the powder, the PIN diodes with gold foils attached were placed in the centre of the vials and more lithium fluoride powder added to fill the vials. The lid was then securely attached and the vial and its contents placed on the PMMA rack and secured with adhesive tape. As for the case of the cadmium covered PIN diodes, the lithium shielded diodes were each irradiated in separate reactor runs to avoid any possible interference with other samples.

The PIN diodes were irradiated in the TC 10 thermal column for a period of 4 minutes at full power. When the contribution of flux during the raising and lowering of power is taken into account this amounts to 5 minutes of full power equivalent irradiation. When the reactor power was reduced to less than 20 watts the TC10 plug was removed and the samples recovered. The PIN diode forward bias was measured and the gold activation foils placed in shielded vials for counting at a latter date.

The activity of the gold foils was determined by counting in a NaI well counter with an efficiency calibration traceable to the national standard. The NaI well crystal was attached to a Canberra multi-channel analyser system. Sufficient counts were accumulated to reduce the statistical uncertainty in the activity to less than 1 %.

The counting dead time was always less than 2%.

The cadmium ratio in the TC-10 channel has been measured with gold foils to be 38. If the spectrum is assumed to consist of a thermal component and a small slowing down component of epithermal neutrons then an estimate can be made of the epithermal flux. (See Appendix E for details.) Assuming a well moderated thermal spectrum with a small slowing down component and using gold foil measurements of the cadmium ratio and the thermal flux gives an estimated epithermal flux of 8×10^{-3} ϕ_o. Where ϕ_o is the thermal flux at the TC-10 irradiation point.

RESULTS

The results for the PIN diodes irradiated in TC 10 are summarised in Table 9-1.

Table 9-1. PIN diode forward bias voltage change in TC-10.

Effective Irradiation time (min)	**Unattenuated thermal fluence (average) n.cm^{-2}**	**Δ V (mV)**	**Estimated epithermal fluence (average) n.cm^{-2}**	**Encapsulation**
5	$3.45\text{x}10^{12}$	59.1	$2.81\text{x}10^{10}$	Bare
5	$3.45\text{x}10^{12}$	46.5	$2.81\text{x}10^{10}$	LiF
5	$3.45\text{x}10^{12}$	45.3	$2.81\text{x}10^{10}$	LiF
5	$3.45\text{x}10^{12}$	42	$2.81\text{x}10^{10}$	LiF
5	$3.45\text{x}10^{12}$	45	$2.81\text{x}10^{10}$	LiF
5	$3.45\text{x}10^{12}$	47.5	$2.81\text{x}10^{10}$	Cd

There is an average of 13.84 mV difference between the shielded and the unshielded PIN diodes. This voltage difference is therefore due to the thermal component of the flux in the TC 10 facility. Assuming negligible attenuation of epithermal neutrons by the Li and Cd shields the remainder of the forward bias voltage change (~ 45.26 mV) must be due to the epithermal component of the TC-10 flux. These measurements result in a PIN diode response for the TC-10 thermal neutron spectrum of 4.01×10^{-12} mV/n.cm^{-2}. If the effective energy of the thermal neutron beam is considered to correspond to the peak thermal flux at 0.025 eV, the known silicon damage KERMA at this energy is 3.3×10^{-14} cGy/n.cm^{2}. This would yield a PIN diode silicon dose response factor of 121.5 mV/cGy (Silicon Damage). This factor is less than what has been measured in other experiments. For example the calibration factor derived from the Van de Graff accelerator measurements was 133 ± 44 mV.cGy^{-1}. The same factor derived from measurements on the well characterised HB11 beam of the Petten HFR is ~ 190 – 200 mV.cGy^{-1}. However the assumption of an effective energy of 0.025 eV is only an approximation since the experimental arrangement in these measurements used cadmium and lithium as the thermal neutron attenuating materials. Therefore the difference in the shielded and bare PIN diode responses will depend on the cadmium cutoff and the ^{6}Li "cutoff" energies. In other words the difference between the spectrum for the unshielded measurements and the spectrum for the shielded measurements will not be a true Maxwellian thermal distribution, only an approximation. The silicon neutron KERMA function also changes significantly over this energy range (ie 0.025 eV ~ 0.5 eV).

Therefore the effective energy of the thermal fluence (silicon damage

KERMA weighted) is greater than the energy of the peak thermal fluence. A calibration factor of 190 mV.cGy^{-1} would give a silicon damage kerma dose of 0.0728 cGy for the 13.84 mV change in forward bias voltage observed in these measurements. In this case if the thermal fluence is taken to be as measured at 3.45×10^{12} n.cm^{-2} then the silicon damage KERMA factor would be 2.11×10^{-14} cGy.n.cm^{-2}, which corresponds to an effective energy of 0.065 eV.

The epithermal flux component of the TC-10 beam is estimated to be $0.00816\phi_o$ which is 2.82×10^{10} n.cm^{-2}. The forward bias voltage change for the shielded PIN diode measurements is 45.26 mV. If the calibration factor derived using the thermal part of the beam is used (i.e. 121.5 mV/cGy) then this voltage change corresponds to 0.373 cGy of silicon damage dose. The KERMA factor becomes 1.32×10^{-11} cGy/n.cm^2 which corresponds to a silicon damage weighted effective energy of ~ 55 keV.

DISCUSSION

From these data it is not possible to confirm that the PIN diodes respond to thermal neutrons as described by the published ASTM silicon damage kerma data. However the results of these measurements are consistent with that data. The forward bias change per cGy calibration factor derived assuming an effective energy of 0.025 eV for the flux measured by gold foils is also in agreement with other measurements of the calibration factor to within experimental uncertainties. A numerical integration of the silicon damage kerma data convolved with a Maxwellian flux distribution may provide a more precise match between the measured voltage changes and the known

damage kerma data. However since this would be an integral over sub cadmium cutoff energies it would not be a sensitive way to show agreement with the exact form of the KERMA curve. A much more accurate knowledge of the neutron spectrum in the now decommissioned MOATA TC-10 facility would be required to draw more accurate conclusions about the PIN diode response function.

MOSFET PASSIVE MODE MEASUREMENTS

MOSFET thermal neutron irradiations were performed simultaneously with the PIN diode irradiations described above. The SiO_2 layer in a MOSFET is known to have a minimal intrinsic sensitivity to fast neutrons however the kovar encapsulation of the MOSFETs used is expected to contribute to some neutron sensitivity especially at lower neutron energies.

The MOSFET threshold voltage was measured immediately prior to attaching the MOSFET to the PMMA rack used to hold the PIN diodes and MOSFETS in the TC-10 column.

RESULTS

The threshold voltage changes observed for each exposure in the TC-10 facility is shown in Table 9-2. The thermal flux quoted is as measured using gold activation foils. The data for the single MOSFET irradiated for 11 minutes was scaled by a factor of 2.2 to normalise this measurement to a 5 minute total irradiation time. The total flux is an estimate of the flux that the MOSFET was exposed to either

bare or inside the LiF shielding. This was estimated for the bare MOSFET case as being equivalent to the thermal fluence as measured by gold foils, and for the shielded MOSFETs it was estimated to be the epithermal component of the beam. That is approximately $0.00816\phi_o$ as derived above for the case of the PIN diodes.

Table 9-2. Measured MOSFET response to thermal neutron irradiation in MOATA TC10 facility.

Irradiation time (min)	Thermal flux	Threshold voltage change (mV)	Total flux	Configuration
11	1.06×10^{13}	1326	1.06×10^{13}	Bare
5	3.45×10^{12}	424	3.45×10^{12}	Bare
5	3.45×10^{12}	54.1	2.82×10^{10}	LiF
5	3.45×10^{12}	63.2	2.82×10^{10}	LiF
5	3.45×10^{12}	51	2.82×10^{10}	LiF
5	3.45×10^{12}	53	2.82×10^{10}	LiF

These data are shown in Figure 9-2 along with a fitted curve showing a threshold voltage change of 50.9 mV for a 5 minute irradiation when the neutron fluence is extrapolated to zero.

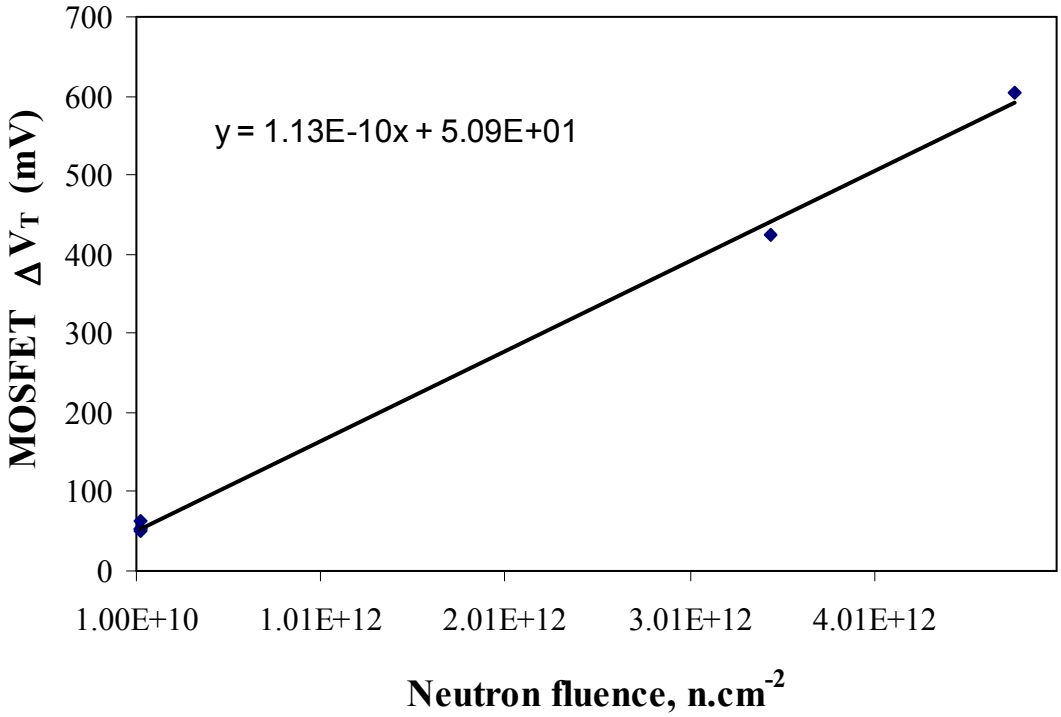

Figure 9-2. MOSFET threshold voltage change as a function of neutron fluence when irradiated in the TC 10 facility on MOATA reactor.

Assuming that the MOSFET responds to neutrons of all energies and gamma rays if the neutron fluence and the gamma dose rate in TC-10 is known the MOSFET response to each component can be determined. This is described as:

$$\Delta V_{total} = \phi_o K_{therm} + \phi_{epi} K_{epi} + D_\gamma K_\gamma \qquad 9\text{-}1$$

Where ϕ_o is the thermal fluence, ϕ_{epi} is the epithermal fluence and D_γ is the gamma dose, K_{therm}, K_{epi} and K_γ are the thermal, epithermal and gamma dose efficiencies respectively.

The thermal fluence was measured using gold foils and the epithermal fluence was estimated assuming a slowing down spectrum with a gold foil cadmium ratio of 38. The gamma dose rate in the TC-10 facility on MOATA has been determined to be 4.8 $Gy.h^{-1}$ using paired Exradin Mg/TE ion chambers[a]. This gives a dose of 8 cGy per minute or 40 cGy for the 5 minute irradiation used for these measurements. As a first approximation a uniform sensitivity over all neutron energies was assumed i.e. $K_{therm} = K_{epi}$. This is considered reasonable and conservative first approximation since the neutron cross sections of the MOSFET constituents will decrease with energy in the epithermal energy range relative to their values at thermal energies. This is shown elsewhere in MCNP models of the MOSFET device (Chapter 5).

For this particular experiment the final impact of the epithermal response term ($\phi_{epi}K_{epi}$) on the determination of the thermal neutron sensitivity is small since $\phi_{epi} << \phi_o$. For epithermal BNCT beams the epithermal response is more significant and an energy dependent neutron response factor must be introduced as described elsewhere (Chapter 5). In this case the threshold voltage change for the unshielded MOSFET in TC-10 becomes:

$$\begin{aligned}\Delta V_{unshielded} &= \phi_o K_{therm} + 0.00816\phi_o K_{therm} + D_\gamma K_\gamma \\ &= 1.00816\phi_o K_{therm} + D_\gamma K_\gamma\end{aligned} \qquad 9\text{-}2$$

Where ϕ_{epi} is taken as $0.00816\phi_o$ as derived from the slowing down spectral component of TC10 (see Appendix). For the shielded MOSFETs the threshold

[a] H Meriaty and BJ Allen, Ansto, unpublished data.

voltage change is:

$$\Delta V_{shielded} = 0.00816\phi_o K_{therm} + D_\gamma K_\gamma \qquad 9\text{-}3$$

Therefore

$$\Delta V_{unshielded} - \Delta V_{shielded} = \phi_o K_{therm} \qquad 9\text{-}4$$

From this relation and the measured data the thermal neutron sensitivity is derived to be 1.08×10^{-10} mV/n.cm^{-2}. Using this value in equation 9-3 gives a value of 47.86 mV for $D_\gamma K_\gamma$. Assuming the gamma dose sensitivity factor of 1.8 mV/cGy as measured for this batch of MOSFETs in an AECL Theratron ^{60}Co field is appropriate for the gamma spectrum in TC-10 these measurements yield a gamma dose of 26.6 cGy for the 5 minute TC-10 irradiation. This is significantly less than the expected dose based on ion chamber measurements. However this does not take into account the attenuation of the gamma dose component through the LiF shield around the MOSFETs.

The diameter of the LiF shields used was 3.5 cm and the length 8 cm. Therefore a MOSFET on the central axis of one of these pots has approximately 1.75 cm of LiF attenuating the gamma dose component that is radially incident, and 4 cm of LiF for the gamma dose component that is axially incident. The total attenuation coefficient for LiF derived from the XCOM1 program of M.J. Berger[192] at a photon energy of 1 MeV is 5.89×10^{-2} cm^2.g^{-1}. The density of the LiF was taken as 2.5 g.cm^{-2}. This gives a linear attenuation coefficient of 0.14725 cm^{-1} and a total attenuation of

0.77 for 1.75 cm of LiF. This would reduce the actual dose to the MOSFET from 40 cGy to 30.9 cGy for a 5 minute irradiation Implicit in this simple estimate of the dose to the MOSFET is an assumption that the gamma photons are normally incident on the side of the cylinder containing the LiF and the MOSFET. No data is available regarding the angular distribution of the gamma flux in the TC-10 facility but in the absence of this data it is reasonable to assume that it is more an isotropic field than a parallel beam due to the large mass of surrounding scattering and moderating material. Therefore there would be some component of the beam incident on the top and bottom of the LiF shield that would experience a significantly greater attenuation than the 0.77 that is expected for the gamma flux entering through the sides of the LiF shield. Attenuation of a 1 MeV photon through the top or bottom of the cylinder would be 0.55. The overall attenuation of the gamma flux reaching the LiF shielded MOSFET will be somewhere in this range. The average of these two values will be taken as the estimate of the attenuation factor, i.e. 0.66±0.11. Therefore based on the previously measured TC-10 gamma dose rate of 4.8 $Gy.hr^{-1}$ the dose inside the lithium shield where the MOSFET is located during a 5 minute irradiation may be estimated as 26.4 cGy ± 4.4 cGy. This is consistent with the experimentally observed value of 26.6 cGy.

When the estimated gamma attenuation is added to equations 9-3 and 9-4 become

$$\Delta V_{shielded} = 0.00816\phi_o K_{therm} + 0.66 D_\gamma K_\gamma \qquad 9\text{-}5$$

$$\Delta V_{unshielded} - \Delta V_{shielded} = \phi_o K_{therm} + 0.34 D_\gamma K_\gamma \qquad 9\text{-}6$$

Using the expected gamma dose rate of 8 cGy per minute and the ^{60}Co determined K_γ of 1.8 mV.cGy^{-1} gives a K_{therm} of 1.01(±0.02) $\times 10^{-10}$ mV/n.cm^{-2}. This value is 6.9% lower than the thermal neutron sensitivity factor neglecting the effect of gamma attenuation in the LiF shields. The LiF attenuation factor is not well known due to the lack of information available about the angular and energy distribution of the gamma flux in the TC-10 facility. Therefore the uncertainty quoted for it spans the range of attenuations expected for a 1 MeV gamma flux incident radially or axially on the LiF MOSFET holders. As can be seen the value of K_{therm} is not highly sensitive to this relatively large uncertainty in the gamma attenuation. This factor could be used for the normalisation of the MOSFET energy dependant neutron response functions determined in Chapter 5.

MOSFET ACTIVE MODE MEASUREMENTS

Greatly increased sensitivity and linearity of dose response can be obtained by using MOSFETs in "active mode". "Active mode" refers to use of the MOSFET with a bias voltage attached to the gate electrode during the irradiation period instead of having the gate at the same potential as the source, drain and substrate during this period. The effect of applying a gate bias is to sweep more of the holes produced into traps along the oxide substrate interface thereby increasing the threshold voltage relative to what it would be if those holes were distributed throughout the oxide layer.

The effect of applying a gate bias during mixed gamma neutron irradiations

was investigated using the MOATA TC-10 facility. A MOSFET was calibrated using a Co 60 Theratron gamma source and then irradiated in TC-10. This process was repeated using a number of different epoxy-lithium fluoride and epoxy-lithium carbonate shields. Gold activation foils were also placed in each shield during the irradiations. The gamma and neutron attenuation factors for each of three different neutron shields were determined.

A 0.6 cc Farmer ionisation chamber in conjunction with a Farmer electrometer was used to monitor the gamma dose delivered to the MOSFETs by the Theratron. The gamma attenuation was also measured by placing the Farmer chamber inside the Li shields and measuring the dose rate.

LiF shields

Cylindrical lithium fluoride / epoxy and lithium carbonate / epoxy shields previously manufactured for biological irradiations (mouse and in-vitro) in the MOATA TC-10 thermal column were used. These shields had various thicknesses and the exact constituency was not determined.

Shield number 1 had internal and external diameters of 1.9 and 5 cm respectively. It was 4.6 cm long with ends that were 1.5 cm thick. It was fabricated from ^{6}LiF epoxy. Shield number 2 had internal and external diameters of 2.5 and 5.5 cm respectively with 1 cm thick endcaps. It was fabricated from natural LiF epoxy. Shield number 3 was made from natural Li_2CO_3 and epoxy and had an internal diameter of 3 cm and an external diameter of 4 cm. The endcaps were 0.5 cm thick.

Because their exact composition (and therefore thermal neutron attenuation factors) were unknown the neutron attenuation factors were measured using gold foil

activation measurements both inside and external to the shields. The neutron attenuation factors were taken as the ratio of the specific activity of gold foils measured inside and outside the shields after corrections for decay had been made.

Similarly the gamma attenuation factors for the shields were measured in the Co-60 Theratron beam using a Farmer ionisation chamber. The gamma attenuation factor was determined as the simple ratio of the dose rate measured inside the shield versus the dose rate without the shield in a 10 x 10 cm beam.

RESULTS

Gamma attenuation factors

The measured gamma attenuation factors are shown in Table 9-3 and Table 9-4. Clearly the maximum correction required for attenuation of gamma rays with these shields is approximately 6% for shield number 2.

Table 9-3. Gamma attenuation factors for the Li-epoxy neutron shields, measurement 1.

Lithium/epoxy neutron shield	**^{60}Co gamma dose rate (cGy.min^{-1})**	**Unattenuated ^{60}Co dose rate (cGy.min^{-1})**	**Attenuation factor**
No shield	38.9	38.9	1.000
1	37.0	38.9	0.951
2	36.5	38.9	0.938
3	38.2	38.9	0.982

Table 9-4. Gamma attenuation factors for the Li–epoxy neutron shields, measurement 2.

Lithium/epoxy neutron shield	Co 60 gamma dose rate (cGy.min^{-1})	Unattenuated ^{60}Co dose rate (cGy.min^{-1})	Attenuation factor
No shield	39.0	39.0	1.000
1	37.4	39.0	0.958
2	37.0	39.0	0.948
3	40.9	41.6	0.983

Table 9-5. Neutron attenuation factors for lithiated neutron shields.

Li Shield	Outer foil specific activity (Bq.mg^{-1})	Inner foil specific activity (Bq.mg^{-1})	Attenuation
1	4948.5	58.16	0.012
2	6065.4	425.1	0.07
2	7665	505.7	0.066
3	4969.7	996.2	0.20
3	6177	1244	0.20

The neutron attenuation factors for the lithiated shields based on gold foil activation are shown in Table 9-5. The results from the series of exposures for MOSFET number 1 using a bias of 5 volts in the ^{60}Co gamma field and the TC-10 neutron field were as shown in Table 9-6. The corresponding results from the series of irradiations of MOSFET number 2 with a 10 volt bias are shown in Table 9-7. Figure 9-3 shows the MOSFET threshold voltage changes as a function of neutron fluence during the 5 minute irradiations in TC-10 using different neutron attenuating shields. Data for both MOSFETs is shown. MOSFET number 1 had a 5 volt bias applied during irradiation and MOSFET number 2 had a 10 volt bias applied during irradiation. The total threshold voltage change was 3598 mV for MOSFET number 1

and 5243 mV for MOSFET number 2. Therefore it may be expected that the MOSFET was operating well beyond its linear dose response range.

Table 9-6. Threshold voltage changes for gamma and thermal neutron irradiations (5v bias).

	Radiation Source	**Lithium shield**	**D_γ (cGy)**	**ϕ_o (n.cm^{-2})**	**ΔV_f**
1	Co 60	1	37.0	0	243.9
2	TC-10	1	40	4.14×10^{10}	202.0
3	Co 60	3	38.2	0	263.0
4	TC-10	3	40	6.9×10^{11}	515.4
5	Co60	3	40.5	0	230.6
6	Co60	2	41.4	0	233.0
7	TC-10	2	40	2.35×10^{11}	399.0
8	Co60	none	38.9	0	210.0
9	TC-10	none	40	3.45×10^{12}	1301

Table 9-7. Threshold voltage changes for gamma and thermal neutron irradiations (10v bias).

	Radiation Source	**Lithium shield**	**D_γ (cGy)**	**ϕ_o (n.cm^{-2})**	**ΔV_f**
1	Co 60	1	39.0	0	350
2	TC-10	1	40	4.14×10^{10}	259.3
3	Co 60	3	40.9	0	399
4	TC-10	3	40	6.9×10^{11}	820.5
5	Co60	2	37.0	0	356
6	TC-10	2	40	2.35×10^{11}	551.4
7	Co60	None	38.5	0	316
8	TC-10	None	40	3.45×10^{12}	1892
9	Co60	None	38.3	0	299

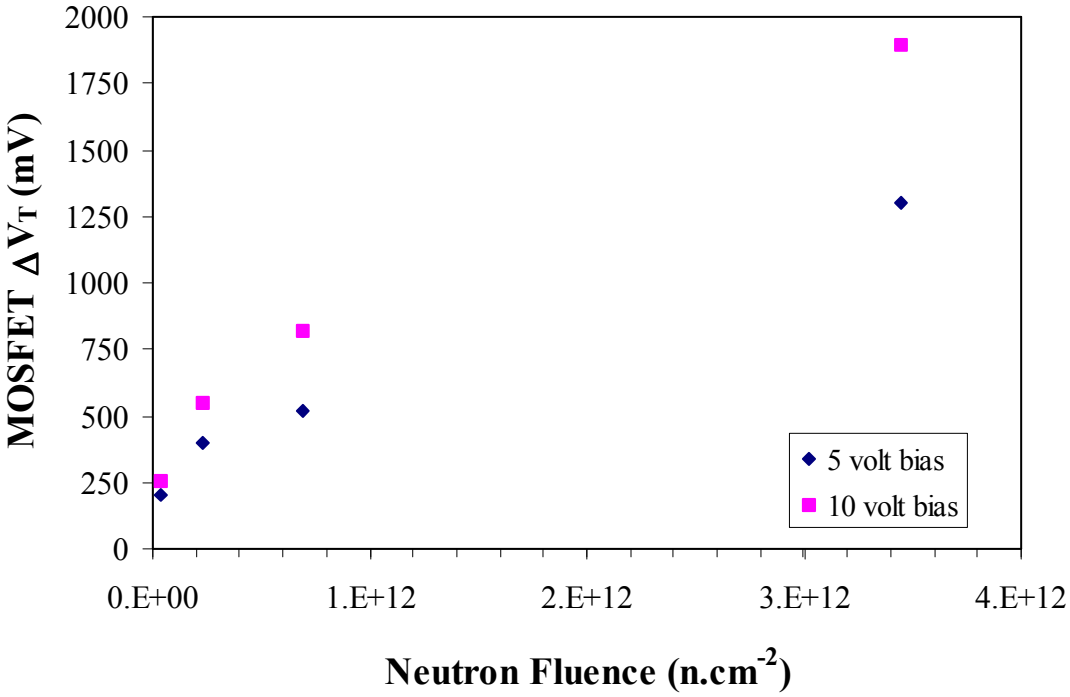

Figure 9-3. MOSFET threshold voltage change as a function of neutron flux in TC 10.

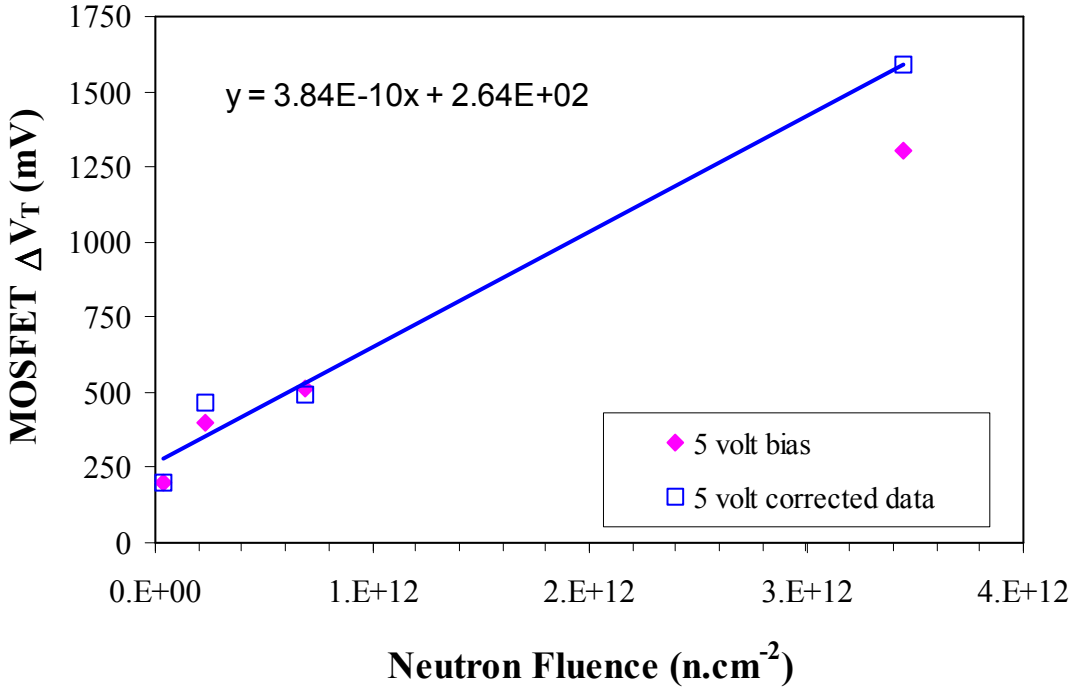

Figure 9-4. Five volt bias MOSFET data corrected for drop off in sensitivity.

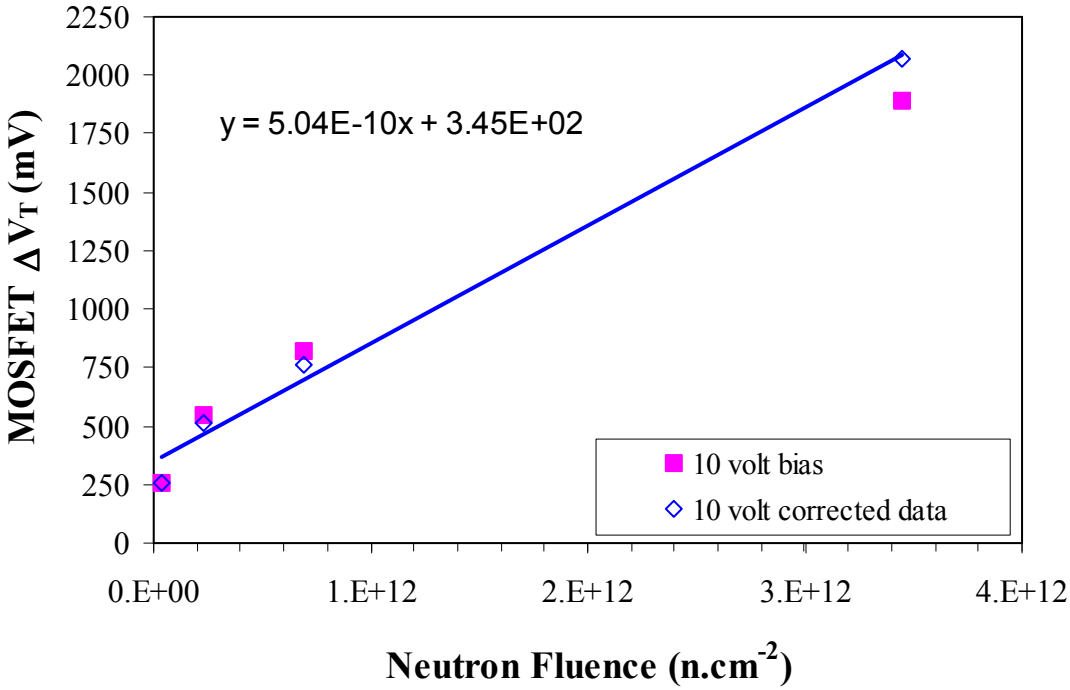

Figure 9-5. MOSFET irradiated with 10 volt gate bias. Both raw data and data corrected for decrease in sensitivity are shown.

By using the ^{60}Co irradiations in between each TC-10 neutron irradiation to determine a new calibration factor the data points can be corrected for the decrease in sensitivity with the large cumulative threshold voltage change. The known gamma dose and the observed threshold voltage change for each ^{60}Co irradiation was used to calculate a new gamma sensitivity which in turn was used to correct the observed voltage change during the subsequent TC-10 irradiation. All voltage changes observed during TC-10 irradiations were corrected back to the voltage change that would be observed for the MOSFET with its initial sensitivity. The initial sensitivity for the 5 volt MOSFET was 6.59 mV.cGy^{-1}. The initial sensitivity for the MOSFET with 10 volts applied to the gate was 8.97 mV.cGy^{-1}.

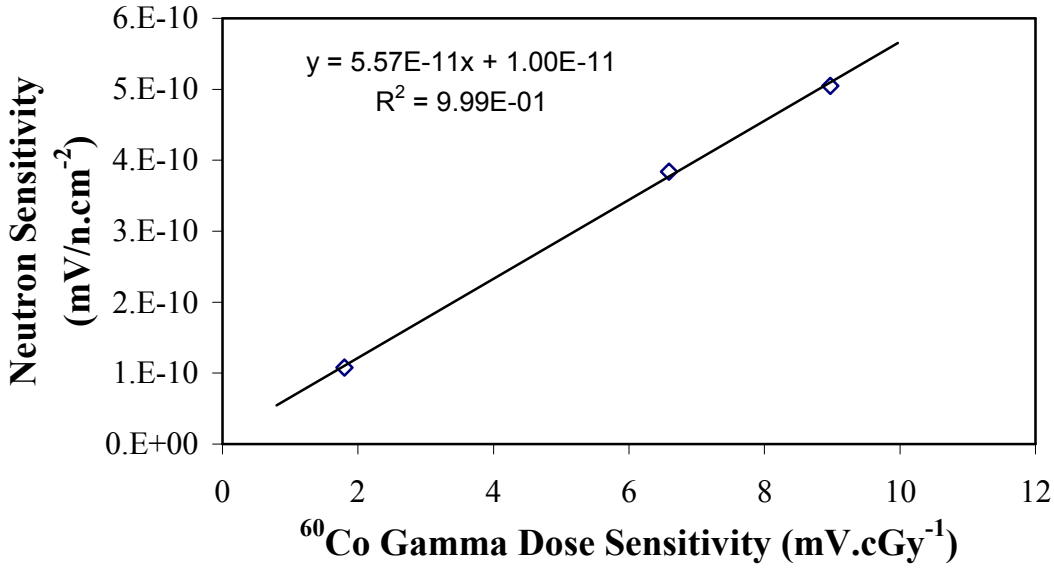

Figure 9-6. Correlation between Neutron Dose sensitivity and gamma dose sensitivity for MOSFETs with 0v, 5v and 10 v bias during neutron and gamma irradiations.

The corrected threshold voltage changes as a function of neutron fluence for the two MOSFETs are shown in Figure 9-4 and Figure 9-5 along with the uncorrected data for comparison. A straight line has been fitted to the corrected data. The intercept of the fitted curve for the 5 volt MOSFET was 264 mV and for the 10 volt MOSFET it was 345 mV. By extrapolating this curve to zero neutron fluence in this manner we obtain a measure of the gamma dose contribution to the MOSFET in the TC-10 field. Assuming that the gamma sensitivity factor for the gamma field in TC-10 is the same as the sensitivity factor for ^{60}Co radiation (ie 6.59 mV.cGy^{-1} for a MOSFET with 5 v on gate and 8.97 mV.cGy^{-1} with 10 v on the gate) we obtain gamma doses for 5 minute irradiations of 40.1 cGy and 38.5 cGy for the 5 v and 10 v MOSFETS respectively. This corresponds to gamma dose rates of 481 cGy.hr^{-1} or 462 cGy.hr^{-1} respectively. These values are in accord with previously measured gamma dose rates of 4.8 Gy.hr^{-1} using paired ionisation chambers.

CONCLUSIONS

By measuring PIN diode neutron dosimeter responses in the MOATA TC-10 thermal column both bare and covered with Li or Cd thermal neutron shielding it was possible to demonstrate that in this irradiation facility the PIN diodes respond to both the thermal component and the epithermal component of the neutron spectrum. Although the TC-10 port is a thermal neutron irradiation facility, because of the shape of the silicon neutron KERMA function, the diode bias voltage shift observed for Li or Cd shielded devices was approximately 75% of the bias voltage change observed for diodes with no Cd or Li shields.

These measurements yielded a PIN diode sensitivity of approximately 4×10^{-12} mV/n.cm^{-2} for the thermal component of the TC-10 spectrum. If the silicon damage KERMA factor for the thermal component is assumed to be 3.3×10^{-14} cGy/n.cm^{-2} (ie assume effective energy of 0.025 eV) this gives an approximate calibration factor of 121.5 mV.cGy^{-1} (silicon damage dose). This agrees to within experimental uncertainties with the factor measured using the Van de Graff accelerator however it is significantly lower than the value of approximately 190 mV.cGy^{-1} derived from measurements in the HB11 epithermal beam on the Petten HFR. It should be noted however that because of the uncertainty present in the assumed spectrum of the TC10 port the calibration factor measured in this chapter is based on an effective energy of 0.025 eV. If the KERMA function from the literature was convolved with a more accurate estimate of the spectrum in TC-10 a more accurate estimate of the diode calibration could be determined. This was not pursued here due to the uncertainties that exist regarding the exact spectrum in TC-10.

The sensitivity of the PIN diodes to the epithermal part of the TC-10 spectrum was found to be 1.60×10^{-9} mV/n.cm^{-2}. This is a factor of 400 greater than the sensitivity to the thermal part of the spectrum. This shows that for thermal neutron beams measurements of the silicon dose using PIN diodes can potentially be confounded by even a very small component of epithermal or fast neutrons. However this in itself suggests that PIN diodes could be applied as quite sensitive monitors of the epithermal or fast components of the spectrum in these environments. This intrinsic low sensitivity can be further diminished by the addition of cadmium or lithiated covers as were employed in the measurements here.

MOSFETs were irradiated with the PIN diodes both with lithiated shields ands without. By taking the difference in the threshold voltage changes for the shielded and unshielded MOSFET measurements it was possible to determine both a thermal neutron sensitivity factor for the MOSFETs and an estimate of the gamma dose in the TC-10 facility. The neutron sensitivity of a bare MOSFET operated with no bias during irradiation was found to be 1.08×10^{-10} mV/n.cm^{-2} for the MOATA TC-10 spectrum. Since the MOSFET neutron response drops off rapidly with increasing neutron energy and the TC10 facility has a gold foil cadmium ratio of ~38 this factor can be reasonably to applied to MOSFETs of the same type in any thermal spectrum. This factor could also be used for the normalization of the Monte Carlo calculated energy dependent neutron response function of the MOSFETs determined in Chapter 5.

The gamma dose measured in TC-10 assuming negligible neutron response of the lithium shielded MOSFETs was found to be 3.19 Gy.hr^{-1}. This is significantly lower than the value of 4.8 Gy.hr^{-1} previously measured using paired ionization

chambers. However when the gamma attenuation of the lithium shields is taken into account the dose rate is found to be 4.8(±0.8) $Gy.hr^{-1}$ which is quite consistent with previous measurements using more conventional ionization chamber techniques.

Similar measurements were repeated using MOSFETs with a bias applied to the gate during irradiation in TC-10. This resulted in much higher sensitivity. To account for changes in intrinsic sensitivity due to the large threshold voltage changes the MOSFETs were calibrated in a standard ^{60}Co field between each irradiation on MOATA. For a MOSFET with a 5 volt bias during irradiation a thermal neutron sensitivity of 3.84×10^{-10} $mV/n.cm^{-2}$ was measured. For a MOSFET with a 10 volt gate bias the thermal neutron sensitivity was 5.04×10^{-10} $mV/n.cm^{-2}$. The corresponding ^{60}Co gamma sensitivities were 6.59 and 8.97 $mV.cGy^{-1}$ respectively.

Using the biased MOSFETs the measured gamma dose rate in TC-10 was 4.81 $Gy.hr^{-1}$ and 4.62 $Gy.hr^{-1}$ for the 5 volt and the 10 volt biased MOSFETs respectively. Again these measurements are in agreement with the previous unbiased MOSFET measurements and ionization chamber measurements. Because of the higher threshold voltage changes for the biased MOSFETs and also due the ^{60}Co calibration performed prior to each measurement in TC-10 these biased MOSFET measurements of gamma dose may be considered more reliable than the unbiased MOSFET results.

The technique used here demonstrates an effective way to measure gamma dose in mixed thermal neutron and gamma fields. By using a bare MOSFET and one or more different thermal neutron shields the neutron component of the MOSFET response can be extrapolated to zero and the remaining response presumed to be due to gamma dose. The short comings of this technique include the relatively large

shields required and the possibility of perturbing the neutron induced gamma field due to the presence of lithiated shields. The size of the shields could be minimized by using materials with higher concentrations of enriched ^{6}Li if necessary. Unfortunately the technique is not so easily applied to mixed fields where there is a large epithermal neutron component because this cannot be attenuated so effectively with simple lithiated shields. As demonstrated elsewhere in this thesis to use neutron shields of a reasonable size in an epithermal neutron beam it is necessary to calculate a neutron spectrum dependent correction factor to account for the MOSFET neutron response.

A direct linear relationship was observed between the neutron sensitivity and the gamma sensitivity of the MOSFETs as the bias voltage on the gate is increased between 0 and 10 volts. This indicates that the ionization caused in the SiO_2 layer during gamma and neutron irradiation of these MOSFETs leads to similar hole trapping phenomenon. This supports the assumption that ionization in the oxide layer during low energy neutron radiation of these MOSFETS is mediated by secondary electron, gamma and x-ray radiation rather than neutrons directly. If direct action by neutrons was contributing significantly to the ionization within the oxide it might be expected that for such a process the change in sensitivity observed as the gate bias increased would not be the same as for gamma fields. In these experiments neutron sensitivity was always proportional to gamma sensitivity. It is most likely that the neutron sensitivity is due to secondary electrons and gamma rays generated in the MOSFET encapsulation.

Future use of MOSFETs for gamma dosimetry in mixed neutron and gamma fields could be simplified by careful selection and optimization of the MOSFET encapsulation materials to minimize neutron sensitivity due to interactions in the

MOSFET encapsulation.

CHAPTER 10 PETTEN HFR HB11 BNCT BEAM MEASUREMENTS: DESCRIPTION OF FACILITY, PHANTOMS, MCNP MODELS AND FOIL ACTIVATION MEASUREMENTS

INTRODUCTION

A series of in phantom measurements using PIN diodes and MOSFETs were performed using the HB11 filtered epithermal neutron beam at the High Flux Reactor (HFR) located in Petten at the European Commission Joint Research Centre (JRC). This neutron beam has been well characterised[193] and is therefore used in the following measurements as a reference beam as well as an epithermal neutron source for measurements in phantoms.

Some of the semiconductor dosimeter measurements described here were part of a set of measurements aimed at verifying a MCNP treatment planning model which is fully described elsewhere by Wallace[194]. Among other things, that work describes the fabrication of a detailed human head phantom as well as the development of a Monte Carlo model of epithermal neutron beams incident on it. Results from some parts of the measurements described here were used in an attempt to validate that Monte Carlo model.

The substance of this current chapter and the two that follow are the experimental measurements themselves. In particular this includes the detailed

characterisation and analysis of the MOSFET and PIN dosimeter responses that are required to give good agreement between the model described by Wallace and the data derived from measurements in the HB11 beam.

MATERIALS AND METHODS

THE HB11 EPITHERMAL NEUTRON BEAM ON THE PETTEN JRC HFR.

The HB11 beam on the High Flux Reactor (HFR) at the EC Joint Research Facility has been customised to provide a high quality epithermal neutron beam specifically for BNCT trials and treatments.

The HFR is a 45 MW light water swimming pool reactor mainly used for materials testing. Initial MCNP simulations[195, 196] of a beam on the HB11 port of the reactor using a filter of Cd(1mm), Al (150mm), S(50mm), Ti (10mm) and Ar (1500mm) predicted a beam with the following characteristics. A neutron flux of 1.1×10^{9} n.cm^{-2} s^{-1}, a fast neutron dose per incident neutron of 7.8×10^{-13} Gy.cm^{2}, a gamma dose of 0.5 Gy per incident 3×10^{12} n.cm^{-2} and an average neutron energy of < 8keV. The treatment point in the HB11 beam is approximately 5 m from the reactor core which was expected to result in a beam with minimal divergence.

The beam design optimised using MCNP 4A simulations and subsequently constructed[197] consisted of a filter made of 1 mm of Cd, 80 mm of Al, 10 mm of Ti, 50 mm of S and 1501.2 mm of liquid Ar. The S and Ar were contained in Al vessels giving a total thickness of Al of 150mm. The filter assembly also included a void of approximately 44 cm thickness which acts as a water shutter in case the main beam shutter fails or the liquid argon is lost. Under normal operation of the beam this

volume is empty but if the beam needs to be shut off in an emergency the volume can be flooded with water. The Al, S and Ti components of the filter define the epithermal neutron spectrum which is transmitted. The cadmium layer removes thermal neutrons from the core entering the beam. The role of the 1.5 m section of liquid argon in the filter is to serve as a gamma ray attenuator. The presence of the argon has minimal effect on the neutron spectrum.

The room arrangement has been described well by Raaijmakers[193]. The beam tube is at a 5° angle to the reactor core and exits the reactor shielding at the same angle. For this reason the HB11 treatment room has been constructed with a 5 cm thick polyethylene wall perpendicular to the beam axis. This facilitates the correct alignment of patients and phantoms within the room. The diameter of the beam can be modified by inserting 19 cm long collimating apertures into the beam line at the point where it exits into the treatment room. These collimators are made of a sandwich of 5 cm of lithiated polyethylene, 9cm of lead and another 5cm of lithiated polyethylene and can define exiting beam diameters of 8 cm , 12 cm or 15 cm.

Raaijmakers[193] undertook a full characterisation of the HB11 beam including thermal neutron fluence, fast neutron dose rates and gamma dose rates in phantoms at different distances from the beam exit hole (0, 20, 30, 40 and 50 cm) and for different aperture sizes (8 cm, 12 cm and 15 cm). The thermal neutron fluence depth dose curve in water phantoms did not depend on the separation of the phantom from the beam exit hole. The absolute value of the thermal neutron fluence (at 2cm depth in a water phantom) was found to change according to the inverse square of the distance between the phantom and a virtual source located at 3 m beyond the beam exit hole. The ratio of the fast neutron and gamma dose to the thermal neutron fluence was

constant with changes in the phantom to beam exit separation.

Increasing the field size from 8 cm to 15 cm resulted in a thermal neutron fluence increase of 52%, a gamma dose rate increase of 67%, and a fast neutron dose rate increase of 6%. There was also a trend towards larger percentage thermal fluences at depth for increased aperture sizes. The vertical and horizontal beam profiles were shown to be similar and therefore the beam has been treated as axially symmetric for the purpose of the measurements described here.

PHANTOMS

Three phantoms were used in the measurements described here. They were, in order of decreasing complexity:

1) A detailed anthropomorphic phantom of the human head. This was fabricated from a human skull, tissue equivalent gel and thermosetting plastic. Its fabrication is described by Wallace[194]. It will be referred to as 'the skull phantom'. Details of the phantom and model pertinent to this particular thesis are described in following sections.
2) A tissue equivalent-gel filled, polycarbonate cylindrical phantom. This phantom is 16 cm in diameter and 23 cm in length. This will be referred to as the cylinder phantom.
3) A cubic solid polymethylmethacrylate (PMMA, also known as perspex or lucite) phantom of side length 15 cm. This will be referred to as the cube phantom.

THE SKULL PHANTOM

As noted above the fabrication of this phantom is fully described by Wallace[194] and is only briefly summarised here. The phantom consisted of a human skull contained in a molded thermoplastic (cellulose acetate) outer skin. This mold was produced from a plaster cast of the skull. Once the molded plastic was completed the skull was placed inside it. A region of low density (essentially a void) was then inserted to represent the oral cavity, nasopharanx and oesophagus. This consisted of expanded polyurethane foam. The remainder of the outer plastic shell was then filled with tissue equivalent gel.

The fabrication of this gel is also described by Wallace[194]. It was based on the recipe for tissue equivalent liquid given by Goodman[198] but modified by the addition of agarose to form a gel. According to Wallace the components of the gel by weight are: water (64.9%), glycerol (26.5%), Urea (4.4%), agar (4.1%). This results in a gel with a density of approximately 1.09 $g.cm^{-3}$ and an elemental composition by weight of H (10.1%), C (13.2%), N (2.1%), O (74.6%). This composition is close to the elemental composition of ICRU 46 grey/white brain matter: H (10.7%), C (14.2%), N (2.2%), O (71.2%).

The top of the skull was sliced transaxially. The top section could be completely removed allowing access to the tissue equivalent gel representing the brain in the intracranial region. To facilitate this the plastic shell also had a removable top section. During the measurements the top of the plastic shell was secured with fine nylon screws. During irradiation, the skull was supported on a jig consisting of a PMMA base plate and a number of upright PMMA rods. See Figure

10-1.

The skull phantom incorporated three hollow PMMA tubes of 1.25 cm outer and 0.95 cm inner diameter. These were oriented orthogonally such that the intersection of all three tubes occurred in the mid region of the brain volume. One tube formed the vertical axis for the measurements, running from superior to inferior. The other two lay along the anterior - posterior axis and the lateral (left - right) axis of the skull respectively. These tubes could be accessed by removing the top section of the plastic shell and the top section of the skull. See Figure 10-2. PIN diodes, MOSFETs or activation foils could then be placed inside the tubes separated by PMMA spacers. This allowed measurements to be made along the three principle axes of the skull.

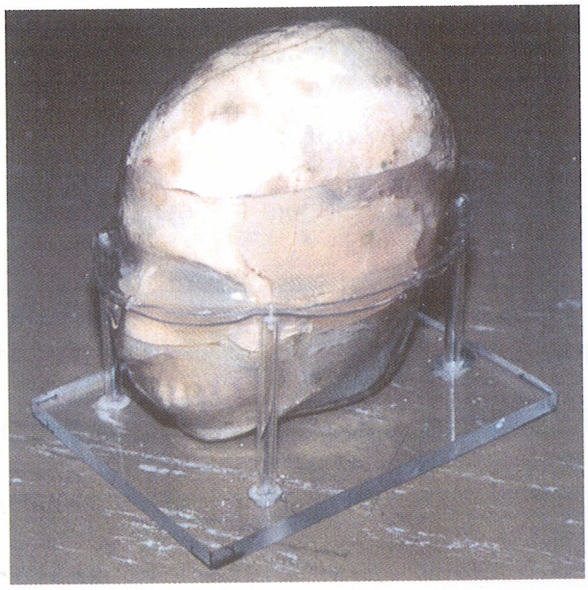

Figure 10-1. Skull phantom assembled and mounted on PMMA jig used for irradiations (image courtesy S Wallace).

Figure 10-2. Skull phantom with top removed for access to dosimeter positions. (image courtesy S Wallace).

MCNP MODEL OF SKULL PHANTOM

The MCNP model of the skull phantom that was used for comparison with the experimental results presented here is a modified version of the MCNP model constructed by S Wallace[194]. The current model is based on the skull geometry defined by Wallace. However for this work several changes were made to material definitions, variance reduction schemes (cell importance factors). Additional tallies and tally multipliers were introduced to allow the calculation of PIN diode responses and MOSFET neutron responses.

The skull geometry was derived from a low resolution CT of the phantom performed using a Varian Ximitron simulator CT as described by Wallace[194]. The skull model is constructed of 5mm × 5mm × 5mm voxels. The model consists of 42 transaxial slices each of which is an array of 40 by 30 voxels. This gives a

parallelepiped 21 cm high, 20 cm from anterior to posterior and 15 cm wide in the lateral direction. The geometry of the skull is therefore defined within a three dimensional array of 50400 cubic 0.5 cm voxels. The transaxial slices are shown in Figure 10-3, Figure 10-4 and Figure 10-5. The saggital slices are shown in Figure 10-6 and Figure 10-7.

The tissue compositions of the skull phantom are based on ICRU 46[199]. The tissue equivalent gel used to fabricate the phantom was prepared to match the composition of ICRU 46 brain as closely as possible[194]. For the purposes of the current MCNP calculations the model was simplified further by setting all soft tissue in the phantom to brain equivalent composition. However due to the delay of several months between phantom fabrication and the actual measurements in the Petten beam allowance was made in the MCNP model for some dehydration of the tissue equivalent gel. For the MCNP model the amount of hydrogen in the form of water in the brain equivalent gel was reduced by 10% for all the brain equivalent parts of the phantom.

The soft tissue components of the phantom were therefore represented in the MCNP model as having the following composition by mass; H (10.66%), C(16.05%), N(2.44%), O(69.3%), Na(0.22%), P(0.44%), S(0.22%), Cl(0.33%) and K(0.33%). This effectively represents the ICRU 46 brain equivalent composition but with a ~10% reduction in the amount of water present.

The density of the brain equivalent material in the model representing the brain and other soft tissue in the MCNP model was 1.047 $g.cm^{-3}$ except for the material of the same composition used to represent the airways which had a density of 0.58 $g.cm^{-3}$.

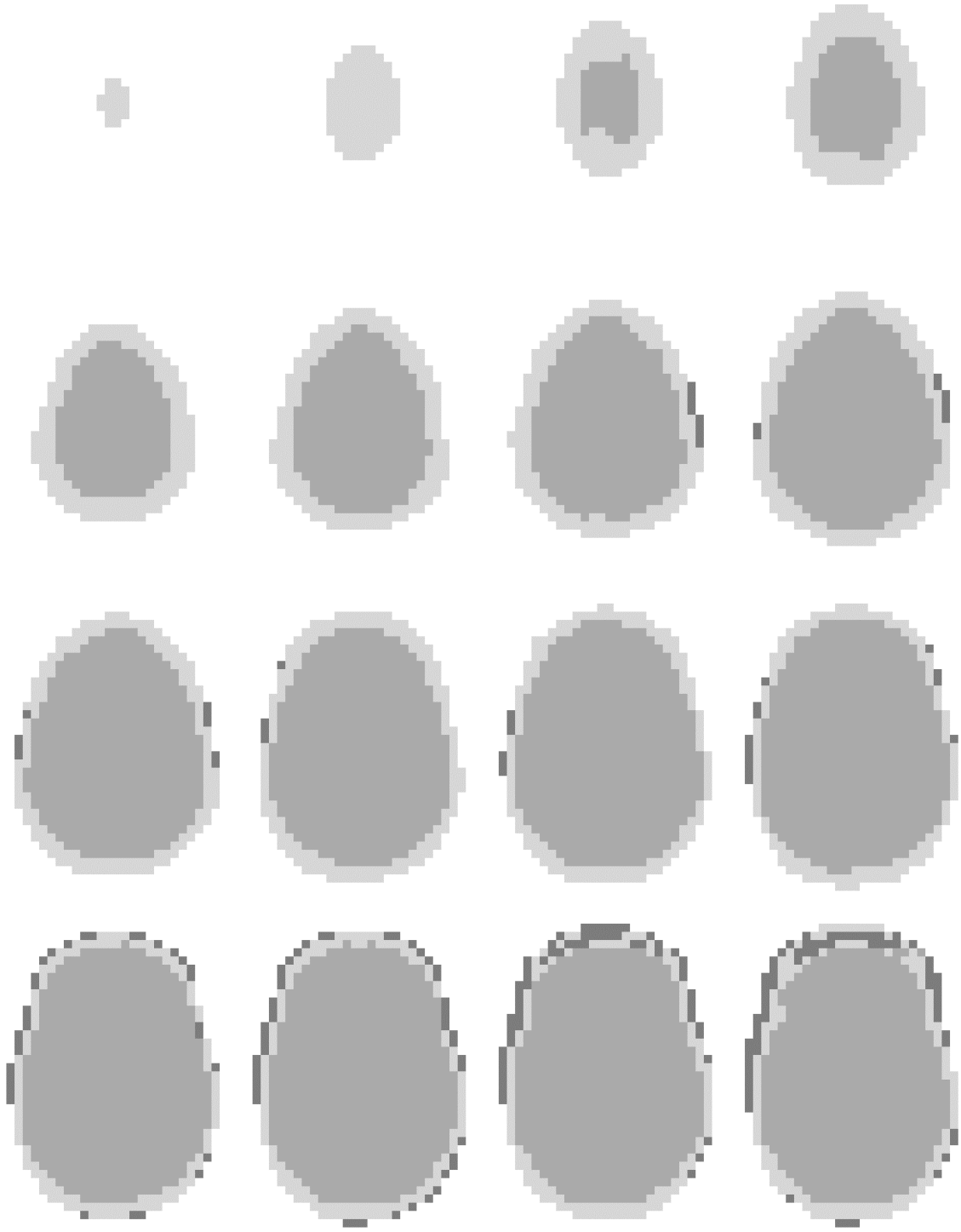

Figure 10-3. Transaxial slices of skull phantom as used for MCNP model (ordered from superior to inferior).

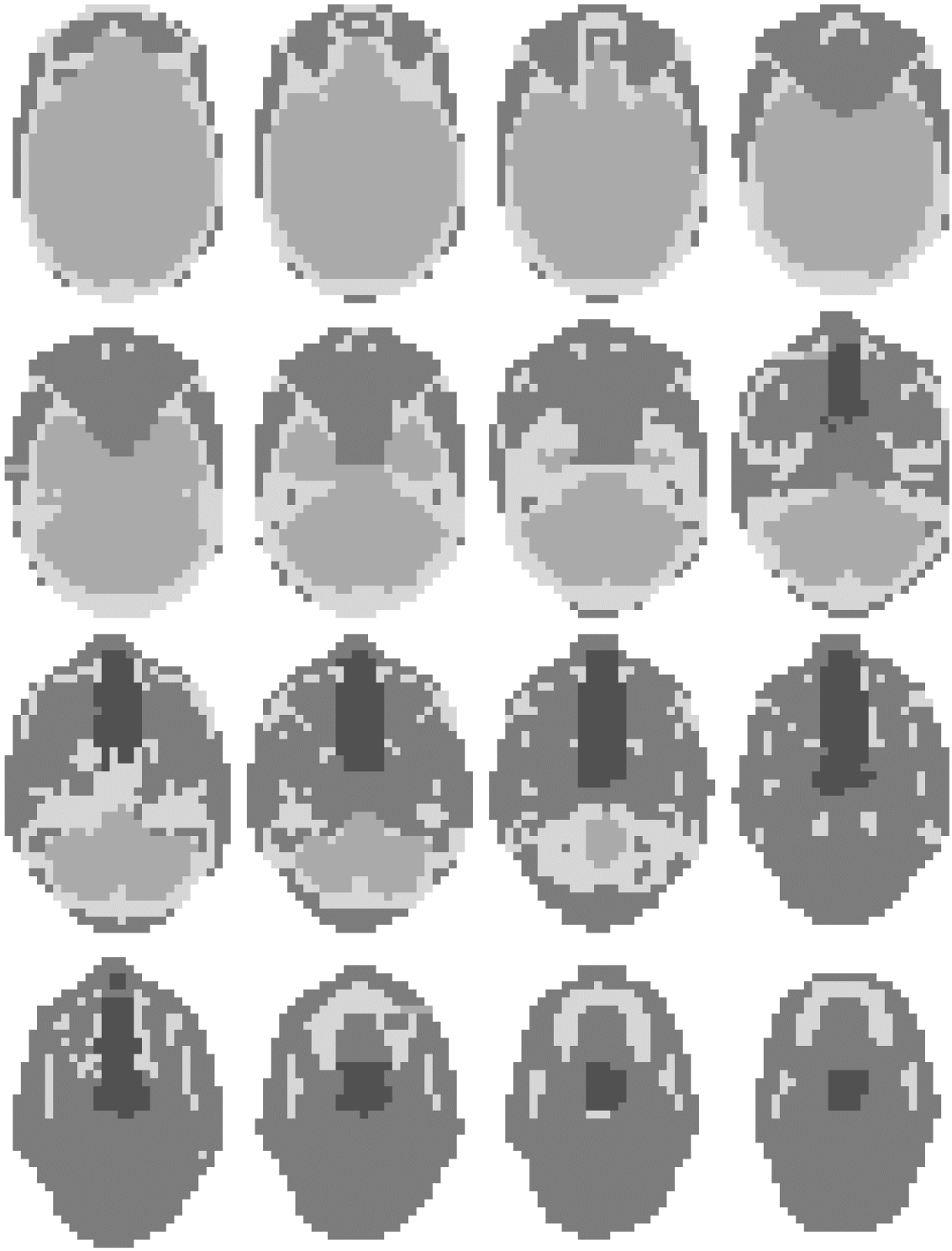

Figure 10-4. Transaxial slices of skull model continued.

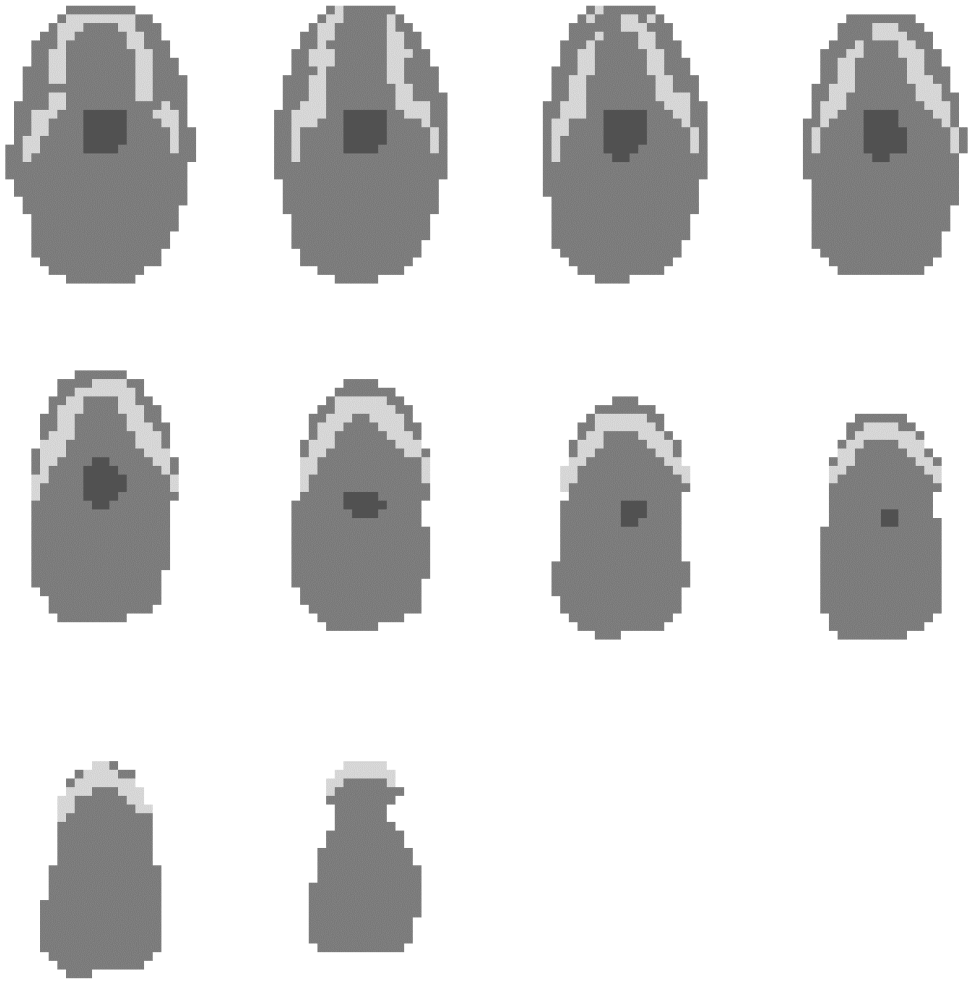

Figure 10-5. Transaxial slices of the skull phantom as used for the MCNP model.

The bone composition of the skull was represented in the MCNP model as per ICRU 46; H(5%), C(21.2%), N(4%), O(43.5%), Na(0.1%), Mg(0.2%), P(8.1%), S(0.3%) and Ca(17.6%). The density of the bone was set to 1.5 $g.cm^{-3}$. This may be a slight over estimate due to the fact that the skull was obtained from an anatomy department and was therefore more dehydrated than bone in vivo. Therefore there is some uncertainty about how accurately this density and the H and O composition of the MCNP skull model represents the real density and H concentration of the skull in the phantom.

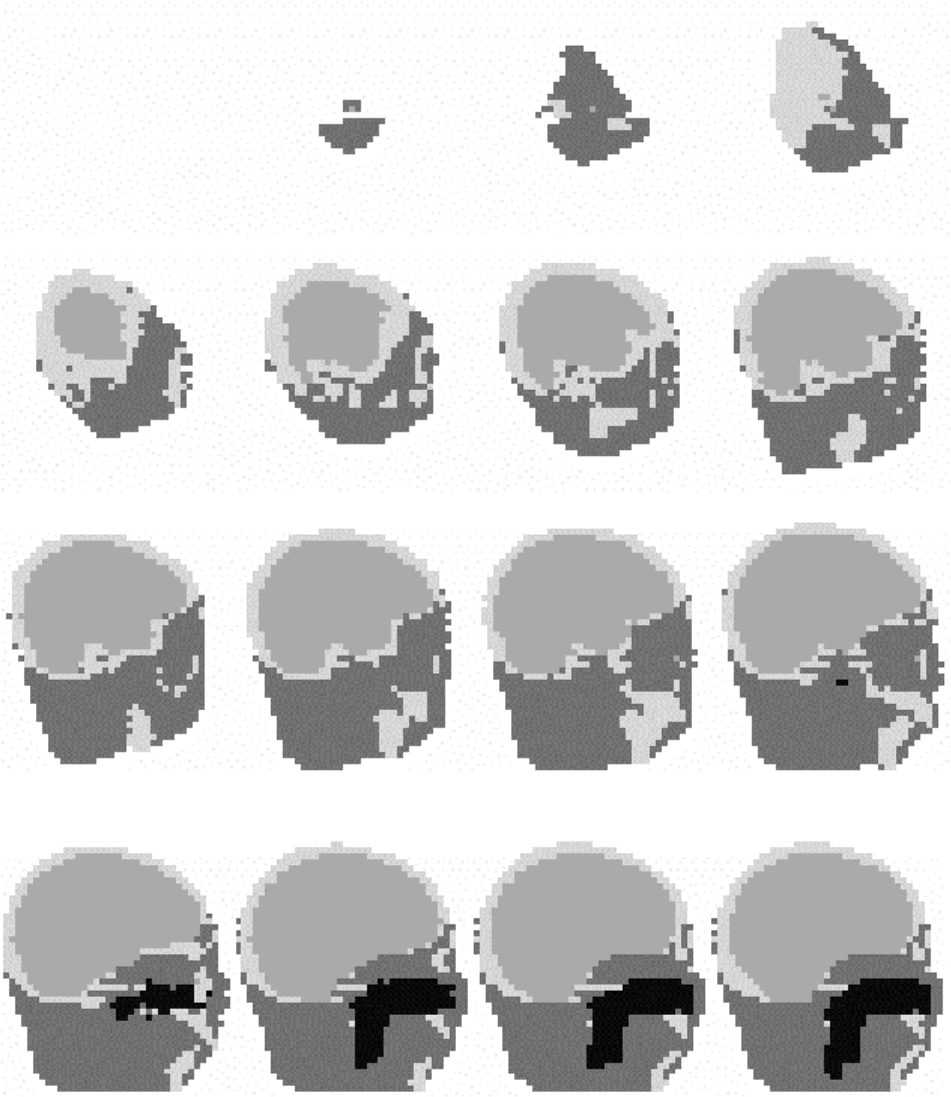

Figure 10-6. Sagittal slices of MCNP skull model.

In the MCNP model used by Wallace[194] extensive use was made of importance factors greater than 1 for both neutrons and photons at depth in the skull phantom. Importance factors were increased with depth along the direction of the incident beam in an attempt to decrease the variance in calculated quantities. For many voxels the importance for neutrons and neutron induced photons was set to values of 64 or 128. This approach was taken to reduce variance and computation time.

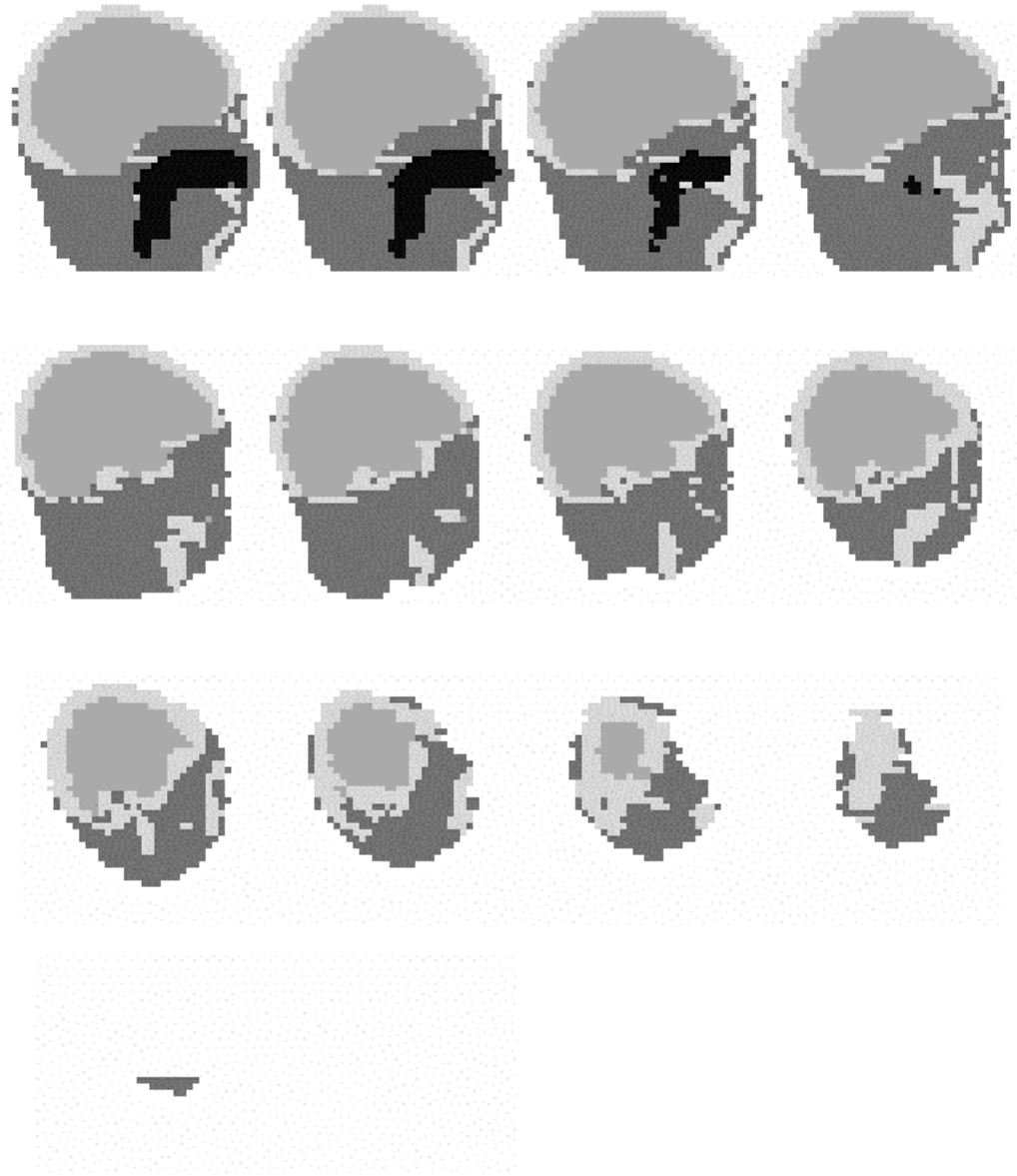

Figure 10-7. Sagittal slices of MCNP model of skull phantom continued.

In the calculations described here all importance factors were less than 4 for both neutrons and photons. This more conservative use of cell importances increases the number of particle histories and the computation time needed to reduce the variance of tallies at depth in the phantom but is less prone to artifacts that could arise when very high cell importances are used. These may occur because with very high importance factors on the distal side of the phantom significant amounts of

computer time are spent tracking very low weight particles that arise from relatively few higher weight particles entering from the source side. The much more conservative use of cell importance factors in the simulation data shown here allows more confidence in the results by minimizing the potential of cell importance artifacts as a source of discrepancy between calculated and measured doses.

The thermal S(α,β) treatment was used throughout the model in appropriate materials using the light water correction table at 300K. The source spectrum and collimator geometry was supplied by P Watkins[a, 194].

Tallies of neutron flux and neutron dose, were made for planes coinciding with the measurement axes of the phantom. Tallies of photon flux, photon dose, silicon damage kerma, MOSFET neutron response and gold foil activation were made for all cells along the measurement axes.

To generate most of the data displayed here the model was run for approximately 37 million particle histories and a total CPU time of approximately 140 hours on a 366MHz PC.

THE CYLINDER PHANTOM

The cylinder phantom consisted of a polycarbonate cylinder of 16 cm diameter and length 23.35 cm. See Figure 10-8. The ends of the phantom were also made of polycarbonate. These ends had a diameter of 18 cm and were attached with fine nylon screws. The cylinder was filled with brain equivalent gel similar to that

[a] P Watkins, private communication to S Wallace, December 1993.

used for the skull phantom and manufactured as described by Wallace[194]. To allow for insertion of dosimeters four PMMA tubes (1.5 cm outer diameter, 1.25 cm inner diameter) were located parallel to the cylinder axis and running the entire length of the cylinder. These were all centred at 2.5 cm from the cylinder axis and distributed at 90° intervals around it. Dosimeters were first loaded into a PMMA tube of 0.95 cm inner diameter and 1.25 cm outer diameter separated by PMMA spacers. These assembled tubes containing the dosimeters and spacers were then inserted into the tubes in the phantom.

During irradiations the cylinder phantom was supported on a PMMA cradle with the central axis of the neutron beam centred on the axis of the cylinder (i.e. coaxial). See Figure 10-9.

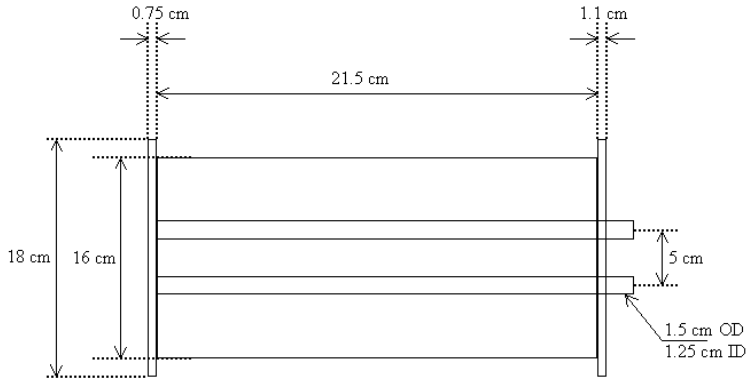

Figure 10-8. Schematic diagram of cylinder phantom showing dimensions.

MCNP MODEL OF CYLINDER PHANTOM

For comparison with the experimental results a MCNP4A simulation of the cylinder phantom exposed in the HB11 beam was performed. The front face of the

cylinder was polycarbonate. With the exception of the front face the external polycarbonate walls of the cylinder were neglected in the model.

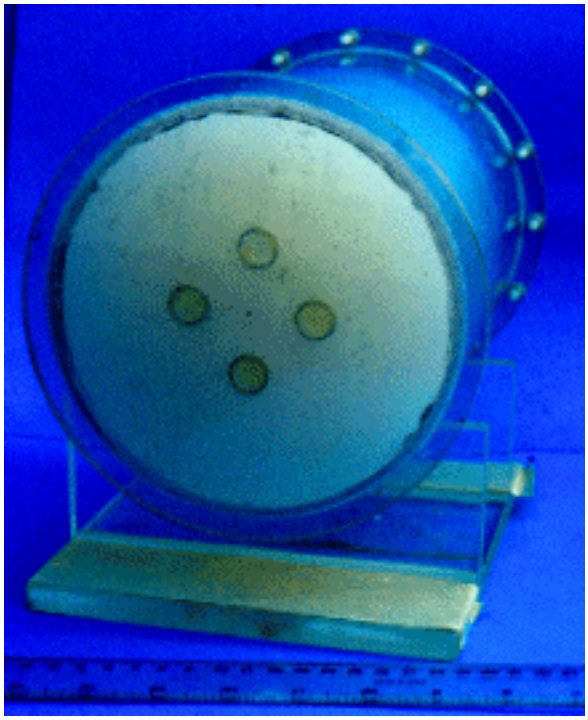

Figure 10-9. Cylinder phantom supported on PMMA alignment jig showing dosimeter access holes parallel to central axis.

For the purposes of the simulation the cylinder geometry was modeled as a cylinder of homogeneous brain equivalent material. Annular tally regions with an inner radius of 2.25 cm and an outer radius of 2.75 cm were used to accumulate a tally of flux and foil activation along the length of the cylinder in 0.5 cm thick slices. These regions corresponded to the radial position of the rods used to hold the detectors in the actual phantom. The PMMA rods and the spacers between detectors were not explicitly modeled in the MCNP simulation. Tally multipliers applied to track length flux tallies were used to generate reaction rates for the foil materials in the annular tally regions at each depth.

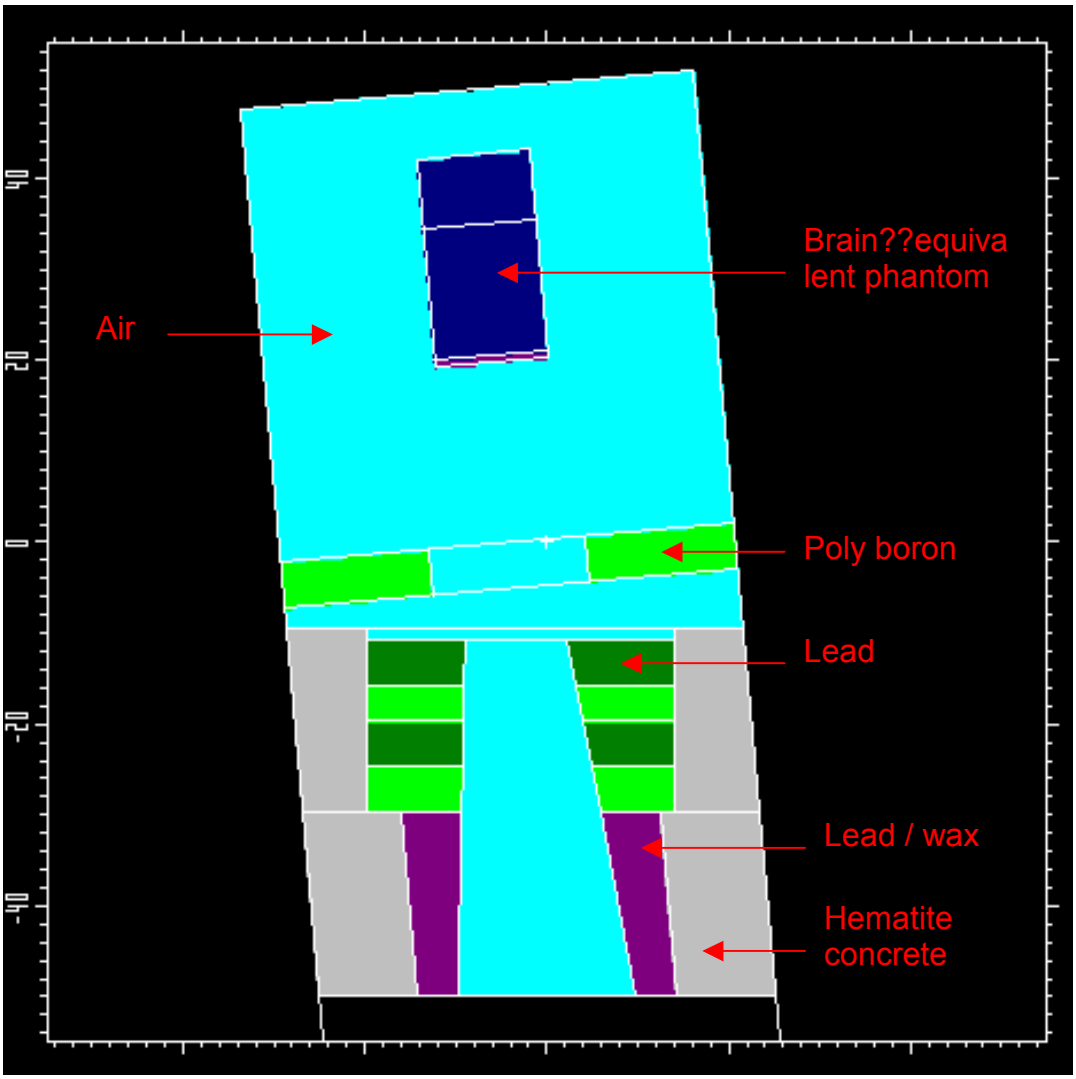

Figure 10-10. MCNP model of tissue equivalent cylinder phantom irradiated in HB11 epithermal neutron beam.

The cylinder phantom was modeled using MCNP as a cylinder containing tissue equivalent gel of the same constituency as the gel used in the skull phantom. The geometry of the MCNP model including the beam and collimator is shown in Figure 10-10. Similar geometry was also used for the simulations of the skull and cube phantoms.

THE CUBE PHANTOM.

The cube phantom consisted of a solid block of PMMA. It was 15cm on edge. It had dosimeter access holes drilled into it from the top surface. These were approximately 2 cm in diameter and approximately 10 cm deep, thus allowing dosimeters to be placed at a number of points along the central axis of the phantom. This phantom was manufactured by the NKI and has been used for numerous measurements in the HB11 beam[200] with various dosimeters. During irradiations it was supported on the treatment table.

FOIL ACTIVATION MEASUREMENTS

Activation foils were used to measure reaction rates on all axes for comparison with Monte Carlo predictions. For this purpose pairs of measurements were performed using bare and cadmium covered gold, copper and manganese foils. All foil activations were measured by the Petten counting laboratory using a sodium iodide or high purity germanium detector. These raw activity data were then corrected for decay and self shielding and specific activities were determined.

CYLINDER

Activation foil measurements were performed in the cylinder phantom using gold, manganese and copper foils. Measurements were performed using bare and

cadmium covered foils. Measurements were performed at multiple depths within the phantom. Several repeats of the gold foil measurements were done. For the gold foils measurements were made at depths of 2, 4, 6, 7 and 8 cm from the front face of the phantom. Measurements were made at points 2.5 cm from the central axis of the phantom. Since there were 4 PMMA access tubes in the phantom, one located in each quadrant it was possible to perform up to four measurements simultaneously at each depth.

For the manganese and copper foils a single bare and cadmium covered foil activation measurement was made at depths of 2 cm and 7 cm.

During measurements the space between detectors in the PMMA tubes was filled with PMMA spacer rods of appropriate length.

CUBE

For the PMMA cube phantom gold foil measurements were performed at depths of 2, 5 and 8 cm from the front surface of the phantom. A cadmium covered gold foil measurement was made at a depth of 2 cm. Unfortunately cadmium covered foil measurements were not performed at 5 or 8 cm depths in this phantom.

SKULL

Only gold foil measurements were performed in the head phantom. A single set of measurements was done using both bare and cadmium covered foils. All of the

bare foils were irradiated during a single exposure of the phantom. All of the cadmium covered foils were irradiated during a separate single exposure of the phantom.

RESULTS: FOIL ACTIVATION VS MONTE CARLO SIMULATIONS

The raw data including activation and exposure times are tabulated in Appendix D. In order to compare the foil activations with MCNP calculations of the expected activation the saturation activity in Bq per atom was calculated for each foil measurement. The corresponding quantity was derived from the MCNP calculations for comparison.

CYLINDER PHANTOM

The cylinder phantom was originally intended to be the simple geometry homogeneous phantom for use as a benchmark for measurements made in the more complex skull phantom. Bare and cadmium covered gold foil measurements at a radius of 2.5 cm and parallel to the phantom axis were consistent between separate sets of measurements.

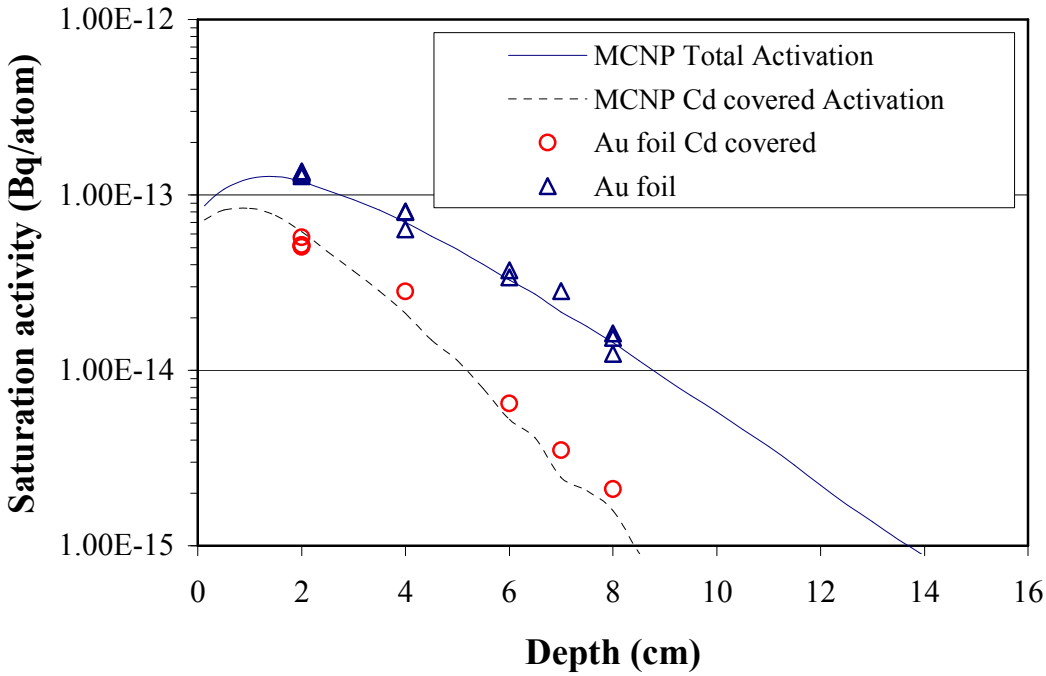

Figure 10-11. Measured activation of bare and cadmium covered gold foils in the tissue equivalent cylinder phantom. Note that the corresponding MCNP results were generated assuming 10% dehydration of the tissue equivalent material.

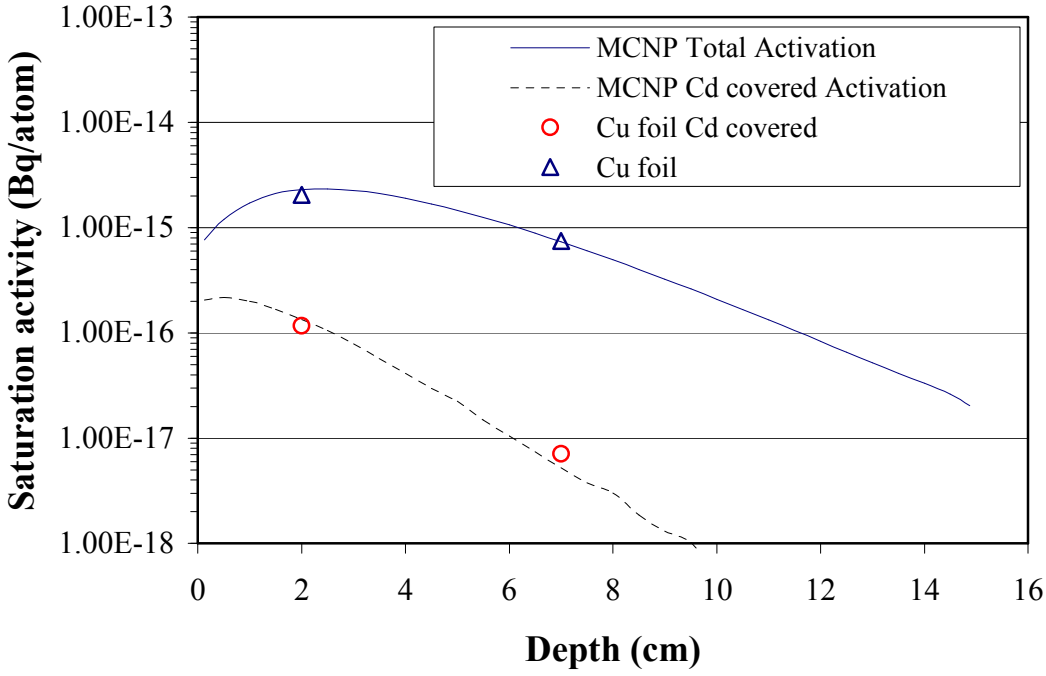

Figure 10-12. Bare and cadmium covered copper foil activation at 2 and 7 cm depths in the cylinder phantom. MCNP results for the activations assume 10% dehydration of the gel.

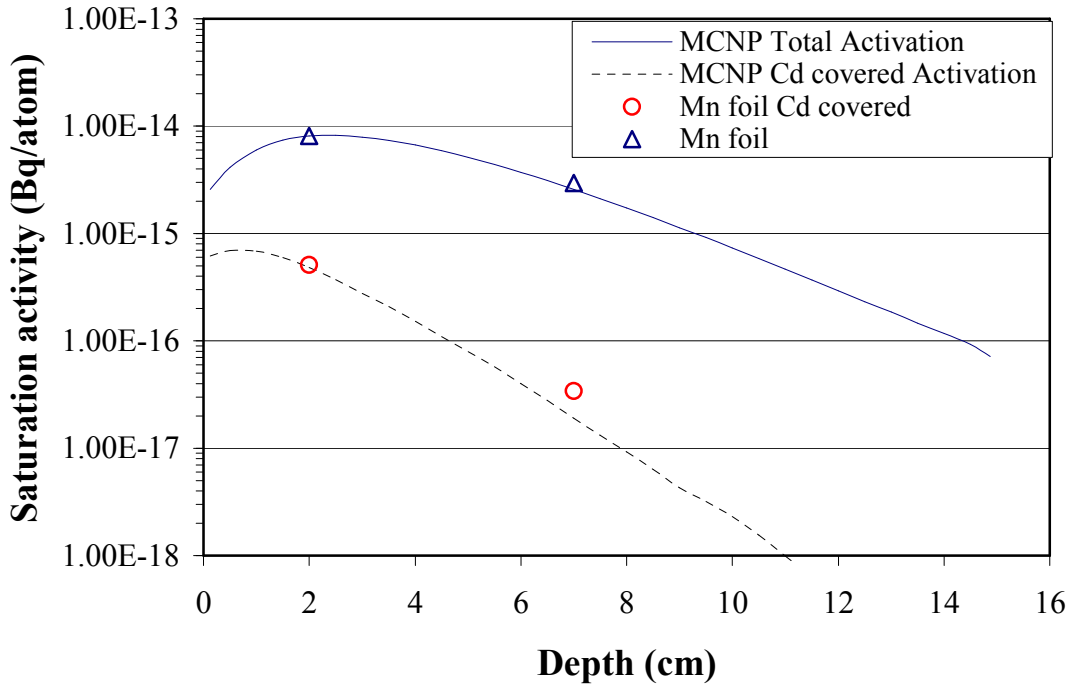

Figure 10-13. Bare and cadmium covered Mn foil activations in the cylinder phantom. MCNP calculated activations assume 10% dehydration of the tissue equivalent gel.

This can be seen in Figure 10-11 where the gold activation foil data from a number of separate exposures is presented on a single graph.

Similar results from measurements at depths of 2 cm and 7 cm for copper and manganese foils are shown in Figure 10-12 and Figure 10-13. The bare and cadmium covered activations with these three types of foils provide measurements spanning an energy range from thermal to 580 keV.

The tissue equivalent gel in the phantoms was produced by S Wallace[194] and for the initial MCNP simulations was assumed to be ICRU 46 brain equivalent material. However poor agreement between foil activation measurements and the Monte Carlo simulations at depth suggested that either the density or the hydrogen content of the gel may have decreased in the interval between fabrication of the phantom and performance of the measurements. The experimental measurements,

particularly for the cadmium covered foils, exceeded the MCNP calculated activations as the depth increased suggesting that the incident neutron spectrum was not being moderated in the phantom as much as would be expected for the assumed constitution of the gel. This effect was greater for the Mn and Cu foils that have higher energy resonances than the Au foils. This was also apparent in later measurements with PIN diodes (see Chapter 11).

If the MCNP model was changed to reflect approximately 10% dehydration of the gel good agreement was achieved between the foil activation (in terms of saturation activities) calculated by the MCNP model and the experimentally measured activation. See the solid and broken curves in Figure 10-11, Figure 10-12 and Figure 10-13.

In this way good agreement was achieved for all of the foil types (Au, Cu, Mn) and also for PIN diode measurements and therefore justifies the assumption that the hydrogen content of the gel was less than originally expected. On this basis a similar adjustment was made to the assumed hydrogen content of the skull phantom.

The details of the HB11 collimator and beam spectrum used for the MCNP simulations were supplied by Watkins[a]. This HB11 source spectrum data had been extensively verified and validated therefore the origin of the initial discrepancy in our results was sought in the details of the phantom and its simulation rather than in the accuracy of the source spectrum.

[a] P Watkins, private communication to S Wallace, December 1993.

PERSPEX CUBE PHANTOM

As noted above only gold foil measurements were made in the perspex cube phantom. These were made at 2, 4 and 8 cm depths. A single cadmium covered gold foil activation was done at 2 cm. When compared to a MCNP simulation the cadmium covered gold activation at 2 cm depth was within 7% of the measured value and the bare gold foil activation at the same depth was within 13% of the measured value. The MCNP calculated bare gold foil activations at 5 cm and 8 cm depths were within 20% of measured values. This data is shown in Figure 10-14.

The good agreement achieved between simulation and measurement for the well defined geometry and material composition of the perspex cube phantom allows confidence in the simulation of the other phantoms.

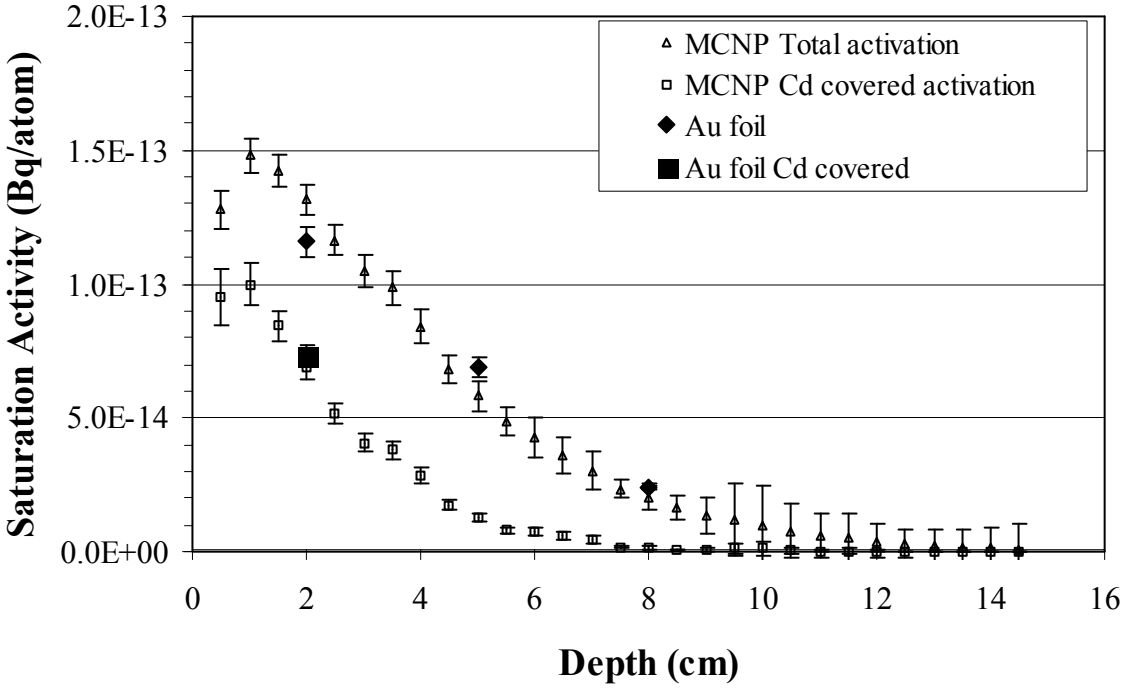

Figure 10-14. Gold foil activation measurements along central axis of perspex cube phantom exposed in HB11 beam.

No adjustments were required to the density or assumed material composition of the perspex phantom in the MCNP simulation to achieve this agreement. By validating the measurement technique and MCNP model these consistent results indirectly support the assumption previously made about the decreased hydrogen content of the cylinder phantom.

SKULL PHANTOM

Gold foil measurements were made at each measurement location in the head phantom. Both bare foils and cadmium covered foils were used. The results of these measurements are presented along three axes; the beam axis from left to right through the head, the vertical (superior-inferior) axis and the horizontal (anterior-posterior) axis. Along with the activation foil measurements are presented MCNP calculations of the expected bare and cadmium covered gold foil activations at each measurement point.

The concordance that was obtained between the MCNP calculated foil activations and the experimental data for the case of the skull phantom was not as good as the agreement that was achievable for the phantoms with simpler geometries. The general trend in the observed discrepancies was for the cadmium covered foil measured data to exceed the activation predicted by the MCNP model. Even decreasing the hydrogen content in the tissue equivalent gel by 10% to allow for dehydration of the gel did not fully correct this effect.

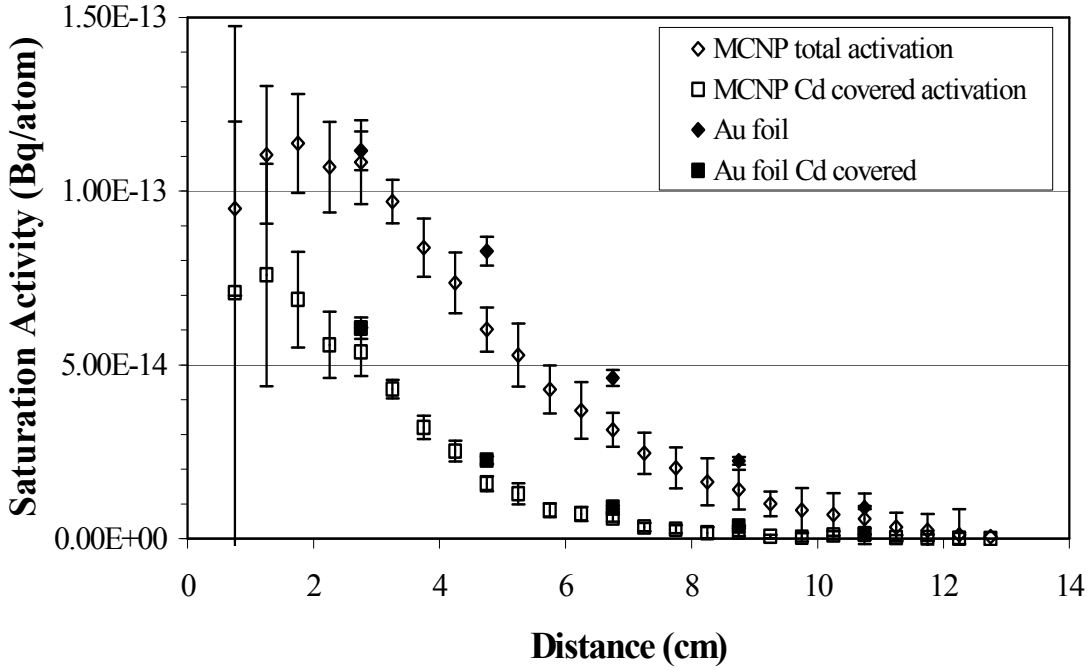

Figure 10-15. Measured and MCNP calculated gold foil activation for bare and cadmium covered foils along the beam axis in the head phantom exposed on HB11.

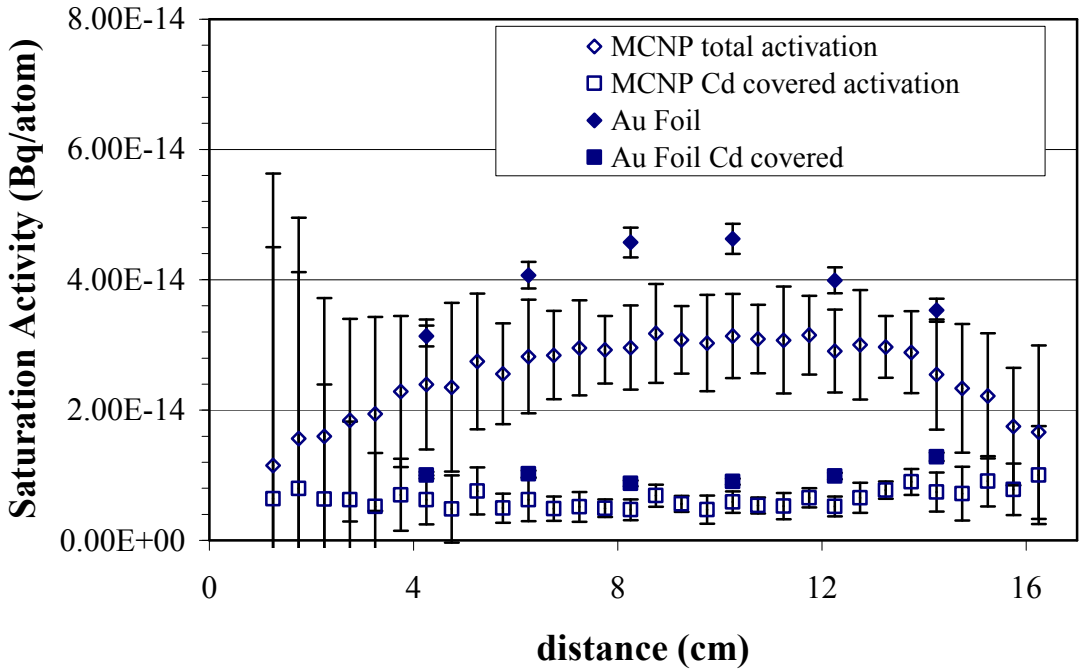

Figure 10-16. Gold foil activation measurements and MCNP calculated activations along the anterior–posterior axis of the head phantom.

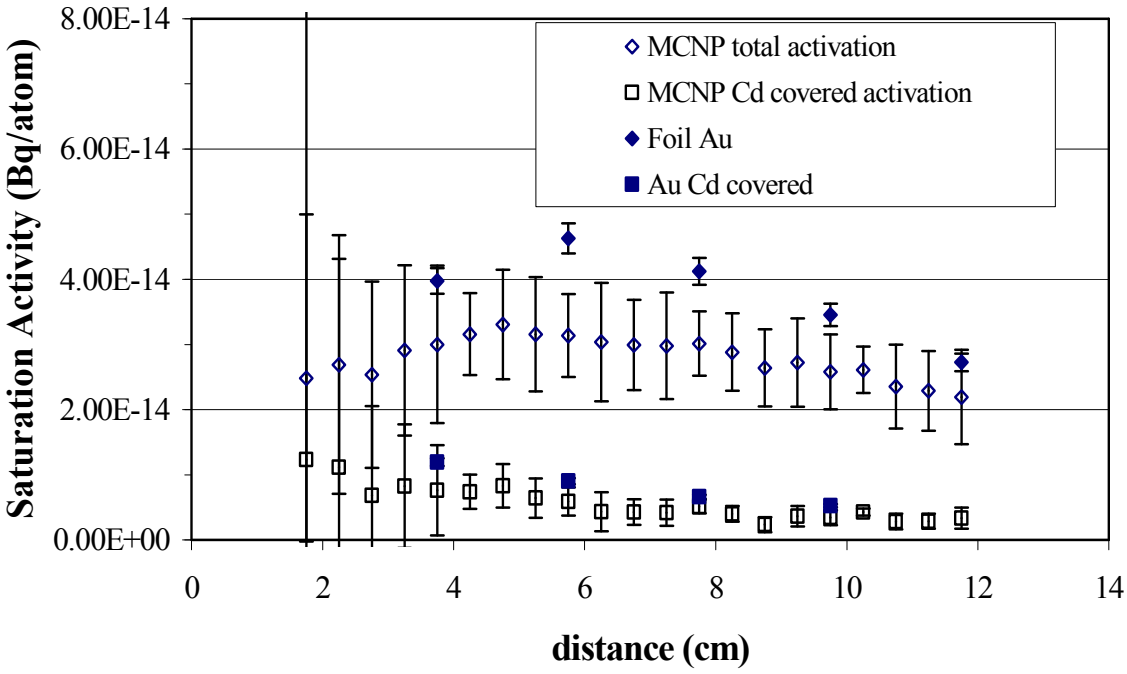

Figure 10-17. Measured and calculated gold foil activations along the vertical axis in the head phantom exposed in the HB11 beam.

There also remains some uncertainty about the exact composition of the bone in the skull since the skull that was used was a one previously used in a teaching laboratory and therefore would be expected to have significantly lower hydrogen content than live bone found in-vivo. In both the skull and the cylinder models the PMMA tubes and spacer rods were not explicitly modeled. This may be expected to introduce some error since both the mass density and the atomic density of hydrogen in PMMA is less than that in tissue. For the PMMA rod that was coaxial with the centerline of the neutron beam some streaming along this lower density channel formed by the PMMA could be proposed. However this cannot account for all of the discrepancy since clearly the foils located along the sagittal and axial axes display an over response along their entire lengths. Most of the depth traversed by neutrons reaching these points is via tissue equivalent gel and not along the PMMA rod

coaxial with the beam. Another proposed explanation[194] is that the beam divergence is actually less than the 10° used in the MCNP model. A more forward directed beam would result in a greater dose at depth.

CONCLUSIONS

MCNP models of a head phantom, a tissue equivalent cylindrical phantom and a cubic PMMA phantom have been generated and simulated in the Petten HFR epithermal neutron beam. Gold, Copper and Manganese activation foil measurements were found to be in approximate agreement with the simulations. In each case the cadmium covered foil measurements at depth overestimated the calculated foil activations. By modifying the hydrogen content of the tissue equivalent gel a better agreement was obtained. This modification to the hydrogen content is reasonable on the basis that the gel used was fabricated well before the phantoms were used in these measurements and it is possible that some dehydration occurred over this period of many weeks. The agreement for the phantoms with simpler geometries was better than that for the more complex skull phantom. In hindsight for the purpose of benchmarking and characterization of the PIN diode and MOSFET dosimeters more emphasis should have been placed on measurements in the simpler phantoms.

The principle aim of the measurements described in this chapter has been to demonstrate that it is possible to experimentally verify MCNP calculations of the neutron flux in the three phantoms used when they are irradiated in the Petten HFR epithermal neutron beam (HB11). This has been achieved within the uncertainties evident in the results given above. On this basis the same MCNP models will be used to calculate silicon displacement damage dose and induced gamma dose for

comparison with experimental measurements using PIN diode dosimeters and MOSFET dosimeters in the same phantoms. Ideally agreement with the MCNP model at least equivalent to that obtained here should be achievable for the PIN diode and MOSFET dosimeters.

CHAPTER 11 PETTEN HFR HB11 BNCT BEAM MEASUREMENTS: PIN DIODE MEASUREMENTS

INTRODUCTION

In this chapter PIN diode measurements of silicon damage dose are described in three phantoms exposed in the Petten HB11 epithermal neutron beam. The methods used will be described in the following order; the PIN diode readout system, measurement and calculation of PIN diode linearity correction and temperature coefficient, PIN calibration exposure in the bare HB11 beam and measurements in the skull, cylinder and cube phantoms. The results of the phantom measurements are then given and compared with MCNP simulations of the same.

MATERIALS AND METHOD

The construction of the phantoms and the details of the corresponding MCNP simulation models are given in the previous chapter and will not be repeated here. A description of the HB11 beam is also found in the previous chapter.

PIN DIODE READOUT

The PIN readout was performed using the circuit built at Ansto[a]. This consisted of a pulsed constant current source of 1 mA. This source gave a 1 mA pulse

[a] Readout circuit built by H Meriaty, Ansto.

of 1 mS duration every 11.2 mS. This current pulse was used to forward bias the PIN diode being measured. The voltage across the PIN junction was connected to the inputs of a FET input operational amplifier. The signal from this amplifier was then feed to a peak detector circuit. This is shown in Chapter 3, (Figure 3-6).

The output voltage from the peak detector was measured using a Keithly digital voltmeter. The voltmeter has a reading resolution of ± 0.1 mV. Repeated measurements of a standard 100 ohm resistor placed across the test points showed a variability of approximately ± 4 mV in the output voltage over a time period of several days. Throughout the course of the measurements at the Petten HFR the standard 100 ohm resistor was used to check on this drift in the circuit. Since the data of interest for the PIN diode measurements is the difference between the PIN threshold voltage before and after the irradiation a small drift that affects both of these readings does not yield significant errors in the final result. The observed changes in the reader output when measuring the 100 ohm standard occurred over the course of days. With few exceptions all measurements of PIN diodes before and after irradiation were separated by no more than several hours. Short term fluctuations in the readout of the PIN diodes arising from noise or other instabilities of undetermined origin were less than 1 mV.

PINs were connected directly to the PIN reader circuit to avoid any voltage drop arising due to resistance of leads and to keep the readout procedure reproducible.

To ensure that the temperature during the PIN diode readout was as constant as possible lead blocks were placed in contact with the outer surface of the PIN diode encapsulation. One block was placed above and one below the diode. During the

interval between readouts these blocks were left on the readout bench and were therefore in thermal equilibrium with the ambient temperature in the Reactor Containment Building (RCB). Throughout the series of measurements this temperature was observed to be 22 ± 1° C. The RCB temperature was monitored via built in thermocouples. The temperature of the lead blocks used to stabilise the temperature of the PIN diodes was measured using a mercury thermometer that was placed in direct contact with them. The readings on the thermometer were observed to agree with the RCB thermocouples to within 0.2 ° C. As far as possible the PIN diodes were handled using forceps to avoid heating them with body heat from the experimenters fingertips. This technique also minimised dose and transfer of contamination to the experimenter.

The PIN diodes were read out immediately prior to setting up the phantom and commencing the irradiation. The forward bias voltage, the time and the temperature were recorded. Following the pre-irradiation readout the PIN diodes were installed in the phantom or mounted in the beam in the case of calibration exposures. Depending on the phantom this involved a 15-30 minute delay between the readout and the commencement of the irradiation. The time of the commencement of the irradiation was taken to be when the in room Gieger Muller monitors installed on the treatment room wall reached half maximum.

At the completion of the irradiation period the beam shutter was closed. The shutter closure takes approximately 6 seconds to complete. Since the shortest exposure (beam on) time used in these experiments was approximately 15 minutes the shutter close time was not considered a significant source of error. The phantom was then quickly disassembled in the treatment room and the PIN diodes removed.

The PIN diodes were then removed to the area adjacent to the treatment room for post irradiation readout. The unread diodes were placed on a lead block to ensure that they were at the ambient temperature prior to readout. Measurements of the temperature in the treatment room showed it to be within approximately ± 1° C of the temperature outside in the RCB. Therefore there was not a large temperature variation between the irradiation and the readout phases of the measurements and there was no need to allow long periods for the PIN diodes to thermally equilibrate when they were removed from the phantom.

LINEARITY CORRECTION

The approximate linear response of forward bias voltage to dose for the PIN diode extends for about 100-200 mV depending on the degree of accuracy required. For radiation exposures that lead to doses with forward bias voltage changes beyond this range it is necessary to apply a correction of some kind to account for the roll off in sensitivity with increasing dose.

The method of correction developed for this work is based on the general shape of the voltage versus dose curve for the PIN diodes used. Once the shape of the curve is known the only other inputs required to determine the correction are the initial calibration factor and the initial forward bias voltage before the PIN was exposed to any radiation. This initial forward bias voltage is referred to here as the "forward bias voltage at birth", $V_f(\text{birth})$, to distinguish it from the initial forward bias voltage for any given measurement, $V_f(i)$.

The general shape of the PIN diode response was determined by exposing a

PIN diode to a constant low dose rate of ^{252}Cf neutrons for approximately 2000 hours at Ansto Laboratories[a]. This data was collected with the PIN diode unconnected to the reader circuit except for the times at which forward bias measurements were made. The neutron spectrum consisted of moderated and unmoderated components since the PIN diode was placed in direct view of the source at the opening of the source entrance channel of a cylindrical boronated wax storage drum. The dose rate at this entrance is not known accurately and the PIN diode calibration was not based on these measurements. Only the shape of the PIN diode response curve was derived from these measurements. The PIN diode change in forward bias voltage as a function of time at a constant rate of exposure is shown in Figure 11-1. The curve fitted to the data in terms of the total change in forward bias voltage (in volts) and exposure time in hours was:

$$\Delta V_f = 4.296(1 - e^{-6.39\times10^{-4}t}) + 0.0016 \qquad 11\text{-}1$$

The line of linear response is based on the gradient of the response curve over the first 10 hours of exposure which corresponded to approximately a 28mV shift in the forward bias voltage. This magnitude of voltage change is a reasonable increment over which to determine the initial slope and a calibration factor given a reader accuracy of at least 0.1 mV. From these two curves, the extrapolated linear response and the curve fitted to the measured data, the ratio of the linear response to the actual response can be determined.

[a] Cf-525 PIN diode measurements performed by H Meriaty, Ansto.

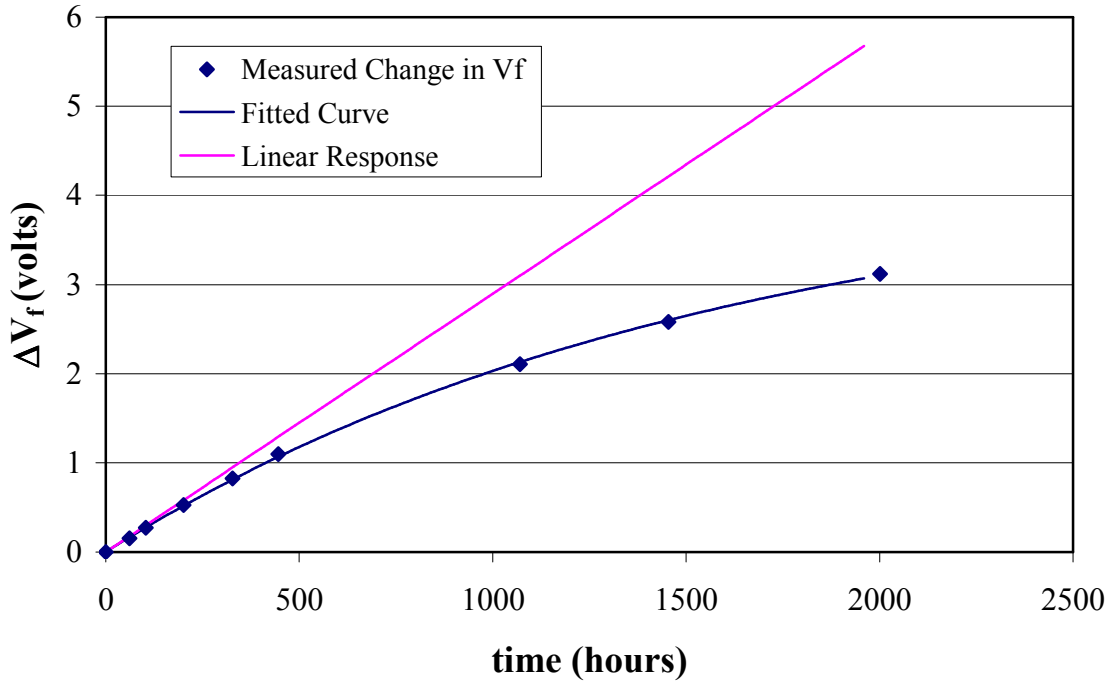

Figure 11-1. PIN forward bias voltage as a function of exposure time with AmBe neutron source.

This ratio is the factor by which the actual measured PIN forward bias voltage needs to be adjusted to give the forward bias voltage that would be observed if the PIN diode responded linearly with dose over its entire time of use.

Since the ordinate is currently in terms of exposure time the ratio was calculated and then plotted as a function of the actual forward bias voltage change relative to V_f(birth). A polynomial curve was fitted to resulting data. This polynomial defines the correction factor to be applied for any given forward bias voltage in order that the same calibration factor can be used for the whole of the useful life of the PIN diodes. The curve describing the correction factor is clearly a continuous slowly increasing function over the range of interest. This is shown along with the polynomial expression in Figure 11-2.

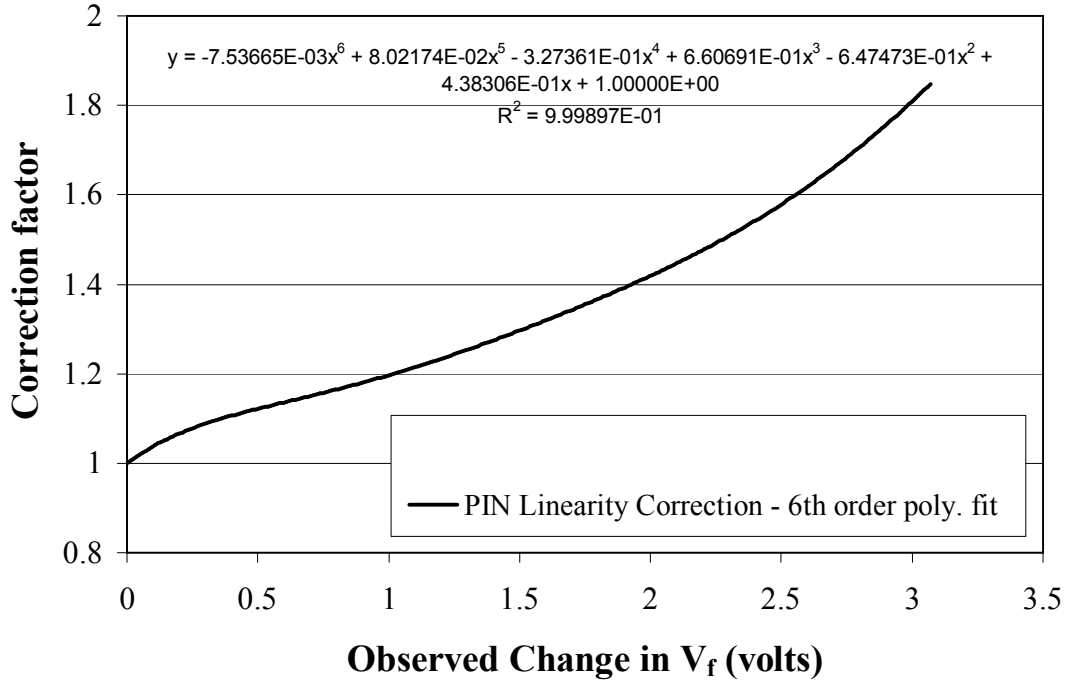

Figure 11-2. Correction factor for PIN diode linearity. A 6th order polynomial fitted to the ratio of the initial linear response to the actual PIN diode response.

As a check of this correction curve and to ensure that no significant errors had propagated through the calculations it was reapplied to the original PIN diode ^{252}Cf exposure data. When linearity corrections derived from this polynomial were applied to the measured data a straight line resulted for the forward bias versus exposure time plot (Figure 11-3). This verified that the calculations were self consistent and no significant rounding or other errors were present.

The polynomial describing the correction factor was applied to all PIN diode forward bias data measured in this series of phantom experiments by means of a spreadsheet calculation to correct for non linearity in all measured data.

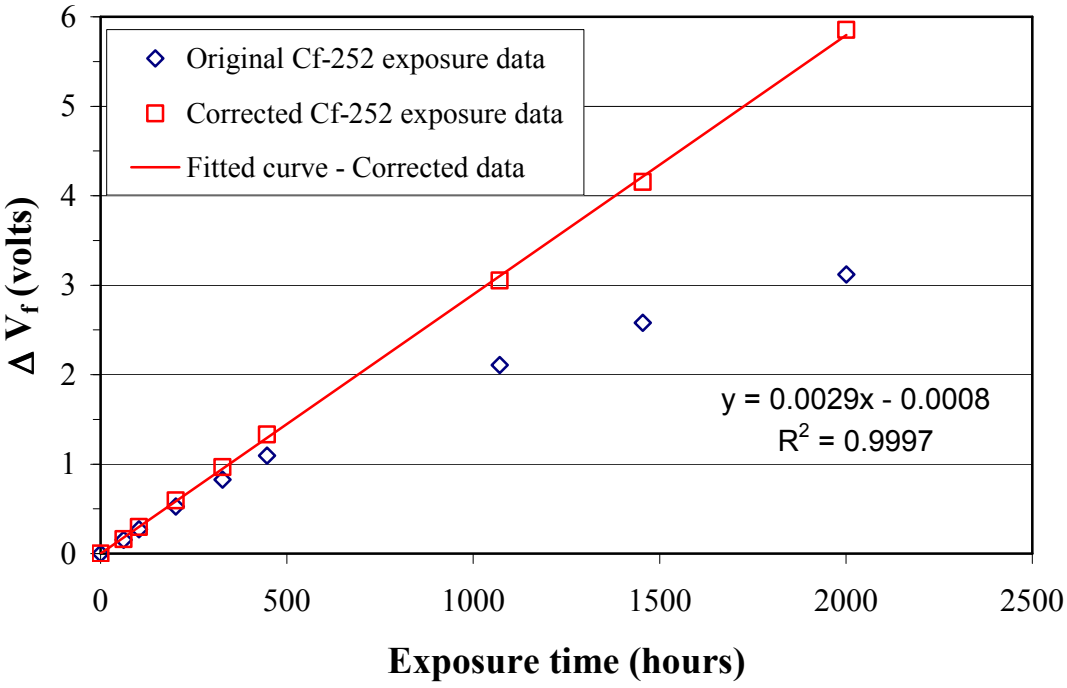

Figure 11-3. Linearity correction applied to the original PIN diode responses showing the resultant straight line for corrected data and verifying the internal consistency of the correction.

TEMPERATURE CORRECTION

As noted above the variation in temperature between the treatment room and the RCB ambient temperature was minimal (usually < 1˚C). This meant that the temperature of the dosimeters at the pre irradiation readout differed very little from the temperature at the post irradiation readout. However in order to apply a correction for any forward bias voltage change that was attributable to temperature effects a characteristic forward bias voltage versus temperature curve was acquired.

A plastic (polyethylene) sheathed PIN diode from the same batch as the dosimeters used for the phantom measurements was immersed in a water bath that was heated to approximately 60˚C. The bath was allowed to cool to room

temperature and was then lowered to approximately 10˚C by the addition of a small quantity of ice. The temperature of the water bath was monitored by means of a mercury thermometer. The average cooling rate was less than 0.5˚C.min^{-1} in order to ensure that the thermometer, PIN diode and water were in equilibrium. Measurements of forward bias voltage were made periodically over the 10-60˚C temperature range which is considered to adequately cover the probable operating temperature range of the dosimeters. These measurements were made with a 1.00 mA forward current from a constant current source. The voltage versus temperature data is displayed in Figure 11-4. It can be seen that over the temperature range measured a least squares linear fit is quite adequate to describe the data. The temperature coefficient is -1.3 mV.˚C^{-1}.

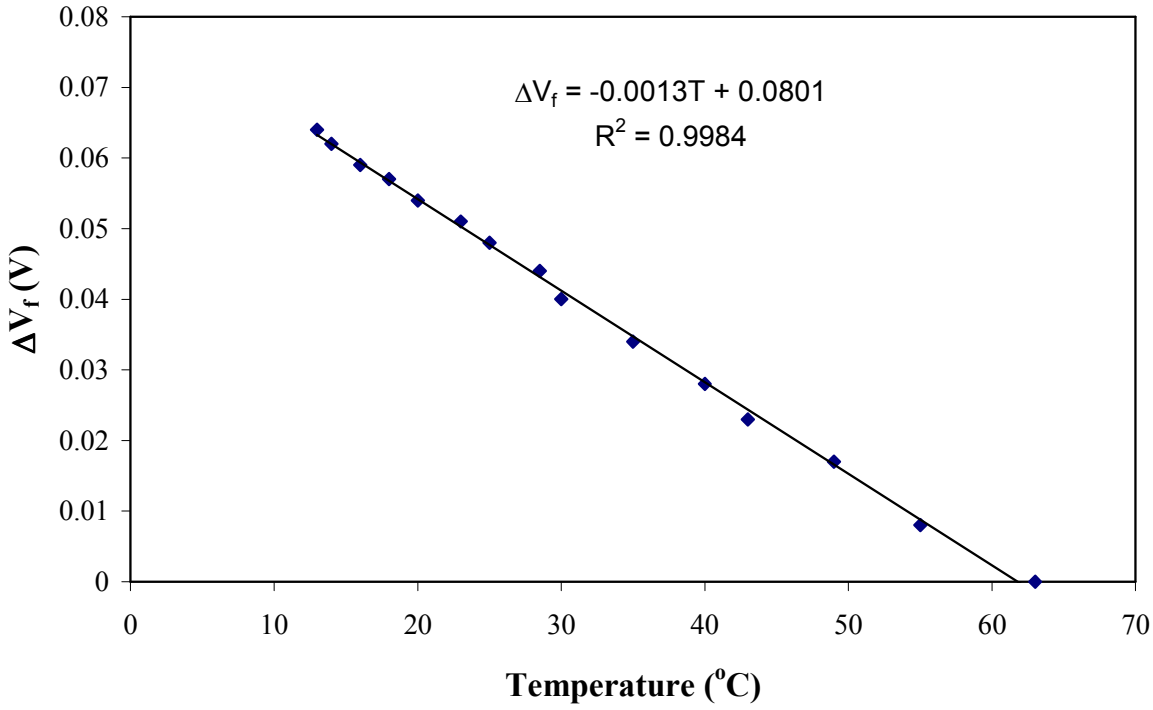

Figure 11-4. Forward bias voltage temperature characteristic of PIN diode dosimeter.

For all of the data collected a temperature correction based on this coefficient was applied whenever there was a temperature difference between the pre and post irradiation forward bias voltage readouts.

CALIBRATION EXPOSURES

The HB11 beam was well characterised prior to and independently of the measurements described here. Therefore measurements in the direct beam with no phantom present provided a good source of epithermal neutrons for determining the calibration of the PIN diodes in terms of threshold voltage change per unit silicon displacement damage KERMA.

This calibration consists of two steps. Firstly from the known spectrum of the neutron beam at the point where the PIN diodes are to be exposed the silicon damage KERMA is calculated. This was done by using a MCNP model of the beam and applying an energy dependant tally dose factor to a flux tally at the measurement point. The tally dose factor was the ASTM data[125] for silicon displacement damage KERMA for silicon. This yields the actual silicon damage dose per unit fluence of the beam. The PIN diodes were then exposed in the beam for a known time at a constant fluence rate. Normalisation factors for the MCNP model were based on gold foil activation measurements. The forward bias voltage change is then known per unit fluence and the MCNP simulation derived fluence to dose factor is used to convert the PIN diode calibration into units of mV per cGy of silicon damage KERMA.

The experimental assembly for the irradiation involved attaching all of the

PIN diodes to a thin (~ 2 mm) aluminium sheet using adhesive tape. This aluminium sheet was then clamped in the beam so that the axis of the beam was normally incident on the sheet of aluminium holding the PIN diodes. All the diodes were at least 2 cm from each other and no absorbent or scattering materials were placed between the beam port and the diodes.

This process was repeated twice for the entire set of diodes used in the HB11 measurements. One irradiation was performed with the 8 cm collimator and another was performed with the 15 cm collimator in place. The distance from the collimator face to the point where the diodes were irradiated was 20cm in both cases. The range of temperatures that existed during these irradiations was from 21.8˚C to 23˚C. All forward bias voltage measurements were adjusted for any temperature differences between the initial and final readouts. The reactor power was set at 45 MW during both irradiations. The first exposure in the 8 cm diameter field was for 20 min 10 sec. The exposure in the 15 cm diameter field was for 20 min 0 sec.

RESULTS

BARE BEAM CALIBRATIONS

The changes in threshold voltage for each PIN diode corrected for temperature and for linearity are shown below in Table 11-1.

Table 11-1. PIN diode ΔV_f changes following calibration exposure in HB11.

PIN Diode Number	Collimator / Field size	ΔV_f per hour of exposure at reactor power of 45MW.
1	8 cm diameter	0.055
2	8 cm diameter	0.076
4	8 cm diameter	0.078
5	8 cm diameter	0.083
6	8 cm diameter	0.095
7	8 cm diameter	0.069
8	8 cm diameter	0.078
9	8 cm diameter	0.068
10	8 cm diameter	0.101
11	8 cm diameter	0.098
12	8 cm diameter	0.087
13	8 cm diameter	0.085
14	8 cm diameter	0.093
1	15 cm diameter	0.138
2	15 cm diameter	0.128
4	15 cm diameter	0.131
5	15 cm diameter	0.127
6	15 cm diameter	0.127
7	15 cm diameter	0.120
8	15 cm diameter	0.119
9	15 cm diameter	0.111
10	15 cm diameter	0.122
11	15 cm diameter	0.124
12	15 cm diameter	0.127
13	15 cm diameter	0.121
14	15 cm diameter	0.116
1	15 cm diameter	0.152
2	15 cm diameter	0.091
4	15 cm diameter	0.100

The Monte Carlo simulation of the experimental set up that was used to derive the fluence to dose factor yields a silicon damage dose of 0.576 cGy h^{-1} for the 15 cm diameter beam. This assumes a MCNP model normalisation factor of 1.857×10^{11} source neutrons per second (based on activation foil measurements). This in turn gives the PIN diode calibrations shown in Table 11-2.

Table 11-2. PIN diode calibration factors as measured in HB11.

PIN Diode Number	**Calibration ($V.cGy^{-1}$ silicon damage KERMA)**
1	0.239
2	0.223
4	0.227
5	0.220
6	0.220
7	0.209
8	0.206
9	0.193
10	0.211
11	0.215
12	0.220
13	0.209
14	0.201

These give an average calibration factor (±1 SD) of 214.9 $mV.cGy^{-1}$. (±11.9 $mV.cGy^{-1}$).

SKULL IRRADIATION RESULTS

All the measured diode forward bias changes were corrected for readout temperature differences and the linearity correction was applied to account for the stage of their life cycle. The calibration factor measured in the free beam appropriate to each individual diode was then applied to each forward bias voltage change. This yields a quantity that is the measured silicon damage dose at the point of measurement. As previously described measurements were made at several points along the major axes of the head phantom. These results are listed in Table 11-3 and Table 11-4 below. Note that during the course of the experiment PIN diode number 3 was found to be defective (suspect internal connections) and use of this diode was discontinued.

Table 11-3. Measured Silicon Damage Doses in Head Phantom, irradiation 1.

Location code	PIN Number	Measured Silicon Damage Dose ($cGy.h^{-1}$)
A1	1	0.281
A2	2	0.146
H4	3	--
H5	4	0.092
H1	5	0.072
H2	6	0.040
H3	7	0.050
V1	8	0.075
V2	9	0.106
V3	10	0.047
V4	11	0.030
V5	12	0.035

Table 11-4. Measured Silicon Damage Doses in Head Phantom, irradiation 2.

Location code	PIN Number	Measured Si Damage Dose ($cGy.h^{-1}$)
H4	1	0.067
A2	2	0.165
H5	4	0.107
H1	5	0.095
H2	6	0.077
H3	7	0.075
V1	8	0.111
V2	9	0.098
V3	10	0.065
A3	11	0.048
A4	12	0.030

TISSUE EQUIVALENT CYLINDER RESULTS

All the measured diode forward bias changes were corrected for readout temperature differences and the linearity correction was applied to account for the stage of their life cycle. The calibration factor measured in the free beam appropriate to each individual diode was then applied to each forward bias voltage change. This yields a quantity that is the measured silicon damage dose at the point of measurement. The measured silicon damage doses are shown in Table 11-5 below.

Table 11-5. Measured silicon damage dose in a tissue equivalent cylinder.

Position, depth in cm	PIN Number	Measured Silicon Damage Dose ($cGy.h^{-1}$)
2	1	0.375
2	2	0.364
2	3	--
2	5	0.313
2	6	0.440
2	7	0.479
7	4	0.042
7	5	0.074
7	6	0.056
7	5	0.064
7	6	0.076
7	7	0.072

PMMA CUBE RESULTS

All the measured diode forward bias changes were corrected for readout temperature differences and the linearity correction was applied to account for the stage of their life cycle. The calibration factor measured in the free beam appropriate to each individual diode was then applied to each forward bias voltage change. This yields a quantity that is the measured silicon damage dose at the point of measurement. The measured silicon damage doses are shown in Table 11-6 below.

Table 11-6. Measured silicon damage dose in perspex (PMMA) cube.

Depth cm	PIN Number	Measured Silicon Damage Dose ($cGy.h^{-1}$)
2	1	0.369
8	2	0.040

COMPARISON OF PIN DIODE RESULTS WITH MONTE CARLO CALCULATIONS

CYLINDER PHANTOM

The comparison of measured data and MCNP generated silicon damage dose in a tissue equivalent cylinder exposed in HB11 is shown in Figure 11-5. The measured data are the absolute silicon damage doses per hour as determined above. The MCNP model normalisation factor of 1.857×10^{11} is based on foil activation data in the bare beam. The only modification that has been made to the original MCNP model is that the hydrogen content of the tissue equivalent gel filling has been reduced by 10% to account for dehydration of the phantom in the interval between fabrication and the measurements described here.

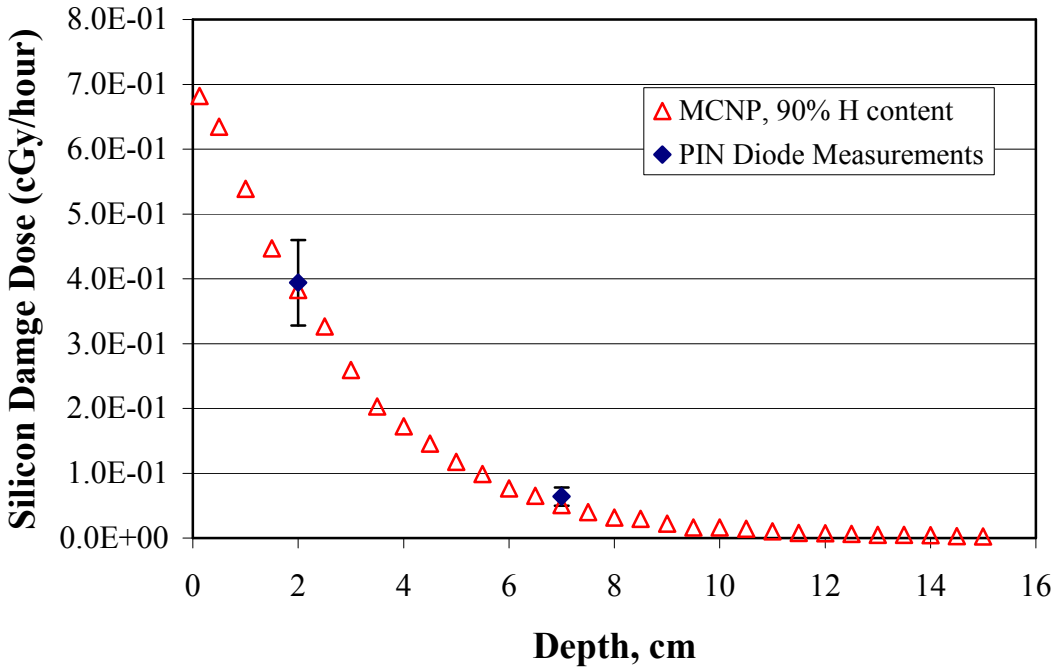

Figure 11-5. Measured and calculated silicon damage dose in a tissue equivalent cylinder exposed to a 15 cm diameter epithermal neutron beam on HB11 facility, Petten. Note that the data points representing the measured data are the average of several measurements (error bars represent ± 1 σ).

PERSPEX (PMMA) CUBE PHANTOM

The MCNP calculated silicon damage dose along the central axis of a PMMA cube exposed in the HB11 beam is shown in Figure 11-6 below. Also shown is the measured PIN diode data. No corrections to the MCNP model were necessary for the cube phantom calculated data to achieve a good agreement with the measured data.

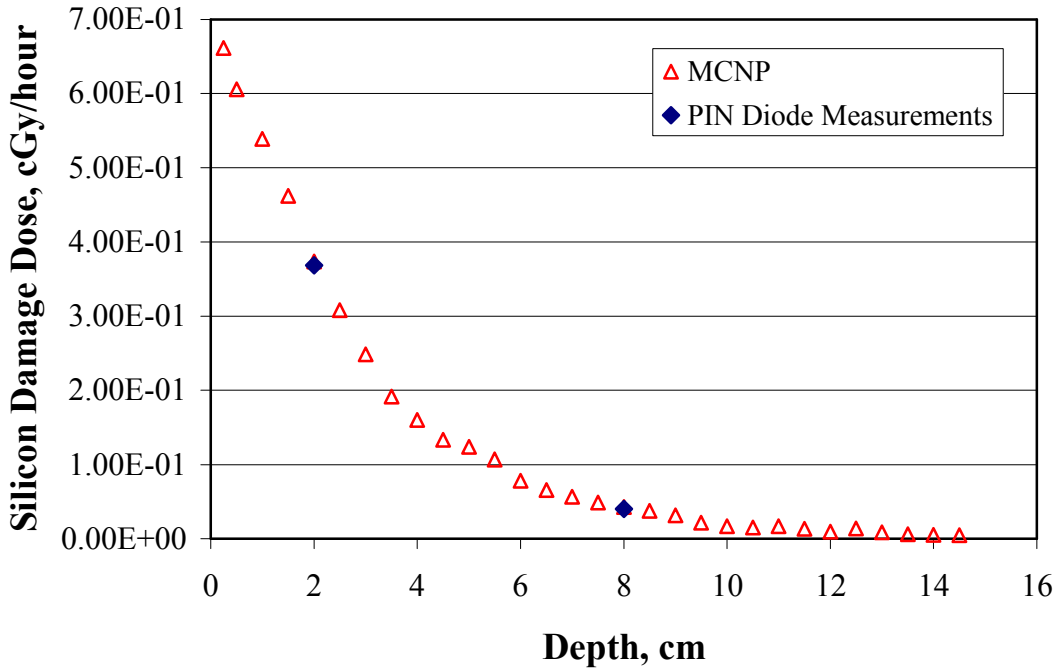

Figure 11-6. PIN diode measurements of silicon damage dose along the central axis of a PMMA cube exposed in the HB11 beam at Petten. MCNP Monte Carlo calculations of the expected silicon damage dose are also shown. The normalisation of the MCNP data is based on foil activation measurements.

SKULL PHANTOM DATA

Because of the more complex geometry involved and due to some presumed dehydration of the tissue equivalent gel used in the skull phantom close agreement between the PIN diode measurements of the silicon damage dose and the MCNP calculated doses were not achieved in the first instance. As was shown above it was necessary to adjust the cylinder hydrogen content in order to achieve a good agreement between the PIN diode results and the MCNP calculations. However having made this correction reasonable agreement was achieved.

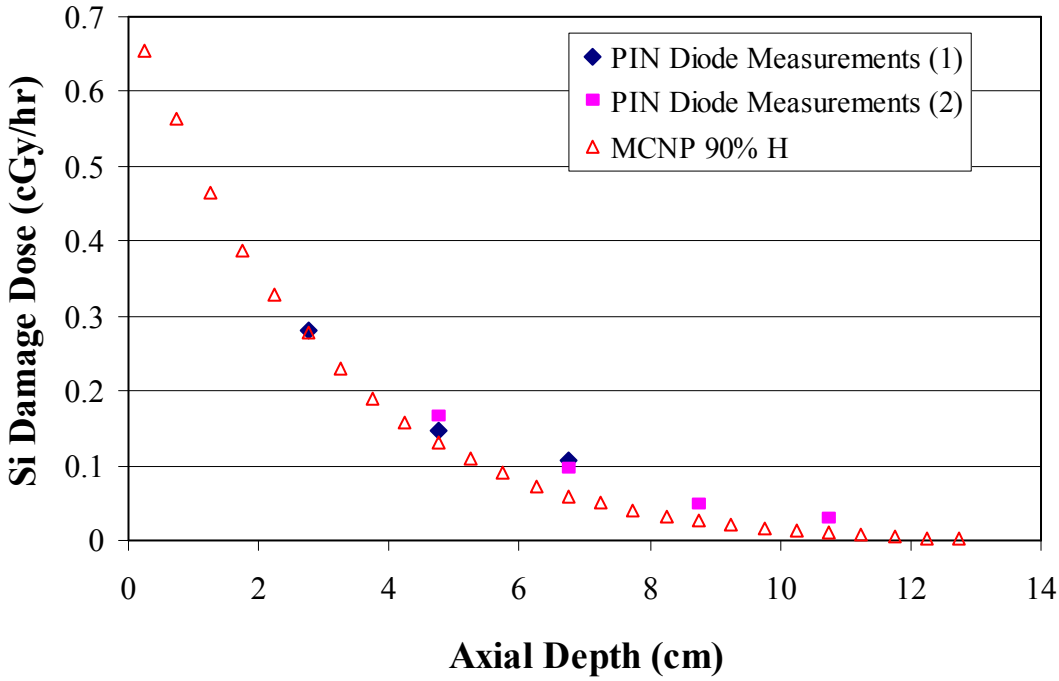

Figure 11-7. Measured silicon damage dose along the beam axis in the skull phantom.

It was therefore assumed that the same inaccuracy may be present in the assumed hydrogen content of the tissue equivalent gel in the head phantom. For this reason the hydrogen content was reduced to 90% in the brain tissue and the MCNP simulation recalculated.

Adjusting the hydrogen content of the brain and soft tissue in the MCNP model of the head still does not yield a close agreement in terms of absolute silicon damage dose. However the trend in the measured data is toward increasing over estimate of the silicon damage dose with increasing axial depth. This suggests that the MCNP model is underestimating the faster component of the neutron spectrum at depth. The explanation for this may be that the tissue equivalent gel was in fact more dehydrated than estimated (i.e. more than 10%).

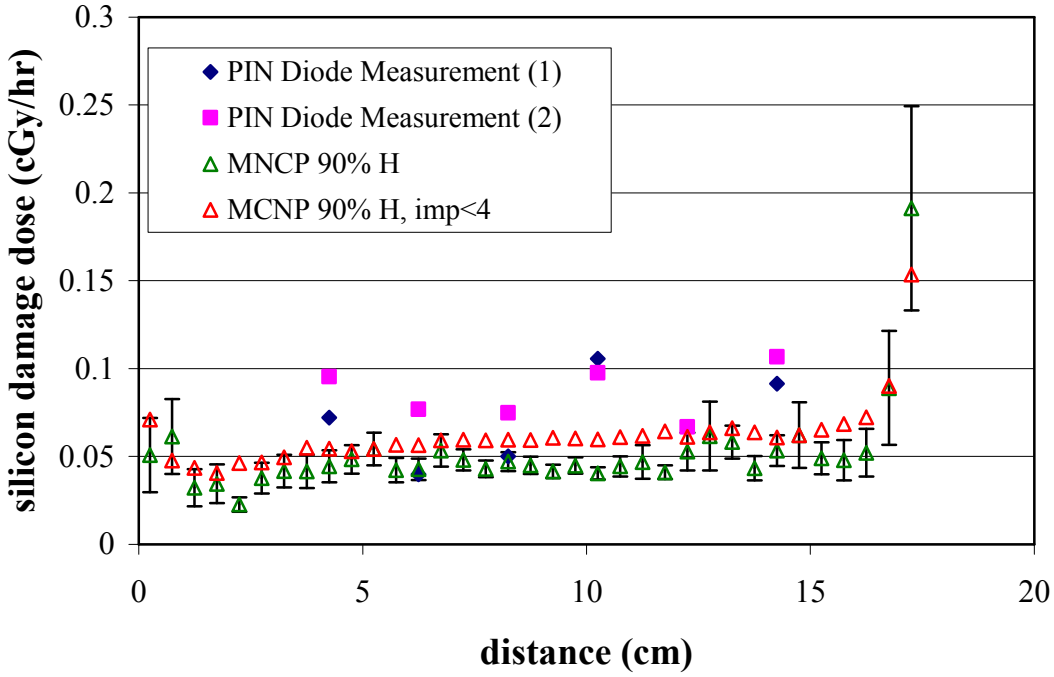

Figure 11-8. Silicon Damage Dose measurements along the sagittal axis of the head phantom. Data from two separate irradiations.

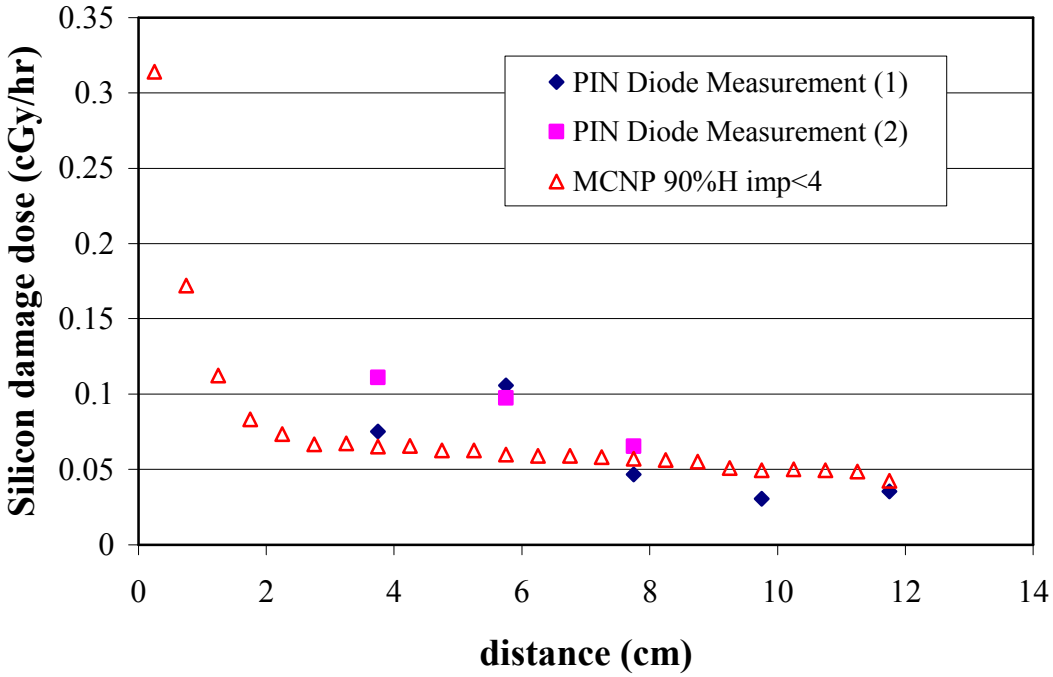

Figure 11-9. Measured Silicon Damage dose along the vertical axis of the skull phantom.

A further inaccuracy in the MCNP model was that the model assumed the ICRP elemental composition and density for the skull component of the head phantom. In fact the skull used to fabricate the head phantom was obtained from an anatomy laboratory and was completely dehydrated. Therefore that actual average density of the skull was less than that assumed in the model and the hydrogen content was negligible.

The under estimate by the model at depth is observed in the data along the sagittal axis as expected. This is also observed for the data on the vertical axis.

CONCLUSIONS

PIN diode dosimeters were calibrated in the well known spectrum of the HB11 epithermal neutron beam on the Petten High Flux Reactor. The calibration is in terms of forward bias voltage change per cGy of silicon displacement damage dose. The resulting average calibration factor was 215 (±12) $mV.cGy^{-1}$ for the batch of 14 diodes used for these measurements.

Measurements were then performed in a PMMA cube phantom and a tissue equivalent cylindrical phantom as well as a detailed tissue equivalent human head phantom. Very good agreement was obtained between MCNP calculated silicon damage dose and the measured values in the PMMA cube phantom. This is due to the well defined geometry, density and composition of this phantom and the well defined source spectrum available for use in the MCNP model.

Similarly good agreement was obtained for the cylindrical phantom once allowance was made for some dehydration of the tissue equivalent gel. For both of

these phantoms the PIN diode measured dose corresponded with the MCNP predicted silicon dose to within better than 3% at depths of 2 cm but was still within 10% at depths of 7 cm and 8 cm.

In the case of the more complex head phantom the agreement at shallow depths up to 5 cm was similar to that observed in the other two phantoms however beyond this depth larger discrepancies were observed (25%-300%). However in absolute terms these errors constitute at most only 2-3 % of the maximum silicon damage dose in the depth dose profile.

It would probably have been more useful to undertake more extensive measurements using the PIN diodes in simpler geometries to eliminate uncertainties associated with the complex geometry and MCNP modelling of the head phantom. However despite these difficulties it was possible to obtain absolute silicon dose agreements that are comparable to the levels of accuracy with which the thermal neutron fluence, epithermal neutron dose rate and gamma dose rate have been determined for this beam[200].

Based on the good agreement between MCNP and PIN diode measurements for the simplest PMMA phantom it can be concluded that the slightly larger uncertainties in the other phantoms can mainly be attributed to the modelling of the phantoms rather than an intrinsic problem with the PIN diode dosimeters.

It has been demonstrated that the effects of temperature and non linearity in PIN response can be overcome allowing the PIN diode to be used as an effective dosimeter in epithermal neutron beams. Any effects of fading can be avoided by measuring at a constant time post irradiation.

If the PIN diode measurements are to be used for more direct measurements

of tissue dose the problem still remains of converting the measured silicon dose to a tissue dose. As has previously been demonstrated by combining the PIN diode measurements with foil activations a tissue equivalent dose can be determined for neutron beams with neutron energies less than approximately 100 keV. However for most existing beams like HB11 the spectral component above 100 keV makes the derived dose conversion method invalid.

It is therefore likely that the PIN diode could be useful for measuring or monitoring neutron doses in BNCT in small volumes in phantoms or in vivo. However in this role it would only be serving as a monitor to validate other Monte Carlo dose calculations from which actual tissue doses could be derived. The small size, immediate readout and absence of the gas supplies and high voltages that are associated with ionisation chamber measurements should be a significant advantage for routine constancy or dose profile measurements. Absolute tissue dose calibrations of epithermal neutron beams would still require these other more established techniques.

CHAPTER 12 PETTEN HFR HB11 BNCT BEAM MEASUREMENTS: MOSFET MEASUREMENTS

INTRODUCTION

MOSFETs were used to measure the gamma dose at points throughout three phantoms exposed in the HB11 epithermal beam. These measurements were compared with MCNP calculations of the expected gamma dose at the measurement points. The methods used will be described in the following order; the MOSFET readout system, measurement and calculation of MOSFET linearity correction and temperature coefficient, MOSFET neutron response calibration exposure in the bare HB11 beam and measurements in the skull, cylinder and cube phantoms. The method used to correct the MOSFET measurements for neutron contributions is then described. The results of the calibration and phantom measurements are then given and compared with MCNP simulations of the same.

MATERIALS AND METHODS

The construction of the phantoms and the details of the corresponding MCNP simulation models are given in Chapter 10 and will not be repeated here. A description of the HB11 beam is also found in Chapter 10.

READOUT SYSTEM

The readout circuit used to determine the change in MOSFET threshold voltage was integrated with the PIN diode readout circuit in that it shared a number of functional units with the PIN readout circuit (Figure 3-6). The MOSFET to be readout was incorporated into a constant current source so that the source drain current was maintained at 40 μA. The supply voltage to this circuit was pulsed by the same pulser circuit as was used for the PIN diode readout. Therefore the source drain current path of the MOSFET was subjected to 1mS 40μA pulse every 11.2 mS. The voltage at the gate of the MOSFET during this pulse was sampled using a peak detector circuit. The voltage at the output of the peak detector was displayed on the Keithly digital voltmeter. The resolution of the voltmeter was 0.1 mV. Variations in the readout voltage due to noise amounted to less than 1 mV.

During the HB11 epithermal beam measurements using MOSFETs a similar procedure to that used with the PIN diodes was followed. The gate bias voltage of the MOSFET was readout immediately prior to placing the MOSFET in the phantom to be measured. During readout the MOSFETs were inserted into a socket to minimise noise pickup and resistance effects in cables. The MOSFETs were handled with forceps and long nosed pliers to minimise temperature variations due to direct handling during readout.

After the pre-irradiation readout the source, drain, gate and substrate leads of the MOSFET were bound with a single strand of fine copper wire. This serves two purposes: 1) It prevents any damage to the MOSFET oxide layer arising from breakdown due to inadvertent electrostatic discharges during handling and

measurement. 2) It ensures that the gate electrode is maintained at the same potential as the source, drain and substrate. This is important for maintaining a constant sensitivity. (Though not specifically demonstrated by any measurements here it is at least possible that electrostatic buildups of charge on the MOSFET holders could effectively place the gate electrode at a potential adequate to induce an electric field in the oxide layer during irradiation that would change the sensitivity of the MOSFET. This phenomena had been observed on previous occasions when MOSFETs were embedded in polycarbonate phantom material and irradiated in linear accelerator electron beams.)

During measurements in the phantoms the MOSFETs were placed in lithium fluoride / epoxy encapsulation to minimise their thermal neutron response. These LiF shielded MOSFETs were then introduced into the phantoms inside the perspex rods as used for the PIN diodes and activation foils. The irradiations were initiated as soon as the MOSFETs had been inserted into the phantom. Following the irradiations the MOSFETs were removed from the phantom and transferred to the readout area outside the treatment room. The temperature difference between the pre and post-irradiation readouts in the RCB was generally less than 0.5°C, similar to that noted for the PIN diode measurements. Again the temperature was monitored by a mercury thermometer on the bench where the readouts were being performed. The MOSFETs were allowed to rest on lead blocks prior to readout in order to allow them to reach temperature equilibrium with the surroundings prior to readout avoiding temperature drifts and therefore threshold voltage drifts during the readout. The gate threshold voltage was measured within 15 to 30 minutes of the completion of the irradiation. However fading effects observed in MOSFETs are so minimal that the exact time of

measurement following irradiation is not very critical.

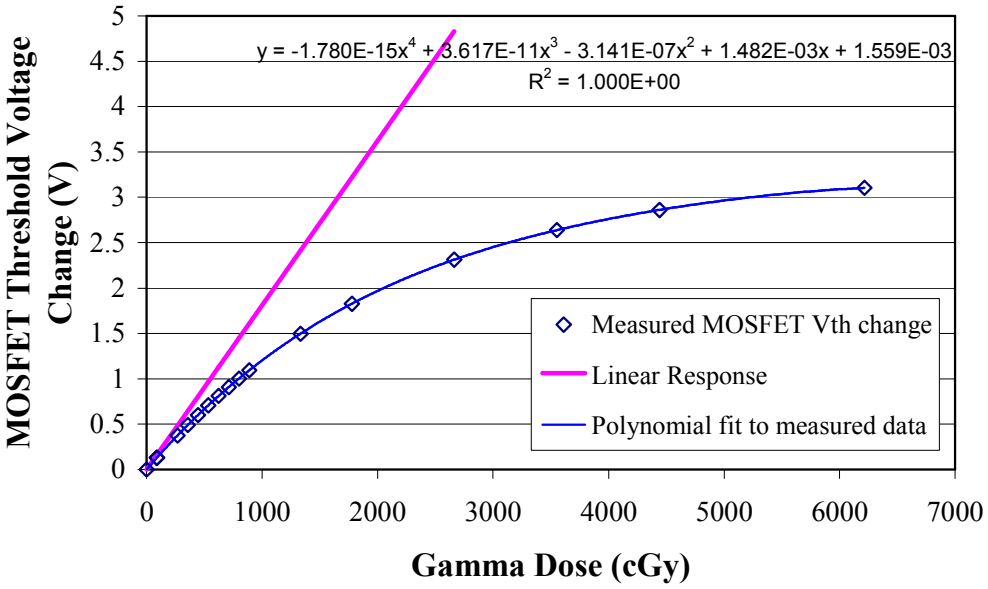

Figure 12-1. MOSFET threshold voltage change as measured in ^{60}Co calibration field.

LINEARITY CORRECTION

The change in the threshold voltage of the unbiased MOSFET when exposed to gamma radiation is shown in Figure 12-1. The threshold voltage response is approximately linear with dose up to approximately 400 mV. Beyond this threshold voltage change it is necessary to apply some correction if the MOSFET is to be used to measure doses without repeated calibrations to correct for the roll off in sensitivity with accumulated dose to the MOSFET.

Once the shape of the MOSFET response curve is measured it is possible to create a linearity correction factor which is a function of the MOSFET forward bias voltage. This factor can be used to normalise the sensitivity of the MOSFET

(threshold voltage change per cGy) at any stage of its exposure history.

To determine this characteristic curve of the MOSFET dosimeters a MOSFET from the same batch as those to be used in the Petten HFR measurements was exposed in a 10 cm x 10 cm Co-60 beam. This beam was produced from a Theratron Co-60 source at Ansto. The MOSFET was placed in a perspex (PMMA) slab phantom at D_{max}. The dose rate at this point was measured to be 29.6cGy/min using a 0.66cc NE2571 ionisation chamber and a NE Farmer 2570 Electrometer.

The MOSFET was exposed for a total of 210 minutes to give a cumulative dose of 6216 cGy and a total change in threshold voltage of 3.155V. A fourth order polynomial was fitted to this data and can be seen from Figure 12-1to fit the data over the entire range very well (R^2>0.999). A line of linear response was extrapolated from the first 426 mV of threshold voltage change.

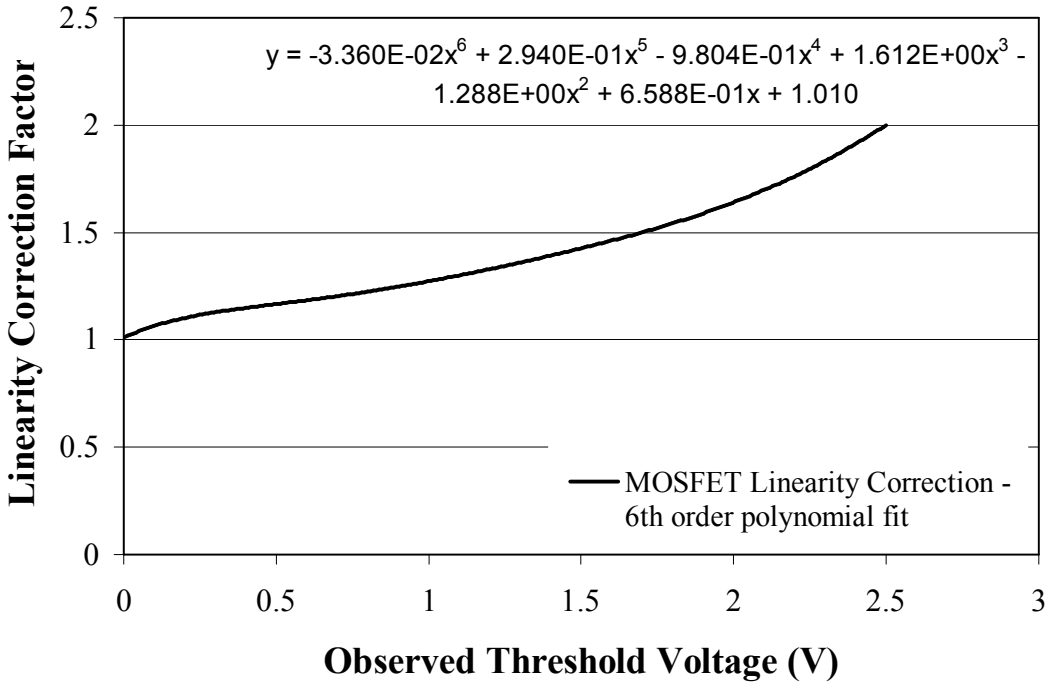

Figure 12-2. The derived linearity correction curve for the MOSFETs.

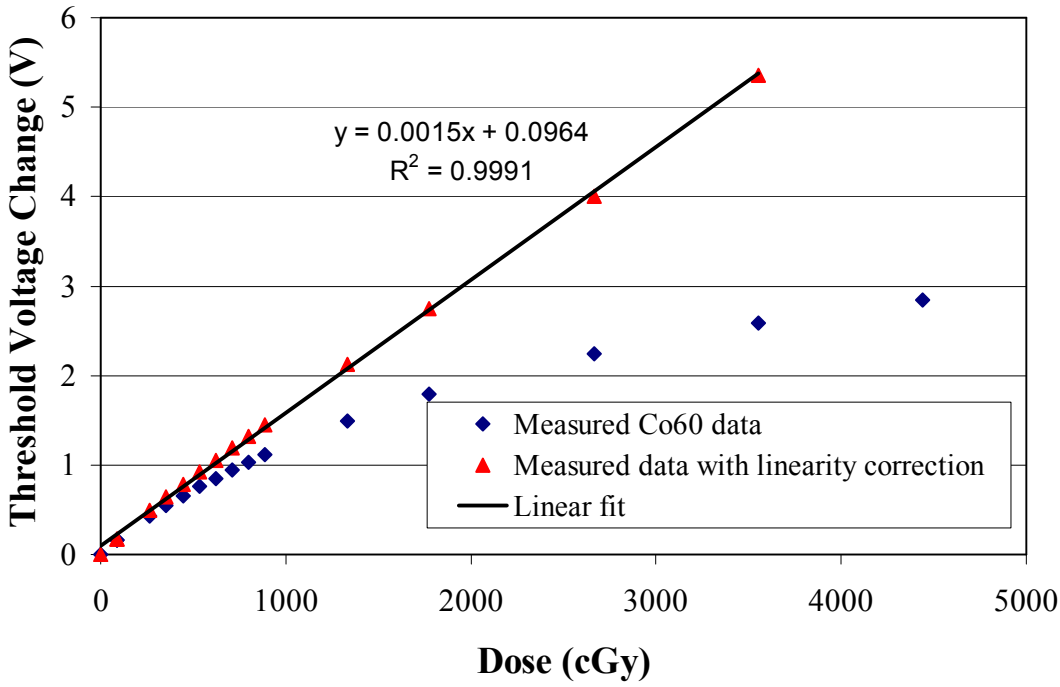

Figure 12-3. The original MOSFET threshold voltage versus dose data with the linearity correction applied. By application of the linearity correction the response is made quite linear over a dose range of several Gy and a threshold voltage range in excess of 5 volts.

TEMPERATURE CORRECTION

The sensitivity of the MOSFET threshold voltage to changes in temperature was determined by immersing the MOSFET covered in a plastic sleeve in a water bath and measuring the threshold voltage. The water bath was slowly heated from ambient temperature (16°C) to 50°C using an electric hotplate. This rate of temperature rise was approximately 1°C per minute. The temperature of the water bath was measured with a mercury thermometer to within ± 0.05 °C. The MOSFET threshold voltage was measured approximately every minute. The range from 16-

50°C covers the expected operating temperature range of the MOSFET when used as a dosimeter in BNCT beams. Over this range the threshold voltage change with temperature was linear. This is shown in Figure 12-4. The temperature coefficient of the threshold voltage was found to be 1.847mV.°C^{-1}.

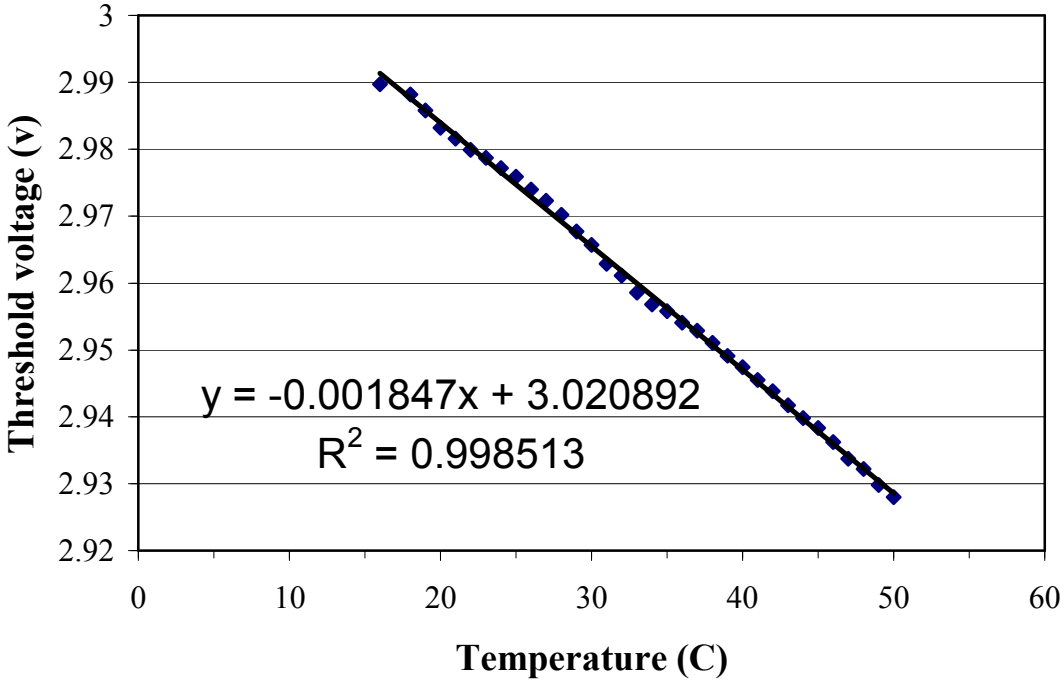

Figure 12-4. MOSFET threshold voltage change as a function of operating temperature.

All threshold voltage changes measured due to irradiations of the MOSFET were corrected for temperature effects by noting the MOSFET readout temperature during the pre and post irradiation readouts. It was assumed that since the MOSFETs were all from the same production batch the temperature coefficient would be the same for all of the MOSFETs used. In general the differences in temperature between pre and post irradiation readouts were less than 0.5°C. Therefore the correction to the change in MOSFET threshold voltage was < 1mV in almost all cases.

CALIBRATION EXPOSURES

The MOSFETs were all exposed at a point 20 cm from the collimator face. During the irradiation the MOSFETs in their lithiated epoxy holders were taped to a 1-2 mm aluminium plate. The gamma dose rate measured using an Mg/Ar ionisation chamber during this calibration exposure was 61 $cGy.hr^{-1}$.For the purposes of calculating the MOSFET neutron responses a threshold voltage equivalent to 61 cGy of gamma dose was subtracted from the observed MOSFET threshold voltage changes.

CORRECTION FOR NEUTRON CONTRIBUTION TO MOSFET RESPONSE

As described in Chapter 5 the energy dependant neutron response of the MOSFET dosimeters was investigated using MCNP4A Monte Carlo simulations. From these MCNP calculations an energy dependant curve was determined that describes the dose deposited (as a proxy for ionisation and creation of electron hole pairs) within the silicon oxide layer of the MOSFET. The curve that was derived was in terms of tallies of electron fluxes or photon KERMAs in the oxide layer. It was not in a form that could immediately be applied to correcting MOSFET threshold voltage changes for contributions from neutron components of the radiation field being measured.

Therefore to make this correction the following process was followed.

For a MOSFET exposed in a mixed neutron gamma field the total threshold voltage change (ΔV_t) is due to a contribution from the gamma component (ΔV_γ) and

the neutron component (ΔV_n).

$$\Delta V_t = \Delta V_\gamma + \Delta V_n \qquad 12\text{-}1$$

For a calibration field where the gamma dose rate is known the gamma contribution to the threshold voltage change can be given as:

$$\Delta V_\gamma = D_\gamma K_{\gamma,l} \qquad 12\text{-}2$$

Where D_γ is the gamma dose (which is known in the mixed radiation calibration field) and $K_{\gamma,l}$ is the MOSFET gamma dose calibration factor ($mV.cGy^{-1}$) which has been determined in a pure photon calibration field. $K_{\gamma,l}$ is assumed to have a constant value for the energies of interest.

From equation 12-1 and equation 12-2 the threshold voltage change due to the neutron contribution can be determined. Assuming that the neutron spectrum, $\Phi_n(E)$ is known in the mixed radiation calibration field then the neutron component of the threshold voltage change can also be written as:

$$\Delta V_n = C \int_0^{E_{\max}} K_{n,l}(E)\Phi(E)dE \qquad 12\text{-}3$$

Where $K_{n,l}(E)$ is the MOSFET neutron energy response function as derived in Chapter 5, where the subscript *n* denotes neutron response and the subscript *l* denotes the case where the MOSFET is covered with its LiF shield. $K_{n,l}(E)$ defines the

relative shape of the MOSFET neutron response curve. It is based on the MCNP calculated electron fluence or photon kerma in the MOSFET silicon oxide layer per source neutron as discussed in Chapter 5. For the mixed radiation calibration field where D_γ is known ΔV_n can be determined by measurement. To determine the integral quantity in equation 12-3, i.e.

$$\int_0^{E_{\max}} K_{n,l}(E)\Phi(E)dE$$

a MCNP simulation is performed where the values of $K_{n,l}(E)$ are used as tally multipliers for a tally cell located at the measurement position in the mixed radiation calibration field. This allows the normalisation constant, C, in equation 12-3 to be determined. This normalisation constant should be independent of the actual neutron spectrum at the point of measurement.

For dose measurements in phantoms the quantity in equation 12-4 needs to be calculated to determine the neutron contribution to the MOSFET threshold voltage change. This can then be subtracted from the measured total threshold voltage change to leave the gamma dose contribution. Unfortunately this requires a knowledge of the neutron spectrum at the desired measurement point.

A possible alternative would be to parameterise the MOSFET neutron response in terms of a second measurement technique such as foil activation or a combination of foil activation and PIN diode measurements. This may allow the determination of an approximate MOSFET neutron response based on measurements only, without the need for accurate foreknowledge of the neutron spectrum at the

measurement point. The other alternative is to use thicker LiF shields in an attempt to minimise the neutron contribution to the overall threshold voltage change of the MOSFET. This approach would require the volume of the dosimeter to be increased significantly thereby losing some of its advantage. Increased LiF shielding will also perturb the neutron field being measured with a corresponding confounding effect on the gamma dose rate which is the object of the MOSFET measurement.

RESULTS AND COMPARISON WITH MCNP

CALIBRATION RESULTS

The results from the calibration exposures in the ^{60}Co gamma calibration facility are shown in summarised form in Table 12-1.

Table 12-1. MOSFET responses measured in ^{60}Co gamma calibration facility.

MOSFET Number	Dose (cGy)	Threshold voltage change (mV)	Sensitivity (mV.cGy^{-1})
1	46.67	58.4	1.25
2	46.67	88.5	1.896
3	46.67	79.0	1.692
4	46.67	90.0	1.928
5	46.67	88.8	1.902
6	46.67	66.0	1.141

The LiF epoxy shielded MOSFET responses measured under free beam conditions on HB11 are summarised in Table 12-2.

Table 12-2. Measured MOSFET responses when exposed in LiF shields in the HB11 beam.

MOSFET number	Threshold voltage change (mV)	Threshold voltage change per hour (mV)
1	28.48	122.3
2	46.38	199.3
3	43.39	186.4
4	49.88	214.3
5	48.92	210.2
6	32.97	141.6
7	46.48	199.7

CYLINDER

A model of the cylinder including the polycarbonate case and the tissue equivalent gel was run. In this model the hydrogen content of the gel was decreased in order to take into account the suspected dehydration of the tissue equivalent gel that had occurred. This was achieved by assuming that the hydrogen lost was in the form of water and that 10% of the water had been lost. The hydrogen and oxygen content of the tissue equivalent gel in the cylinder model was decreased accordingly. As previously described this adjustment has enabled reasonably good fitting of the PIN diode data and the activation foil data and is therefore considered to yield a more accurate model of the neutron flux within the phantom. With this model the induced gamma dose at the location of the MOSFETs (in a 2.5 cm diameter annulus around the cylinder axis) is shown in Figure 12-5.

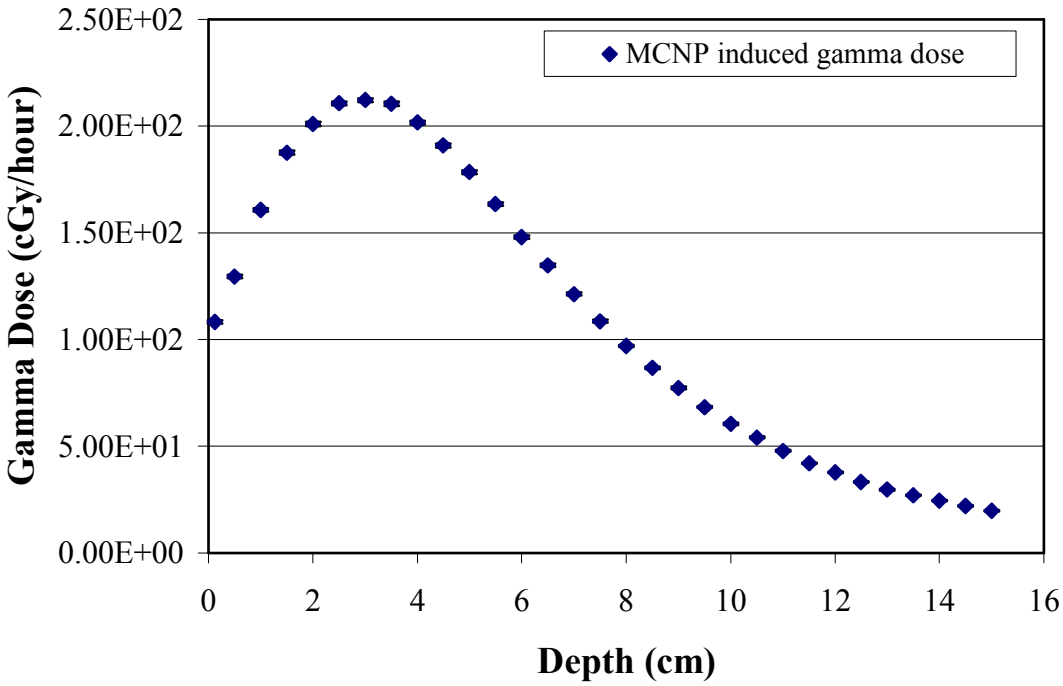

Figure 12-5. Neutron induced gamma dose along a coaxial annulus of 2.5 cm in the cylinder phantom calculated using MCNP. The tissue equivalent gel was assumed to be dehydrated by a factor of 10%.

Tallies of the track length estimates of neutron flux multiplied by the MOSFET neutron response functions derived in Chapter 5 were also included in the model. These are shown in Figure 12-6 where the curves for each of the three response functions are normalised to unity at their maximum points. In this form it can be seen that any of the tally quantities used in Chapter 5 as a proxy for neutron induced contribution to MOSFET response lead to the same overall neutron response for any given position in the phantom.

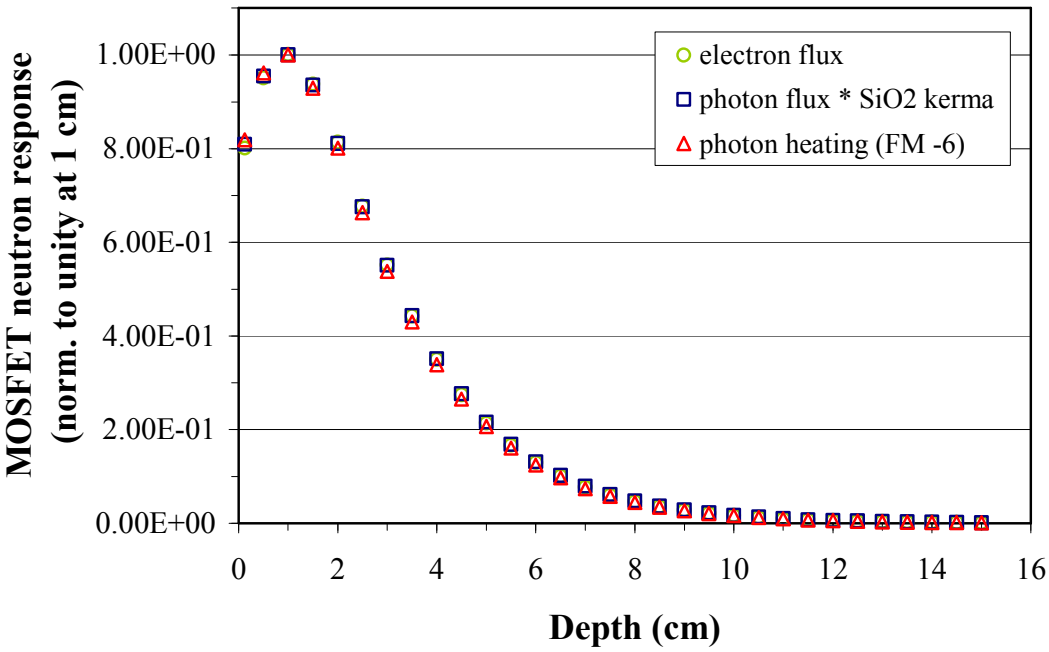

Figure 12-6. The calculated neutron response of MOSFET dosimeters positioned along a 2.5 cm radius annulus in the cylinder phantom. For comparison MOSFET responses derived from the three response functions are normalised to unity at their maximum point.

When the MOSFET measurements at 2 cm and at 7 cm depths are corrected for the neutron contribution to their threshold voltage shift based on these response functions the remaining component of their response corresponds to the measured gamma dose at these points. This is shown in Figure 12-7 along with the MCNP calculated induced gamma dose. Very poor consistency is observed in this case. The measurement at 2 cm is approximately the same as the induced gamma dose rate, implying no external source of gamma dose is present. The measurement at 7 cm is approximately the same as the measurement at 2 cm and therefore exceeds the calculated induced gamma dose rate by approximately 80 cGy/hr. The primary source of uncertainty is probably the accuracy of the MCNP predicted MOSFET neutron responses and induced gamma doses at these points due to flux depression caused by

the lithiated shields as discussed below.

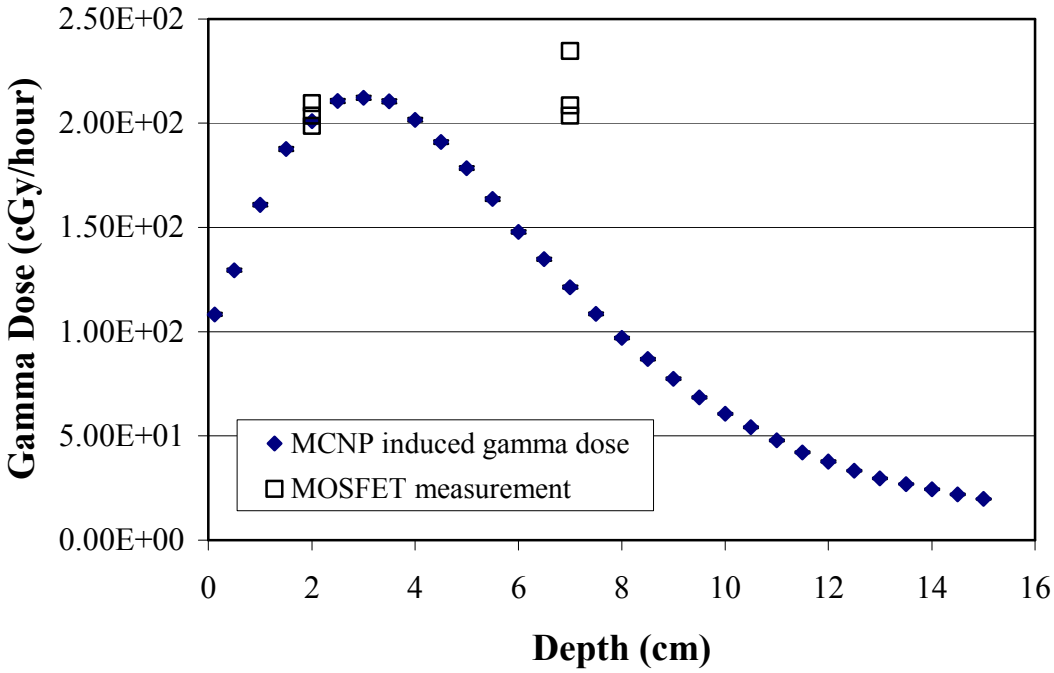

Figure 12-7. Three separate measurements of gamma dose using MOSFETs at 2 and 7 cm depths in the cylinder phantom.

Other possible sources of inaccuracies lie in the less than perfect knowledge of the tissue equivalent gel composition (i.e. possible density and hydration changes). Some inaccuracies may also arise due to approximations present in the geometry assumed for the cylinder model. The MOSFET measurements were performed by inserting the MOSFETs complete with lithiated epoxy shield into 1 cm diameter PMMA tube parallel to the cylinder axis at a distance 2.5 cm from the axis. The MOSFETs were located along this tube by means of PMMA spacers. However the MCNP model assumed that the cylinder phantom consisted of a polycarbonate cylinder filled with tissue equivalent gel. This difference may lead to small errors in both the calculated MOSFET neutron response function and also the induced gamma dose.

In Figure 12-7 the MCNP calculated induced gamma dose at the measurement point in a tissue equivalent phantom is shown. This does not take into account any perturbation of the neutron field (or induced gamma field) that may be caused by the presence of the lithiated shielding.

To try to explain the discrepancy between the measured and calculated gamma dose rates a MCNP simulation was performed to determine the effect of the lithiated shields on the neutron flux and the gamma dose rate in the phantom. The cylinder phantom was modelled in the HB11 beam with a lithiated shield of the same dimensions as the ones used in the measurements included at 2 cm depth on the axis of the cylinder. A separate simulation was performed with the MOSFET shield centred at 7 cm depth on the cylinder axis. These two depths correspond to the points at which measurements were made. The neutron flux was tallied along the central axis. The gamma flux was also tallied along the central axis and multiplied by a tissue dose function. The neutron flux distribution for a cylinder phantom irradiated in the HB11 beam with and without lithiated MOSFET shields is shown in Figure 12-8 and Figure 12-9. At 2 cm the flux with $E < 0.5$ eV accounts for approximately 70% of the total flux. When a MOSFET shield is introduced this flux is reduced to ~3-4% of the total unperturbed neutron flux. At 7 cm the $E < 0.5$eV flux accounts for approximately 95% of the total flux. With the introduction of a MOSFET shield this again falls to approximately 3-4% of the unperturbed total flux at this depth.

For the neutron flux with $E > 0.5$ eV the introduction of a MOSFET shield at 2 cm results in about a 20% reduction. At 7 cm the corresponding reduction in neutron flux with $E > 0.5$ eV is only about 2 – 3 %.

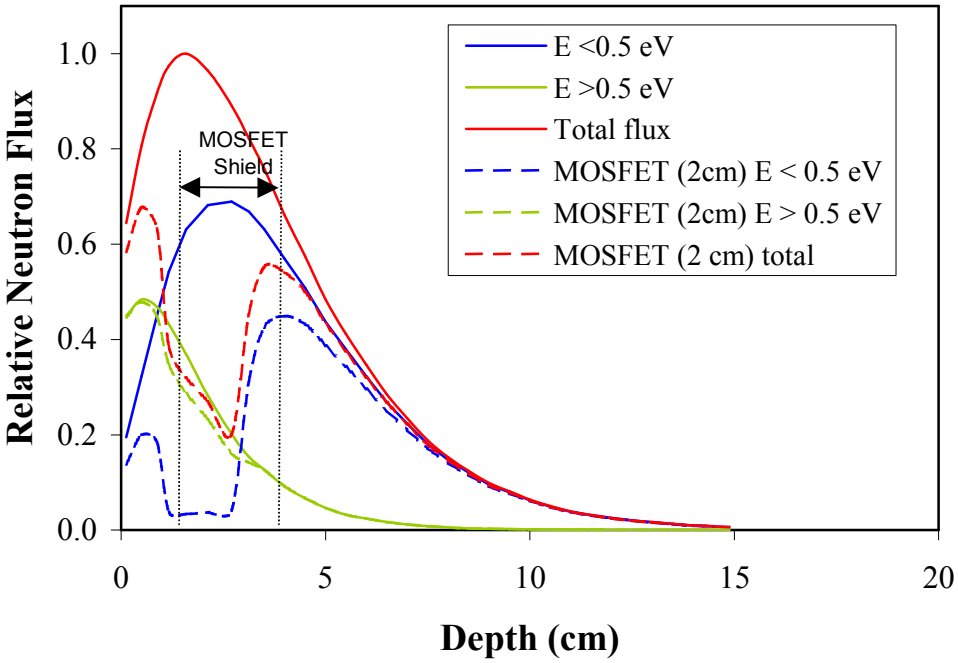

Figure 12-8. The effect of a lithiated MOSFET shield located at 2cm depth on the thermal, epithermal and total neutron flux in a cylindrical phantom exposed in the HB11 beam.

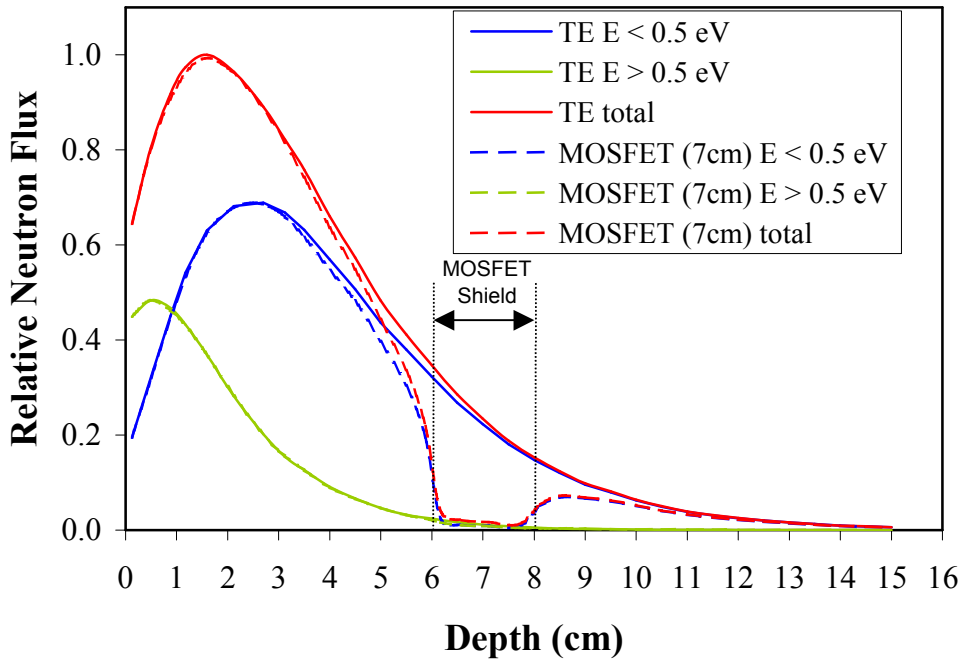

Figure 12-9. Neutron flux perturbation when a lithiated MOSFET shield is places at a depth of 7 cm in the cylinder phantom.

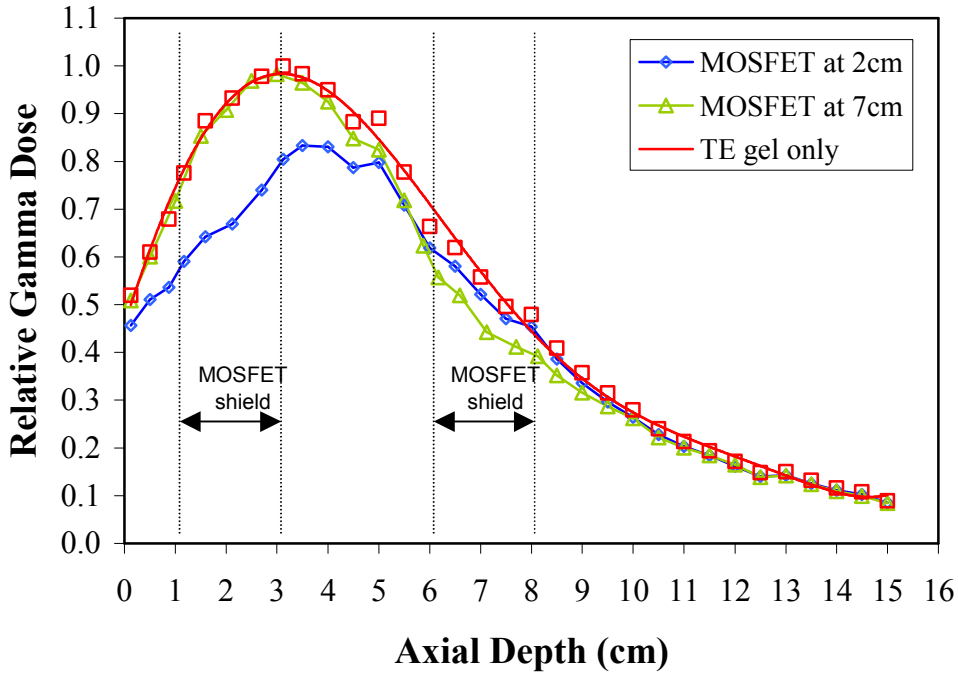

Figure 12-10. Neutron induced gamma dose in cylinder phantom irradiated in HB11 showing the effect of a lithiated MOSFET shield at 2 cm and at 7 cm depth on the central axis of the phantom.

The induced gamma dose rate in the cylinder phantom with a MOSFET shield at 2 cm and at 7 cm is shown in Figure 12-10. At 2 cm depth the presence of the lithiated shield leads to a 25 –30% reduction in induced gamma dose.

With a MOSFET shield at 7cm depth the gamma dose reduction effect is still evident but is only 15 –20% of the unperturbed gamma dose at that point.

On the basis of these estimates it is concluded that the induced gamma component of the measured gamma dose rates in the cylinder should be corrected by 30% at 2 cm and by 20% at 7 cm. Exactly what component of the measured gamma dose is induced gammas and what fraction comes from external sources is not know. An upper estimate of the total gamma dose can be arrived at by assuming that induced gamma dose accounts for all of the measured gamma dose.

In this case the measured dose rate of 205 $cGy.hr^{-1}$ at 2 cm and at 7 cm becomes 267 $cGy.hr^{-1}$ and 246 $cGy.hr^{-1}$ at 2 and 7 cm respectively. A large component of the induced gamma dose is due to hydrogen gamma rays. Due to the fall off in the $H(n,\gamma)$ cross section with energy the largest impact on the induced gamma dose rate is seen where the lithium shields impact on the thermal neutron flux the most (i.e. at shallow depths in the phantom). The impact is still observable at 7 cm depth but is much less.

CUBE

An MCNP model of the perspex cube in the HB11 beam was run. This model included tallies of the neutron induced gamma dose in the cube as well as neutron tallies multiplied by the MOSFET neutron response functions. The three differently derived response functions discussed in Chapter 5 were included. These were energy dependent histogram response functions of electron flux, SiO_2 photon kerma and the FM –6 tally of photon heating in the MOSFET junction calculated using a detailed model of the MOSFET package and junction. The resulting tallies along the central axis of the cube were recorded. These results are shown below in Figure 12-11. The data is shown normalised to unity at the maximum point in each curve, which occurs at a depth of 1cm for all of the curves.

The MCNP statistical uncertainties are approximately 2% or less for the majority of the data points displayed. Clearly using all three different response curves yields the same result.

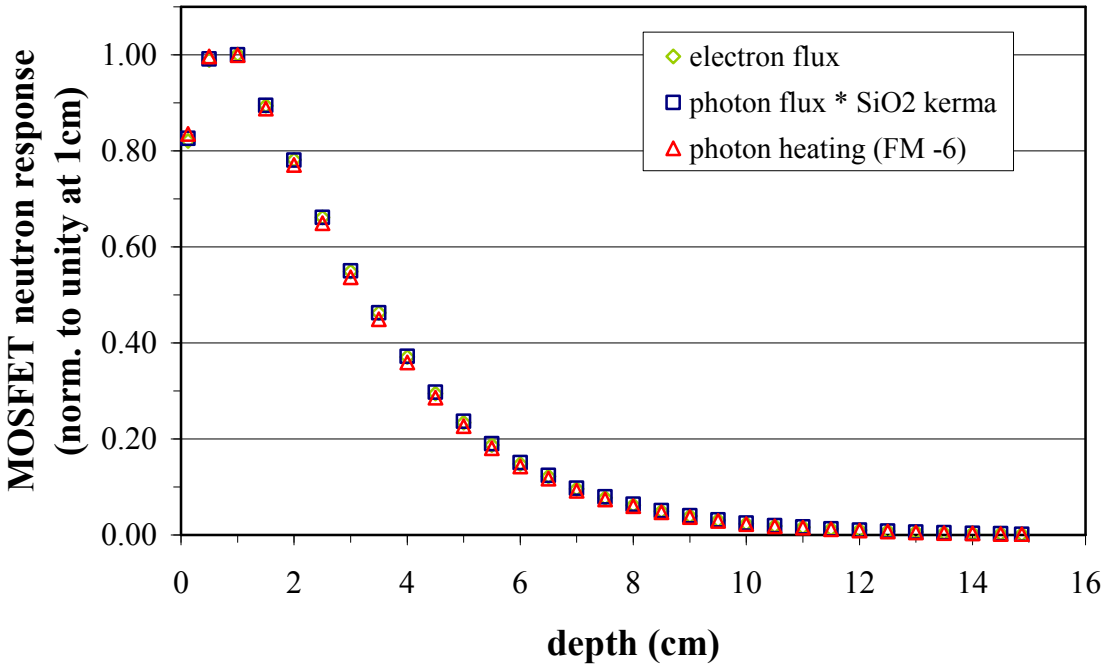

Figure 12-11. MOSFET relative neutron response along the central axis of the perspex cube phantom exposed in the HB11 epithermal neutron beam. The responses calculated using electron flux, photon kerma and photon heating in the silicon oxide layer are all shown. The curves derived by the three different methods are normalised to unity at a depth of 1 cm.

The induced gamma tissue dose was tallied in the same central axis cells of the phantom. This component of the dose will only include the gamma dose that is generated due to neutron interactions within the cube phantom itself. The other main component of the gamma dose would be those originating from the epithermal beam filters and collimators as well as whatever fraction of reactor core gammas reach the treatment point. These will be considered in more detail below. The induced gamma dose is shown in Figure 12-12.

A maximum induced gamma dose of approximately 170 cGy.hr^{-1} is reached at depths between 2.5 and 3.5 cm in the phantom.

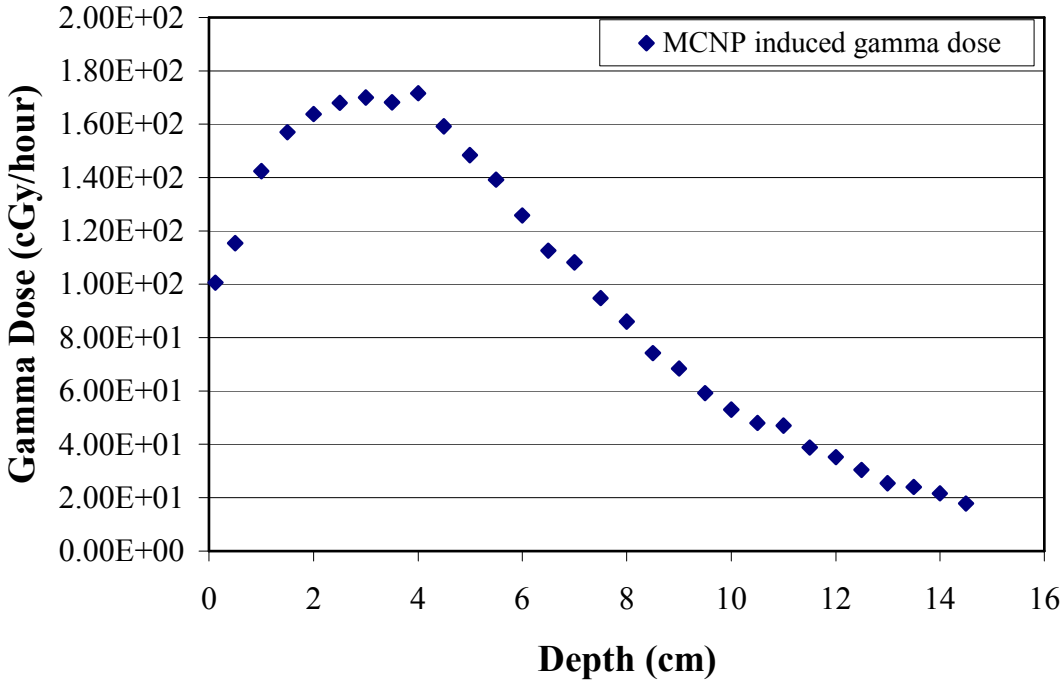

Figure 12-12. MCNP calculation of neutron induced gamma radiation dose along the central axis of the perspex cube phantom exposed in the HB11 epithermal neutron beam.

MOSFET measurements were performed at 2, 5 and 8 cm depths within the perspex phantom. One measurement was performed at each depth using the same MOSFET. A second measurement was performed at the 8 cm depth using a second MOSFET.

The measured threshold voltage changes for each of these MOSFETs were corrected for the neutron contribution to the MOSFET measurement. The MOSFET neutron response curves calibrated in the bare HB11 beam were used for this correction along with the MOSFET gamma sensitivity calibrations performed using the Petten standard Co-60 calibration facility.

The MOSFET measurements of the total gamma dose at the three measurement points in the phantom is shown in Figure 12-13.

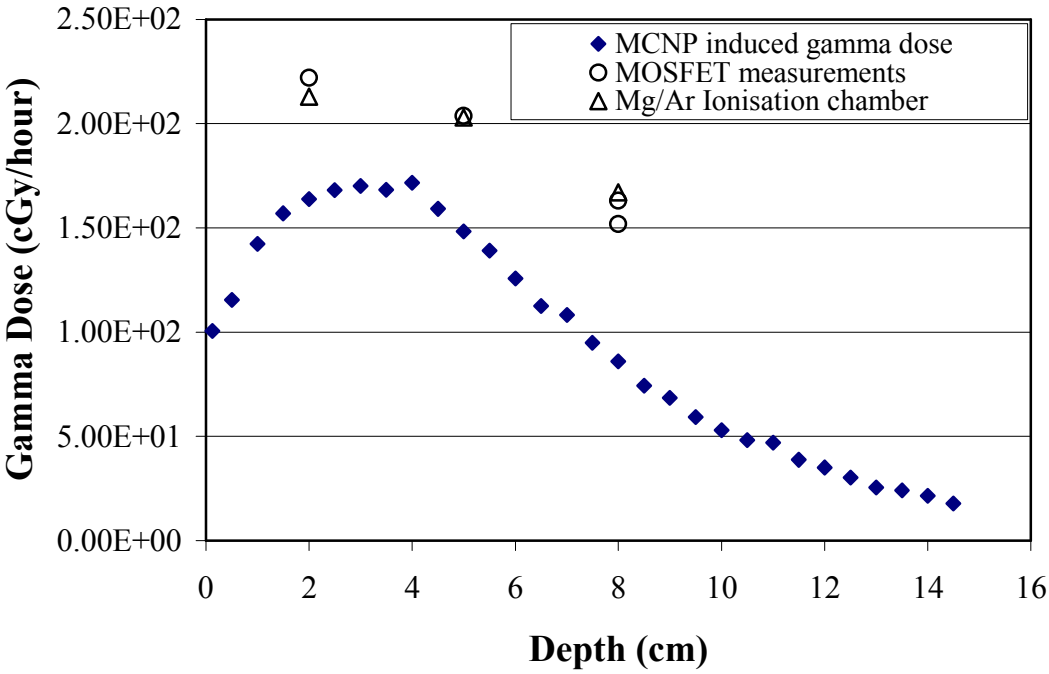

Figure 12-13. Gamma dose measured using MOSFET dosimeters at three points along the central axis of the perspex cube phantom exposed in the HB11 epithermal neutron beam. The MOSFT data have been corrected for the neutron contribution to the measurement using MCNP derived neutron response functions. The MCNP calculated induced gamma dose is also shown as are measurements using a Mg/Ar ionisation chamber (with lithiated end cap).

It can be seen from Figure 12-13 that there is a fraction of the total gamma dose as measured using the MOSFETs that is not accounted for by gamma dose induced by neutrons in the phantom alone. The difference is probably due to gamma rays originating in the filter components and other sources external to the phantom. On the basis of the data above this would be approximately 60 $cGy.hr^{-1}$ at each of the measurement points.

It can also be assumed that the presence of the MOSFET shields leads to a neutron and gamma flux suppression similar to that demonstrated in the cylinder phantom. If this is taken into account the upper estimate of the total gamma dose (assuming no beam gamma contribution to the MOSFET measurements) would be

approximately 20-30% greater than measured in the presence of the lithiated MOSFET shields.

SKULL

The lithium covered MOSFET measurement results along the three axes of the skull phantom are shown below. Poorer agreement was obtained in the skull phantom than in the PMMA cube phantom. However a general pattern similar to the tissue equivalent cylinder phantom results is present. The MOSFET measurement at approximately 2.5 cm depth along the beam axis gives a gamma dose rate comparable to the MCNP calculated induced gamma dose rate.

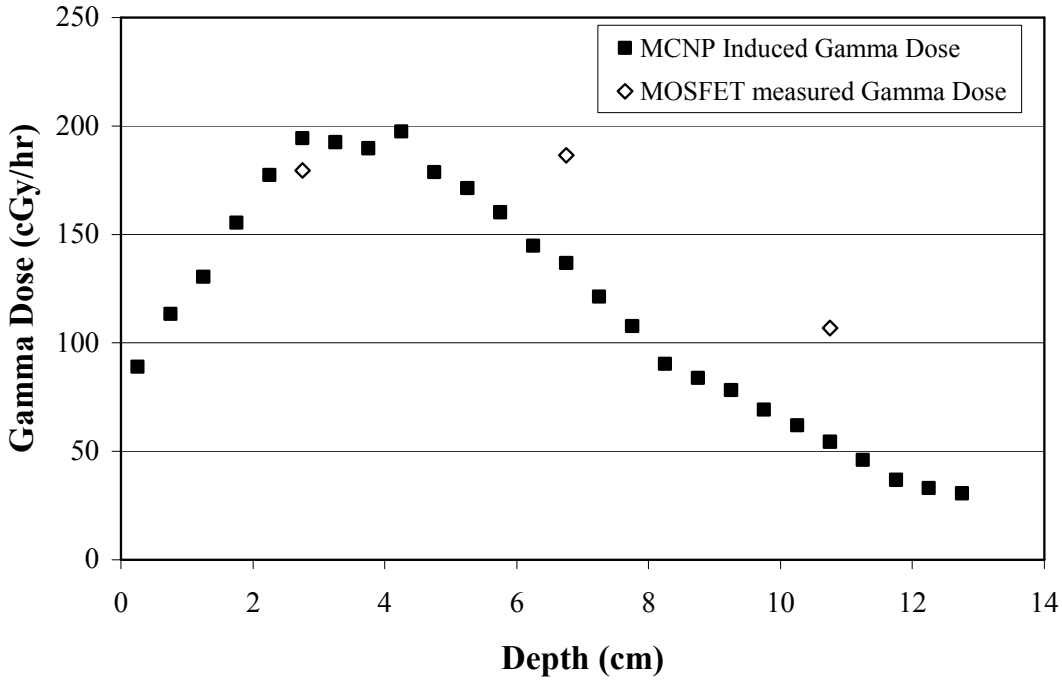

Figure 12-14. MOSFET measured gamma dose in skull phantom along beam axis. MOSFET measurements corrected for neutron contribution. Also shown is the MCNP calculated induced gamma dose.

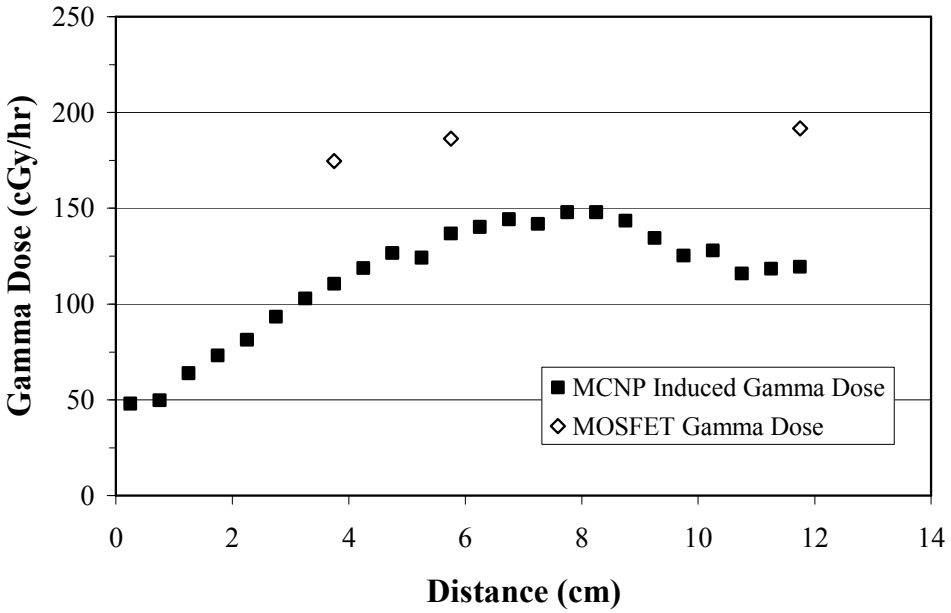

Figure 12-15. MOSFET measured and MCNP calculated gamma dose along vertical axis of skull phantom.

However the MOSFET measurement of gamma dose at greater depths exceeds the MCNP calculated induced gamma dose rate by approximately 40 –50 $cGy.hr^{-1}$. This depression at shallow depths was also observed in the cylinder phantom but not in the PMMA phantom.

MOSFET measurements corrected for linearity and temperature effects as well as neutron response for the vertical axis of the skull phantom are shown in Figure 12-15 and for the anterior-posterior axis in Figure 12-16. Both of these sets of data correspond to measurement points at depth in the phantom. The MOSFET measurements follow the general shape of the calculated induced gamma dose rate but exceed the value of the MNCP induced gamma dose rate by approximately 50 – 70 $cGy.hr^{-1}$. This difference is of a similar magnitude to the expected dose rate in the HB11 beam.

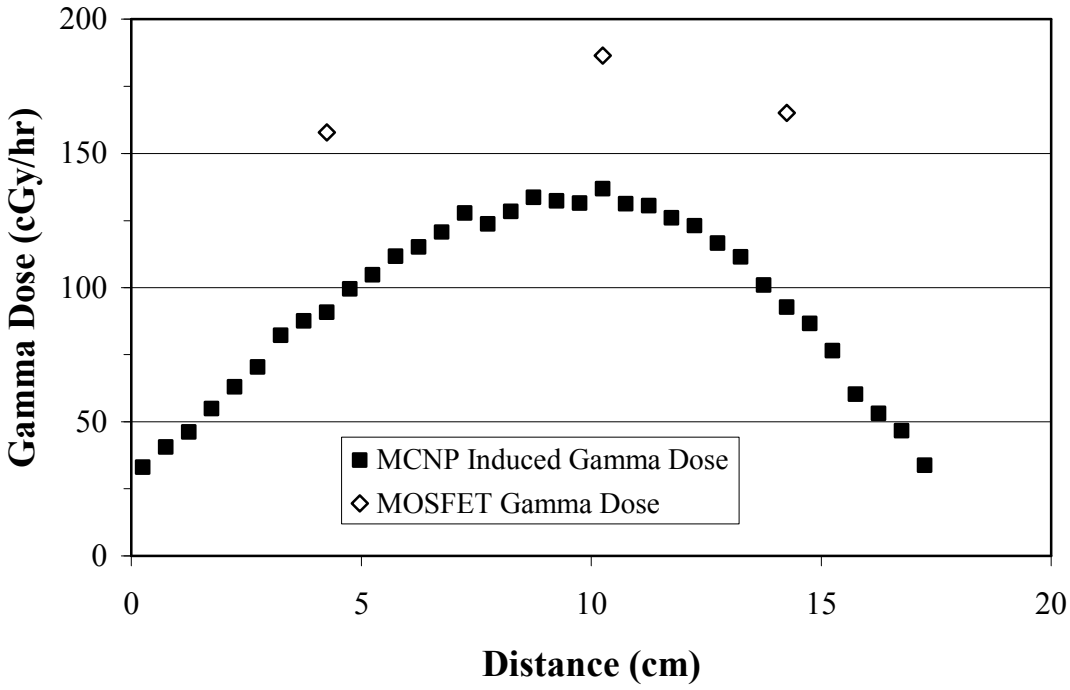

Figure 12-16. Horizontal axis. MOSFET measured gamma dose and MCNP induced gamma dose in skull phantom.

During the calibration measurements for the MOSFETs a dose rate of 61 $cGy.hr^{-1}$ was measured in the bare beam. However a gamma flux originating from the beam port would be expected to be forward directed and therefore should contribute more to measurement points closer to the surface of the phantom on which the beam is incident. In contrast to this the difference between the MCNP calculated induced gamma dose and the measured gamma dose does not reduce with increased depth in the phantom. Therefore if a gamma flux originating external to the phantoms is the hypothesised explanation for the difference between the measured gamma dose and the calculated induced gamma dose then the external gamma field must be quite isotropic.

For the cube phantom at 2 cm depth the magnitude of the correction to account for the neutron contribution is equivalent to approximately 20% of the total

threshold voltage change. At a depth of 5 cm this has reduced to 8% and at a depth of 8 cm the neutron contribution is about 3%. The corrections for the other two phantoms were a similar proportion of the total threshold voltage change at comparable depths.

CONCLUSIONS

MOSFETs were applied as gamma dosimeters in phantoms exposed to an epithermal neutron beam. The MOSFET neutron sensitivity was determined by irradiating the lithiated polymer covered MOSFETs in the bare HB11 beam. In this way the energy dependant MOSFET neutron response functions were calibrated.

In a simple well defined PMMA cube phantom it was possible to produce gamma dose measurements that agreed with Mg/Ar ionisation chamber measurements. MCNP calculated induced gamma doses in this phantom were approximately 60 $cGy.hr^{-1}$ less than the measured total gamma dose rates in the phantom. (Note that the ionisation chamber measurements were performed with a lithiated end cover in place as per the procedure used by Raaijmakers at that time[43,200].)

When more complex phantoms are considered the comparison between the measured total gamma dose using MOSFETs is less consistent. For both the tissue equivalent gel filled cylinder phantom and the skull phantom the MOSFET measurements at 2 – 2.5 cm yielded dose rates consistent with the calculated induced gamma dose rate alone. At greater depths the MOSFET measurements exceed the calculated induced gamma dose rate by approximately 60 $cGy.hr^{-1}$.

The presence of the lithiated covers on the MOSFETs will perturb the neutron flux in the locality of the MOSFET. This leads to an underestimate of the true gamma dose rate at the measurement point. The upper limit of this underestimate was calculated to be 30% of the induced gamma dose rate at a depth of 2cm in the cylinder phantom and dropped off with increasing depth. The total measured gamma dose consists of induced and beam gamma components and the lithiated shield only perturbs the induced component. Therefore the actual correction to the measured gamma dose rate at any point will always be less than 30%. The required corrections would probably be similar for the skull phantom. This effect should be similar in all phantoms and was not observed to cause any discrepancy between the MOSFET and ion chamber measurements where these were possible in the PMMA cube phantom. However the ionisation chamber measurements are expected to display a similar underestimate also due to the lithiated cap used on the Mg/Ar chamber.

It has been demonstrated here that MOSFETs can probably be applied to gamma dosimetry in mixed epithermal neutron and gamma fields. However further work is required in order to make MOSFETs useful dosimeters for this application. Reducing the neutron response by modifying the encapsulation of the MOSFETs should lead to more accurate results especially near the regions of peak thermal flux. For the current encapsulation and lithiated shields the correction neutron contribution is approximately 20% of the total MOSFET response. Removing the kovar encapsulation and replacing it with a material of minimal neutron interaction cross sections would reduce the magnitude of the neutron correction that needs to be applied. This would be preferable to increasing the amount of lithiated shielding around the MOSFETS which may reduce the neutron response but will perturb the

system being measured too much.

CHAPTER 13 MOSFET AND PIN DIODE MEASUREMENTS IN THE BMRR EPITHERMAL NEUTRON BEAM

INTRODUCTION

Measurements using the MOSFET and PIN diode dosimeters were performed in the epithermal neutron beam at the Brookhaven Medical Research Reactor (BMRR). These measurements were performed using the same type of MOSFET and PIN diode detectors as were used for the other experiments described in this thesis.

For the measurements on the BMRR epithermal beam the MOSFETs were encapsulated in a thicker ^{6}LiF shield than was the case for the measurements on the Petten HB11 epithermal neutron beam. The MOSFET measurements were performed with a bias applied to the gate electrode to increase sensitivity. The phantom used here was a 15 cm cube phantom consisting of polymethyl methacrylate (PMMA). This avoided the problems experienced with dehydration of the tissue equivalent gel in the Petten series of measurements.

MATERIALS AND METHODS

BMRR EPITHERMAL NEUTRON BEAM

The Brookhaven Medical Research Reactor (BMRR) commenced operation in 1959 and at that time was used to provide a thermal neutron beam for the initial trials of BNCT[201]. The epithermal beam has more recently been used in clinical trials of BNCT for glioblastoma until it the reactor was shut down for political reasons in

2000.

The reactor[17, 201] has a maximum operating power of 3 MW and is moderated and cooled with light water. The core is surrounded by a graphite reflector. The reactor has a number of irradiation facilities including the epithermal neutron irradiation facility (ENIF). The ENIF opens into an epithermal neutron irradiation room. The exit port of the beam in the irradiation room is approximately 177 cm from the centre of the reactor core.

The epithermal neutron spectrum at the beam exit port[17, 201] is produced by a series of filters which neutrons from the core must pass through. The core itself is surrounded with graphite reflector. The next layer along the beam line consists of 19 cm of Bi which acts as a gamma ray attenuator. The Bi is followed by a 12 cm thick void. A combination of Al and AlO_3 occupies the next position in the filter arrangement (*A* and *B* in Figure 13-1 below) and serves as the principle moderator of the fission neutrons from the core. This is followed by a thin layer of Cd and a further thin layer of Bi to reduce the thermal neutron and gamma components respectively. The wall of the irradiation room surrounding the beam exit port is lined with lead and lithiated polyethylene. The beam is collimated with lithiated polyethylene collimators. These consists of polyethylene containing Li_2CO_3 (93% enriched ^6Li) with an overall ^6Li content of 7% by weight and 7.9% hydrogen by weight. The original 7.6 cm thick collimator with an exit aperture of 8 cm may be exchanged with a 15.2 cm thick collimator to obtain a larger beam diameter of 12 cm. The 12 cm beam diameter was used for all of the experimental measurements described in this chapter.

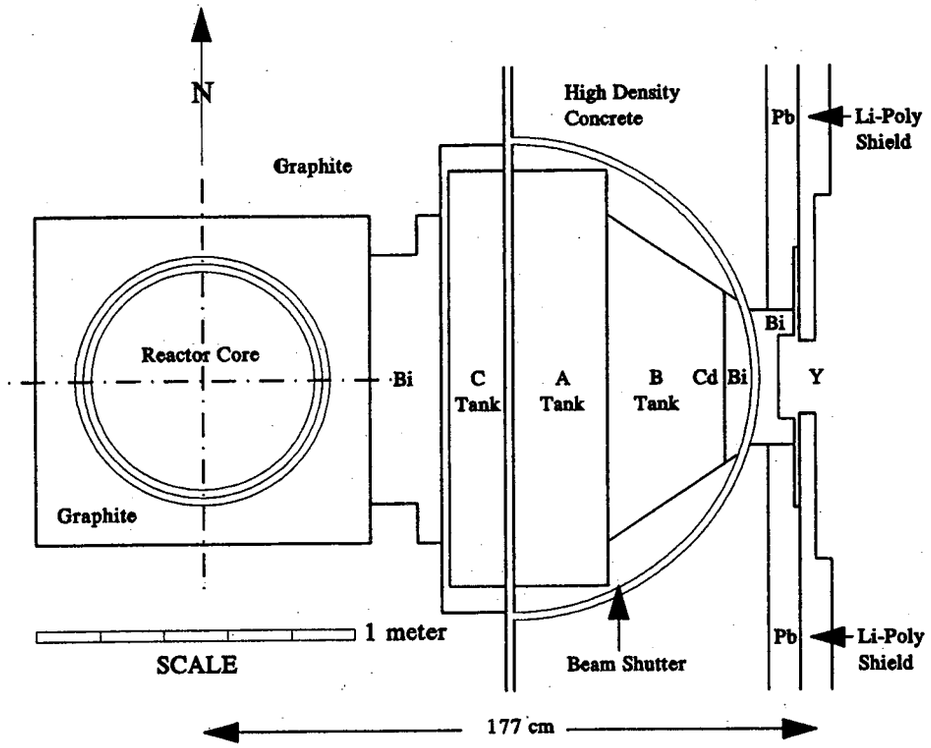

Figure 13-1. The epithermal neutron beam at the BMRR. (Diagram from Liu et al[17])

PHANTOM

The phantom used for these measurements was constructed from square slabs of polymethylmethacrylate (PMMA). These were 15 cm square and 2.5cm thick. A stack of six of these slabs was used to obtain a total phantom thickness of 15cm. All of the PMMA slabs had two holes on diagonal corners (diameter 12.5mm, centred 2 cm from each edge) to allow a PMMA bolt to be inserted into each corner to secure the stack of PMMA slabs together. In this way air gaps and spaces between slabs were eliminated and the stack of slabs was securely held together to enable accurate and reproducible positioning at any angle.

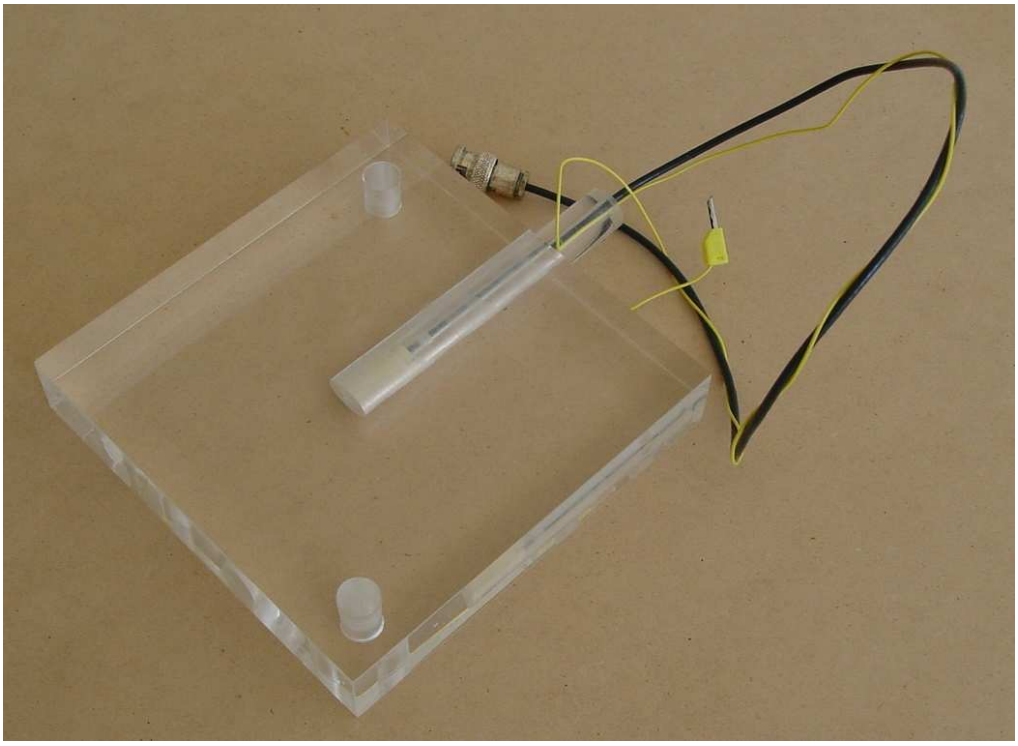

Figure 13-2. One slab of the PMMA phantom showing MOSFET probe inserted into dosimeter access hole.

Additional PMMA slabs were fabricated with holes penetrating from the edge of the slab to the centre allowing insertion of dosimeters into the midline of the phantom (Figure 13-2). In combination with the other 2.5cm thick PMMA slabs this meant that dosimeters could be located at depths of 1.25 cm, 3.75cm, 6.25 cm, 8.25cm, 11.25 cm, etc (i.e. increments of 2.5 cm starting at a depth of 1.25 cm). The dosimeters were inserted into these holes on lengths of solid PMMA rod to eliminate any voids in the phantom. In the case of the MOSFETs this rod was 16mm in diameter and had a 5 mm hole along its axis in order to allow cables to be connected to the MOSFET.

MCNP MODEL

An MCNP model of the collimators and the phantom used in the measurements was performed. This was based upon geometry and spectral information supplied by B Liu[a]. The model consisted of a 15 cm PMMA cube of density 1.17 $g.cm^{-2}$ divided into transaxial slices of 0.5cm thickness. Tallies of silicon damage kerma, induced photon dose and three different estimates of MOSFET neutron response were calculated (Chapter 5) in each of these slices within a cylinder of 1.0 cm diameter along the beam axis. The parallel neutron source was defined as a plane at the exit hole of the collimator. A 7.6cm thick Li-polyethylene collimator material with a conical beam port was used. This did not actually collimate the beam in the model but was present for any small scattering contribution it may make.

PIN

A set of PIN diode calibration measurements were performed in the BNL epithermal beam in air with no phantom present. In phantom measurements were performed on the central axis of the phantom at depths of 1.25 cm, 6.25 cm and 8.75 cm.

PIN READOUT CIRCUIT

The PIN diode readout system used was an improved version of the one used

[a] B Liu, private communication to BJ Allen, May 1996.

in previous measurements. The main difference being that in the final readout stage a sample and hold circuit was used rather than a peak detector circuit. It was designed by A Rosenfeld and produced by P Ihnat of the University of Wollongong, Department of Engineering Physics. The main parameter of importance, the current through the PIN junction was 1 mA as previously used. A similar duty cycle was used (i.e. ~ 1 mS duration pulses at intervals of ~10 mS).

DESCRIPTION OF PIN MEASUREMENTS

The phantom was located at the beam exit hole in the collimator. The centre of the beam was aligned with the central (measurement) axis of the PMMA phantom. The forward bias voltage of the PIN diodes was measured immediately before each irradiation (i.e. 1- 2 minutes prior to opening the beam shutter). The beam shutter takes approximately 10 seconds to open and shut. No correction was made for this since the shortest exposure was 5 minutes. Therefore the opening time of the shutter would be approximately 3% of the total exposure time in this case. After each irradiation the PIN diodes were readout within 2-3 minutes of shutter closure.

The diodes were readout in the irradiation room and the periods of each irradiation ranged from 5 minutes to 15 minutes. Therefore it was assumed that no temperature changes occurred over this time and so it was not necessary to apply any temperature corrections to the forward bias voltage changes before and after the irradiations. This assumption was supported by observations of the temperature in the irradiation room. This was observed to be constant at 75°F.

MOSFET

Both lithium shielded and bare MOSFETS were used to perform measurements at various depths in the PMMA phantom and in air on the axis of the beam at the exit of the collimator.

READOUT

The readout system used for the MOSFET measurements was also an updated version of the readout system used elsewhere in this thesis. It was integrated with the PIN diode readout system described above. The current used to define the threshold condition was 42 μA which corresponds to the approximate thermostable point of the MOSFETs when new.

DESCRIPTION OF MOSFET MEASUREMENTS

Gamma dose measurements were performed using MOSFETS encapsulated in lithiated shields. These shields were thicker than the shields used for measurements on the HB11 beam at Petten. Therefore the neutron contribution to the response of the detector was expected to be less. The MOSFETS were assembled with cables attached and housed in lithiated polymethylmethacrylate shields. These can be seen in Figure 13-3.

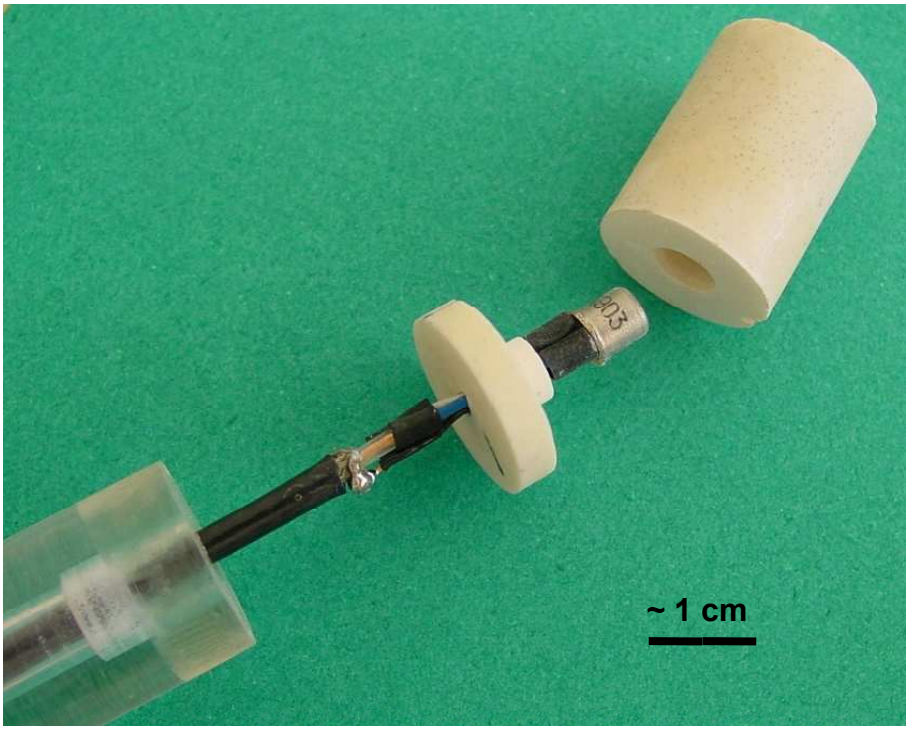

Figure 13-3. MOSFET dosimeters in lithiated shields with PMMA rods and cables permanently attached.

Greater accuracy was also achieved by using the MOSFETS in active mode. A bias of 5 volts was applied to the gate electrode during the irradiations to increase their sensitivity. This meant that larger threshold voltage shifts were observed and therefore the relative error in determining the threshold voltage change was reduced.

The phantom was assembled and located at the face of the beam port. The central axis of the phantom was aligned with the central axis of the beam. Prior to each measurement the MOSFET dosimeters were inserted vertically into the recessed PMMA slab which was located at the depth in the phantom where a measurement was required. Immediately prior to the irradiation (i.e. within approx 1 minute of vacating the room and opening the beam shutter) the MOSFET threshold voltage was measured. The accuracy of these measurements was to better than 1 mV. After the threshold voltage was measured a 5.0 volt bias was applied to the gate electrode and

the shutter was opened. The irradiations were performed for durations of between 5 minutes and 15 minutes at a reactor power of 3 MW. As for the PIN diode measurements the beam shutter opening and closing time was approximately 10 seconds and no correction was made for this.

Following the closure of the shutter the bias voltage was disconnected and the final threshold voltage was measured. This measurement was generally performed within 2-3 minutes of the beam being shut off.

Due to the limited number of measurements being performed and the use of the MOSFETS in active mode (biased during measurements) no linearity corrections were applied for this series of measurements. Temperature corrections were also not performed for the measurements described here because the MOSFETs were not removed from the irradiation room for readout and the irradiation room had a constant temperature to within less than 1°C.

One measurement was performed without the phantom in the beam. For this measurement the MOSFET probes were located so that the actual MOSFET (encapsulated in LiF PMMA shielding) was located on the central axis of the epithermal neutron beam. The threshold voltage shift from this measurement was attributable to the MOSFET neutron response as well as the gamma dose component that originates in the core of the reactor and the beam filters. The gamma dose rate during this measurement was assumed to be known based on previous beam characterisation measurements by others at BNL[202]. The MOSFET gamma dose sensitivity is also known based on calibration of the MOSFETs in a 6 MV linac photon beam at the Illawarra Cancer Care Centre.

RESULTS

PIN DIODE MEASUREMENTS

The PIN diode forward bias voltage changes in volts per hour at a reactor power of 3 MW are shown in Table 13-1. The values shown are the average of pairs of measurements at each depth with a relative mean error of ~ 10% for each data point.

This data is shown plotted with MCNP calculated silicon damage kerma for the same experimental arrangement. Since we did not perform any foil activation measurements during this series of experiments it is not possible to determine an independent factor to normalize between measurements and the number of source neutrons per hour in the MCNP model.

Table 13-1. PIN diode forward bias voltage shifts for PIN diodes exposed in BMRR beam along central axis of PMMA phantom.

Depth (cm)	**Forward bias voltage change. $mV.hr^{-1}$**
In air	228
1.25	210
6.25	52
8.75	40

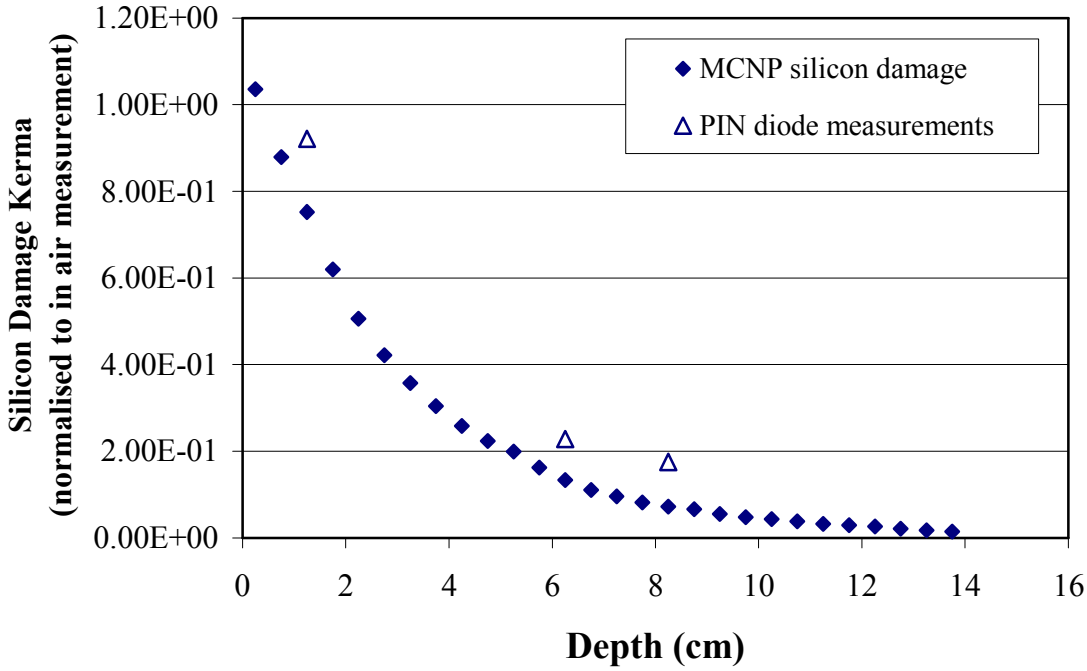

Figure 13-4. Comparison of MCNP and measured silicon damage kerma in 15 x 15 cm PMMA cube phantom exposed in BMRR epithermal neutron beam.

Therefore to compare between the calculated PIN diode dose in the phantom and the measured PIN diode voltages in the phantom the normalization of the MCNP model was based on the calculated and measured response for a PIN diode exposed in the bare beam.

MOSFET MEASUREMENTS

The results of the measurements in air and at various depths in the phantom in the BMRR epithermal neutron beam are shown in Table 13-2. The threshold voltage changes in the MOSFET photon sensitivity calibration measurements at the Illawarra Cancer Care Centre are shown in Table 13-3.

Table 13-2. Threshold voltage changes observed for Lithium shielded MOSFETs exposed in the BMRR epithermal neutron beam.

MOSFET	Depth (cm)	Threshold voltage change (mV)	Time (minutes)	Threshold voltage change per hour (mV)
Li 1	0 (in air)	75	6	750
Li 1	1.25	417	15	1668
Li 1	3.75	137	5	1644
Li 1	6.25	107	5	1284
Li 1	8.75	72	5	864

Table 13-3. Calibration of MOSFET in Li shielding in 6MV linac beam at Illawarra Cancer Care Centre.

MOSFET	Depth (cm)	X-ray Dose (cGy)	Threshold voltage change (mV)	MOSFET gamma sensitivity ($mV.cGy^{-1}$)
Li 1	1.5	40	247	6.175
Li 2	1.5	40	257	6.425

These threshold voltage changes are plotted in Figure 13-5 with no corrections. Also shown on the same graph is the calculated gamma depth dose profile[a] in a PMMA phantom exposed in the BMRR beam.

The gamma depth dose profile is normalised to unity at its maximum. The threshold voltage changes were normalised so that the measurement at 1.25 cm depth corresponded to 93% of the maximum dose for the calculated gamma dose profile (i.e. to match the calculated % gamma dose at a depth of 1.25cm).

[a] B Liu private communication, May 1996.

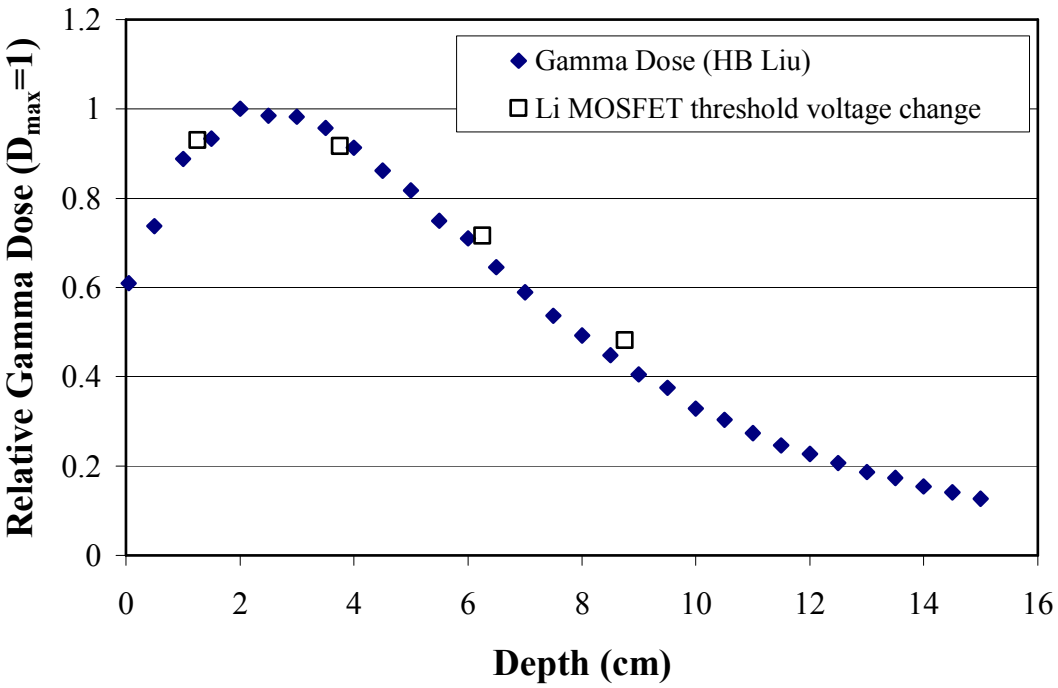

Figure 13-5. BMRR epithermal neutron beam. Calculated gamma dose profile in 15 cm cubic PMMA phantom[a]. The measured data points are the normalised lithium shielded MOSFET threshold voltage changes. No other corrections have been applied.

To take into account the neutron contribution to the MOSFET response the MCNP derived MOSFET neutron response functions were used as neutron tally multipliers in a MCNP4a simulation of the cube phantom exposed in the BMRR beam. All three MOSFET neutron response functions were used to see if there were any differences. For the purpose of comparison the neutron responses calculated using the three different tallies were normalised to unity at 0.25 cm depth on the central axis of the cube phantom.

These three curves are shown in Figure 13-6. There is negligible difference between them for the first 10 cm of depth. Beyond 10 cm a non significant variation of < 0.1% of the response at 0.25 cm depth is observed.

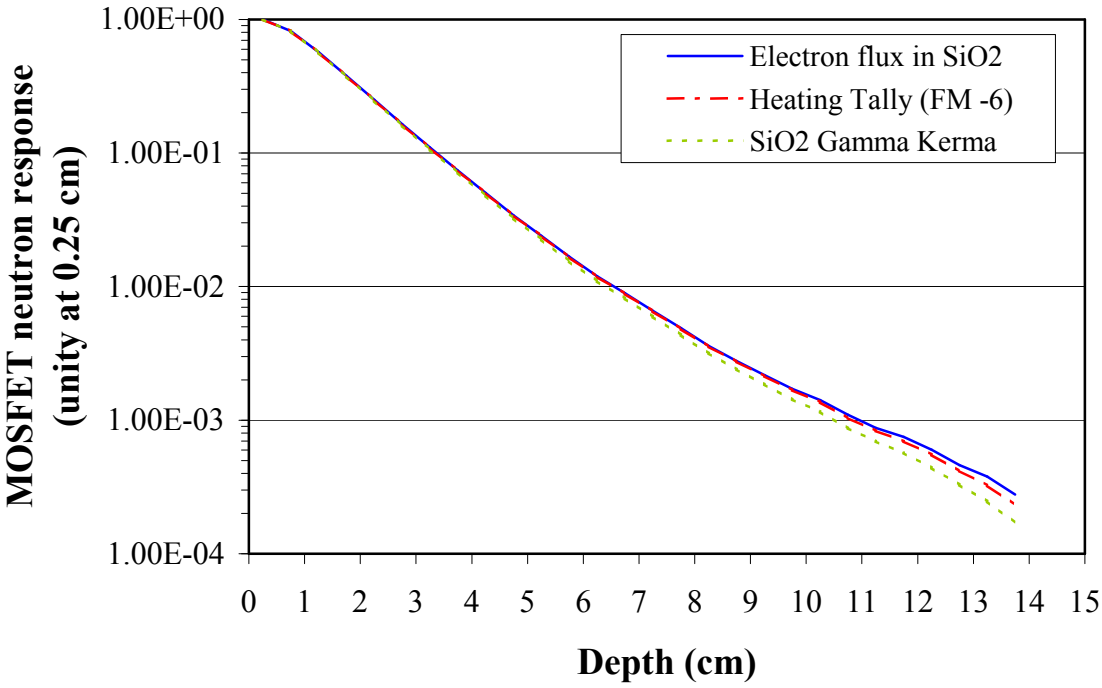

Figure 13-6. Comparison of calculated MOSFET neutron responses in 15 cm cube PMMA phantom.

By combining the MCNP calculated MOSFET neutron response in air in the BMRR beam with the measured threshold voltage shift and the known gamma dose rate in air in the beam the neutron response curves can be calibrated to give absolute values.

To determine the absolute values of the neutron contributions to the MOSFET threshold voltage change the following process was followed.

The gamma dose rate in air at the midline of the beam[202] at the face of the Li-poly collimator was assumed to be approximately 84 $cGy.hr^{-1}$. The observed threshold voltage change of the Li shielded MOSFET at this point was 750 $mV.hr^{-1}$ (see Table 13-2 above). From Table 13-3 the sensitivity of the MOSFET to gamma rays is 6.175 $mV.cGy^{-1}$.

Therefore the expected change in threshold voltage per hour at this point due to the gamma dose rate is 518.7 $mV.hr^{-1}$ (that is: 84$cGy.hr^{-1}$ × 6.175 $mV.cGy^{-1}$). The observed threshold voltage change per hour was 750 $mV.hr^{-1}$. Therefore the threshold voltage change per hour due to the neutron response of the MOSFET at this point in the bare beam is 231.3 $mV.hr^{-1}$ (that is: 750 $mV.hr^{-1}$ – 518.7 $mV.hr^{-1}$).

This value is then used to determine the absolute value of the MCNP calculated MOSFET neutron response in air in terms of $mV.hr^{-1}$ per tallied neutron response. When this calibration factor is applied to the calculated neutron responses along the central axis of the phantom the appropriate correction for a MOSFET at any point along the axis can be seen. This is shown in Figure 13-7. Under the current assumptions this correction amounts to a 9.7% correction at a depth of 1.25 cm a 1.3% correction at a depth of 3.75 cm. For depths greater than this the magnitude of the correction is too small to take into account compared to other uncertainties in the measurements.

When these corrections are applied to the total threshold voltage shifts measured by the Li shielded MOSFET along the central axis of the phantom the results shown in Figure 13-8 are obtained. These are plotted with the calculated gamma depth dose profile which was provided by HB Liu but has been renormalised for comparison.

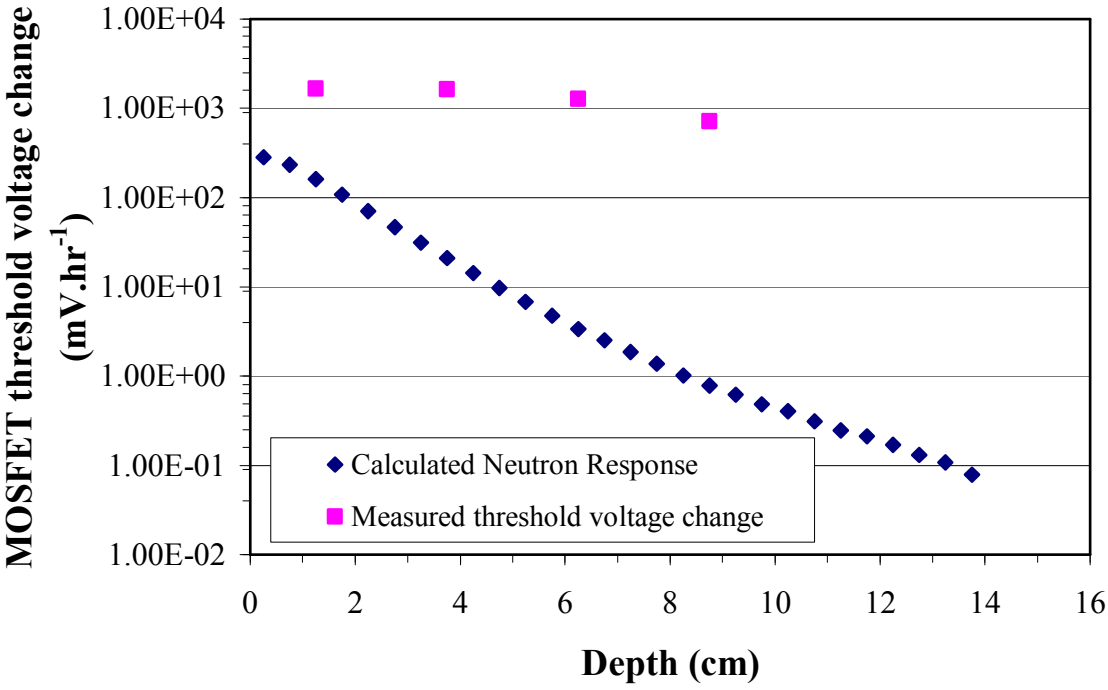

Figure 13-7. The measured total threshold voltage change along the axis of the phantom exposed in the BMRR beam. The threshold voltage change due to neutrons as calculated using MCNP and normalised using an in air measurement is shown in terms of $mV.hr^{-1}$.

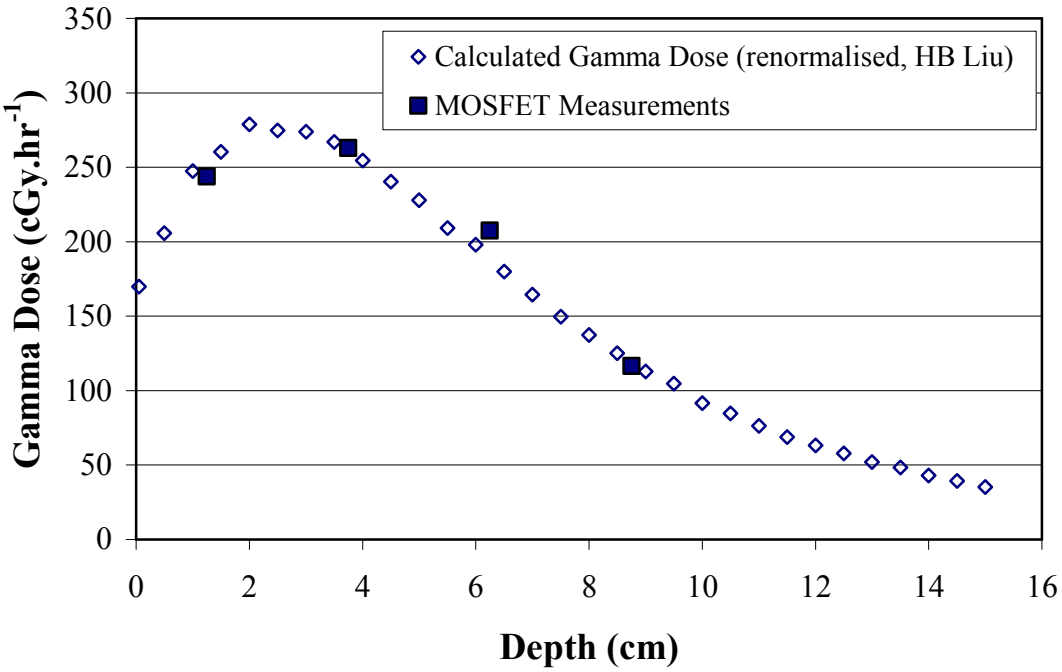

Figure 13-8. MOSFET measured gamma dose in PMMA phantom exposed in BMRR beam.

DISCUSSION

It can be seen from Figure 13-5 that apparently good agreement is observed between MOSFET threshold voltage measurements and the expected gamma depth dose profile relative to the gamma D_{max} in the BMRR beam. This apparent agreement is in part fortuitous since Figure 13-7 shows that there is a significant neutron contribution to the MOSFET response at the shallower depths in the phantom. Once this is taken into account an absolute gamma dose profile can be obtained as shown Figure 13-8.

However to obtain such a concordance between the measurements and a calculated gamma depth dose profile provided by B Liu[a] it was necessary to renormalize the gamma dose rate provided by B Liu by multiplying by a factor of 0.68. That is the MOSFET measurements give results approximately 30% lower than the anticipated gamma dose rate. It is highly probably that this discrepancy is due to the presence of the relatively large lithiated covers on the MOSFETs. As well as attenuating the neutron contribution to the MOSFET threshold voltage change these shields suppress the local neutron field and thereby also perturb (reduce) the gamma dose in the phantom close to the measurement point. Note that the induced gamma dose suppression due to the presence of lithiated shields in the cylinder phantom exposed in the Petten HB11 beam was approximately 30%. This is likely in this set of measurements due to the use of larger shields than were used for the previous measurements in the Petten beam.

CHAPTER 14 CONCLUSIONS

Despite increasing sophistication of conventional radiotherapy (e.g. stereotactic radiotherapy and intensity modulated radiotherapy) and chemotherapeutic techniques the prognosis for patients with glioblastomas and malignant melanomas remains poor. The current round of BNCT clinical trials (and most of the previous clinical trials) have been directed at these two tumor types. The increased number of epithermal beam facilities where trials are taking place and the improved understanding of the pharmacokinetics and microdosimetric aspects of the two most established boron pharmaceuticals (BPA, BSH) means that the data necessary to assess the efficacy of BNCT for these tumors is accumulating at an increasing rate. Advances in accelerator technology and the trend towards near threshold minimal moderation accelerator sources mean that if the efficacy of BNCT is demonstrated the possibility of BNCT treatment facilities in medical centres without the need for a reactor neutron source is becoming more plausible. Similarly the BNCT treatment planning tools necessary for efficient and accurate calculation of patient doses are becoming more streamlined and have a form that would be quite familiar to radiotherapists and dosimetrists used to performing conventional radiotherapy treatment planning.

It is in this context that the current thesis investigates the use of two semiconductor radiation detectors for measuring dose distributions in epithermal neutron beams. Changes in PIN diode forward bias voltage due to silicon displacement damage have been used previously for fast neutron dosimetry (MeV energies). This work is the first (to the best knowledge of the author) dedicated

specifically to determining the utility of forward bias voltage changes in PIN silicon detectors for neutron dosimetry in BNCT epithermal neutron beams. It is also the first to characterise the neutron response of a particular MOSFET device and then attempt to use MOSFETS purely as gamma detectors in BNCT epithermal beams correcting for the neutron response. (Complementary work by G Kaplan[136] has shown that MOSFETS with boron or ^{235}U radiators can be used for mapping thermal neutron distributions in epithermal beams).

MOSFET NEUTRON RESPONSE

The response of MOSFET changes in threshold voltage is principally determined by the entrapment of holes in the silicon oxide insulating layer under the gate electrode when the device is irradiated with photons or electrons. The intrinsic response of the silicon oxide to neutron irradiation is minimal. However when the MOSFET junction is encapsulated in standard electronic device packaging such as a kovar TO-18 can then significant neutron sensitivity is observed. This is due to the dose deposited in the silicon oxide layer by secondary electrons and photons generated as a result of neutron reactions in the device packaging. To determine the energy dependency of this neutron response for the MOSFETs used in this thesis the MCNP Monte Carlo code was used. A detailed model of the MOSFET and its package was constructed and the photon and electron dose deposited in the silicon oxide layer was calculated for a range of incident neutron energies from thermal to fast neutrons. A similar calculation was performed with a lithiated Perspex shield (~ 1.8mm thick) incorporated into the model. This reduced the MOSFET neutron

response by several orders of magnitude at thermal and low energies. A thicker lithiated shield (~5mm thick) was also modelled and further reduced the low energy neutron response. The absolute values of these calculated relative neutron energy response functions were later normalised by exposing the MOSFET in a neutron beam with known gamma dose and neutron spectrum. These absolute neutron response functions could then be used to make corrections to MOSFET measurements in phantoms. Future applications of MOSFETs to gamma dosimetry in mixed radiation fields would benefit from using MOSFETs with minimal encapsulation. This would minimise the amount of neutron shielding (lithium) required and minimise any perturbation on the neutron field near the point of measurement. Potentially a graphite encapsulation would lead to less neutron response.

IDEAL BEAM STUDY OF PIN DIODE TISSUE EQUIVALENT DOSE MEASUREMENTS

The neutron energy response function of PIN diodes (as measured by forward bias voltage change following irradiation) follows the silicon displacement damage KERMA function. Silicon displacement damage KERMA is not directly proportional to tissue KERMA at all energies of interest for epithermal neutron beams used in BNCT. Therefore measurements with PIN diodes (eg depth dose profiles) do not necessarily represent tissue dose distributions. For fast neutron fields (MeV energy range) approximate equivalence can be achieved where the fast neutron contribution dominates both the silicon and tissue dose.

By using a series of Monte Carlo ideal beams incident on a cylindrical tissue equivalent phantom it is possible to calculate the silicon dose, tissue dose and expected foil activations at points within the phantom. It is possible to use these arrays of doses and activations to generate (by regression) a set of coefficients that allow the tissue dose to be expressed as a linear combination of silicon displacement damage and foil activation. For some energy ranges it possible to determine a set of coefficients that are the same for each ideal beam within the energy range of interest. It was shown that it is possible to express tissue dose as a function of silicon damage dose and foil activations with reasonable accuracy for the energy range from thermal to 100 keV. The accuracy of the obtainable relationship between silicon dose foil activation and tissue dose increases when the maximum energy is reduced. Up to incident energies of 50 keV the tissue dose can be parameterised as a combination of silicon dose and foil activation with an accuracy of better than 10% for depths along the central axis. Most of the depth dose profile shows a better agreement than this. Up to 100 keV the maximum discrepancy increases to 20% but again this is restricted to the superficial depths.

In practice this means that in some epithermal neutron beams (eg accelerator beams with maximum neutron energies of approximately 100 keV or thereabout) tissue dose could be measured by means of a PIN diode measurement and a bare foil activation (Au, Cu or Mn) measurement. This may provide a simple and quick method for mapping tissue dose in these environments. For beams with higher maximum neutron energies (most reactor epithermal neutron beams) the technique as developed here is not applicable.

MEASUREMENT OF PIN DIODE ENERGY RESPONSE IN AN ACCELERATOR NEUTRON BEAM

The PIN diodes used in this thesis were exposed to approximately monoenergetic neutrons in the energy range 90 - 890 keV using a Van de Graaff proton accelerator and lithium target. These measurements demonstrated that the forward bias voltage change of the PIN diodes matched the expected silicon displacement damage KERMA function over this energy range. On this basis the ASTM displacement damage KERMA function for silicon[125] was used in calculations of PIN diode (forward bias voltage) response in this thesis. This result was anticipated but was verified for completeness and confidence that the silicon displacement KERMA could be used to calculate PIN diode response for the other experiments in this thesis. An approximate sensitivity of 130±44 $mV.cGy^{-1}$ (silicon dose) was also determined for the PIN diodes based on these measurements.

MOSFET CHARACTERISATION USING MEDICAL LINAC

For similar reasons the MOSFETs used in this thesis were investigated in well characterised medical linac (Varian 2100C) x-ray beams. Measurements of the MOSFET sensitivity for gate potentials between 0 and 15 volts were performed. A second order polynomial was found to fit the sensitivity versus gate bias voltage and this allows the MOSFET sensitivity to be determined for any potential applied to the MOSFET gate during irradiation. Dose depth profiles measured using the MOSFET from D_{max} to 10 cm depth in RMI solid water material were found to be in agreement

with dose depth data measured using a Farmer ionisation chamber. Similar measurements with the MOSFET kovar cap removed also showed good agreement. More detailed measurements were performed in the buildup region using MOSFETs with and without the kovar encapsulation present. It was found that when the kovar was removed good agreement with both Monte Carlo (MCNP) calculations and ionisation chamber measurements of dose in the buildup region. When a kovar cap was present the surface dose was over estimated by the MOSFET in the first several millimetres of depth.

Measurements were also performed with the MOSFET at the surface of the phantom using different incident beam angles. An angular dependence (reflecting the dose buildup distributions for beams incident on a slab phantom at different angles was observed. Anisotropy of the angular response of the MOSFET in isolation or in equilibrium situations is negligible for high energy gamma rays.

X-ray dose enhancement effects were studied for low energy x-rays obtained from a Pantak Therapax superficial x-ray unit. When MOSFET responses were normalised to the 6MV sensitivity observed using a linac beam the low energy x-ray measurements showed an over response of approximately six times at an average x-ray energy of 30 keV for a MOSFET without a kovar cap. For a MOSFET with a kovar cap the over response was approximately 8-9 times at an average x-ray energy of 50 keV. These results also suggest the advantage of using a low Z, low neutron cross section encapsulation for MOSFETs used in BNCT beams.

MOSFET AND PIN DIODE MEASUREMENTS IN A THERMAL NEUTRON BEAM

By exposing PIN diodes in the TC-10 thermal column of the Ansto Moata reactor with and without cadmium or lithium shielding it was possible to determine the thermal neutron contribution to the PIN diode response per unit thermal flux (as measured using gold foils). This allowed a sensitivity factor of approximately 121 $mV.cGy^{-1}$ to be derived for the PIN diodes. However the uncertainty in this value is probably quite large.

MOSFET measurements in the TC-10 beam with various thicknesses of lithiated shields allowed the neutron contribution to the MOSFET response to be determined. The thermal neutron sensitivity for MOSFETs in passive mode was determined to be approximately 1.01×10^{-10} $mV/n.cm^{-2}$ using this approach.

Further measurements in the thermal column using the MOSFET in active mode and calibrated against a theratron Co-60 source yielded a gamma dose rate in the TC-10 column of 4.7 ± 0.1 $Gy.hr^{-1}$ which is in good agreement with the previously measured gamma dose rate of 4.8 $Gy.hr^{-1}$. For a MOSFET with a 5 volt bias during irradiation a thermal neutron sensitivity of 3.84×10^{-10} $mV/n.cm^{-2}$ was measured. For a MOSFET with a 10 volt gate bias the thermal neutron sensitivity was 5.04×10^{-10} $mV/n.cm^{-2}$. The corresponding ^{60}Co gamma sensitivities were 6.59 and 8.97 $mV.cGy^{-1}$ respectively. A direct linear relationship is therefore observed between gamma and neutron sensitivities for applied gate potentials between 0 and 10 volts.

PIN DIODE MEASUREMENTS IN PETTEN HB11 EPITHERMAL NEUTRON BEAM

Silicon damage dose using PIN diodes was measured in a several phantoms exposed in the Petten HB11 BNCT beam. A human head phantom and cylindrical tissue equivalent phantom were constructed by S Wallace. The original MCNP simulations of these phantoms in the Petten HB11 beam were also performed by S Wallace. A 15 cm cube perspex phantom was also used. This thesis concerns the measurements performed in these phantoms and the associated MCNP calculations based on modified versions of the original models.

Very good agreement was obtained between the measured and calculated absolute silicon damage doses in the Perspex cube phantom. Good agreement was also achieved (discrepancies of < 10%) in the tissue equivalent cylinder phantom once allowance was made form some dehydration of the gel used in phantom construction. For the more complex and detailed head phantom discrepancies between measured and calculated absolute silicon doses of 25-300% were observed at depth in the phantom. However it should be noted that these disagreements only amount to 2-3% errors as a proportion of the maximum silicon damage dose.

These results support the application of small easy to use PIN diodes as dosimeters for BNCT. While they do not directly yield tissue equivalent dose they would allow validation of calculated dose distributions indirectly. They will be most sensitive to the faster components of the neutron spectrum but also have a useful response to thermal and epithermal components.

MOSFET GAMMA DOSE MEASUREMENTS IN PETTEN HB11 EPITHERMAL NEUTRON BEAM

MOSFETs were used to measure gamma doses in the same three phantoms as were used for the PIN diode measurements. For the Perspex cube phantom good agreement was observed between lithium shielded MOSFETs and ionisation chamber measurements. The MCNP calculated induced gamma dose was approximately 60cGy.hr^{-1} less than the total measured dose.

The measured results in the cylinder and head phantoms were not able to be compared with ionisation chamber results but were compared to calculated MCNP induced gamma dose distributions. There were some inconsistencies in these two sets of data with the measured gamma dose at a depth of 2 cm appearing to be too low. This discrepancy was resolved by a more detailed MCNP model of the cylinder phantom which included the lithiated shield around the MOSFET. It is clear that within the first few cm of the surface the presence of a lithiated shield suppresses the thermal flux to such an extent that the measured gamma dose is incorrect. Although explicitly modelling the lithiated shield in the phantom leads to consistent results this defeats the purpose of using the shielded MOSFET for experimental determination of gamma dose. It is therefore concluded that to be useful for gamma measurements the MOSFET encapsulation must be modified so that lithiated shielding is not necessary. A MOSFET with graphite encapsulation may eliminate the need for shielding and would also have the advantage of decreasing the magnitude of the neutron sensitivity correction required.

It should be noted that at depths way from the thermal neutron maximum the presence of the lithiated shielding around the MOSFET does not seem to make a large impact on the measured gamma dose. This is born out by MCNP simulations.

PIN DIODE AND MOSFET MEASUREMENTS USING THE BMRR EPITHERMAL BEAM

Measurements using PIN diodes and MOSFETs were performed in the BMRR epithermal neutron beam in a Perspex cube phantom. Reasonable agreement was observed between calculations and measurements for the PIN diodes.

In the case of the MOSFETs the lithiated shield used in this case were approximately 5 mm thick and therefore probably lead to a significant thermal flux depression around the measurement point. For this reason although good agreement was observed for the relative gamma depth dose curve the absolute measured results were approximately 30 % lower than expected. This is probably due to the effect of neutron and consequent gamma flux depression.

SUMMARY

The response of PIN diodes was measured in quasi-monoenergetic neutron beams and found to be proportional to silicon damage KERMA. The response of the same silicon PIN diodes was measured in a reactor thermal neutron field and found to be consistent with the accelerator measurements. Ideal beam Monte Carlo modelling

was used to show that PIN diode measurements when combined with bare foil activation could be used to experimentally measure tissue dose in neutron spectra with maximum energies up to approx 100 keV.

PIN diode measurements were then performed in phantoms in two epithermal neutron beams. Where the beam parameters and the phantom composition and geometry was well defined good agreement was obtained. Small size and ease of readout (including possible realtime dose readout) make PIN diodes useful for epithermal neutron dose mapping and verification of dose calculations.

MOSFET responses were measured in well characterised medical x-ray beams. The MOSFET x-ray sensitivity was determined for various gate potentials and for different x-ray energies. The neutron energy response as a function of neutron energy was determined using MCNP calculations. The thermal neutron response of MOSFETs was measured in a reactor thermal neutron column.

Measurements of gamma doses in phantoms exposed in two epithermal neutron beams were then attempted. It was possible to obtain dose profiles using MOSFETs however the use of lithiated shielding perturbed the neutron field at the measurement point leading to a lower than expected measured gamma dose near the thermal flux maxima.

In order to use MOSFETs for gamma dosimetry in mixed epithermal neutron / gamma fields it will be necessary to optimise the the encapsulation to minimse neutron response and obviate the need for extra neutron shielding which has the effect of perturbing the field being measured.

APPENDIX A MCNP4A MODEL OF MOSFET

MCNP4A model of mosfet including smaller lithiated shielding cap (as used in Petten HB11 experiments) for purposes of determining mosfet neutron energy response.

```
c       cells to define mosfet - modified to include 6LiF cap
1   1 -8.4 7 -8 -10                    $ mos top plate
2   1 -8.4 1 -7 -10 11                 $ mos can/tube
3   4 -8.4 2 -3 -11 13 14 15           $ inner can top plate
4   4 -8.4 1 -2 -11 12                 $ inner can tube
5   5 -2.23 1 -2 -12 13 14 15          $ glass plug at base of mos
6   4 -8.4 -6 9 -13                    $ lead 1
7   4 -8.4 -6 9 -14                    $ lead 2
8   4 -8.4 -6 9 -15                    $ lead 3
9   2 -2.4 3 -4 -16 17 -18 19          $ silicon chip
10  3 -2.4 4 -5 -16 17 -18 19          $ sio2 layer
11  0 -7 6 -11                         $ empty space in can
12  0 -22 -20                          $ empty space beneath
13  0 -1 9 13 14 15 -24                $ ditto
14  0 -21 22 23 -20                    $ empty space around can
15  0 21 -20                           $ empty space above lif cap
16  0 20                               $ rest of universe
      17  0 -6 5 -11 13 14 15          $ space above chip below lead
tops
18  0 -5 3 -11 13 16            $ "round chip bel. surf
19  0 -5 3 -11 14 -17           $ "round chip bel. surf
20  0 -5 3 -11 15 18 -16 17     $ "round chip bel. surf
21  0 -5 3 -11 -19 -16 17       $ "round chip bel. surf
22  6 -1.69 8 -21 -23           $  lif top of cap
23  6 -1.69 -8 -23 10 1         $  lif around can
24  6 -1.69 -1 -23 24 9         $  lif around lead volume
25  6 -1.69 -9 -23 22           $  lif base i.e. bottom disc of cap

c       planes to define the mosfet
1  pz 0                   $ base of mos
2  pz 0.230               $ underside of ni/au substrate
3  pz 0.250               $ upper side if Ni/Au substrate
4  pz 0.280               $ upper side of si chip
5  pz 0.295               $ upper side of sio2/Al
6  pz 0.300               $ plane for top of leads
7  pz 0.480               $ underside of Ni lid
8  pz 0.500               $ upperside of Ni lid
9  pz -0.556                $ plane for bottom end of leads
10  cz 0.232              $ cyl for outer of ni can
11  cz 0.212              $ cyl for inner of ni can
12  cz 0.192              $ cyl for inner of inside half can ni/au
13  c/z 0.15 0 0.02       $ lead number 1
14  c/z -0.15 0 0.02      $ lead number 2
15  c/z 0 0.15 0.02       $ lead number 3
      16  px 0.1               $ planes to define the sides of si &
sio2chip
17  px -0.1                $     ditto
18  py 0.1                 $     ditto
19  py -0.1                $     ditto
20  so 2                   $  sphere about origin
```

```
21  pz 0.84              $  plane for top of Lif cap
22  pz -1.156            $ plane for base of lif cap
23  cz 0.475             $ cylinder for outer of lif
      24  cz 0.296             $ cylinder for inner of lif (larger
dia part)

c       define materials
mode n p e
imp:n 1 1 1 1 1 1 1 1 1 1 1 1 1 1 0 1 1 1 1 1 1 1 1 1
imp:p 2 2 2 2 2 2 2 2 2 2 2 2 2 2 0 2 2 2 2 2 2 2 2 2
imp:e 2 2 2 2 2 2 2 2 2 2 2 2 2 2 0 2 2 2 2 2 2 2 2 2
      m1   26000.55c -0.54 28000.50c -0.29  27059.50c -0.17 estep=100
$kovar
m2   14000.50c 1 estep=100                    $ silicon
m3   14000.50c 10 8016.50c 20 13027.35c 0.1  estep=100    $ sio2/al
m4   26000.55c -0.54 28000.50c -0.29  27059.50c -0.17
       79197.35c -0.034 estep=100 $ Kovar/Au for leads and inner can
m5   5010.50c -0.0074 5011.56c -0.0296 13027.50c -0.01
           11023.50c -0.041 8016.50c -0.535 14000.50c -0.377 estep=20
           $glass
m6   3006.50c -0.133 9019.50c -0.423 6012.50c -0.268
     1001.50c -0.036 8016.50c -0.143 $lif resin mix
c       data card to describe source tally etc
sdef  sur=20 nrm=-1 dir=d1 erg=d2 par=1
sb1   -21 2
si2   h 0.001e-6 0.01e-6
sp2   d 0 1
c        tallies
*f8:p 10
fc8 sio2 pulse height tally
f4:p (9 10)
fc4 photon tally in mosfet
e4  0.001 0.003 0.005 0.007 0.01 0.03 0.05 0.07 0.1 0.3
     0.5 0.7 1.0 3.0 5.0 7.0 10.0 15.0
f14:p (9 10)
fc14 photon heating using -6 multiplier
fm14   1 3 -6
f24:p (9 10)
f24c photon tally in mosfet times silicon gamma kerma (plotxs)
de24   .015       .025       .0375      .0525      .0649999
         .125       .175       .25        .35        .425
         .511       .556       .65        .75        .9
         1.415      1.58       1.83       2.25       2.75
         3.75       4.25       4.75       5.25       5.75
         6.75       7.25       7.75       9          11
         17
df24  2.284222E-11  8.190444E-12 3.495018E-12
         1.782612E-12  1.211255E-12 7.141306E-13
         8.353256E-13  1.163867E-12 1.662457E-12
         2.048793E-12  2.466298E-12 2.665177E-12
         3.094492E-12  3.518312E-12 4.126257E-12
         5.918366E-12  6.46583E-12  7.166327E-12
         8.336321E-12  9.68157E-12  1.226261E-11
         1.359546E-11  1.493106E-11 1.629781E-11
         1.76978E-11   2.046066E-11 2.190036E-11
         2.330236E-11  2.704061E-11 3.290582E-11
         5.116297E-11
f34:e (9 10)
fc34 electron tally in mosfet
e34  0.001 0.004 0.007 0.01 0.03
      0.05 0.1 0.2 0.5 0.7 1.0 2.0 5.0 10.0
f44:n (9 10)
fc44 silicon oxide average neutron dose
fm44 1 3 -4
prdmp -120 -120
ctme 120
```

MCNP4A model of mosfet including thicker lithiated shielding cap (as used in BMRR, BNL experiments) for purposes of determining mosfet neutron energy response.

```
c       cells to define mosfet - modified to include 6LiF cap
c       modified for large LiF shield as used for BNL experiments
1   1 -8.4 7 -8 -10                   $ mos top plate
2   1 -8.4 1 -7 -10 11                $ mos can/tube
3   4 -8.4 2 -3 -11 13 14 15          $ inner can top plate
4   4 -8.4 1 -2 -11 12                $ inner can tube
5   5 -2.23 1 -2 -12 13 14 15         $ glass plug at base of mos
6   4 -8.4 -6 9 -13                   $ lead 1
7   4 -8.4 -6 9 -14                   $ lead 2
8   4 -8.4 -6 9 -15                   $ lead 3
9   2 -2.4 3 -4 -16 17 -18 19         $ silicon chip
10  3 -2.4 4 -5 -16 17 -18 19         $ sio2 layer
11  0 -7 6 -11                        $ empty space in can
12  0 -22 -20                         $ empty space beneath
13  0 -1 9 13 14 15 -24               $ ditto
14  0 -21 22 23 -20                   $ empty space around can
15  0 21 -20                          $ empty space above lif cap
16  0 20                              $ rest of universe
17  0 -6 5 -11 13 14 15         $ space above chip below lead tops
18  0 -5 3 -11 13 16            $ "round chip bel. surf
19  0 -5 3 -11 14 -17           $ "round chip bel. surf
20  0 -5 3 -11 15 18 -16 17     $ "round chip bel. surf
21  0 -5 3 -11 -19 -16 17       $ "round chip bel. surf
22  6 -1.69 8 -21 -23           $  lif top of cap
23  6 -1.69 -8 -23 10 1         $  lif around can
24  6 -1.69 -1 -23 24 9         $  lif around lead volume
25  6 -1.69 -9 -23 22 25        $  lif base ie bottom disc of cap
26  7 -8.96 -9 22 -25           $  copper cabble thru base

c       planes to define the mosfet
1  pz 0                   $ base of mos
2  pz 0.230               $ underside of ni/au substrate
3  pz 0.250               $ upper side if Ni/Au substrate
4  pz 0.280               $ upper side of si chip
5  pz 0.295               $ upper side of sio2/Al
6  pz 0.300               $ plane for top of leads
7  pz 0.480               $ underside of Ni lid
8  pz 0.500               $ upperside of Ni lid
9  pz -0.5                $ plane for bottom end of leads
10  cz 0.232              $ cyl for outer of ni can
11  cz 0.212              $ cyl for inner of ni can
12  cz 0.192              $ cyl for inner of inside half can ni/au
13  c/z 0.15 0 0.02       $ lead number 1
14  c/z -0.15 0 0.02      $ lead number 2
15  c/z 0 0.15 0.02       $ lead number 3
16  px 0.1                $ planes to define the sides of si & sio2chip
17  px -0.1               $     ditto
18  py 0.1                $     ditto
19  py -0.1               $     ditto
20  so 2                  $  sphere about origin
21  pz 1.3             $  plane for top of Lif cap
22  pz -1.1            $  plane for base of lif cap
23  cz 0.8             $  cylinder for outer of lif
24  cz 0.3             $  cylinder for inner of lif (larger dia part)
25  cz 0.075           $  cylinder for cable tru base of shield

c       define materials
mode n p e
imp:n 1 1 1 1 1 1 1 1 1 1 1 1 1 1 0 1 1 1 1 1 1 1 1 1
imp:p 2 2 2 2 2 2 2 2 2 2 2 2 2 2 0 2 2 2 2 2 2 2 2 2
```

```
imp:e 2 2 2 2 2 2 2 2 2 2 2 2 2 2 2 0 2 2 2 2 2 2 2 2 2 2
m1   26000.55c -0.54 28000.50c -0.29  27059.50c -0.17 estep=100 $kovar
m2   14000.50c 1 estep=100                    $ silicon
m3   14000.50c 10 8016.50c 20 13027.50c 0.1  estep=100    $ sio2/al
m4   26000.55c -0.54 28000.50c -0.29  27059.50c -0.17
        79197.35c -0.034 estep=100 $ Kovar/Au for leads and inner can
m5   5010.50c -0.0074 5011.56c -0.0296 13027.50c -0.01
     11023.50c -0.041 8016.50c -0.535 14000.50c -0.377 estep=20
     $ glass
m6   3006.50c -0.1366 9019.50c -0.433 6012.50c -0.258
     1001.50c -0.0347 8016.50c -0.1377 $lif resin mix, 43%PMMA, 57%LiF
m7   29000.50c 1
c       data card to describe source tally etc
sdef  sur=20 nrm=-1 dir=d1 erg=d2 par=1
sb1   -21 2
si2   h 0.001e-6 0.01e-6
sp2   d 0 1
c        tallies
*f8:p 10
fc8 sio2 pulse height tally
f4:p (9 10)
fc4 photon tally in mosfet
e4  0.001 0.003 0.005 0.007 0.01 0.03 0.05 0.07 0.1 0.3
      0.5 0.7 1.0 3.0 5.0 7.0 10.0 15.0
f14:p (9 10)
fc14 photon heating using -6 multiplier
fm14   1 3 -6
f24:p (9 10)
f24c photon tally in mosfet times silicon gamma kerma (plotxs)
de24   .015       .025       .0375      .0525      .0649999
         .125       .175       .25        .35        .425
         .511       .556       .65        .75        .9
         1.415      1.58       1.83       2.25       2.75
         3.75       4.25       4.75       5.25       5.75
         6.75       7.25       7.75       9          11
         17
df24  2.284222E-11  8.190444E-12 3.495018E-12
         1.782612E-12  1.211255E-12 7.141306E-13
         8.353256E-13  1.163867E-12 1.662457E-12
         2.048793E-12  2.466298E-12 2.665177E-12
         3.094492E-12  3.518312E-12 4.126257E-12
         5.918366E-12  6.46583E-12  7.166327E-12
         8.336321E-12  9.68157E-12  1.226261E-11
         1.359546E-11  1.493106E-11 1.629781E-11
         1.76978E-11   2.046066E-11 2.190036E-11
         2.330236E-11  2.704061E-11 3.290582E-11
         5.116297E-11
f34:e (9 10)
fc34 electron tally in mosfet
e34  0.001 0.004 0.007 0.01 0.03
       0.05 0.1 0.2 0.5 0.7 1.0 2.0 5.0 10.0
f44:n (9 10)
fc44 silicon oxide average neutron dose
fm44 1 3 -4
prdmp -120 -120 1
ctme 120
```

APPENDIX B MCNP4A MODEL OF SOLID WATER PHANTOM IN LINAC BEAM

```
c model of block of solid water in 10x10cm 6mv linac beam
1   1 -1.04 -1 2 -3 4 -5 6 #(47 -48 49 -50 -1 2) $cube excl tally core
2   0 -2 $ volume below cube                    imp=0
3   0  3 2 $ volume to right of cube             "
4   0 -4 2 $ volume to left of cube              "
5   0  5 2 $ volume to front of cube             "
6   0 -6 2 $ volume behind cube                  "
7   0  7 -3 4 -5 6 $ volume above source         "
8   0  1 -8 -3 4 -5 6 $ above cube below coll.   imp=1
9   0  8 -9 -10 11 -12 13 $ apperture in coll.   imp=1
10  0  9 -7 -3 4 -5 6 $ abov coll below source   imp=1
11  0  8 -9 4 -11 6 -5 $ coll. imp=0
12  1 -1.04 47 -48 49 -50 -1 14
13  1 -1.04 47 -48 49 -50 -14 15
14  1 -1.04 47 -48 49 -50 -15 16
15  1 -1.04 47 -48 49 -50 -16 17
16  1 -1.04 47 -48 49 -50 -17 18
17  1 -1.04 47 -48 49 -50 -18 19
18  1 -1.04 47 -48 49 -50 -19 20
19  1 -1.04 47 -48 49 -50 -20 21
20  1 -1.04 47 -48 49 -50 -21 22
21  1 -1.04 47 -48 49 -50 -22 23
22  1 -1.04 47 -48 49 -50 -23 24
23  1 -1.04 47 -48 49 -50 -24 25
24  1 -1.04 47 -48 49 -50 -25 26
25  1 -1.04 47 -48 49 -50 -26 27
26  1 -1.04 47 -48 49 -50 -27 28
27  1 -1.04 47 -48 49 -50 -28 29
28  1 -1.04 47 -48 49 -50 -29 30
29  1 -1.04 47 -48 49 -50 -30 31
30  1 -1.04 47 -48 49 -50 -31 32
31  1 -1.04 47 -48 49 -50 -32 33
32  1 -1.04 47 -48 49 -50 -33 34
33  1 -1.04 47 -48 49 -50 -34 35
34  1 -1.04 47 -48 49 -50 -35 36
35  1 -1.04 47 -48 49 -50 -36 37
36  1 -1.04 47 -48 49 -50 -37 38
37  1 -1.04 47 -48 49 -50 -38 39
38  1 -1.04 47 -48 49 -50 -39 40
39  1 -1.04 47 -48 49 -50 -40 41
40  1 -1.04 47 -48 49 -50 -41 42
41  1 -1.04 47 -48 49 -50 -42 43
42  1 -1.04 47 -48 49 -50 -43 44
43  1 -1.04 47 -48 49 -50 -44 45
44  1 -1.04 47 -48 49 -50 -45 46
45  1 -1.04 47 -48 49 -50 -46 2
46  0  8 -9 10 -3 6 -5 $ coll. imp=0
47  0  8 -9 11 -10 6 -13 $ coll. imp=0
48  0  8 -9 11 -10 12 -5 $ coll. imp=0

c planes for phantom
1 pz 0          $top of phantom
2 pz -30        $bottom of phantom
3 px 15         $side of phantom
4 px -15        $side of phantom
5 py 15         $side of phantom
6 py -15        $side of phantom
7 pz 100.1      $plane at source
8 pz 50         $collimator
9 pz 95.1       $collimator
10 px 2.5       $collimator apeture
```

```
11 px -2.5    $collimator apeture
12 py 2.5     $collimator apeture
13 py -2.5    $collimator apeture
c planes for tallies
14 pz -0.1
15 pz -0.2
16 pz -0.3
17 pz -0.4
18 pz -0.5
19 pz -0.6
20 pz -0.7
21 pz -0.8
22 pz -0.9
23 pz -1
24 pz -1.2
25 pz -1.4
26 pz -1.6
27 pz -1.8
28 pz -2.0
29 pz -3
30 pz -4
31 pz -5
32 pz -6
33 pz -7
34 pz -8
35 pz -9
36 pz -10
37 pz -11
38 pz -12
39 pz -13
40 pz -14
41 pz -15
42 pz -16
43 pz -17
44 pz -18
45 pz -19
46 pz -20
c planes for sides of tallies
47 px -0.25
48 px 0.25
49 py -0.25
50 py 0.25
100 pz 100

mode p e
m1   1001 8.09 6012 67.22 7014 2.41 8016 19.84
     20000 0.13 estep=40 $Brain ICRU 92
imp:p 1 0 0 0 0 0 0 1 1 1 0 1 1 1 1 1 1 1
      1 1 1 1 1 1 1 1 1 1 1 1 1 1
      1 1 1 1 1 1 1 1 1 1 1 1 1 0 0 0
imp:e 1 0 0 0 0 0 0 1 1 1 0 1 1 1 1 1 1 1
      1 1 1 1 1 1 1 1 1 1 1 1 1 1
      1 1 1 1 1 1 1 1 1 1 1 1 1 0 0 0
sdef pos 0 0 100 vec 0 0 -1 dir 1 erg=d1 rad=d2 sur=100
si1  0.45 0.55   0.65  0.75 0.9   1.125 1.375
     1.750 2.250 2.750 3.5   4.250 4.75 5.5   7.0
sp1  0    0.002  0.005 0.01 0.025 0.049 0.056
     0.089 0.091 0.064 0.062 0.029 0.009 0.006 0.001
si2  0.01
fq0  u e
f4:p 12 13 14 15 16 17 18 19 20 21 22
     23 24 25 26 27 28 29 30 31 32 33
     34 35 36 37 38 39 40 41 42 43 44
fm4  1 1 -6
fc4  photon heating tally
f14:e 12 13 14 15 16 17 18 19 20 21 22
     23 24 25 26 27 28 29 30 31 32 33
     34 35 36 37 38 39 40 41 42 43 44
fc14  electron tally
*f8:e 12 13 14 15 16 17 18 19 20 21 22
     23 24 25 26 27 28 29 30 31 32 33
     34 35 36 37 38 39 40 41 42 43 44
```

```
fc8  electron pulse height tally
nps 100
```

APPENDIX C MCNP4A MODEL OF TISSUE EQUIVALENT CYLINDER FOR IDEAL BEAM STUDIES OF PIN DIODE

```
c model of a TE cylinder phantom for the purposes comparing ideal
beams
c in tissue and Si damage kerma. E=0.25e-6
1     2 -1.04 -150 101 -102
2     2 -1.04 -150 102 -103
3     2 -1.04 -150 103 -104
4     2 -1.04 -150 104 -105
5     2 -1.04 -150 105 -106
6     2 -1.04 -150 106 -107
7     2 -1.04 -150 107 -108
8     2 -1.04 -150 108 -109
9     2 -1.04 -150 109 -110
10    2 -1.04 -150 110 -111
11    2 -1.04 -150 111 -112
12    2 -1.04 -150 112 -113
13     2 -1.04 -150 113 -114
14     2 -1.04 -150 114 -115
15     2 -1.04 -150 115 -116
16     2 -1.04 -150 116 -117
17     2 -1.04 -150 117 -118
18     2 -1.04 -150 118 -119
19     2 -1.04 -150 119 -120
20     2 -1.04 -150 120 -121
21     2 -1.04 -150 121 -122
22     2 -1.04 -150 122 -123
23     2 -1.04 -150 123 -124
24     2 -1.04 -150 124 -125
25     2 -1.04 -150 125 -126
26     2 -1.04 -150 126 -127
27     2 -1.04 -150 127 -128
28     2 -1.04 -150 128 -129
29     2 -1.04 -150 129 -130
30     2 -1.04 -150 130 -131
31     2 -1.04 -150 131 -132
101     2 -1.04 -152 151 101 -102
102     2 -1.04 -152 151 102 -103
103     2 -1.04 -152 151 103 -104
104     2 -1.04 -152 151 104 -105
105     2 -1.04 -152 151 105 -106
106     2 -1.04 -152 151 106 -107
107     2 -1.04 -152 151 107 -108
108     2 -1.04 -152 151 108 -109
109     2 -1.04 -152 151 109 -110
110     2 -1.04 -152 151 110 -111
111     2 -1.04 -152 151 111 -112
112     2 -1.04 -152 151 112 -113
113     2 -1.04 -152 151 113 -114
114     2 -1.04 -152 151 114 -115
115     2 -1.04 -152 151 115 -116
116     2 -1.04 -152 151 116 -117
117     2 -1.04 -152 151 117 -118
118     2 -1.04 -152 151 118 -119
119     2 -1.04 -152 151 119 -120
120     2 -1.04 -152 151 120 -121
```

```
121    2 -1.04 -152 151 121 -122
122    2 -1.04 -152 151 122 -123
123    2 -1.04 -152 151 123 -124
124    2 -1.04 -152 151 124 -125
125    2 -1.04 -152 151 125 -126
126    2 -1.04 -152 151 126 -127
127    2 -1.04 -152 151 127 -128
128    2 -1.04 -152 151 128 -129
129    2 -1.04 -152 151 129 -130
130    2 -1.04 -152 151 130 -131
131    2 -1.04 -152 151 131 -132
201    2 -1.04 150 -151 101 -103
202    2 -1.04 150 -151 103 -132
203    2 -1.04 152 -153 101 -103
204    2 -1.04 152 -153 103 -132
205    2 -1.04 132 -140 -153
300    0 -100
301    0 140
302    0 153 100 -140
303    0 -153 -101 100

c    Surface Cards
100   py -0.1
101   py 0.0
102   py 0.25
103   py 0.75
104   py 1.25
105   py 1.75
106   py 2.25
107   py 2.75
108   py 3.25
109   py 3.75
110   py 4.25
111   py 4.75
112   py 5.25
113   py 5.75
114   py 6.25
115   py 6.75
116   py 7.25
117   py 7.75
118   py 8.25
119   py 8.75
120   py 9.25
121   py 9.75
122   py 10.25
123   py 10.75
124   py 11.25
125   py 11.75
126   py 12.25
127   py 12.75
128   py 13.25
129   py 13.75
130   py 14.25
131   py 14.75
132   py 15.25
140   py 23.0
150   cy 0.25
151   cy 2.25
152   cy 2.75
153   cy 8.0

c    data cards
mode n
m1    1001 -5.55 6012 -75.58 8016 -18.88
      $polycarbonate
m2   1001 -10.7 6012 -14.5 7014 -2.2 8016 -71.2
     11023 -0.2 15031 -0.4 16032 -0.2 17000 -0.3 19000 -0.3
     $Brain ICRU 92
mt2  lwtr.01t
mt1  poly.01t
m51   79197 1 $gold
m52   29000 1 $ copper
```

```
m53   25055.50c 1 $Manganese
c     m54   49115 1 $ indium
c     no indium xsections present
imp:n 1 66r 0 0 0 1
c
c    Source definition.
c    ==================
sdef  sur=101 pos=0.0 0.0 0.0 dir=1 erg=0.25e-6 rad=d1
si1     5
c
c     G E N E R A L  program data
c     ===========================
fq0  f t $vertical listing of cell scores in each tally
c    tally cards
f4:n  1 29i 31 101 29i 131
fc4  neutron flux
e4   1e-9 3e-9 1e-8 3e-8 1e-7 3e-7 1e-6 3e-6 1e-5 3e-5 1e-4 3e-4
     1e-3 3e-3 1e-2 3e-2 1e-1 3e-1 1 3 14.5
fq4   f e
f14:n  1 29i 31 101 29i 131
fc14  neutron dose
e14    0.414e-6 1e-5 1e-4 4e-4 3e-2 1e-1 1.4e-1 2e-1 4e-1 1.45e1
fq14  f e
c     f24:n  1 29i 31 101 29i 131
c     fc24  30ppm 10B dose
c     f34:p  1 29i 31 101 29i 131
c     fc34   photon dose
f44:n  1 29i 31 101 29i 131
fc44  silicon damage cGy
e44  0.414e-6 1e-5 1e-4 4e-4 3e-2 1e-1 1.4e-1 2e-1 4e-1 1.45e1
fq44 e f
c    neutron tissue dose conversion
de14 2.5e-8 2e-6 2e-5 2e-4 2e-3 2e-2 1.05e-1 1.05e+00
     1.05e+1 1.55e+1 $MeV
df14 1.5e-11 1.73e-12 7.51e-13 2.29e-12 2.10e-11 1.89e-10
     6.95e-10 2.56e-9 5.98e-9 7.03e-9 $Kerma cGy*cm**2
c    30ppm B10 dose conversion
c    de24 1e-8 2.5e-8 3.6e-8 2.51e-7 6.84e-7 1.86e-6 5e-6
c     1.37e-5 3.73e-5 1.01e-4 2.75e-4 7.49e-4 2.03e-3 $MeV
c    df24 4.14e-10 2.62e-10 2.19e-10 8.76e-11 5.43e-11 3.27e-11
c     1.91e-11 1.2e-11 7e-12 4.41e-12 2.7e-12 1.64e-12
c     9.8e-13 $Kerma cGy*cm**2 30ppmB10 dose only
c    photon tissue dose conversion
c    de34 1e-3 2e-3 5e-3 1e-2 2e-2 5e-2 1e-1 2e-1 5e-1 1e+0
c     2e+0 5e+0 1e+1 2e+1 $Mev
c    df34 5.99e-08 1.8e-8 3.24e-9 7.75e-10 1.75e-10 3.24e-11
c     4.04e-11 9.46e-11 2.63e-10 4.94e-10 8.29e-10
c     1.52e-9 2.48e-9 4.38e-9 $Kerma cGy*cm**2
de44  2.24068e-09 $Si damage kerma (MeV energy)
      3.69425e-09 $cGy*cm**2*sec
      6.09079e-09
      1.0042e-08  1.31589e-08 1.45429e-08 1.60723e-08 1.77626e-08
      1.96307e-08 2.16954e-08 2.39771e-08 2.64988e-08 2.92856e-08
      3.23656e-08 3.57697e-08 3.95316e-08 4.36892e-08 4.82839e-08
      5.33619e-08 5.89743e-08 6.51765e-08 &.20311e-08 7.96066e-08
      8.79788e-08 9.72321e-08 1.07458e-07 1.18759e-07 1.31249e-07
      1.45053e-07 1.60309e-07 1.77168e-07 1.95801e-07 2.16393e-07
      2.39151e-07 2.64305e-07 2.92101e-07 3.22821e-07 3.56772e-07
      3.94294e-07 4.35765e-07 4.81594e-07 5.32243e-07 5.88218e-07
      6.5008e-07  7.18454e-07 7.94014e-07 8.7752e-07  9.69806e-07
      1.0718e-06  1.18453e-06 1.30911e-06 1.44679e-06 1.59895e-06
      1.76711e-06 1.95295e-06 2.15835e-06 2.38535e-06 2.63622e-06
      2.91347e-06 3.49344e-06 4.48567e-06 5.75971e-06 7.39562e-06
      9.49614e-06 1.21933e-05 1.56565e-05 2.01034e-05 2.58132e-05
      3.31448e-05 4.25588e-05 5.46466e-05 7.01676e-05 9.00971e-05
      1.15687e-04 1.48545e-04 1.90735e-04 2.44909e-04 3.14469e-04
      4.03787e-04 5.18473e-04 6.65732e-04 8.54816e-04 1.09761e-03
      1.31626e-03 1.49151e-03 0.0016901   1.91514e-03 2.17014e-03
      2.45909e-03 2.78652e-03 3.15754e-03 3.57796e-03 4.05435e-03
      4.59418e-03 5.20589e-03 5.89905e-03 0.0066845   7.57453e-03
      8.58307e-03 0.0097259   0.0110209   0.0124883   0.0141511
      .0160353    0.0181703   0.0205897   0.0233312   0.0264377
```

```
      .0299578   .0339467      .0384666    .0435884    .0493922
      .0559687   .0634207      .0718651    .0814339    .0922766
      .104563    .118486       .134262     .147242     .156739
      .166847    .177608       .189063     .201256     .214236
      .228053    .242761       .258418     .275085     .292826
      .311712    .331816       .353216     .375996     .400246
      .426059    .453538       .482789     .513926     .547071
      .582355    .619913       .659894     .702454     .747758
      .795984    .84732        .901968     .96014     1.02206
     1.08798   1.15815       1.23285     1.31236     1.397
     1.4871    1.58301       1.6851      1.79378     1.90947
     2.03262   2.16371       2.30326     2.45181     2.60993
     2.77826   2.95744       3.14818     3.35122     3.56735
     3.79743   4.04234       4.30305     4.58057     4.876
     5.19047   5.52522       5.88157     6.2609      6.66469
     7.09453   7.55209       8.03915     8.55762     9.10954
     9.69706  10.3224       10.9882     11.6969     12.4513
     13.044   13.4581       13.8853     14.3261     14.7808
df44  1.139608e-13 $Si damage kerma (kerma)
      8.872022e-14 $cGy*cm**2*sec
      6.911985e-14
      5.382809e-14  4.698947e-14   4.467793e-14    4.249707e-14
      4.042712e-14  3.845414e-14   3.658561e-14    3.479285e-14
      3.307903e-14  3.146068e-14   2.991504e-14    2.845421e-14
      2.705426e-14  2.572107e-14   2.44644e-14     2.32737e-14
      2.214843e-14  2.108652e-14   2.009261e-14    1.913243e-14
      1.820844e-14  1.73249e-14    1.649836e-14    1.570998e-14
      1.496096e-14  1.423965e-14   1.354101e-14    1.285803e-14
      1.221635e-14  1.163057e-14   1.10634e-14     1.05213e-14
      1.00054e-14   9.516939e-15   9.023816e-15    8.575672e-15
      8.172521e-15  7.780097e-15   7.406513e-15    7.048285e-15
      6.712682e-15  6.374564e-15   6.064049e-15    5.78651e-15
      5.494637e-15  5.231793e-15   4.968984e-15    4.714971e-15
      4.477693e-15  4.260399e-15   4.053349e-15    3.862171e-15
      3.687897e-15  3.507276e-15   3.334228e-15    3.170209e-15
      2.878356e-15  2.541229e-15   2.240582e-15    1.982931e-15
      1.75226e-15   1.549848e-15   1.371894e-15    1.20275e-15
      1.063582e-15  9.378355e-16   8.263944e-16    7.314748e-16
      6.441276e-16  5.681734e-16   5.024657e-16    4.410407e-16
      1.01183e-15   4.943858e-15   8.634314e-15    1.310663e-14
      1.935209e-14  2.556637e-14   3.365582e-14    4.320152e-14
      5.229323e-14  5.955156e-14   6.725444e-14    7.583962e-14
      8.567795e-14  9.688433e-14   1.092836e-13    1.230059e-13
      1.383673e-13  1.556411e-13   1.778341e-13    2.030548e-13
      2.268539e-13  2.540585e-13   2.842102e-13    3.170536e-13
      3.540249e-13  3.939739e-13   4.406613e-13    4.95467e-13
      5.550313e-13  6.170442e-13   6.830327e-13    7.464381e-13
      8.175346e-13  9.01417e-13    9.916632e-13    1.207613e-12
      1.045831e-12  7.946789e-13   1.469681e-11    2.524801e-12
      2.318469e-12  2.133843e-12   1.964938e-12    1.742369e-12
      1.335893e-12  7.838897e-13   5.806286e-13    2.368042e-12
      9.439942e-12  2.663609e-11   3.885624e-11    3.409585e-11
      2.740755e-11  2.339778e-11   2.084227e-11    1.923364e-11
      1.807755e-11  1.760321e-11   1.725335e-11    1.697778e-11
      1.721205e-11  1.735033e-11   1.789191e-11    1.79938e-11
      1.830144e-11  1.893635e-11   2.015418e-11    3.295358e-11
      2.475467e-11  1.825112e-11   1.927201e-11    2.032588e-11
      2.377295e-11  3.696862e-11   3.332297e-11    3.059793e-11
      3.840454e-11  3.099449e-11   2.43371e-11     2.229745e-11
      2.90611e-11   3.056374e-11   3.218565e-11    3.494228e-11
      4.293426e-11  4.585451e-11   3.461053e-11    4.448711e-11
      3.479863e-11  3.671302e-11   3.579939e-11    4.098488e-11
      4.192978e-11  3.951167e-11   3.454923e-11    4.516524e-11
      3.919306e-11  3.578532e-11   3.857847e-11    4.53553e-11
      5.11644e-11   4.973329e-11   5.391368e-11    5.51605e-11
      4.520707e-11  5.365942e-11   5.938245e-11    5.248903e-11
      5.205755e-11  5.609426e-11   5.755874e-11    5.699389e-11
      5.581579e-11  5.464705e-11   5.652209e-11    5.488637e-11
      5.700434e-11  5.752392e-11   5.801822e-11    5.762e-11
      5.699998e-11  5.770559e-11   5.832971e-11
f54:n 1 29i 31 101 29i 131
fc54  Gold Activation
```

```
e54   0.414e-6 0.5e-6 14.5
fm54  1 51 102
fq54  f e
f64:n 1 29i 31 101 29i 131
fc64  Copper Activation
e64   0.414e-6 0.5e-6 14.5
fm64  1 52 102
fq64  f e
f74:n 1 29i 31 101 29i 131
fc74  Manganese Activation
e74   0.414e-6 0.5e-6 14.5
fm74  1 53 102
fq74  f e
c    f84:n 1 29i 31 101 29i 131
c    fc84  Indium Activation
c    e84   0.414e-6 0.5e-6 14.5
c    fm84  1 54 102
c    fq84  f e
c     no indiumxs present in tables
```

APPENDIX D LONG COUNTER CALIBRATION FOR ANSTO VAN DE GRAFF MEASUREMENTS

Before the PIN diode measurements were commenced the long counter was calibrated using a AmBe neutron source of known activity (The 4π fluence was known to be 6.5×10^5 $n.cm^{-2}.s^{-1}$). For this calibration the AmBe source was placed 2 cm from the centre of the target along the axis of the beam line. The AmBe source was in a brass housing of dimensions 28 × 28 × 30 mm. To determine the geometric counting dependence of the AmBe source / long counter arrangement the source detector distance was varied from 45 cm to 207 cm. The number of counts was recorded at each location of the long counter as shown below. The distance was corrected to take into account the effective centre the long counter. The effective centre of the detector is located approximately 6 cm behind the front face of the detector for neutrons of approximately 4.2 – 4.5 MeV such as are emitted from the AmBe source[203].

Table D-1. Change in efficiency of long counter as function of source counter distance.

Distance (cm)	Effective Distance (cm)	Counts per second (-background)	Incident neutrons	Geometric Efficiency (counts per neutron incident on face)
205	211	7.305	821	8.89e-3
165	171	9.405	1250	7.58e-3
125	131	9.253	2130	6.47e-3
85	91	13.78	4420	5.52e-3
45	51	24.356	14100	4.60e-3

The sensitive area of the long counter was taken to be the entire front face of the detector. This face has a radius of 15 cm and therefore an area of 707 cm^2. From Figure D-1 below it can be seen that the long counter efficiency tends to increase with distance from the neutron source. This is due primarily to two effects. The first is that the neutron source though not large relative to the source - detector distance is of finite size and is therefore not the ideal point source assumed in the calculation of the number of incident neutrons. That is, the $1/r^2$ assumption will not be completely correct especially at shorter distances between the source and detector. The second and more significant effect is that at greater source – detector distances a larger proportion of the neutrons impinging on the detector are closer to normal incidence than for lesser separations. Neutrons impinging on rim of the detector at angles of up to 20° when the detector is 40 cm from the source have less chance of being detected than those impinging on the rim at angles of up to 4° when the detector is 211 cm from the source. Therefore as the source detector distance increases the fraction of impinging neutrons which yield counts from the detector also increases.

Because the effective centre of the Long Counter detector varies with the energy of the incident neutrons a small correction to the actual source – detector distance was required for each of the different energies used to irradiate the PIN diode. For all of the PIN diode irradiations the actual distance between the Li target on the accelerator and the face of the long counter was 207 cm. These corrections to the effective location of the detector are based on those given by Fowles[203] and are shown in Table D-2.

Based on these corrections to the actual distance of 207 cm between the counter and the target / source, geometric efficiencies for the long counter were

derived. These geometric efficiencies only take into account the effect of the location of the long counter relative to the neutron source. They do not include a factor for the intrinsic energy dependence of the long counter neutron detection sensitivity.

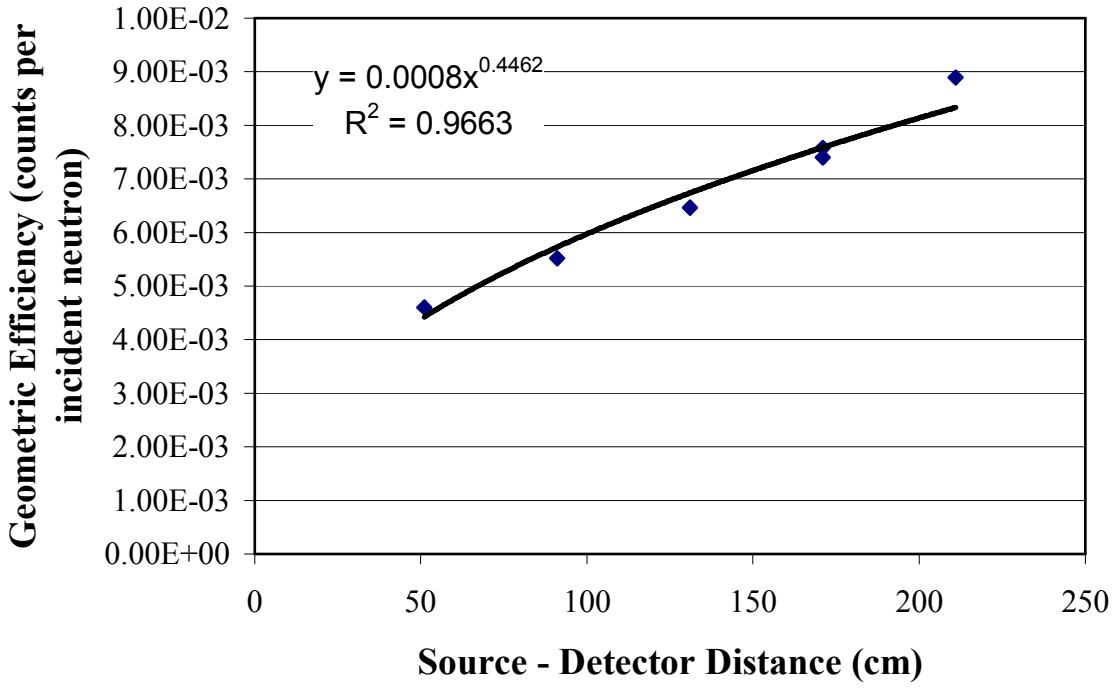

Figure D-1. Geometric Efficiency of Long Counter used to monitor neutron flux for PIN diode irradiations on the Ansto Van de Graff accelerator.

Table D-2. Variation of effective centre of long counter with neutron energy.

Nominal neutron energy (keV)	Distance of effective centre behind front face of detector (cm)
90	1.7
141	2.0
165	2.0
196	2.1
230	2.2
350	2.75
891	3.75
4000	6.0

The geometric efficiencies of the long counter for the experimental setup were derived by extrapolating a curve fitted to the efficiency versus distance data shown in Figure D-1. Use of this curve gives geometric efficiency factors for the nominal neutron energies as shown in Table D-3. That is Table D-3 shows geometric efficiencies corrected for the effective centre of the long counter for each of the neutron energies used to irradiate the PIN diode.

The efficiency of the long counter is relatively energy independent for energies above approximately 1.5 MeV. However since all of the neutrons that we are dealing with will be below this energy it is necessary to make a further energy dependant correction to the long counter efficiency.

Table D-3. Geometric efficiency factors for the Long Counter showing the minimal energy dependence of the geometric efficiency factor due to the change in effective centre of the detector at different neutron energies.

Nominal Neutron Energy (keV)	Geometric Efficiency of Long Counter
90	0.0083
141	0.0083
165	0.0083
196	0.0083
230	0.0080
350	0.0083
891	0.0083

The approximate energy dependence of the long counter was derived from data given by Fowler[203]. The energy dependant efficiencies are as shown in Table D-4. The

efficiency of the long counter taking into account both the geometric and the energy dependant factors is given in Table D-5.

Table D-4. Approximate energy dependant efficiencies for the long counter [203].

Nominal Neutron Energy keV	Relative efficiency (=1 at E > 1.5 MeV)
90	0.863
140	0.871
165	0.875
196	0.879
230	0.885
350	0.902
891	0.984

Table D-5. Overall long counter efficiency at the position and nominal neutron energies used.

Nominal Neutron Energy keV	Relative efficiency (=1 at E > 1.5 MeV)
90	0.007158
140	0.007229
165	0.007262
196	0.007297
230	0.007348
350	0.007498
891	0.008197

APPENDIX E ESTIMATE OF MOATA TC-10 NEUTRON EPITHERMAL FLUX

The cadmium ratio, R_{Cd} is the ratio of activities of bare and cadmium covered foils irradiated under the same conditions:

$$R_{Cd} = \frac{Activation_{Bare}}{Activation_{Cd\ covered}} \qquad \text{E-1}$$

If the spectrum is considered to consist of a Maxwellian thermal component and a *1/E* slowing down component the reaction rate *R* can be represented as:

$$R = \sigma_o \phi_o + I\theta \qquad \text{E-2}$$

Where σ_o is the thermal cross section, ϕ_o is the thermal fluence, *I* is the resonance integral and θ is the flux per unit lethargy. The resonance integral *I* is just:

$$I = \int_{E_1}^{E_2} \frac{\sigma(E)dE}{E} \qquad \text{E-3}$$

Where the limit E_1 is generally taken as the cadmium cutoff (about 0.55eV for 1mm thick Cd), and E_2 is an upper limit of 2 MeV.

From

$$R_{Cd} = \frac{Activation_{Bare}}{Activation_{Cd\ covered}} \qquad \text{E-1}$$

And

$$R = \sigma_o \phi_o + I\theta \qquad \text{E-2}$$

the cadmium ratio can be written as:

$$R_{Cd} = \frac{\sigma_o \phi_o + I\theta}{I\theta} \qquad \text{E-4}$$

Therefore

$$\theta = \frac{\sigma_o \phi_o}{I(R_{Cd} - 1)} \qquad \text{E-5}$$

For simple approximate calculations the resonance integral can be considered to be made up of two components, the resonance part and the *1/v* part upon which the resonance component is superpositioned, i.e.:

$$I = I_{1/v} + I_r \qquad \text{E-6}$$

For Au197 the total measured resonance integral is 1558 barns. The 4.9 eV resonance component I_{r1} is 1180 barns and the 61 eV resonance component I_{r2} is 36 barns. The total resonance component I_r is thus 1216 barns. Therefore the *1/v* component $I_{1/v}$ is 342 barns. The resonance integral must be corrected for self shielding effects. The self shielding correction is applied to the resonance part of the integral. For 20 μm gold foils in a 1/E spectrum the selfshielding factor for the resonance part of the spectrum is approximately 0.4. When this is applied to I_{r1} and I_{r2}

the total effective *I* becomes 828 barns. The thermal cross section, σ_o, is taken as 98 barns. When the corrected value of *I* and the measured R_{Cd} of 38 is substituted into equation E-5 we get an expression for the flux per unit lethargy at ~ 5 eV (for a Au197 foil) in terms of the known thermal flux.

$$\theta = \frac{\phi_o}{313} \qquad \text{E-7}$$

Therefore in first decade (1 eV – 10 eV) the epithermal flux is approximately $2.3\phi_o/313$, and from 10 eV – 100 eV approximately $0.23\phi_o/313$ and similarly for the remainder of the epithermal spectrum. (N.B. 2.3 lethargy units per decade.) This gives a total epithermal fluence of approximately $0.00816\phi_o$.

APPENDIX F FOIL ACTIVATION DATA

Table F-1. Gold foil measured activation in the cylinder phantom exposed in HB11 epithermal neutron beam.

Foil type	Foil #	Activity (Bq)	Mass (mg)	Bq/mg	Bq/atom	Exposure time (minutes)	Sat Act (Bq)	Depth (cm)	Cover
AU	2	3.29E+03	16.44	2.00E+02	6.55E-17	15	2.44555E-14	2	cd
AU	13	7.39E+03	15.06	4.91E+02	1.60E-16	15	5.99412E-14	4	
AU	19	4.17E+02	16.58	2.52E+01	8.23E-18	15	3.07572E-15	6	cd
AU	51	1.88E+03	16.81	1.12E+02	3.66E-17	15	1.36815E-14	8	
AU	53	1.12E+04	16.46	6.82E+02	2.23E-16	15	8.33743E-14	2	
AU	50	8.44E+03	17.09	4.94E+02	1.62E-16	15	6.03507E-14	4	
AU	52	4.47E+03	17.32	2.58E+02	8.45E-17	15	3.15597E-14	6	
AU	47	1.94E+03	16.35	1.19E+02	3.88E-17	15	1.4485E-14	8	
AU	32	6.63E+03	16.96	3.91E+02	1.28E-16	15	4.77428E-14	4	
AU	48	1.55E+03	17.05	9.08E+01	2.97E-17	15	1.1095E-14	8	
AU	33	4.68E+03	16.88	2.77E+02	9.06E-17	15	3.3852E-14	2	
AU	22	7.23E+02	6.6	1.09E+02	3.58E-17	15	1.33775E-14	4	cd
AU	15	3.43E+03	14.49	2.37E+02	7.74E-17	15	2.8902E-14	6	
AU	28	1.07E+02	6.18	1.73E+01	5.65E-18	15	2.11186E-15	8	cd
AU	35	1.45E+04	15.44	9.38E+02	3.07E-16	20.15	8.53531E-14	2	
AU	45	4.35E+03	16.08	2.71E+02	8.85E-17	20.15	2.46321E-14	2	cd
AU	37	1.29E+04	15.66	8.26E+02	2.70E-16	60.4666	2.5132E-14	7	
AU	44	9.33E+02	17.08	5.46E+01	1.79E-17	60.4666	1.66306E-15	7	cd
AU	4	1.54E+04	16.65	9.27E+02	3.03E-16	20	8.50297E-14	2	
AU	5	4.48E+03	15.11	2.96E+02	9.70E-17	20	2.71864E-14	2	cd
AU	29	1.61E+04	17.04	9.43E+02	3.09E-16	20.0666	8.61872E-14	2	

Continued next page …

Table F-1. Continued. (Gold foil measured activation in the cylinder phantom exposed in HB11 epithermal neutron beam.)

Foil type	Foil #	Activity (Bq)	Mass (mg)	Bq/mg	Bq/atom	Exposure time (minutes)	Sat Act (Bq)	Depth (cm)	Cover
AU	46	4.47E+03	17	2.63E+02	8.61E-17	20.0666	2.40516E-14	2	cd
AU	18	1.44E+04	16.29	8.85E+02	2.90E-16	20.0166	8.11002E-14	2	
AU	20	4.37E+03	16.43	2.66E+02	8.69E-17	20.0166	2.43458E-14	2	cd
AU	93	8.46E+02	3.758	2.25E+02	7.37E-17	20.0166	2.06322E-14	2	Li
AU	105	7.38E+02	3.287	2.24E+02	7.34E-17	20.0166	2.05644E-14	2	Li

Table F-2. Copper and Manganese foil measured activation in the cylinder phantom exposed in HB11 epithermal neutron beam.

Foil type	Foil #	Activity (Bq)	Mass (mg)	Bq/mg	Bq/atom	Exposure time (minutes)	Sat Act (Bq)	Depth (cm)	Cover
CU	2	1.53E+04	13.287	1.15E+03	1.22E-16	68.58333	2.04867E-15	2	
CU	10	8.00E+02	13.347	5.99E+01	6.37E-18	68.58333	1.06848E-16	2	cd
CU	15	1.41E+04	13.449	1.05E+03	1.12E-16	180.01666	7.49382E-16	7	
CU	11	1.22E+02	13.407	9.07E+00	9.64E-19	180.01666	6.46924E-18	7	cd
MN	3	7.10E+05	30.64	2.32E+04	2.11E-15	68.58333	7.99969E-15	2	
MN	6	3.72E+04	30.91	1.20E+03	1.10E-16	68.58333	4.15994E-16	2	cd
MN	22	5.47E+05	30.7	1.78E+04	1.63E-15	180.01666	2.93999E-15	7	
MN	17	5.10E+03	30.21	1.69E+02	1.54E-17	180.0167	2.78551E-17	7	cd

Table F-3. Gold foil measured activation in the NKI PMMA cube phantom exposed in HB11 epithermal neutron beam.

Foil type	Foil #	Activity (Bq)	Mass (mg)	Bq/mg	Bq/atom	Exposure time (minutes)	Sat Act (Bq)	Depth (cm)	Cover
AU	x	9.66E+03	12.45	7.76E+02	2.54E-16	15.1666	9.37E-14	2	
AU	83	2.13E+03	3.726	5.72E+02	1.87E-16	30.0333	3.5E-14	2	cd
AU	98	2.81E+03	3.192	8.82E+02	2.88E-16	25.73333	6.29E-14	5	
AU	200	4.56E+03	12.076	3.78E+02	1.24E-16	29.51666	2.35E-14	8	

Table F-4. Bare gold foil measured activation in the skull phantom exposed in HB11 epithermal neutron beam.

Foil type	Foil #	Activity (Bq)	Mass (mg)	Bq/mg	Bq/atom	Exposure time (minutes)	Sat Act (Bq)	Position in phantom
AU	34b	1.99E+04	16.970	1.18E+03	3.84E-16	29.9666	7.19714E-14	a1
AU	24	6.74E+03	6.450	1.05E+03	3.42E-16	29.9666	6.40339E-14	a2
AU	49	5.20E+03	16.300	3.19E+02	1.04E-16	29.9666	1.95441E-14	a3
AU	6	1.77E+03	15.315	1.16E+02	3.78E-17	29.9666	7.07501E-15	a4
AU	31	6.32E+03	15.902	3.97E+02	1.30E-16	29.9666	2.43396E-14	h1
AU	76	8.62E+03	16.168	5.33E+02	1.74E-16	29.9666	3.26488E-14	h2
AU	21	4.08E+03	6.430	6.34E+02	2.07E-16	29.9666	3.88466E-14	h3
AU	9	9.04E+03	16.642	5.43E+02	1.78E-16	29.9666	3.3261E-14	h4
AU	7	7.23E+03	16.592	4.36E+02	1.43E-16	29.9666	2.66978E-14	h5
AU	36	8.64E+03	17.078	5.06E+02	1.66E-16	29.9666	3.09987E-14	v1
AU	27	4.11E+03	6.570	6.25E+02	2.05E-16	29.9666	3.82985E-14	v2
AU	128	9.31E+03	16.455	5.66E+02	1.85E-16	29.9666	3.46477E-14	v3
AU	30	8.33E+03	16.967	4.91E+02	1.61E-16	29.9666	3.00716E-14	v4
AU	38	6.38E+03	16.748	3.81E+02	1.25E-16	29.9666	2.33332E-14	v5

Table F-5. Cadmium covered gold foil measured activation in the skull phantom exposed in HB11 epithermal neutron beam.

Foil type	Foil #	Activity (Bq)	Mass (mg)	Bq/mg	Bq/atom	Exposure time (minutes)	Sat Act (Bq)	Position in phantom
AU	16b	5.71E+03	4.330	1.32E+03	4.32E-16	84.65	2.87E-14	a1
AU	11	7.10E+03	14.505	4.89E+02	1.60E-16	84.65	1.07E-14	a2
AU	41	1.29E+03	16.402	7.86E+01	2.57E-17	84.65	1.71E-15	a3
AU	14	4.47E+02	16.600	2.70E+01	8.82E-18	84.65	5.87E-16	a4
AU	75	1.19E+03	3.709	3.22E+02	1.05E-16	84.65	7.00E-15	h1
AU	87	1.18E+03	3.605	3.28E+02	1.07E-16	84.65	7.14E-15	h2
AU	16a	9.75E+02	3.465	2.81E+02	9.21E-17	84.65	6.13E-15	h3
AU	82	1.18E+03	3.710	3.17E+02	1.04E-16	84.65	6.92E-15	h4
AU	84	1.57E+03	3.805	4.11E+02	1.35E-16	84.65	8.96E-15	h5
AU	80	1.30E+03	3.400	3.84E+02	1.25E-16	84.65	8.35E-15	v1
AU	97	1.19E+03	4.100	2.90E+02	9.47E-17	84.65	6.31E-15	v2
AU	34a	8.03E+02	3.770	2.13E+02	6.97E-17	84.65	4.63E-15	v3
AU	101	5.74E+02	3.390	1.69E+02	5.54E-17	84.65	3.68E-15	v4

REFERENCES

[1] Solares GR, Cano G, Palano J, Zamenhof R, "High resolution quantitative autoradiography and its application to microdosimetry of boron neutron capture therapy", in "Topics in Dosimetry and treatment planning for neutron capture therapy" edited by Zamenhof R, Solares G and Harling O, Advanced Medical Publishing Madison, Wiosconsin 1994, pp13-27.

[2] Charlton DE, Allen BJ, "Monte carlo Calculations of Ion Passages Through Brain Endothelial nuclei During Boron Neutron Capture Therapy", *Int. J. Radiat. Biol*, 1993, 64:6, pp739-747.

[3] Ziegler JF, 1992, TRIM Version '92 (Yorktown , IBM Research).

[4] ICRU (1989) International Commission on Radiation Units and Measurements, *Tissue Substitutes in radiation Dosimetry and Measurement, ICRU Report 44* (International Commission on Radiation Units, Bethesda, Maryland).

[5] Thermal Neutron Cross Sections downloaded from XS averaged from JENDL3.2, Courtesy of T.Nakagawa at JAERI accessed via *http://www.dne.bnl.gov/CoN/* on 11 Apr 2001.

[6] Blue TE, Gupta N, Woollard JE, "A calculation of the energy dependence of the RBE of neutrons", Phys Med Biol 1993 (38):1693-1712.

[7] Moss RL, "Review of Reactor Based Neutron Beam Development for BNCT Applications" in *Advances in Neutron Capture Therapy* edited by Soloway AH et al, Plenum Press, New York, 1993, pp1-7.

[8] Storr GJ, "Assessment of Ideal Neutron beams for Neutron Capture Therapy", *Rad. Res*. 131, pp235-242 (1992).

[9] Yanch JC, Harling OK, "A Monte Carlo Study of Ideal Beams for Epithermal Neutron Beam Development for Boron Neutron Capture Therapy" in *Progress in Neutron Capture Therapy for Cancer* edited by Allen BJ et al, Plenum Press New York 1992, pp 133-136.

[10] Choi JR, Clement SD, Harling OK, Zamenhof RG, "Neutron Capture Therapy Beams at the MIT Research Reactor" in *Neutron Beam Design, Development, and Performance for Neutron Capture Therapy*, edited by Harling OK et al, Plenum Press New York 1990. pp 201 - 218.

[11] Yanch JC, Zhou XL, Brownell GL, "A Monte Carlo Investigation of the Dosimetric Properties of Monoenergetic Neutron Beams for Neutron Capture Therapy" Rad. Res., 126:1-20, 1991.

[12] Wallace SA, Allen BJ, Mathur JN, "Monte Carlo calculations of epithermal boron neutron capture therapy with heavy water", Phys Med Biol, 1995 Oct;40(10):1599-608

[13] _____, Current status of neutron capture therapy, May 2001, IAEA-TECDOC-1223, IAEA Vienna 2001.

[14] Greenwood RC, "The design of Filtered Epithermal Neutron Beams for BNCT" in "Workshop on NCT", BNL Jan 1986, pp123-142, BNL-51994.

[15] Choi JR, Clement SD, Harling OK, Zamenhof RG, "Neutron Capture Therapy Beams at the MIT Research Reactor" in "Neutron Beam Design, Development, and Performance for Neutron Capture Therapy", Edited by OK Harling et al Plenum Press NY 1990, pp201-218.

[16] Ross D, Constantine G, Weaver DR, Beynon TD, "Designing an epithermal neutron beam for boron neutron capture therapy for a DIDO type reactor using MCNP", Nucl Instr & Meth, 1993, A334:596-606.

[17] Liu HB, Brugger RM, Rorer DC, Tichler PR, Hu JP, "Design of a high flux epithermal neutron beam using 235U fission plates at the Brookhaven Medical Research Reactor", Med Phys, 1994, 21(10):1627-1631.

[18] Wangler TP, Stokes RH, "The radio frequency quadrapole linear accelerator", 1981, IEEE Trans Nucl Sci NS-28(2):1494-1499.

[19] Wu TH, Brugger RM, Kunze JF, "Low Energy Accelerator Based Neutron Sources for Neutron Capture Therapy in *Advances in Neutron Capture Therapy* edited by Soloway AH et al, Plenum Press, New York, 1993, pp 105-108.

[20] Dolan TJ, Ottewitte, EH, Wills EE, Neuman WA, Woodal DM, "Non Reactor Neutron Sources for BNCT", EGG-BNCT-8319.

[21] Brugger R, Kunze J, "Performance Report: Accelerator based epithermal neutron source for neutron capture therapy", (1991), DOE/ER/13035—T2, DE-FG07-90ER13035.

[22] Yanch JC, Shefer RE, Hughey BJ, Klinkowstein, "Accelerator Based Epithermal Neutron Beams for Neutron Capture Therapy" in *Advances in Neutron Capture Therapy* edited by Soloway AH et al, Plenum Press, New York, 1993, pp 95 - 98.

[23] Allen DA, Beynon TD, "What is the best proton energy for accelerator-based BNCT using the 7Li(p,n)7Be reaction?", Med Phys 2000 May;27(5):1113-8

[24] Zimin S, Allen BJ. "Evaluation of useful neutron flux for accelerator boron neutron capture therapy using the 7Li(p,n) reaction", Australas Phys Eng Sci Med 1998 Dec;21(4):193-9.

[25] Lee CL, Zhou XL, Kudchadker RJ, Harmon F, Harker YD, "A Monte Carlo dosimetry-based evaluation of the 7Li(p,n)7Be reaction near threshold for accelerator boron neutron capture therapy", Med Phys 2000 Jan;27(1):192-202.

[26] Tanaka K, Kobayashi T, Sakurai Y, Nakagawa Y, Ishikawa M, Hoshi M. "Irradiation characteristics of BNCT using near-threshold 7Li(p, n)7Be direct neutrons: application to intra-operative BNCT for malignant brain tumours" Phys Med Biol 2002 Aug 21;47(16):3011-32

[27] Gierga DP, Yanch JC, Shefer RE, "An investigation of the feasibility of gadolinium for neutron capthure synovectomy", 2000, Med Phys 27(7) 1685-1692.

[28] Howard WB, Yanch JC, Grimes SM, Massey TN, Al-Quaraishi, Jacobs DK, Brent CE, "Measurement of the 9Be(p,n) thick target spectrum for use in accelerator based BNCT" , 1996, Med Phys 23 :1233-1235.

[29] Wang CKC, Moore BR, "Thick Beryllium target as an epithermal neutron source for neutron capture therapy", Med Phys 1994, 21(10):1633-1638.

[30] Randers-Pehrson G, Brenner DJ, "A practical target system for accelerator-based BNCT which may effectively double the dose rate",Med Phys 1998 Jun;25(6):894-6.

[31] Colonna N, Beaulieu L, Phair L, Wozniak GJ, Moretto LG, Chu WT, Ludewigt BA, "Measurements of low-energy (d,n) reactions for BNCT. Boron Neutron Capture Therapy", Med Phys 1999 May;26(5):793-8.

[32] Burlon AA, Kreiner AJ, White SM, Blackburn BW, Gierga DP, Yanch JC, "In-phantom dosimetry for the 13C(d,n)14N reaction as a source for accelerator-based BNCT", Med Phys 2001 May;28(5):796-803.

[33] Yanch JC, Kim JK, Wilson MJ. Design of a californium-based epithermal neutron beam for neutron capture therapy. Phys Med Biol 1993 Aug;38(8):1145-55

[34] Yanch JC, Zamenhof RG, "Dosimetry of 252Cf source for neutron radiotherapy with and without augmentation by boron neutron capture therapy", Radiation Research, 1992, (131):249-256.

[35] Laramore GE, Wootton P, Livesey JC et al, "Boron Neutron Capture Therapy: A mechanism for achieving a concomitant tumour boost in fast neutron radiotherapy", Int J Radiation Oncology Biol Phys 28(5):1135-1142.

[36] Paquis P, Pignol JP, Breteau N., "Radiotherapy of high grade glioma: use of fast neutrons, therapy and enhancement by neutron capture", Neurochirurgie, 2000 Feb;46(1):23-33.

[37] Burmeister J, Kota C, Maughan RL. "Dosimetry of the boron neutron capture reaction for BNCT and BNCEFNT", Strahlenther Onkol 1999 Jun;175 Suppl 2:115-8

[38] Burmeister J, Kota C, Maughan RL, Waker AJ, "Miniature tissue-equivalent proportional counters for BNCT and BNCEFNT dosimetry", Med Phys 2001 Sep;28(9):1911-25.

[39] Kota C, Maughan RL, Tattam D, Beynon TD. "Use of low-pressure tissue equivalent proportional counters for the dosimetry of neutron beams used in BNCT and BNCEFNT", Med Phys 2000 Mar;27(3):535-48.

[40] Maughan RL, "An update on Neutron Radiotherapy" in "Teletherapy Past and Present: Proceedings of the 1996 AAPM Summer School" edited by Mackie TR, Palta JR, Advanced Medical Publishing, Madison Wisconson. pp723-759.

[41] Nigg DW, Wemple CA, Risler R, Hartwell JK, Harker YD, Laramore GE, "Modification of the University of Washington Neutron Radiotherapy Facility for optimization of neutron capture enhanced fast-neutron therapy", Med Phys 2000 Feb;27(2):359-67.

[42] Rogus RD, Harling OK, Yanch JC, "Mixed field dosimetry of epithermal neutron beams for boron neutron capture therapy at the MITR-II research reactor", Med Phys,1994, 21(10):1611-1625.

[43] Raaijmakers CPJ, Watkins PRD, Nottelman EL, Verhagen HW, Jansen JTM, Zoetelief J, Mijnheer BJ, "The neutron sensitivity of dosimeters applied to boron neutron capture therapy", Med Phys, 1996, 23(9):1581-1589.

[44] Martsolf SW, Johnson JE, Vostmyer CE, Albertson BD, Binney SE. "Practical considerations for TLD-400/700-based gamma ray dosimetry for BNCT applications in a high thermal neutron fluence", Health Phys 1995 Dec;69(6):966-70

[45] Gambarini G, Agosteo S, Marchesi P, Nava E, Palazzi P, Pecci A, Rosi G, Tinti R.Appl Radiat Isot, "Discrimination of various contributions to the

absorbed dose in BNCT: Fricke-gel imaging and intercomparison with other experimental results", 2000 Oct-Nov;53(4-5):765-72

[46] Gambarini G, Monti D, Fumagalli ML, Birattari C, Salvadori P. "Phantom dosimeters examined by NMR analysis: a promising technique for 3-D determinations of absorbed dose", Appl Radiat Isot, 1997 Oct-Dec;48(10-12):1477-84

[47] Farajollahi AR, Bonnett DE, Tattam D, Green S, "The potential use of polymer gel dosimetry in boron neutron capture therapy", Phys Med Biol, 2000, 45:N9-N14.

[48] Bond VP, Laster BH, Wielopolski, "The equal effectiveness ratio:a quantitative approach to the evaluation of compounds for boron neutron capture therapy", Radiation Res, 1995, 141:287-293.

[49] Barendsen GW, "The relationships between RBE and LET for different types of lethal damage in mammalian cells: biophysical and molecular mechanisms", Radiation Res, 1994, 139:257-270.

[50] Blue TE, Gupta N, Woollard JE, "A calculation of the energy dependence of the RBE of neutrons", Phys Med Biol, 1993, 38:1693-1712.

[51] Woollard JE, Blue TE, Gupta N, Gahbauer RA. "Development and calculation of an energy dependent normal brain tissue neutron RBE for evaluating neutron fields for BNCT" Health Phys 2001 Jun;80(6):583-9

[52] Beck-Bornholdt HP, "Quantification of relative biological effectiveness, dose modification factor and therapeutic gain factor", Strahlenther. Onkol., 1993, 169:42-47.

[53] Allen BJ. "Dose modification factors in boron neutron capture therapy", Strahlenther Onkol 1993 Jan;169(1):29-33

[54] Coderre JA, Morris GM, "The radiation biology of Boron Neutron Capture Therapy", Radiat Res, 1999, 151:1-18

[55] Fukuda H, Hiratsuka J, Honda C et al, "Boron neutron capture therapy of malignat melanoma using ^{10}B-paraboronophenylalanine with special reference to evaluation of radiation dose and damage to the skin" Radiat Res 1994, 138:435-442.

[56] Fike JR, Gobbel GT, "Central nervous system radiation injury in large animal models" in "Radiation Injury to the Nervous System" edited by Gutin PH, Leibel SA and Sheline GE, Raven Press Ltd New York 1991, pp 113-135.

[57] Burger PC, Boyko OB, "The pathology of central nervous system radiation injury", in "Radiation Injury to the Nervous System" edited by Gutin PH, Leibel SA and Sheline GE, Raven Press Ltd New York 1991, pp 191-208.

[58] Morris GM, Coderre JA, Whitehouse EM, Micca P, Hopewell JW. 'Boron neutron capture therapy: a guide to the understanding of the pathogenesis of late radiation damage to the rat spinal cord" Int J Radiat Oncol Biol Phys 1994 Mar 30;28(5):1107-12

[59] Warren BA, "The Vascular morphology of Tumours" in Tumor Blood Circulation: Angiogenesis, Vascular Morphology and Blood Flow of Experimental and Human Tumors", Edited by HI Peterson, CRC Press, Florida. pp 1-47.

[60] Stewart PA, Farrell CL, Del Maestro RF, "The effect of cellular microenvironment on vessels in the brain. Part 1: Vessel structure in tumour, peritumour and brain from humans with malignant glioma", Int J Radiat Biol, 1991, 60(1/2):125-130.

[61] Farrell, Cl, Farrell CR, Stewart PA, Del Maestro RF, Ellis CG, "The functional microcirculation in a glioma model", Int J Radiat Biol,1991, 60(1/2):131-137.

[62] Morris GM, Coderre JA, Hopewell JW, et al, "Response of the central nervous system to boron neutron capture irradiation: evaluation using rat spinal cord model", Radiother Oncol, 1994, 32:249-255.

[63] Morris GM, Coderre JA, et al "Boron neutron capture irradiation of the rat spinal cord: effects of variable doses of borocaptate sodium", Radiother Oncol 1996, 39:253-259.

[64] Barendsen GW, "Influence of fractionation on normal tissue tolerance", in "Radiation Injury to the Nervous System" edited by Gutin PH, Leibel SA and Sheline GE, Raven Press Ltd New York 1991, pp 57-67.

[65] Hall EJ, "A determination of oxygen enhancement ratio for 252Cf using cultured mammalian cells", Brit J Radiol, 1972, 45:284.

[66] Jain RK, "Determinants of Tumor Blood Flow: A Review", Cancer Research 1988, 48:2641-2658.

[67] Gregoire V, Sindic C, Gahbauer RA, Wambersie A. "Alteration of the blood-brain barrier after irradiation: implication in boron neutron capture therapy" Strahlenther Onkol 1993 Sep;169(9):534-42

[68] Morris GM, Micca PL, Rezvani M, Hopewell JW, Coderre JA. "Boron neutron capture therapy: effects of split dose and overall treatment time" J Neurooncol 2001 Apr;52(2):101-10

[69] Zaider M, Rossi HH, "The synergistic effects of different radiations", Radiat Res, 1980, 83:732-739.

[70] Kellerer AM, Rossi HH, "A generalized formulation of dual radiation action", Radiation Res, 1978, 75:471-488.

[71] Suzuki S, "Survival of chinese hampster V79 cells after irradiation with a mixture of neutrons and ^{60}Co γ rays: experimental and theoretical analysis of mixed irradiation", Radiation Res, 1993, 133:327-333.

[72] McNally NJ, Ronde J, Folkard M, "Interaction between x-ray and α particle damage in V79 cells", Int J Radiat Biol 1988, 53(6):917-920.

[73] Zaider M, Wuu CS, "The biological effects of mixed radiation fields on cellular systems of variable radiosensitivity (OER and cell cycle stage)", in "Topics in Dosimetry and treatment planning for neutron capture therapy" edited by

Zamenhof R, Solares G and Harling O, Advanced Medical Publishing Madison, Wiosconsin 1994, pp55-66.

[74] Haselsberger K, Radner H, Gossler W, Schlagenhaufen C, Pendl G. "Subcellular boron-10 localization in glioblastoma for boron neutron capture therapy with Na2B12H11SH" J Neurosurg 1994 Nov;81(5):741-4

[75] Haritz D, Gabel D, Huiskamp R. "Clinical phase-I study of Na2B12H11SH (BSH) in patients with malignant glioma as precondition for boron neutron capture therapy (BNCT)" Int J Radiat Oncol Biol Phys 1994 Mar 30;28(5):1175-81

[76] Mallesch JL, Moore DE, Allen BJ, et al, "The pharmacokinetics of p-boronophenylalanine.fructose in human patients with glioma and metastatic melanoma", Int. J. Rad. Oncol. Biol. Phys. 28:5, pp1183-1188, 1994.

[77] Kiger WS, Palmer MR, Riley KJ, Zamenhof RG, Busse PM. "A Pharmacokinetic Model for the Concentration of 10B in Blood after Boronophenylalanine-Fructose Administration in Humans" Radiat Res 2001 Apr;155(4):611-618

[78] Ryynanen P, Kangasmaki A, Hiismaki P, Coderre J, Diaz AZ, Kallio M, Laakso J, Kulvik M, Savolainen S. "Non-linear model for the kinetics of 10B in blood after BPA-fructose complex infusion" Phys Med Biol 2002 47(5):737-45

[79] Kubota R, Yamada S, Ishiwata K, Tada M, Ido T, Kubota K. "Cellular accumulation of 18F-labelled boronophenylalanine depending on DNA synthesis and melanin incorporation: a double-tracer microautoradiographic study of B16 melanomas in vivo" Br J Cancer 1993 Apr;67(4):701-5

[80] Ono K, Masunaga SI, Kinashi Y, Takagaki M, Akaboshi M, Kobayashi T, Akuta K. "Radiobiological evidence suggesting heterogeneous microdistribution of boron compounds in tumors: its relation to quiescent cell population and tumor cure in neutron capture therapy" Int J Radiat Oncol Biol Phys 1996 Mar 15;34(5):1081-6

[81] Wyzlic IM, Tjarks W, Soloway AH, Anisuzzaman AK, Rong FG, Barth RF. "Strategies for the design and synthesis of boronated nucleic acid and protein components as potential delivery agents for neutron capture therapy" Int J Radiat Oncol Biol Phys 1994 Mar 30;28(5):1203-13

[82] Liu L, Barth RF, Adams DM, Soloway AH, Reisfeld RA. "Critical evaluation of bispecific antibodies as targeting agents for boron neutron capture therapy of brain tumors" Anticancer Res 1996 Sep-Oct;16(5A):2581-7

[83] Novick S, Quastel MR, Marcus S, Chipman D, Shani G, Barth RF, Soloway AH. "Linkage of boronated polylysine to glycoside moieties of polyclonal antibody; boronated antibodies as potential delivery agents for neutron capture therapy". Nucl Med Biol 2002 Feb;29(2):159-67

[84] Yanagie H, Tomita T, Kobayashi H, Fujii Y, Nonaka Y, Saegusa Y, Hasumi K, Eriguchi M, Kobayashi T, Ono K. "Inhibition of human pancreatic cancer growth in nude mice by boron neutron capture therapy" Br J Cancer 1997;75(5):660-5

[85] Barth RF, Yang W, Rotaru JH, Moeschberger ML, Boesel CP, Soloway AH, Joel DD, Nawrocky MM, Ono K, Goodman JH. "Boron neutron capture therapy of brain tumors: enhanced survival and cure following blood-brain barrier disruption and intracarotid injection of sodium borocaptate and boronophenylalanine" Int J Radiat Oncol Biol Phys 2000 Apr 1;47(1):209-18

[86] Barth RF, Yang W, Bartus RT, Rotaru JH, Ferketich AK, Moeschberger ML, Nawrocky MM, Coderre JA, Rofstad EK. "Neutron capture therapy of intracerebral melanoma: enhanced survival and cure after blood-brain barrier opening to improve delivery of boronophenylalanine" Int J Radiat Oncol Biol Phys 2002 Mar 1;52(3):858-68

[87] Yang W, Barth RF, Rotaru JH, Boesel CP, Wilkie DA, Bresnahan JC, Hadjiconstantinou M, Goettl VM, Joel DD, Nawrocky MM. "Boron neutron capture therapy of brain tumors: functional and neuropathologic effects of

blood-brain barrier disruption and intracarotid injection of sodium borocaptate and boronophenylalanine" J Neurooncol 2000 Jul;48(3):179-90

[88] Nichols TL, Kabalka GW, Miller LF, Khan MK, Smith GT. Improved treatment planning for boron neutron capture therapy for glioblastoma multiforme using fluorine-18 labeled boronophenylalanine and positron emission tomography. Med Phys 2002 Oct;29(10):2351-8

[89] J. Capala, R. Ma, A.Z. Diaz, A.D. Chanana, J.A. Coderre "Implementation of BNCT treatment planning procedures" In IAEA-TECDOC-1223, "Current status of neutron capture therapy." Vienna: International Atomic Energy Agency; 2001. p. 206-215.

[90] R.G. Zamenhof, M.R. Palmer, P.M. Busse "Clinical treatment planning for subjects undergoing boron neutron capture therapy at Harvard-MIT" In IAEA-TECDOC-1223, "Current status of neutron capture therapy." Vienna: International Atomic Energy Agency; 2001. p. 206-215.

[91] Zamenhof R, Redmond E, Solares G et al "Monte Carlo based treatment planning for boron neutron capture therapy using custom designed models automatically generated from CT data", Int J Radiation Oncology Biol Phys 35(2):383-397.

[92] Harling OK, Rogus R, Choi JR, Moulin DJ, Zamenhof RG, Yanck JC, "Dosimetry and dose control for clinical trials of neutron capture therapy at the MITR_II reactor" in "Topics in dosimetry an treatment planning for neutron capture therapy", Zamenhof RG, Solares G, Harling O, Editors, Advanced Medical Publishing, Madison Wisconsin 1994.

[93] Wojnecki C, Green S. "A preliminary comparative study of two treatment planning systems developed for boron neutron capture therapy: MacNCTPlan and SERA" Med Phys 2002 Aug;29(8):1710-5

[94] See detailed online manual that can be accessed at: http://www.cs.montana.edu/~bnct/

[95] Kotiluoto P, Hiisamaki P, Savolainen S. “Application of the new MultiTrans SP3 radiation transport code in BNCT dose planning” Med Phys 2001 Sep;28(9):1905-10

[96] Albertson BJ, Blue TE, Niemkiewicz J. “An investigation on the use of removal-diffusion theory for BNCT treatment planning: a method for determining proper removal-diffusion parameters” Med Phys 2001 Sep;28(9):1898-904

[97] Sauerwein W, Zurlo A, "The EORTC Boron Neutron Capture Therapy (BNCT) Group: achievements and future projects", Eur J Cancer 2002 Mar;38 Suppl 4:S31-4

[98] Smilowitz HM, Micca PL, Nawrocky MM, Slatkin DN, Tu W, Coderre JA. "The combination of boron neutron-capture therapy and immunoprophylaxis for advanced intracerebral gliosarcomas in rats", J Neurooncol 2000;46(3):231-40

[99] Diaz AZ, Coderre JA, Chanana AD, Ma R, "Boron neutron capture therapy for malignant gliomas", Ann Med 2000 Feb;32(1):81-5

[100] Hideghety K, Sauerwein W, Haselsberger K, Grochulla F, Fankhauser H, Moss R,Huiskamp R, Gabel D, de Vries M. "Postoperative treatment of glioblastoma with BNCT at the Petten irradiation facility (EORTC protocol 11,961)" Strahlenther Onkol 1999 Jun;175 Suppl 2:111-4

[101] Barth RF, Yang W, Bartus RT, Rotaru JH, Ferketich AK, Moeschberger ML, Nawrocky MM, Coderre JA, Rofstad EK., "Neutron capture therapy of intracerebral melanoma: enhanced survival and cure after blood-brain barrier opening to improve delivery of boronophenylalanine", Int J Radiat Oncol Biol Phys 2002 Mar 1;52(3):858-68

[102] Fukuda H, Honda C, Wadabayashi N, Kobayashi T, Yoshino K, Hiratsuka J, Takahashi J, Akaizawa T, Abe Y, Ichihashi M, Mishima Y. "Pharmacokinetics of 10B-p-boronophenylalanine in tumours, skin and blood of melanoma

patients: a study of boron neutron capture therapy for malignant melanoma" Melanoma Res 1999 Feb;9(1):75-83

[103] Dagrosa MA, Viaggi M, Kreimann E, Farias S, Garavaglia R, Agote M, Cabrini RL,Dadino JL, Juvenal GJ, Pisarev MA. "Selective uptake of p-borophenylalanine by undifferentiated thyroid carcinoma for boron neutron capture therapy", Thyroid 2002 Jan;12(1):7-12

[104] Miura M, Morris GM, Micca PL, Lombardo DT, Youngs KM, Kalef-Ezra JA, Hoch DA,Slatkin DN, Ma R, Coderre JA., "Boron Neutron Capture Therapy of a Murine Mammary Carcinoma using a Lipophilic Carboranyltetraphenylporphyrin", Radiat Res 2001 Apr;155(4):603-610

[105] Allen BJ, Wallace SA, Carolan MG, "Can epithermal BNCT treat primary and metastatic liver cancer?" in Advances in NCT, vol 1, B Larsson, J Crawford, R Weinreich, Elsevier Science 1997 pp.118-121.

[106] Yanagie H, Tomita T, Kobayashi H, Fujii Y, Nonaka Y, Saegusa Y, Hasumi K,Eriguchi M, Kobayashi T, Ono K. "Inhibition of human pancreatic cancer growth in nude mice by boron neutron capture therapy", Br J Cancer 1997;75(5):660-5

[107] De Vita, Hall, Cancer: Principles and Practice of Oncology, 6th Edition, Lippincott Williams & Wilkins

[108] Nelson JS, Tsukada Y, Shoenfeld D et al, "Necrosis as a prognostic criterion in malignant supratentorial astrocytic gliomas", Cancer 52(3): 550-554, 1983.

[109] Barth RF, Soloway AH, Fairchild RG, "Boron Neutron Capture Therapy for Cancer", *Scientific American*, October 1990, pp100-107.

[110] Sweet WH., "Early history of development of boron neutron capture therapy of tumors" J Neurooncol 1997 May;33(1-2):19-26

[111] Fairchild RG, Benary V, Kalef-Ezra J, et al "An Optimised Epithermal Neutron Beam for Neutron Capture Therapy (NCT) at the Brookhaven Medical Research Reactor (BMRR)" in *Progress in Neutron Capture Therapy for Cancer* edited by Allen BJ, et al, Plenum Press New York 1992, pp1-6.

[112] Barth RF, Soloway AH, Fairchild RG, Brugger RM, "Boron Neutron Capture Therapy for Cancer", *Cancer* 1995 70:12, pp2995-3007.

[113] Hatanaka H, Sano K, Yasukochi H, "Clinical results of Boron Neutron Capture Therapy" *in Progress in Neutron Capture Therapy for Cancer* edited by Allen BJ, et al, Plenum Press New York 1992, pp 561-568.

[114] Hideghety K, Sauerwein W, Haselsberger K, Grochulla F, Fankhauser H, Moss R, Huiskamp R, Gabel D, de Vries M. "Postoperative treatment of glioblastoma with BNCT at the petten irradiation facility (EORTC protocol 11,961)" Strahlenther Onkol 1999 Jun;175 Suppl 2:111-4

[115] Sauerwein W, Zurlo A; EORTC Boron Neutron Capture Therapy Group. "The EORTC Boron Neutron Capture Therapy (BNCT) Group: achievements and future projects" Eur J Cancer 2002 Mar;38 Suppl 4:S31-4

[116] J.Burian, M.Marek, J.Rataj, et al "Report on the First Patient Group of the Phase I BNCT Trial at the LVR-15 Reactor" accessed on 28 April 2003 at http://www.csvts.cz/cns/news/030311r.pdf

[117] Beth Israel Deaconess Medical Centre / MIT BNCT web site.

[118] Chadha M, Capala J, Coderre JA, Elowitz EH, Iwai J, Joel DD, Liu HB, Wielopolski L, Chanana AD. "Boron neutron-capture therapy (BNCT) for glioblastoma multiforme (GBM) using the epithermal neutron beam at the Brookhaven National Laboratory" Int J Radiat Oncol Biol Phys 1998 Mar 1;40(4):829-34

[119] A.Z. Diaz "The Phase I/II BNCT Trials at the Brookhaven medical nresearch reactor: Critical considerations", In IAEA-TECDOC-1223, "Current status of neutron capture therapy." Vienna: International Atomic Energy Agency; 2001. p. 257–267.

[120] Sauerwein W, Hideghety K, Rassow J, *et al.* First clinical results from the EORTC phase I trial "Postoperative treatment of glioblastoma with BNCT at the Petten irradiation facility." In IAEA-TECDOC-1223, "Current status of

neutron capture therapy." Vienna: International Atomic Energy Agency; 2001. p. 250–256.

[121] Verbakel WF, Sauerwein W, Hideghety K, Stecher-Rasmussen F. "Boron concentrations in brain during boron neutron capture therapy: in vivo measurements from the phase I trial EORTC 11961 using a gamma-ray telescope" Int J Radiat Oncol Biol Phys 2003 Mar 1;55(3):743-56

[122] Messenger GC, Ash MS, "The effects of radiation on electronic systems" Van Nostrand Reinhold NewYork 1992, p198.

[123] Rogers VC, HarrisL, Steinman DK, Bryan DE, "Silicon Ionisation and Displacement KERMA d\for Neutrons from Thermal to 20 MeV", IEEE Trans Nucl Sci, 1975, NS-22(6): 2326-2329.

[124] Ougouag, AM, Williams JG, Danjaji MB, Yang JL, Meason JL, "Differential displacement KERMA cross sections for neutron interactions in Si and GaAs", IEEE Trans Nucl Sci, 1990, NS-37(6 part II):1937-1944.

[125] ASTM Committee E-10, "Standard Practice for Characterising Neutron Energy Fluence Spectra in Terms of an Equivalent Monoenergetic Neutron Fluence for Radiation Hardness Testing of Electronics", 1993, ASTM E 722-93, American Society for Testing and Materials.

[126] Swartz JM, Thurston MO, Analysis of the Effect of Fast Neutron Bombardment on the Current-Voltage Characteristic of a Conductivity Modulated p-i-n Diode, Journal of Applied Physics 1966, 37(2):745-755.

[127] Van Antwerp WR, Youngblood JE, Calculated and Measured Displacement Damage in Silicon for Monoenergetc Neutrons, IEEE Trans Nucl Sci, 1977, NS-24 (6): 2521-2526.

[128] Aschalom M, Florian RJ, Tatcher M, "Neutron Dosimetry: an PIN diode reader", November 1985, Fermi National Accelerator Laboratory, FN-426.

[129] Nagarkar V, Entine G, Stoppel L, CirignanoL, Swinehart P, "Solid State Neutron Dosimeter for Space Applications", IEEE Trans Nucl Sci 1992, 39(4); 966-970.

[130] Speers RR, "Neutron Energy Dependence of Excess Charge Carrier Lifetime degradation in Silicon", IEEE Trans Nucl Sci. 1968 NS-15(5): 9-17.

[131] Various reader circuits were constructed throughout the course of this work. This one which was used for the measurements at Petten was initially prototyped on a breadboard and then constructed on a printed circuit board by H Meriaty at ANSTO.

[132] All work in this thesis was performed with PIN diodes fabricated from low resistivity silicon. It was later demonstrated by Anatoly Rosenfeld (Centre for Medical Radiation Physics, University of Wollongong) that a PIN diode with a base of high purity, high resistivity silicon can achieve greater linear range and greater sensitivity when used as a dosimeter.

[133] Zhou X, Lim KY, Lim D, "A simple and Unambiguous definition of threshold voltage and its implications in Deep-Submicron MOS device modelling", IEEE Trans Electron Dev. 1999, 46(4):807-809.

[134] Rosenfeld AB, Lerch ML, Kron T, Brauer-Krisch E, Bravin A, Holmes-Siedle A, Allen BJ, "Feasibility study of online high-spatial-resolution MOSFET dosimetry in static and pulsed x-ray radiation fields", IEEE Trans Nucl Sci, 2001, 48(6):2061-2068.

[135] Buehler MG, Blaes BR, Soli GA, Tardio GR, "On-chip, pMOSFET dosimetry", IEEE Trans Nucl Sci 1993, 40:1442-1449.

[136] Kaplan G, "Integral and pulse mode silicon dosimetry for dose verification on radiation oncology modalities", PhD Thesis, Department of Engineering Physics, University of Wollongong, 2001.

[137] Freeman R, Holmes-Siedle "A simple model for predicting radiation effects in MOS devices", IEEE Trans Nucl Sci, 1978, NS-25 (6):1216-1225.

[138] McGarrity JM, "Considerations for hardening MOS devices and circuits for low radiation doses", IEEE Trans Nucl Sci 1980, NS-27 (6): 1739-1744.

[139] Fleetwood DM, Winokur PS, Riewe LC, Flament O, Paillet P, Leray JL, "The role of electron transport and trapping in MOS Total Dose modeling", 1999, IEEE Trans. Nucl. Sci. NS-46 (6): 1519 - 1525.

[140] Hughes RC, "Charge carrier transport phenomenon in amorphous SiO2: Direct Measurement of the drift mobility and lifetime" Phys Rev Lett 30, 1333 (1973).

[141] Brown DB, Dozier CM, "Electron Hole recombination in irradiated SiO2 from a microdosimetry viewpoint", IEEE Trans Nucl Sci., 1981, NS-28(6):4142-4144.

[142] Dozier CM, Brown DB, "Effect of photon energy on the response of MOS devices", IEEE Trans Nucl Sci 1981, NS-28(6): 4137-4141.

[143] Boesch HE, McGarrity JM, IEEE Trans Nucl Sci., 1976, NS-23 (6): 1520

[144] Sour JR, Chiu KY, IEEE Trans Nucl Sci, 1977, NS-24(6): 2040

[145] Curtis OL, Srour JR, Chiu KY, J Appl Phys, 1974, 45, 4506.

[146] Messenger GC, Ash MS, "The effects of radiation on electronic systems"Van Nostrand Reinhold NewYork 1992, p 298.

[147] Long DM, Millward DG, Wallace J, "Dose enhancement effects in semiconductor devices", IEEE Trans Nucl Sci, 1982, NS-29(6): 1980-1984.

[148] Fleetwood DM, Winokur PS, Lorence LJ, Beezhold W, Dressendorfer PV, Schwank JR, "The response of MOS devices to dose-enhanced low energy radiation", IEEE Trans Nucl Sci, 1986 NS-33 (6): 1245-1251.

[149] Hamm RN, "Dose calculations for Si-SiO_2Si layered structures irradiated by x-rays and ^{60}Co gamma rays", IEEE Trans Nucl Sci NS-33(6): 1236-1239.

[150] Soubra M, Cygler J, Mackay G, Thompson I, Ribes A, "Evaluation of dual bias, dual metal oxide silicon semiconductor field effect transistor detector as radiation dosimeters", Med Phys, 1994, 21:567-572.

[151] Temperature stabilisation using the pn junction in the MOSFETs has been developed and refined by A Rosenfeld at the University of Wollongong.

[152] Kronenberg S, Bruker GJ, "The use of hydrogenous material for sensitizing pMOS dosimeters to neutrons", IEEE Trans Nucl Sci, 42(1): 20-26.

[153] Blamires NG, Totterdel DHJ, Holmes-Siedle A, Adams L, "PMOS Dosimeters: Long term annealing and neutron response", IEEE Trans Nucl Sci, 1986, 33(6):1310-1314.

[154] J.L. Titus and C.F. Wheatley, "Experimental Studies of Single Event Gate Rupture and Burnout in Vertical Power MOSFETs", *IEEE Trans. Nuc. Sci.,* NS-43, 533, April 1996

[155] A.B. Rosenfeld, M.G. Carolan, G.I. Kaplan, E.J.Allen, V.I. Khivrich, "MOSFET Dosimeters: The Role of Encapsulation on Dosimetric Characteristics in Mixed Gamrna-Neutron and Megavoltage X-ray Fields", in *IEEE Trans. Nuc. Sci.* 1995, *NS42, N6 Dec 1995* pp1870-1877.

[156] Soubra M, Cygler J, Mackay G, Evaluation of a dual bias dual metal oxide-silicon semiconductor field effect transistor detector as radiation dosimeter, Med Phys 1994 Apr;21(4):567-72.

[157] Gladstone DJ, Chin LM, Automated data collection and analysis system for MOSFET radiation detectors, Med Phys 1991 May-Jun;18(3):542-8

[158] Dong SL, Chu TC, Lan GY, Wu TH, Lin YC, Lee JS. Characterization of high-sensitivity metal oxide semiconductor field effect transistor dosimeters system and LiF:Mg,Cu,P thermoluminescence dosimeters for use in diagnostic radiology, Appl Radiat Isot 2002 Dec;57(6):883-91.

[159] Dong SL, Chu TC, Lee JS, Lan GY, Wu TH, Yeh YH, Hwang JJ. Estimation of mean-glandular dose from monitoring breast entrance skin air kerma using a high sensitivity metal oxide semiconductor field effect transistor (MOSFET) dosimeter system in mammography, Appl Radiat Isot 2002 Dec;57(6):791-9

[160] Hintenlang KM, Williams JL, Hintenlang DE. A survey of radiation dose associated with pediatric plain-film chest X-ray examinations, Pediatr Radiol 2002 Nov;32(11):771-7

[161] Sessions JB, Roshau JN, Tressler MA, Hintenlang DE, Arreola MM, Williams JL, Bouchet LG, Bolch WE, Comparisons of point and average organ dose within an anthropomorphic physical phantom and a computational model of the newborn patient, Med Phys 2002 Jun;29(6):1080-9

[162] Pomije BD, Huh CH, Tressler MA, Hintenlang DE, Bolch WE, Comparison of angular free-in-air and tissue-equivalent phantom response measurements in p-MOSFET dosimeters, Health Phys 2001 May;80(5):497-505.

[163] Peet DJ, Pryor MD, Evaluation of a MOSFET radiation sensor for the measurement of entrance surface dose in diagnostic radiology, Br J Radiol 1999 Jun;72(858):562-8

[164] Bower MW, Hintenlang DE, The characterization of a commercial MOSFET dosimeter system for use in diagnostic x ray, Health Phys 1998 Aug;75(2):197-204

[165] Butson MJ, Rozenfeld A, Mathur JN, Carolan M, Wong TP, Metcalfe PE A new radiotherapy surface dose detector :the MOSFET. Med Phys 1996 May;23(5):655-8

[166] Kron T, Rosenfeld A, Lerch M, Bazley S, Measurements in radiotherapy beams using on-line MOSFET detectors, Radiat Prot Dosimetry 2002;101(1-4):445-8.

[167] Rosenfeld AB, MOSFET dosimetry on modern radiation oncology modalities, Radiat Prot Dosimetry 2002;101(1-4):393-8.

[168] Quach KY, Morales J, Butson MJ, Rosenfeld AB, Metcalfe PE., Measurement of radiotherapy x-ray skin dose on a chest wall phantom. Med Phys 2000 Jul;27(7):1676-80

[169] Scalchi P, Francescon P, Calibration of a mosfet detection system for 6-MV in vivo dosimetry, Int J Radiat Oncol Biol Phys 1998 Mar 1;40(4):987-93.

[170] Ramani R, Russell S, O'Brien P, Clinical dosimetry using MOSFETs, Int J Radiat Oncol Biol Phys 1997 Mar 1;37(4):959-64

[171] Chuang CF, Verhey LJ, Xia P, Investigation of the use of MOSFET for clinical IMRT dosimetric verification, Med Phys 2002 Jun;29(6):1109-15

[172] Orion I, Rosenfeld AB, Dilmanian FA, Telang F, Ren B, Namito Y, Monte Carlo simulation of dose distributions from a synchrotron-produced microplanar beam array using the EGS4 code system, Phys Med Biol 2000 Sep;45(9):2497-508.

[173] Kaplan GI, Rosenfeld AB, Allen BJ, Booth JT, Carolan MG, Holmes-Siedle A, Improved spatial resolution by MOSFET dosimetry of an x-ray microbeam, Med Phys 2000 Jan;27(1):239-44

[174] Howell RW, Goddu SM, Rao DV, Design and performance characteristics of an experimental cesium-137 irradiator to simulate internal radionuclide dose rate patterns, J Nucl Med 1997 May;38(5):727-31.

[175] Gladstone DJ, Chin LM, Real-time, in vivo measurement of radiation dose during radioimmunotherapy in mice using a miniature MOSFET dosimeter probe, Radiat Res 1995 Mar;141(3):330-5.

[176] Gladstone DJ, Lu XQ, Humm JL, Bowman HF, Chin LM, A miniature MOSFET radiation dosimeter probe, Med Phys 1994 Nov;21(11):1721-8

[177] Edwards CR, Green S, Palethorpe JE, Mountford PJ, The response of a MOSFET, p-type semiconductor and LiF TLD to quasi-monoenergetic x-rays. Phys Med Biol 1997 Dec;42(12):2383-91

[178] Kron T, Duggan L, Smith T, Rosenfeld A, Butson M, Kaplan G, Howlett S, Hyodo K, Dose response of various radiation detectors to synchrotron radiation, Phys Med Biol 1998 Nov;43(11):3235-59

[179] Kelleher A, Lane W, Adams L, "A design solution to increasing the sensitivity of pMOS dosimeters: the stacked RADFET approach", IEEE Trans Nucl Sci 1995, 42(1):48-51.

[180] Conneely C, O'Connel BO, Hurley P, Lane W, Adams I, "Strategies for millirad sensitivity in PMOS dosimeters", IEEE Trans Nucl Sci, 1998, 45:1475-1480.

[181] Rosenfeld AB, Kaplan GI, Kron T, Allen BJ, Dilmanian A, Orion I, Ren B, Lerch MLF, Holmes-Seidle A, "MOSFET dosimetry of an X-ray microbeam", IEEE Trans Nucl Sci, 1999, 46(6):1774-1780.

[182] MCNP – A general Monte Carlo N-Particle transport Code Version 4A, La-12625-M, Nov 1993.

[183] Van de Graff irradiation facility, Australian Nuclear Science and Technology Organisation, Lucas Heights NSW Australia.

[184] Kron T, Duggan L, Smith T, Rosenfeld A, Butson M, Kaplan G, Howlett S, Hyodo K. Dose response of various radiation detectors to synchrotron radiation. Phys Med Biol. 1998 Nov;43(11):3235-59.

[185] GAMMEX RMI, P.O. Box 620327 Middleton, WI 53562-0327 USA.

[186] Mohan R, Chui C, Lidofsky L. Energy and angular distributions of photons from medical linear accelerators, Med Phys 1985 Sep-Oct;12(5):592-7

[187] Butson MJ, Yu P, Kan M, Carolan M, Young E, Mathur JN, Metcalfe PE. Skin dose reduction by a clinically viable magnetic deflector. Australas Phys Eng Sci Med. 1997 Jun;20(2):107-11.

[188] Briesmeister JF, MCNP – A General Monte Carlo N-Particle Transport Code, LA-12625M, 1993, p 2-59.

[189] Allen BJ, Corderoy-Buck S, Mallesch JL, Crotty K, Moore DE, “Local control of subcutaneous murine melanoma xenografts in nude mice by neutron capture therapy, 1992, Melanoma Research 2:253-262.

[190] Allen BJ, Neutron capture therapy research in Australia. Pigment Cell Res. 1989 Jul-Aug;2(4):235-9.

[191] Allen, BJ, Corderoy-Buck, S, Moore DE, Mishima Y, Ichihashi M, "Local Control of Murine Melanoma Xenografts in Nude Mice by Neutron Capture Therapy" in Progress in Neutron Capture Therapy for Cancer (1992) , Allen BJ, Moore DE, Harrington BV Editors, Plenum Press NY pp 425-428.

[192] XCOM1 (Version 1.3) M J Berger 17 June 1991, on KAERI web site.

[193] Raaimakers CPJ, Konijnenberg MW, Mijnheer BJ Clinical Dosimetry of an epithermal neutron beam for boron neutron capture therapy; dose distributions under reference conditions. Int J Radiat. Oncol. Biol Phys 37: 941-951, 1997.

[194] Wallace S, PhD Thesis, University of Wollongong 1996.

[195] Gabel D, Goals of the European Collaboration on Boron Neutron Capture Therapy, in Progress in Neutron Capture Therapy for Cancer, Allen BJ, Moore DE, Harrington BV Eds, Plenum Press New York 1992. P32.

[196] Watkins P, Constantine G, Stecher Rasmussen F, Freundenreich W, Moss RL, Ricchena "MCNP Calculations for the design and characterisation of the Petten BNCT Epithermal neutron Beam in Progress in Neutron Capture Therapy for Cancer, Allen BJ, Moore DE, Harrington BV Eds, Plenum Press New York 1992. P 71.

[197] Moss Rl, Stecher-Rasmussen F, Ravensberg K, Constantine G, Watkins P, "Design, Construction and Installation of and Epithermal Neutron Beam for BNCT at the High Flux Reactor Petten" in Progress in Neutron Capture Therapy for Cancer, Allen BJ, Moore DE, Harrington BV Eds, Plenum Press New York 1992. p 63.

[198] Goodman LJ, Health Physics 24:71, 1973.

[199] ICRU, Photon, electron, proton and neutron interaction data for body tissues, ICRU Report 46, 1992

[200] Raaijmakers CPJ, Konijnenberg MW, Herhagen HW, Mijnheer BJ, “Determination of Dose Components in phantoms irradiated with an

epithermal neutron beam for boron neutron capture therapy", Med Phys 1995, 22(3):321-329.

[201] Liu HB, Greenberg DD, Capala J, Wheeler F, "An improved neutron collimator for brain tumour irradiations in clinical boron neutron capture therapy", Med Phys 23(12):2051-2060, Dec 1996

[202] HB Liu, RM Brugger, DD Greenberg, DC Rorer, JP Hu, HM Hauptman, "Enhancement of the Epithermal Neutron Beam used for Boron Neutron Capture Therapy" Int J Radiation Oncology Biol Phys. Vol 28, No. 5, pp 1149-1156, 1994.

[203] WD Allen, "Flat Response Counters" in "Fast Neutron Physics: Part 1", JB Marion and JL Fowler Editors, Interscience Publishers NY 1960, p366.